Graduate School Form
30 Updated 12/26/2015

PURDUE UNIVERSITY
GRADUATE SCHOOL
Thesis/Dissertation Acceptance

This is to certify that the thesis/dissertation prepared

By Katie Nicole Lawrence

Entitled

TUNING OPTOELECTRONIC PROPERTIES OF SMALL SEMICONDUCTOR NANOCRYSTALS THROUGH SURFACE LIGAND CHEMISTRY

For the degree of Doctor of Philosophy

Is approved by the final examining committee:

Rajesh Sardar
Chair

Barry Muhoberac

Chengde Mao

Garth Simpson

To the best of my knowledge and as understood by the student in the Thesis/Dissertation Agreement, Publication Delay, and Certification Disclaimer (Graduate School Form 32), this thesis/dissertation adheres to the provisions of Purdue University's "Policy of Integrity in Research" and the use of copyright material.

Approved by Major Professor(s): Rajesh Sardar

Approved by: Eric C. Long 6/6/2016

Head of the Departmental Graduate Program Date

TUNING OPTOELECTRONIC PROPERTIES OF SMALL SEMICONDUCTOR NANOCRYSTALS THROUGH SURFACE LIGAND CHEMISTRY

A Dissertation

Submitted to the Faculty

of

Purdue University

by

Katie N. Lawrence

In Partial Fulfillment of the

Requirement for the Degree

of

Doctor of Philosophy

August 2016

Purdue University

Indianapolis, Indiana

For my family; together we have succeeded. This accomplishment is as much yours as it is mine. Thank you for your love and support.

ACKNOWLEDGEMENTS

Nothing is possible without the Lord. Through the good and the bad, I know He is with me. I thank God for the blessings He has bestowed upon me and the strength to hold fast to my goals. *1st Corinthians 1:8.*

To my loving and supportive husband, we finally made it. Without your support, none of this would have been possible. I know it wasn't always easy, and I really appreciate you putting up with my stressed out mood swings and my many, many tears. And thank you for being such a wonderful daddy. To my dearest Luka, you are mommy's greatest accomplishment. Thank you for always putting a smile on my face, even after a long day. And to Stella, thank you for keeping me company while I studied for cumulative and class exams and wrote numerous manuscripts. I love my beautiful little family. Together we did we accomplished this goal.

To my parents, Doug and Pam Foster, it is your never ending support that brought me to this point in my life. Mom, thank you for late night study sessions on "LaMer and Vinegar". You are probably the only person who truly knows how hard I fought to get to here… mostly because you were right there making sure I did. Daddy, thank you for always being proud of me, even when I wasn't proud of myself. Your love and support has never gone unnoticed. You are the hardest working person I know, and I like to think I tend to take after you.

To my Grandparents, you are the anchors in my life. Grandma, you introduced me to science at an early age. Our nature walks and outside classrooms are some of my first memories, and I truly believe they helped shape my future as a chemist. Grandpa, your will to do anything you put your mind to is a true inspiration. And the name you have made for yourself is nothing short of awe-inspiring. I hope to do the same one day. Thank you for showing me anything is possible.

To my aunts, Linda and Dee; uncles, Rob and Mick; and cousin, Elyse; thank you for your moral support. You all have been there for me through my high school, undergraduate, and graduate school. Thank you for always listening and for being my constant cheerleaders. Thank you for care packages, visits, and prayers. I can never express how much all of that has meant to me and how much each of you means to me. Elyse, never lose sight of what's important in life and never accept the word "no". Nothing is impossible and with a lot of hard work, sweat, and tears, you can accomplish anything you want in life.

To my parents, in-laws, and extended family, thank you all for being a shoulder to lean on and my ultimate support system. I want to give you a very big thank you for taking care of Luka when mommy needed to work. I never once had to worry that he was missing out because mommy wasn't there. I always knew he was surrounded by loving family.

To my friends, Jessica, Kelly, and Meghan, thank you for keeping me lucid. I know you have all questioned my sanity along the way, but I truly believe that you girls have kept me grounded. I really appreciate our talks and our girl's nights. Thank you.

To those educators who really took time to influence my life, thank you. You made this all possible. To my lab both past and present, Gayatri, Thakshila, Meghan, Charles, Sukanta, and Dr. Sardar, thank you for your support and help along the way. It has been your actions that shaped my career as a graduate student.

Lastly, I want to extend a special thank you to a few AMAZING people I've had the privilege of getting to know both at IUPUI and Ball State. Cary, you are probably one of the most underappreciated yet most deserving people at IUPUI. I'm sorry that other people can't realize just how much you do each and every day. Whenever I had a problem or something needed fixed, you were always there to help. I really appreciated it! Thank you! Kitty and Summer, thank you for always finding the answer to my questions and doing it with a smile. You both went above and beyond to help me through this process. Dr. Long and Barry, thank you for always being my confidants. I have really appreciated our talks, whether they be about hedgehogs, spilled nail polish, people living in cardboard boxes, or "occasionally" chemistry. Dr. Ganezda, Dr. Lang, and Dr. Storhoff, I want to send a special thank you for helping prepare me for my graduate career. My time at Ball State was a wonderful experience and each of you helped make it that way. Additionally, I want to thank my committee members: Dr. Sardar, Dr. Muhoberac, Dr. Mao, and Dr. Simpson. I appreciate all you have done for me.

In conclusion, thank you, my reader. I hope this dissertation provides insight into the questions you pursue. Best wishes.

TABLE OF CONTENTS

Page

Page

Page

Page

Page

Page

LIST OF TABLES

Table Page

LIST OF FIGURES

Figure Page

Figure Page

Figure Page

Figure Page

Figure Page

LIST OF ABBREVIATIONS

AOP	advanced oxidation processes
Au	gold
Cd	cadmium
Cu	copper
CV	cyclic voltammetry
DAQ	data acquisition card
DCM	dichloromethane
DCTB	2-[(2E)-3-(4-tert-butylphenyl)-2-methylprop-2 enylidene]malononitrile
DDT	dodecanethiol
DFT	density functional theory
DMPD	dimethyl-4-phenylenediamine
EDS	energy-dispersive X-ray spectroscopy
e/h	electron/hole
eV	electron volt
FE-SEM	field-emission scanning electron microscopy
FET	field-effect transistor
FTIR	fourier transform infrared spectroscopy

fwhm	full width half maxima
HDA	hexadecylamine
$HO^{\bullet}$	hydroxide
HOMO	highest occupied molecular orbital
HRTEM	high-resolution transmission electron microscopy
HT	1-hexanethiol
In	indium
LDA	local density approximation
LED	light emitting diode
LSPR	localized surface plasmon resonance
LUMO	lowest unoccupied molecular orbital
MALDI-TOF MS	matrix assisted laser desorption/ionization time of flight mass spectrometry
MPTES	(3-mercaptopropyl)triethoxysilane
MSN	magic-sized nanocluster
NC	nanocluster
NIR	near infrared
nm	nanometer
NHE	normal hydrogen electrode
NMR	nuclear magnetic resonance
NP	nanoprism
NS	nanostructure
$O^{\bullet-}$	superoxide

OLA	oleylamine
PEG	poly(ethylene glycol)
PL-QY	photoluminescence quantum yield
PMHS	poly(methylhydrosiloxane)
PMT	photomultiplier tube
QD	quantum dot
QRE	quasi-reference electrode
S	sulfur
SAXS	small-angle X-ray scattering
Sb	antimony
Se	selenium
SEM	scanning electron microscopy
SERS	surface enhanced Raman spectroscopy
SH	thiol
SNC	semiconductor nanocluster
STEM	scanning transmission electron microscopy
TCSPC	time-correlated single photon counting
Te	telluride
TEM	transmission electron microscopy
THF	tetrahydrofuran
TMEDA	tetramethylethylenediamine
TOP	trioctylphosphine
TOPO	trioctylphosphine oxide

TPP	triphenylphosphine
UPS	ultraviolet photoemission spectroscopy
UV-vis	ultraviolet-visible
XPS	x-ray photoelectron spectroscopy
XRD	x-ray diffraction

LIST OF PUBLICATIONS

1. **Lawrence, K. N.;** Liyanage, T.; Teunis, M. B.; Sardar, R. Localized Surface Plasmon Resonance-Enhanced Photocatalytic Performance of Ternary Semiconductor Nanocrystals. Manuscript in Progress.
2. Teunis, M. B.; **Lawrence, K. N.;** Dutta, P.; and Sardar, R. Ultra-small Organolead Halide Nanoparticles with Tunable White-Light Emission. Manuscript in Progress 2016.
3. **Lawrence, K. N.;** Dutta, P.; Nagaraju, M.; Muhoberac, B. B.; Tenuis, M.; and Sardar, R. Dual Role of Metal-Carboxylate Ligands: Reversible Exciton Delocalization and Passivation of Nonradiative Trap-States in Molecule-Like CdSe Semiconductor Nanocrystals. Submitted to Chemistry of Materials 2016.
4. **Lawrence, K. N.**; Jana, A.; Teunis, M. B.; Mandal, M.; Kumbhar, A.; and Sardar, R. Investigating the Control by Quantum Confinement and Surface Ligand Coating of Photocatalytic Efficiency in Chalcopyrite Copper Indium Diselenide Nanocrystals. Chemistry of Materials 2016, 28 (4), 1107–1120.
5. Joshi, G. K.; Deitz-McElyea, S.; Liyanage, T.; **Lawrence, K N..**; Mali, S.; Sardar, R.; Korc, M. Label-Free Nanoplasmonic-Based Short Noncoding RNA Sensing at Attomolar Concentrations Allows for Quantitative and Highly Specific Assay of MicroRNA-10b in Biological Fluids and Circulating Exosomes. ACS Nano 2015, 9 (11), 11075-11089.

6. **Lawrence, K.N.**; Sardar, R.; Johnson, M.; Dolai, S.; Kumbhar, A. Solvent-like ligand-coated ultrasmall cadmium selenide nanocrystals: Strong electronic coupling in a self-organized assembly. Nanoscale 2015, 7, 11667-11677.
7. **Lawrence, K. N.**; Dolai, S.; Lin, Y.-H.; Dass, A.; Sardar, R. Enhancing the physicochemical and photophysical properties of small (<2.0 nm) CdSe nanoclusters for intracellular imaging applications. RSC Advances 2014, 4, 30742-30753.

ABSTRACT

Lawrence, Katie N. Ph.D., Purdue University, August 2016. Tuning Optoelectronic Properties of Small Semiconductor Nanocrystals through Surface Ligand Chemistry.
Major Professor: Rajesh Sardar.

Semiconductor nanocrystals (SNCs) are a class of material with one dimension <100 nm, which display size, shape, and composition dependent photophysical (absorption and emission) properties. Ultrasmall SNCs are a special class of SNCs whose diameter is <3.0 nm and are strongly quantum confined leading to a high surface to volume ratio. Therefore, their electronic and photophysical properties are fundamentally dictated by their surface chemistry, and as such, even a minute variation of the surface ligation can have a colossal impact on these properties. Since the development of the hot injection-method by Bawendi et al., the synthetic methods of SNCs have evolved from high-temperature, highly toxic precursors to low-temperature, relatively benign precursors over the last 25 years. Unfortunately, optimization of their synthetic methods by appropriate surface ligation is still deficient.

The deficiency lies in the incomplete or inappropriate surface passivation during the synthesis and/or post-synthetic modification procedure, which due to the high surface to volume ratio of ultrasmall SNCs, is a significant problem. Currently, direct synthetic methods produce SNCs that are either soluble in an aqueous media or soluble in organic solvents therefore limiting their applicability. In addition, use of insulating ligands hinder

SNCs transport properties and thus their potential application in solid state devices. Appropriate choice of surface ligation can provide 1) solubility, 2) stability, and 3) facilitate exciton delocalization.

In this dissertation, the effects of appropriate surface ligation on strongly quantum confined ultrasmall SNCs was investigated. Due to their high surface to volume ratio, we are able to highly control their optical and electronic properties through surface ligand modification. Throughout this dissertation, we utilized a variety of ligands (e.g. oleylamine, cadmium benzoate, and PEGn-thiolate) in order to change the solubility of the SNC as well as investigate their optical and electronic properties. First delocalization of the excitonic wave function 1) into the ligand monolayer using metal carboxylates and 2) beyond the ligand monolayer to provide strong inter-SNC electronic coupling using poly(ethylene) glycol (PEG)-thiolate was explored. Passivation of the Se sites of metal chalcogenide SNCs by metal carboxylates provided a two-fold outcome: (1) facilitating the delocalization of exciton wave functions into ligand monolayers (through appropriate symmetry matching and energy alignment) and (2) increasing fluorescence quantum yield (through passivation of midgap trap states). An ~240 meV red-shift in absorbance was observed upon addition of $Cd(O_2CPh)_2$, as well as a ~260 meV shift in emission with an increase in PL-QY to 73%. Through a series of control experiments, as well as full reversibility of our system, we were able to conclude that the observed bathochromic shifts were the sole consequence of delocalization, not a change in size or relaxation of the inorganic core, as previously reported. Furthermore, the outstanding increase in PL-QY was found to be a product of both passivation and delocalization effects.

Next we used poly(ethylene) glycol (PEG)-thiolate ligands to passivate the SNC and provide unique solubility properties in both aqueous and organic solvents as well as utilized their highly conductive nature to explore inter-SNC electronic coupling. The electronic coupling was studied: 1) as a function of SNC size where the smallest SNC exhibited the largest coupling energy (170 meV) and 2) as a function of annealing temperature, where an exceptionally large (~400 meV) coupling energy was observed. This strong electronic coupling in self-organized films could facilitate the large-scale production of highly efficient electronic materials for advanced optoelectronic device applications.

Strong inter-SNC electronic coupling together with high solubility, such as that provided by PEG-thiolate-coated CdSe SNCs, can increase the stability of SNCs during solution-phase electrochemical characterization. Therefore, we utilized these properties to characterize solution-state electrochemical properties and photocatalytic activity of ternary copper indium diselenide ($CuInSe_2$) SNCs as a function of their size and surface ligand chemistry. Electrochemical characterization of our PEG-thiolate-coated SNCs showed that the thermodynamic driving force ($-\Delta G$) for oxygen reduction, which increased with decreasing bandgap, was a major contributor to the overall photocatalytic reaction. Additionally, phenol degradation efficiency was monitored in which the smallest diameter SNC and shortest chain length of PEG provided the highest efficiency. The information provided herein could be used to produce superior SNC photocatalysts for a variety of applications including oxidation of organic contaminants, conversion of water to hydrogen gas, and decomposition of crude oil or pesticides. Therefore, we

believe our work will significantly advance quantitative electrochemical characterization of SNCs and allow for the design of highly efficient, sustainable photocatalysts resulting in economic and environmental benefits.

CHAPTER 1. INTRODUCTION TO COLLOIDAL SEMICONDUCTOR NANOCRYSTALS

1.1 Motivation

Semiconductor nanocrystals (SNCs), commonly known as quantum dots (QDs), are a class of nanomaterial with one of their dimensions <100 nm, which display size-, shape-, and composition-dependent photophysical (absorption and emission) properties. Since the development of the hot injection method-based synthesis of monodispersed metal (M = Cd, Zn, and Pb) chalcogenide (E = S, Se, and Te) SNCs by Bawendi et al.,[1] the field of SNC related-research has evolved dramatically over the last 25 years to include: (1) development of new synthetic methods, (2) characterization of size-, shape- and surface ligand-dependent photophysical properties, and (3) bio-imaging and solid-state device applications. One of the most interesting features of SNCs is their size-dependent optical and electronic properties, which means that ideally, these properties can be finely controlled by tuning the SNC diameter without changing its chemical composition and/or structure. This concept is so powerful that it has expedited the growth of nanotechnological research and development.

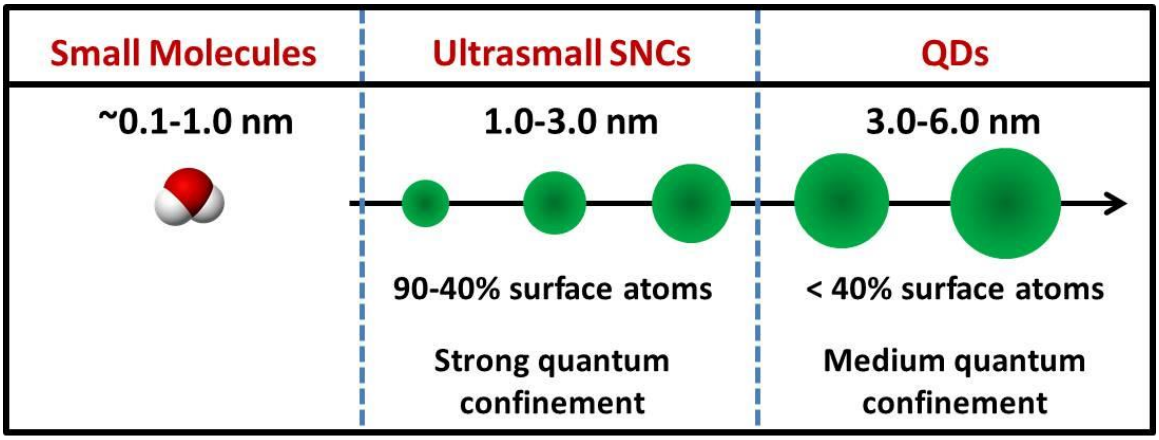

Figure 1.1: Comparison of small molecules, ultrasmall SNCs, and QDs. Magic sized SNCs can be classified as ultrasmall SNCs if <3.0 nm, however, not all ultrasmall SNCs are magic-sized SNCs as a thermodynamically stable crystal structure is required to be classified as a MSN.

Magic-sized nanocrystals (MSNs) possess thermodynamically stable crystal structures[2-8]and have been of substantial interest because of their unique optical and electronic properties. MSNs were first spectrally identified by Peng et al. in 2001 but not isolated.[9] Over the last 15 years, several research groups have (1) studied the growth processes (e.g., continuous and quantized) of (ME)x MSNs with $13 \leq x \leq 34$, (2) isolated nearly gram scale quantities, and (3) explored their photophysical and electronic properties. [6,10-16]Among the various compositions, CdSe MSNs are the most well studied, and have provided a bridge between small molecules and larger QDs therefore improving our molecular level understanding and providing the basis for many new multidimensional superstructures.[4,17] (Figure 1.1) Furthermore, it has been shown that during synthesis, these MSNs serve as structural intermediates for larger SNCs and anisotropic nanostructures (NSs).[6,7,12] MSNs can be classified as ultrasmall SNCs (<3.0 nm diameter), however, not all ultrasmall SNCs are MSNs as a thermodynamically stable crystal structure is required to be categorized as a MSN. Ultrasmall SNCs have an

extremely large surface to volume ratio which increases with decreasing size (e.g. 76 % atoms are on the surface for 1.2 nm SNCs and 45% for 2.5 nm SNCs), eventually leading to quantum confinement.[18] Therefore, their electronic and photophysical properties are largely dictated by their surface chemistry, and as such, a minute variation of the surface chemistry can have an enormous impact on these properties.

These surface ligands can be introduced either through synthesis or post-synthetic ligand exchange. The synthesis of colloidal ultrasmall SNCs requires the use of ligands in order to keep them in solution. These synthetic methods have evolved greatly over the past 15 years. In 2001, two methods were introduced to obtain SNCs <2.0 nm. Solviev et al.[11] utilized a single-source molecular approach to synthesize $(CdSe)_{32}$, while Landes et al.[10] lowered the reaction temperature of Bawendi's original hot injection method[1] from 360℃ to 130℃ to produce SNCs as small as 1.6 nm in diameter. However, up to this point, highly toxic dimethyl cadmium was utilized as the predominant source of cadmium, and therefore large scale synthesis for practical applications of ultrasmall SNCs would require a change in precursor.[6] Concurrent to Solviev and Landes, Peng et al. developed a relatively benign cadmium precursor in which cadmium oxide in the presence of alkylphosphonic acid replaced the extremely toxic dimethyl cadmium to synthesize high quality cadmium-based ultrasmall SNCs.[12,13]The importance of this new precursor is that it slowed nucleation time leading to more controlled growth, and therefore a more monodispersed ultrasmall SNC synthesis. Following this breakthrough in synthetic design, SNCs have been synthesized using a myriad of methods including, but not limited to, high temperature[5,25], alkylphosphine precursor-based[12,13,16,26], and low temperature nonphosphinated syntheses[27,28].

Strongly quantum confined SNCs exhibit many useful properties such as (1) fast charge separation and slow recombination which are important for light harvesting[19,20] and (2) deep-trap[8,16,21] or a combination of deep trap and broad band PL which are key for optoelectronic devices,[2,5,22-24] all of which are strongly surface ligand dependent. Therefore, even a minute variation in SNC surface ligand chemistry will have enormous impact on their properties. Unfortunately, optimization of their synthetic methods by appropriate surface ligation is deficient.

This deficiency lies in the incomplete or inappropriate surface passivation during the synthesis and/or post-synthetic modification, which due to the high surface to volume ratio of ultrasmall SNCs, is a significant problem. Currently, direct synthetic methods produce SNCs that are either soluble in an aqueous media or soluble in organic solvents therefore limiting their applicability. In addition, use of insulating ligands[8,12,16,21-24,26,29-38] hinder SNCs transport properties and thus their potential application in solid state devices. Appropriate choice of surface ligation can provide 1) solubility, 2) stability, and 3) facilitate exciton delocalization.

In this dissertation, the effects of appropriate surface ligation on strongly quantum confined ultrasmall SNCs was investigated. Due to their high surface to volume ratio, we are able to highly control their optical and electronic properties through surface ligand modification. Throughout this study, we utilized a variety of ligands (e.g. oleylamine (OLA), cadmium benzoate ($Cd(O_2CPh)_2$), and PEGn-thiolate) in order to change the solubility of the SNC as well as investigate their optical and electronic properties. First we explored the dual effect $Cd(O_2CPh)_2$ ligands had on CdSe SNCs: 1) delocalization of exciton wave functions of the SNC into the ligand monolayer and 2) increased

photoluminescence quantum yield (PL-QY). Both delocalization and high PL-QY are beneficial to the design of solid state devices. Next, we utilized poly(ethylene) glycol (PEG)-thiolate ligands to provide unique solubility properties in both aqueous and organic solvents and investigated delocalization of the exciton wave function beyond the ligand monolayer. Due to the high conductivity and low insulating nature of the PEG-thiolate ligand, expansion of the SNC wave function beyond the ligand monolayer was possible which facilitated inter-SNC delocalization known as electronic coupling. The entanglement of inter-SNC wave functions creates artificial solids which are useful for enhanced charge transport in solid state devices. Lastly, we utilized the knowledge of enhanced solubility and charge transport properties gained in the first two sections to characterize the electrochemical properties and photocatalytic activity of ternary copper indium diselenide ($CuInSe_2$) SNCs. This knowledge is vital for advanced oxidative processes (AOPs) such as alternative energy production (H_2 evolution) and decomposition of common pollutants. Therefore, our combined work has the ability to further enhance bioimaging and solid state device material as well as explore the photocatalytic activity of ultrasmall SNCs through the exploration of ligand dependent delocalization, electronic coupling, and electrochemical characterization.

1.2 Electronic Properties of SNCs

SNCs have confined dimensions that lead to unique physical and photophysical properties.[17,23,39-50] These electronic properties are due to quantum-size effects which are a result of quantum confinement, which is the confinement of electrons or photons, or from the high surface-to-volume ratio as the size of the SNC decreases.[52] These two

effects are rarely divided and therefore will be discussed in unity throughout this dissertation with an emphasis on the surface ligand effects of quantum-confined SNCs.

1.2.1 Quantum Confinement

Quantum confinement occurs when an exciton is confined to a very small volume. As the size is reduced, the electronic excitations shift to higher energy.[49] When describing this phenomenon, often a "particle-in-a-box" model is used as visualization. In this model, the probability of finding a particle at an isolated potential is confined by a potential barrier. The energy of this particle is dictated by the particle mass, box size, and

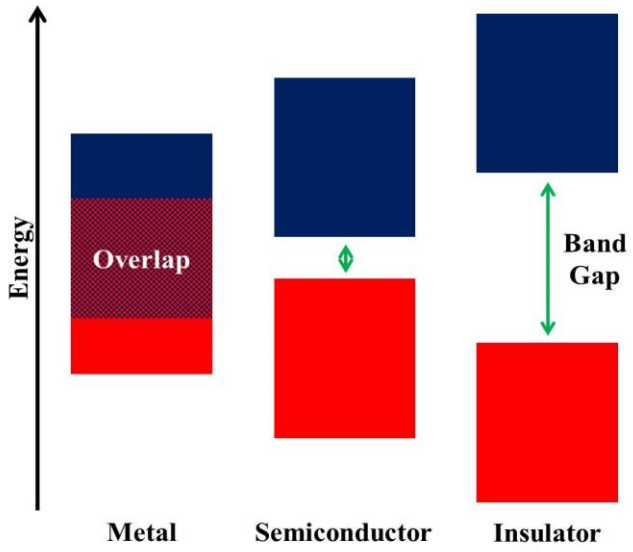

Figure 1.2: Simplified band gap comparison between metal (no band gap), semiconductor (small band gap), and insulator (large band gap). The optical and electronic properties of these materials rely on the energy of the bandgap and occupancy of their bands. For example, the bandgap of insulators is too large for thermal excitation of electrons at room temperature; therefore, no conduction.[52] Metals, on the other hand, are able to conduct electrons readily due to their band overlap. Semiconductors lie in between the two extremes. Excitation at room temperature can cause the electron in the valence band to be excited to the conduction band thus causing conduction. This is why semiconductors, although only mediocre conductors, are so important. Their unique atomic structure allows for their conductivity to be highly controlled through manipulation surface ligation, electric currents, electromagnetic fields, or even light that is applied which makes it possible to make devices that can amplify and convert sunlight to usable electricity.

principle quantum number; therefore, the energy of the particle can be increased by decreasing the particle size.[52] This same idea can be applied to the quantum confinement effect; however, an understanding of the basic band structure of SNCs is required.

Semiconductors are unique materials whose properties lie between metals, which conduct electricity and heat, and insulators, which do not conduct electricity or heat. (Figure 1.2) A band structure is the difference between the valence band and conduction band.[39,51,52] A valence band consists of the occupied bonding orbitals while the conduction band is made up of the unoccupied anti-bonding orbitals. Although a band is considered to contain an infinite number of energy levels, the difference in energy between the upper edge of the valence band and the lower edge of the conduction band is called the bandgap. In the ultrasmall size range, the spacing between the energy levels is large and the upper most energy level of the valence band could be referred as the highest occupied molecular orbital (HOMO) and the lowest most energy level of the conduction band could be referred as the lowest unoccupied molecular orbital (LUMO).[39,53] These MO levels can be compared to small molecules and as such, ultrasmall SNCs bridge the gap between molecule and QD. (Figure 1.1) The quantum confinement effect of SNCs is, therefore, observed when an electron is excited to the LUMO and becomes electrostatically bound to the hole that was created in the HOMO. This electron/hole (e/h) pair can be termed as an exciton and can be formed by association of free carriers (unbound electrons or holes) or by direct photoexcitation.[54] The exciton is then delocalized over space, defined as the Bohr radius (a_o) (Eq 1.1), where $\hbar^2$ is the reduced Planck's constant, κ is the dielectric constant of the material, $m_{e,h}$ is the mass of the electron or hole, and e is the elementary charge.[39]

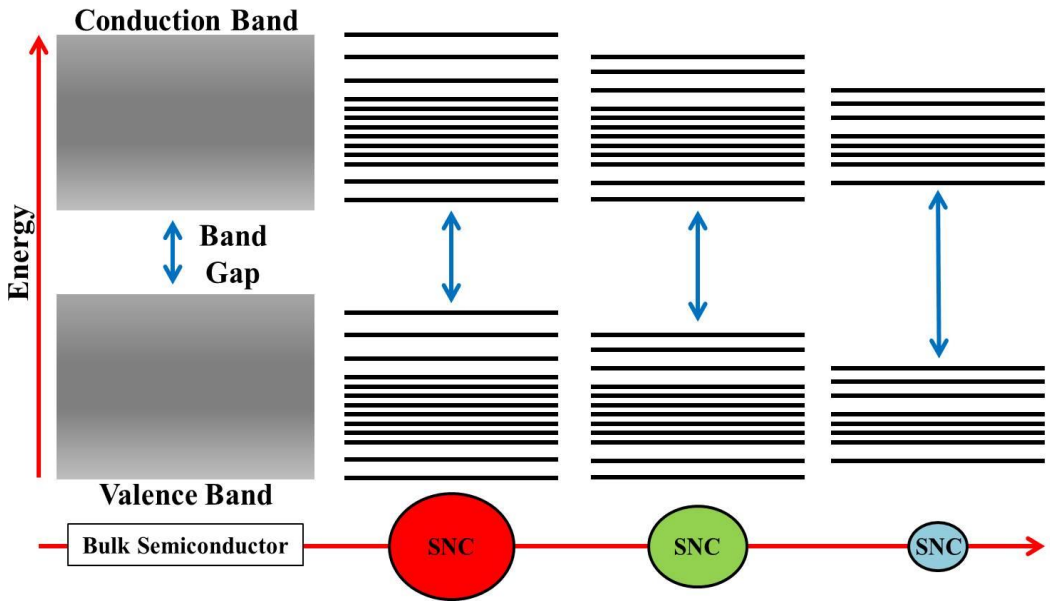

Figure 1.3: Schematic depiction of the transition from bulk semiconductors to SNCs. The continuous energy levels shown by the valence and conduction band gives way to discrete energy levels more like the molecular level which has a single HOMO-LUMO bandgap. (Adopted from reference 57.)

$$a_0 = \hbar^2 \kappa / m_{e,h} e^2 \qquad (1.1)$$

In a nanomaterial such as an SNC, which has a radius smaller than its Bohr radius, quantum confinement dictates the energy of the exciton which results in discrete energy levels with molecule-like HOMO and LUMO orbitals, as described above.[52,55,56] (Figure 1.3)[57] These discrete energy states are caused by discontinuity of the bands due to the fewer number of atoms present in nanomaterials and therefore fewer oribtals.[52,56] Due to these atomic-like levels, SNCs act like molecules as they interact with light via their electronic transition dipoles, classifying them as "molecule-like".[39,53] However, the Bohr radius is material dependent and thus each material will experience quantum confinement at different sizes; as L.E. Brus described in 1984. Brus was the first to give a theoretical calculation for SNCs using CdS and CdSe SNCs and therefore demonstrate

that both material and size play an important role; as the size of the SNC increases, the bandgap decreases.[56,58] Using a spherical volume, he defined the wave function (discussed in detail below) where $E_{g(SNC)}$ is the band gap energy of the SNC, E_{bulk} is the band gap energy of bulk semiconductor, R is the radius of the SNC, m_e^* is the effective mass of the excited electron, m_h^* is the effective mass of the excited hole, h is Planck's constant, ε_0 is the permittivity of vacuum, and ε_r is the relative permittivity. [56,30]

$$E_{g(SNC)} = E_{bulk} + \frac{h^2}{8R^2}\left(\frac{1}{m_e^*} + \frac{1}{m_h^*}\right) - \frac{1.786e^2}{4\pi\varepsilon_0\varepsilon_r R^2} \qquad (1.2)$$

The first term to the right represents the band gap energy of bulk materials (dependent on material). The second term represents the energy due to the quantum confinement effect, which has an inverse R^2 dependence on the band gap energy. Lastly, the subtractive term stems from the columbic interaction energy of the exciton, which has an inverse R^2 dependence. Note: the numerical value comes from the wave function overlap integrals and can vary slightly from material to material as discussed by Brus.[56]

1.2.2 Wave Function

Due to the highly quantum-confined nature of SNCs, their fundamental composition of electrons takes on a wavelike nature. A wave function is a "mathematical function used in quantum mechanics to describe the propagation of the wave associated with a particle using Schrödinger's equation".[59] When simplified, one can find that the solution yields all of the wave functions whose amplitudes are zero at the boundary of the confinement and their discrete energies associated are given by the following equation (assuming a particle in the box model).[39] Here n_j take on integer values and a, b, and c are the separation between the energy levels.

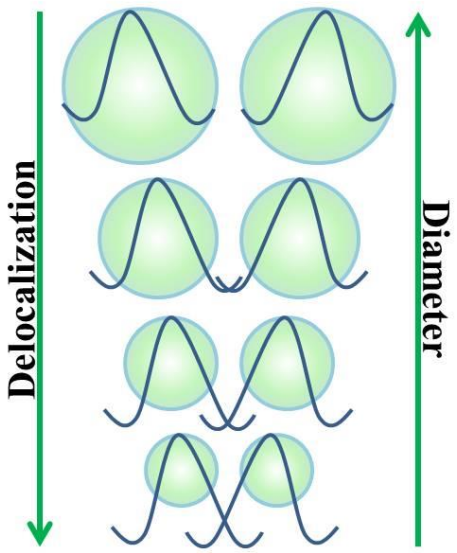

Figure 1.4: Expansion of the wave function outside of SNC core upon decrease in SNC diameter resulting in an increase in exciton delocalization and inter-SNC coupling potential.

$$E = \frac{\hbar^2 \pi^2}{2\,m}\left(\frac{n_1^2}{a^2} + \frac{n_2^2}{b^2} + \frac{n_3^2}{c^2}\right) \qquad (1.3)$$

"The square of the absolute value of the function evaluated at a given point in space is therefore proportional to the probability of finding the particle in that particular area" as shown above.[39] The wave function allows for the transport of excitons making it extremely important for electronic devices.[46,60-62] In smaller SNCs, the kinetic energy of the exciton is higher than the coulombic interaction energy of the e/h pair. Therefore, as the diameter of the SNC decreases, the exciton wave function more easily fills the core and begins to expand past the core boundary (expansion of the confinement dimension or "box"). [48,63,64] (Figure 1.4) This expansion can cause the wave function to expand into the ligand monolayer[46,60,63] or surpass this layer and entangle with neighboring SNC wave functions (electronic coupling) [64-67]. The ability for the wave function of ultrasmall SNCs to delocalize is in contrast to larger SNCs in which the wave function is confined to the

core and therefore undergoes no exciton delocalization. This will be discussed in greater detail in section 1.4. Additionally, the extent to which delocalization of the wave function can occur is dependent on surface ligation. [46,60]

1.3 Surface Modification of SNCs

SNCs are rarely unpassivated (unless in vacuum); a ligand passivates the surface and provides unique optical and electronic properties.[37] Surface passivating ligands (1) stabilize the nonradiative trap states, (2) solubilize the SNC to maintain their colloidal states, and (3) improve charge transport properties in thin-films. Since ultrasmall SNCs have a large surface to volume ratio and ligands affect the energy of the surface states,

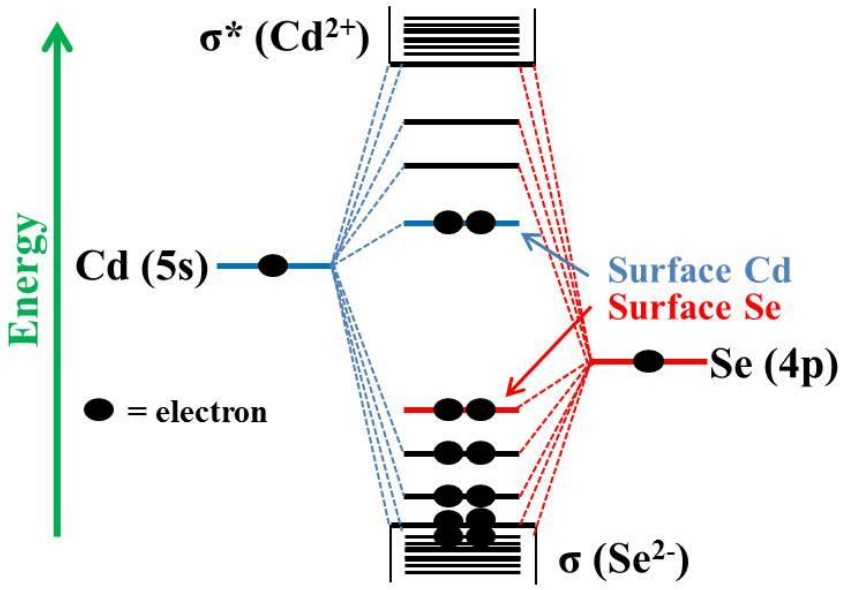

Figure 1.5: Simplified molecular orbital diagram of quantum-confined CdSe SNC with surface states. Due to fewer electron-donating pairs present on the surface of CdSe SNCs, cadmium surface states (blue) are lower in energy compared to the core cadmium energy states. Likewise, there are more electron-accepting pairs present at the surface of CdSe SNCs; therefore, surface selenium sites (red) are higher in energy than their core counterparts. *Image drawn using ChemDraw and not drawn to scale. (Adopted from reference 52.)

altering or removing these molecules can largely dictate the overall optical, electronic, and electrochemical properties of the SNC.

As the ratio of surface to core atoms increases, the properties of these surface atoms begin to dominate the entire particle, and as such, the surface atoms are chemically different than their core atoms. (Figure 1.5) This is due to the termination of the semiconductor lattice at the surface. If these surface sites are left unpassivated, dangling bonds are created which are unbounded orbitals that protrude from the surface of the SNC and are the origin of trap states.[39] For example, fluorescence emission can be significantly modulated by changing the nanocrystal surface. It's often comprised of two emission bands, one at higher energy which is a property of direct recombination (band edge emission) and another at lower energy resulting from recombination at intraband

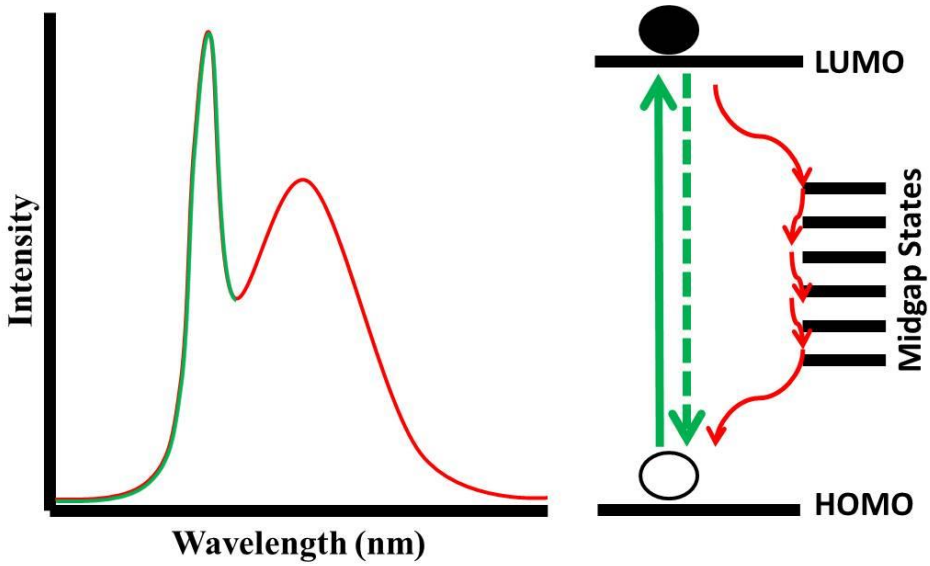

Figure 1.6: Depiction of trap state effects. Left: Combination of band edge (green) and broad band (red) emission. Right: Route of excited electron upon relaxation. Solid green arrow represents excitation (absorption), dashed green arrow signifies radiative recombination (band edge emission), and red arrows represent possible trapping of the relaxing electron into midgap states (broad band emission). *Images drawn using ChemDraw and not drawn to scale.

defect sites located on the surface of the SNC (broad band emission). (Figure 1.6) When considering CdSe SNCs, deep trap emission arises when Se^{2-} sites are left unpassivated making the nanocrystals prone to surface trapping of holes that reside on the sp^3 orbitals of the selenium.[40] This leads to the broad band emission stemming from surface defects. (Figure 1.5 and 1.6) However, upon passivation of these sites, the surface defects are extinguished and the fluorescence spectrum is one of band edge. Therefore, proper choice of surface ligation can strongly enhance the SNCs optical and electronic properties.

Surface passivating ligands can be introduced both during synthesis or post-synthesis to enhance solution dispersion, stability, and to expand their potential applications by modulating the SNCs properties.[37] Several synthetic methods have been developed to prepare group II–VI[2,5,8,16,21,24,68-70] and IV–VI[25] SNCs and further tune their PL properties by controlling their surface ligand chemistry.[38] Currently, long-chain hydrocarbon-containing aliphatic amines, phosphine, phosphonic acids, and phosphine oxide are utilized during synthesis to stabilize the SNC and impart controllability of size and morphology.[8,12,16,21-24,26,29-38] However, SNCs passivated by long hydrocarbon chain-containing ligands are only soluble in organic solvents, which are incompatible with biological systems. They are also electrically insulating, which leads to poor carrier mobilities and conductivities therefore rendering them useless as materials for many solid state devices such as thin-film-based optoelectronic devices. Thus, most commonly a post-synthetic ligand exchange reaction in which the bulky native ligands are replaced with smaller organic ligands[45,71,72] inorganic ions[66,73-75] , and/or metal chalcogenide complexes[44,76,77] is performed. However, these exchange reactions often suffer from (1) structural rearrangement of the SNCs [37,45,65], (2) discontinuity of the electron transport

process, (3) lack of electronic coupling, and/or (4) addition of trap states.[30,75] Furthermore, SNCs coated with small molecules are often unstable leaving them vulnerable to rapid oxidation even in ambient environments[45] as well as only soluble in high boiling solvents[44-46,66,78,79] making device fabrication extremely difficult. Lastly, the above ligands are not water-soluble and therefore, cannot be used in biological systems. In order to use SNCs for nanobiotechnology, additional ligand exchanges or a process of encapsulation must be employed. Encapsulation of hydrophobic ligand-coated SNCs with phospholipids or polymers made of poly(ethylene glycol) (PEG) have been used to prepare water soluble SNCs.[35,80-83] In this manner, the SNC is encased in the water soluble media in order to transport the SNC through an aqueous solution. However, during the encapsulation process, the hydrodynamic radii of the SNCs increases which can cause a severe reduction in renal clearance and eventual cellular death. On the other hand, post-synthetic ligand exchange reactions using various thiolate ligands have been widely utilized to enhance their solubility without a significant increase in hydrodynamic radii. However, thiols are known to quench the PL-QY due to trapping of the photogenerated holes that prevents radiative recombination of excitons.[84] Table 1.1 provides an overview of some commonly used ligands, their binding site, and their drawbacks.

Due to these drawbacks, common methods of ligation for materials used in bioimaging and solid state devices are currently deficient. In this dissertation, the effects of appropriate surface ligation are extensively studied. In chapter 2, we discuss the dual nature of metal carboxylates for surface passivation and delocalization into the ligand monolayer. Next, we introduced a direct synthesis and purification procedure for

Table 1.1: Overview of commonly used surface ligands.

Ligand	Structure	Binding Cite	Drawbacks
Trioctylphosphine oxide (TOPO)	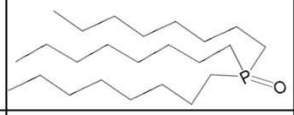	Metal	Toxic, electrically insulating, only soluble in organic solvents
Phosphonic acid	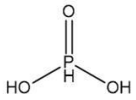	Metal	Toxic, electrically insulating, only soluble in polar solvents
Pyridine	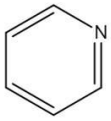	Metal	Toxic, electrically insulating, addition of trap states, only soluble in organic solvents
Oleylamine (OLA)	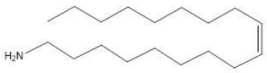	Metal	Electrically insulating, only soluble in organic solvents
Chloride	Cl^-	Metal	Poor stability, structural rearrangment
Cadmium oleate ($Cd(oleate)_2$)	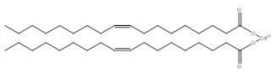	Chalogenide	Structural rearrangement of SNC
Hexanethiol (HT)	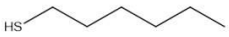	Metal	Quench PL-QY

poly(ethylene glycol) thiolate-coated SNCs, which allow the SNCs to be soluble in a wide range of solvents both aqueous and organic in nature while maintaining stability, promoting electronic coupling, and crack-free film preparation. The solvent-like character of PEG, along with their low hydrodynamic radii, allow for strong inter-SNC interaction though entanglement of excitonic wave functions, discussed in greater detail in chapter 3. Lastly, we utilize prior knowledge gained to study the electrochemical and

photocatalytic properties of ternary SNCs due to enhanced charged transport properties stemming from exciton delocalization into the ligand monolayer.

1.4 Exciton Delocalization and Electronic Coupling

As mentioned above, ligands can impart solubility, stability, and conductivity to the SNCs; however, recently it has been demonstrated that these ligands are also capable of tailoring the bandgap of SNCs by facilitating electron delocalization. Exciton delocalization is the process in which the electronic wave function expands outside the SNC core. (See Figure 1.4) When an exciton delocalizes, it utilizes the wave function to "displace" the exciton from the confined core in the ground state, which reduces the excitonic bandgap that is observed by a marked red-shift of the peak position. Exciton delocalization has been of immense interest since the early work of Frenkel[85] and Wannier[86] due to their applicability in electronic device fabrication. As briefly mentioned, excitons that are formed readily by photoexcitation can dissociate into free carriers which are unbound electrons and holes and can be used for photovoltaic devices whereas excitons that remain bound can emit light and are used for laser media.[40,54] If the interaction between the electron and hole is assumed negligible, which is determined by the expansion of the wave function, then the e/h pair is considered to be comprised of free carriers. However, when attractive coulombic interaction binds the e/h pair, it is deemed an exciton. Excitons are set apart from free carriers by the spatial magnitude of the electronic excited state being increased through sharing of the excitation among the core and ligation of the material which is determined by entanglement of the excitonic wave functions.[54] However, in nanoscale materials the physical dimensions of the material, not the Coulomb interaction of the e/h pair, dictates the delocalization of these

excitons. The kinetic energy of the excitons is higher than Coulomb interaction of the e/h pair in strongly confined ultrasmall SNCs than intermediate or weakly confined larger SNCs, therefore smaller SNCs have greater ability to undergo delocalization of exciton wave function which results in the expansion of the confinement box. (Figure 1.1) The exciton delocalization can therefore cause the wave function to expand to the ligand monolayer or surpass this layer and entangle with neighboring SNCs (electronic coupling).

In order for the SNCs to participate in strong electronic coupling, their electron and/or hole wave functions are required to expand past the SNC and ligand monolayer, overlap, and entangle with neighboring SNC wave functions. Strong inter-SNC electronic coupling is a prerequisite for enhanced charge transport properties[46,60] either to or from the material which can result in an increase in solid-state device efficiency. Due to the high surface to volume ratio of ultrasmall SNCs, surface ligation plays a critical role in delocalization of the exciton and ultimately inter-SNC electronic coupling, as discussed previously. If the ligand is bulky or insulating in nature such as the long-chain aliphatic ligands, the wave function will be unable to extend past the ligand monolayer and thus the SNC will be unable to interact with neighboring SNCs. On the other hand, if the ligand doesn't provide adequate protection, the SNC can undergo oxidation. Luther et al., reported that exposure to air resulted in blue shifting and weakening of the first excitonic transition in the absorption spectra of SNCs film thus indicating a reduction in their inter-SNC coupling and possibly overall SNC size.[71] Upon changing the SNC size, the electronic and electrochemical properties are significantly altered; therefore, a rational

approach to obtain desired optoelectronic properties of SNCs should involve appropriate surface passivation without changing SNC size, shape, or core composition.

Exciton delocalization has been demonstrated by a few groups, including Weiss et al.[87] and Teunis et al.[63], in which both groups achieved hole delocalization causing up to 220 and 610 meV absorbance red-shifts, respectively, using strong coordinating ligands (phenyldithiocarbamate) attached to II-VI and IV-VI NCs. Likewise, modification using thiol, selenol, or tellurol has also shown similar effects.[37,63,64,67,88]Although delocalization into the ligand monolayer as proven to be successful at modulating the band gap, enhancing electronic coupling, and facilitating charge transport, to date, the covalent bonding nature of the post-synthetic ligand exchange, as well as size and/or structural rearrangement of the SNC, has rendered this process irreversible.[63,87]

1.5 Electrochemical Determination of Bandgap

1.5.1 Current Methods

In order to determine if a SNC is capable of participating in exciton delocalization with ligand monolayers, it is necessary to determine their energy level positions, (e.g. HOMO and LUMO) which cannot be determined by optical absorption measurements. Energetic positions of these orbitals are determined by the material and size of the SNC as well as the surface chemistry, therefore, understanding their electronic structure is vital for future applications. Theoretical determination of orbital positions by various techniques including ionization and electron affinities have been based on effective mass approximations (EMA)[89], tight-binding (TB)[90], charge patching[91], and semi-empirical pseudopotential (SEMP)[92] models. For example, theoretical calculations are often used to calculate the bandgap of the material such as those reported by Zhang et al., in which

they utilized the local density approximation (LDA) to calculate the bandgap of silicon.[93] However, it is well known that LDA values are ~ 40% underestimated, and as such, should not be considered ideal quantitative approximations of the HOMO and LUMO positions.[94-96] Likewise, many other theoretical approximations, such as density functional theory (DFT) and other hybrid systems also underestimate SNC bandgap[97], whereas, some calculations including EMA, consistently overestimate orbital positions. In combination with theoretical approximations, many analytical techniques have been used. The most popular analytical techniques are (1) X-ray photoelectron (XPS) and (2) ultraviolet photoemission (UPS) spectroscopy measurements, and (3) cyclic voltammetry (CV) [98-109]. UPS is often used due to its ability to "map out the entire valence band structure, including the band-edge and surface state contributions".[110] However, the high intensity and high energies of the ultraviolet radiation used in UPS measurements may induce shifts in these energetic positions as reported by Yi et al.[111] Additionally, XPS is often coupled with UPS, which uses synchrotron radiation to investigate the empty conduction band states.[98,99,107,112] However, of the above three methods, cyclic voltammetry is the most convenient due to its (1) ambient conditions, (2) low cost, and (3) ability to analyze thin films as well as colloids.[107,108] Therefore, electrochemistry proves to be the most versatile and accurate method of determining energetic orbital positions.

1.5.2 Electrochemistry

Figure 1.7 demonstrates how solution phase electrochemistry occurs as the current flows between the working (or indicator) and counter (or auxiliary) electrode. In our system we utilize a three electrode system; therefore, the potential of the working

electrode is varied with respect to the reference (nonpolarizable) electrode. This controlled potential causes the chemical species in solution to be oxidized or reduced. Therefore, changes in potential vary the energy level of the working electrode in order to allow for the exchange of electrons from the HOMO of the SNC to the working electrode (oxidation) when a positive potential is applied (Figure 1.7 A→B) and from the working

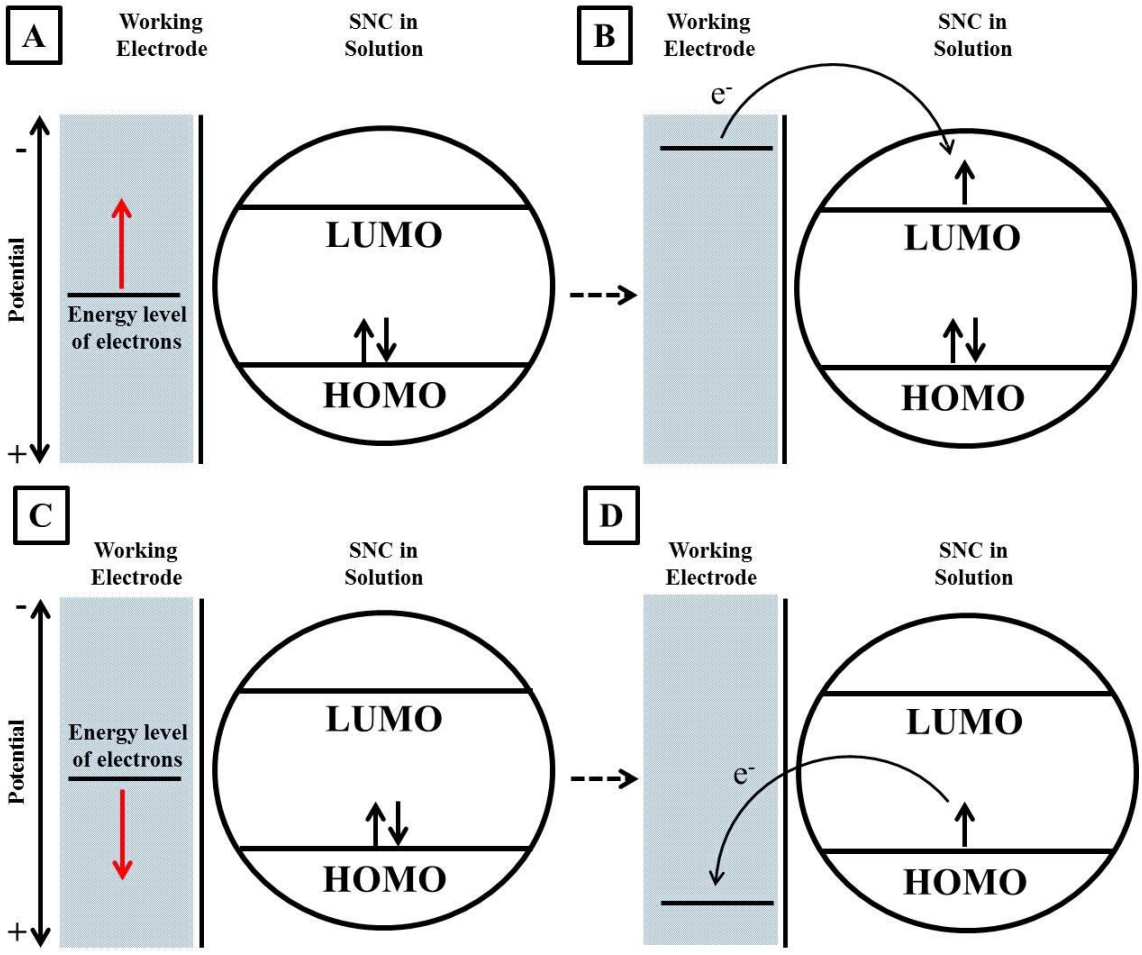

Figure 1.7: Representation of (A) decrease in potential energy (red arrow) of the working electrode and the subsequent (B) reduction, in which the electron is transferred from the working electrode to the LUMO of the SNC in solution (curved arrow). Reverse process representation (C) increase in potential energy (red arrow) of the working electrode and the subsequent (D) oxidation, in which the electron in the HOMO of the SNC in solution is transferred to the working electrode (curved arrow). *Electrons are represented as black arrows, representing their opposite spin states.[113]

electrode to the LUMO (reduction) upon decreasing the potential (Figure 1.7 C→D).[113] This SNC electron transfer can then be measured by the changes in current as the potential of the electrode is varied. CV technique allows one to observe both the forward and reverse reactions simultaneously, e.g. oxidation and reduction potentials. Figure 1.8 is an example of a typical voltammogram. As the scan progressively increases the negative potential, the current rises to a peak and then decays in a regular manner. This peak is the product of an alignment between the working electrode potential and the LUMO of the SNC allowing for the transfer of electrons (Figure 1.7 C →D). The CV switching potential is then reached (change in potential sign) and the scan progresses to

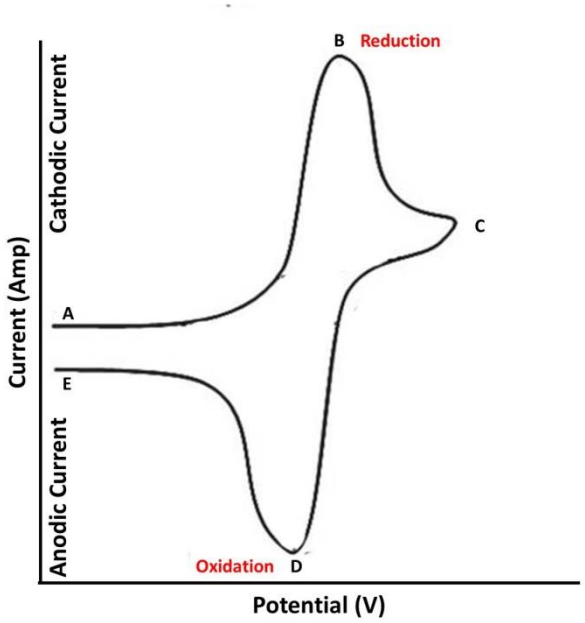

Figure 1.8: Schematic representation of the CV technique. The reduction process occurs from (A) the initial potential to (C) the switching potential. Here the potential is scanned negatively to cause a reduction (cathodic current). At (B) the maximum reduction potential of the species has been reached resulting in a peak. The scan then switches potential at (C) and scans positively to point (E). In this region, oxidation occurs (anodic current). At point (D) the maximum oxidation potential has been reached resulting in a peak.

more positive potential causing an oxidative (anodic) peak due to the appropriate alignment between the working electrode potential and the SNC HOMO (Figure 1.7 A→B). However, the utility of CV is highly dependent on the analyte being studied.

1.5.3 Limitations of Electrochemistry by Sample Preparation

There are many size- and composition-dependent electrochemical determinations of various SNCs using CV technique where the SNCs were deposited as a film onto an electrode surface, such as with copper-based ternary ($CuInSe_2$, Cu_2SnSe_3, and CuZnSeS) SNCs[100-103] or many other chalcogenide (CdSe or CdS).[47,113-116] However, current sample preparation does not accurately represent the electrochemical characteristics such as HOMO and LUMO positions of diffused and isolated SNCs for a variety of reasons. First, these SNCs, usually deposited as a film, are presented in their aggregated state and therefore no longer follow the quantum confinement effects, meaning they now act as a bulk material and lack distinct orbitals.[113] Also, these films are typically comprised of SNCs coated in an insulated ligand coating such as OLA or dodecanethiol (DDT). Insulating ligands cause a dramatically slowed electron transfer that could trigger chemical byproduct reactions inside the film causing an overall change in morphology and degradation of the sample. Therefore, quantitative information about the HOMO and/or LUMO positions is seldom accurately portrayed.

On the other hand, using dispersed SNCs would overcome the limitations faced by the above mentioned films. However, commonly used ligand-passivated SNCs are only soluble in solvents such as toluene, hexane, and/or chloroform, and due to their narrow potential window, these solvents are not suitable for electrochemical characterization of large band-gap ultrasmall SNCs. [47,50,104,108,113,114,117-120] Reports of

dispersed SNCs (CdSe[47,104,108,114,117,118], CdTe[117,119,120], CdS_xSe_{1-x}[119], and $CdSe_xTe_{1-x}$[50]) all used N,N-dimethylformamide (DMF)/electrolyte solution, which has a small potential window presenting problems as the SNC decreased in size and consequently increased in oxidation and reduction potential peak separation. Also, in all of these cases, multiple peaks were observed, which could be due to a poorly cleaned (presence of free, unbound surface passivating ligands) or a poorly passivated (surface trap states) SNCs.[104-106] Lastly, in contradiction to the rules of quantum confinement, the electrochemical bandgap (E_{gap}^{el}) was found to be smaller than the optical bandgap (E_{gap}^{opt}). Eq. 1.4 clearly illustrates the relationship in which E_{gap}^{el} is the sum of the E_{gap}^{opt} and the coulombic interaction. Here the coulombic interaction is represented by $J_{e/h}$, which can be defined as the electrostatic interaction between the e/h pair.[103]

$$E_{gap}^{el} = E_{gap}^{opt} + J_{e/h} \quad (1.4)$$

1.5.4 Enhanced Electrochemical Analysis

In order to overcome current sample preparations resulting in electrochemical limitations for the determination of HOMO and LUMO positions, the above mentioned PEG-thiolate ligand modification was developed, which allows for high solubility in a wide range of solvents such as electrochemically friendly acetonitrile or dichloromethane.[113] PEG is a solvent-like ligand allowing for not only solubility in various solvents but also enhanced charge transport ability[64,121-123], characteristics pertinent to accurately portray the solution phase electrochemistry. Solubility gained from the use of PEG-thiolate as a ligand allows for a large potential window to accurately capture and quantitate the HOMO and LUMO positions from the oxidation and reduction

peaks of the solution phase voltammograms. The solution acquired voltammograms can then be used as onset potentials from which the oxidation and subsequent reduction peaks appeared. (See Figures 1.7 and 1.8) Therefore, PEG allows the SNCs to undergo electrochemical determination of the HOMO and LUMO orbitals in an electrochemically friendly solvent without aggregation and provides the necessary conductivity to allow for fast electron transport to and from the electrode. This process provides vital information about the SNCs' orbital positions and ability to delocalize and therefore, can be applied to a variety of applications.

1.6 Applications of SNCs

Due to their size-dependent electronic and optical properties, as discussed previously, SNCs have gained considerable attention for their applications in solid state devices such as light-emitting diodes (LEDs)[5,17,124-127], photodetectors[128-131], field-effect transistors (FET) [75,132,133], and photovoltaics[36,134-136]. They have also gained a great deal of attention for their use in bioimaging[42,121] or as photocatalysts[137-139] for conversion of water to hydrogen gas, oxidation of organic contaminants, or decomposition of crude oil or pesticides. (Figure 1.9) As discussed, these versatile colloidal SNCs can be modified using different surface passivating ligands for specific applications. For example, SNCs passivated by water soluble ligands can be used for bioimaging, drug delivery systems, or even as photocatalysts. Whereas, those stabilized by small organics or polymers are often used for optical or electronic purposes such as solid state devices, photovoltaics or photodiodes.

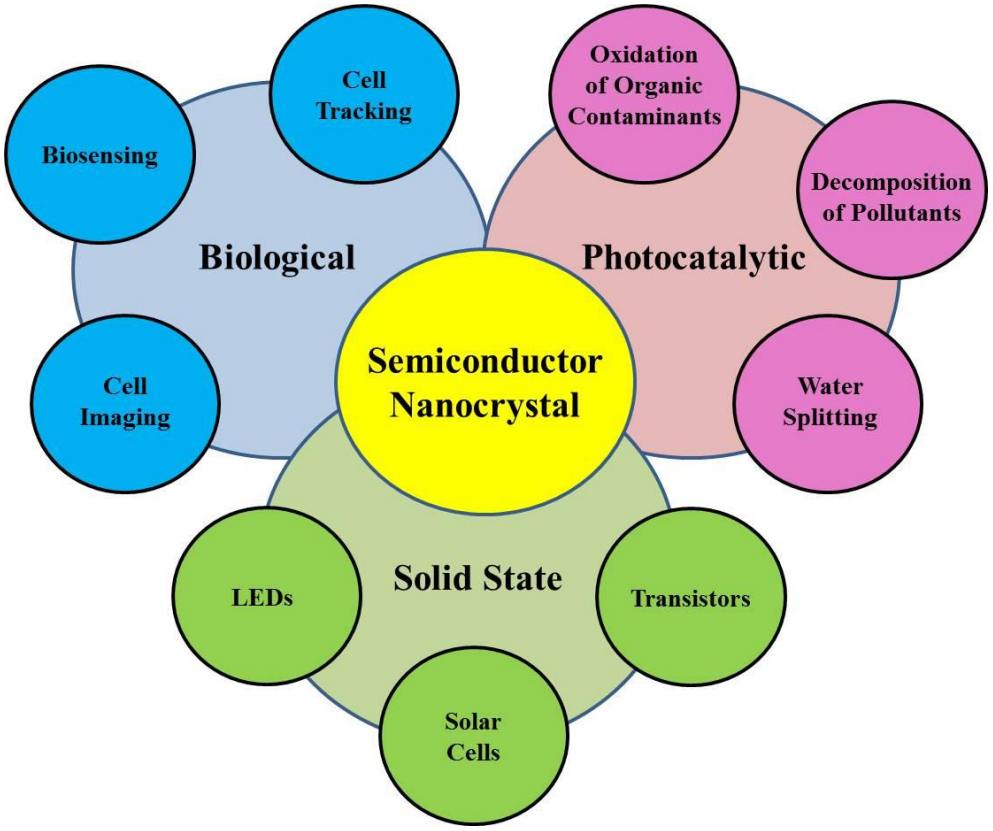

Figure 1.9: Depiction of the many versatile SNC applications.

1.6.1 Solid State Devices

Solid state devices such as LEDs and FET are widely used in our society and are transforming the field of semiconductor-based nanotechnology. SNC LEDs have narrow emission bands and have shown nearly 30% efficiency in converting electrical power to light. They have also shown long-term stability against photochemical and current-induced degradation when compared with their bulk counterparts.[53] As discussed previously, because of their quantum confinement effects, SNCs act more like molecules as they interact with light via their electronic transition dipoles, yet their ability to delocalize causes unique photophysical properties over molecules. For example, in

molecules, the wave function is localized on just one or a few bonds whereas in SNCs, the wave function is delocalized over many unit cells with little probability density at the surface. Therefore, barring no defects internally or on the surface, a SNC has the capability of near unity PL-QY and partial protection from environmental quenching.[53] Therefore, SNCs show extreme promise as materials for bright LEDs, such as those produced by Rosenthal, et al.[5,124] In 2010, their group reported one of the first examples of ultrasmall SNC (<2.0 nm) electroluminescence and pure white light emission (0.333, 0.333). This work has long been explored and expanded by many researchers and is currently comprised of LEDs of the entire color spectrum with external quantum efficiencies improving yearly.[17,125-127] Likewise, FET has also benefitted from strongly quantum-confined SNCs. Such as the work by Murray et al. in which PbSe SNC FETs allocate reversible switching between n- and p-type transport providing options for compatible metal oxide semiconductor circuits allowing for range of low-cost applications.[133]

1.6.2 Solar Cells

Another SNC application is the photovoltaic or solar cell. There has been immense research done on solar cells since 1839 when Alexandre-Edmond Becquerel observed the first interaction between semiconductors and solar radiation via an electrode in a conductive solution exposed to light.[140,141] This, indirectly, established the basis of the photovoltaic effect which is the principle that photovoltaic devices such as solar cells follow.[142-145] The name photovoltaic describes the cells ability to convert light from the sun directly to electric power also known as the photovoltaic effect.[144] The basic workings of the solar cell include: absorption of photons, formation of electron hole pair,

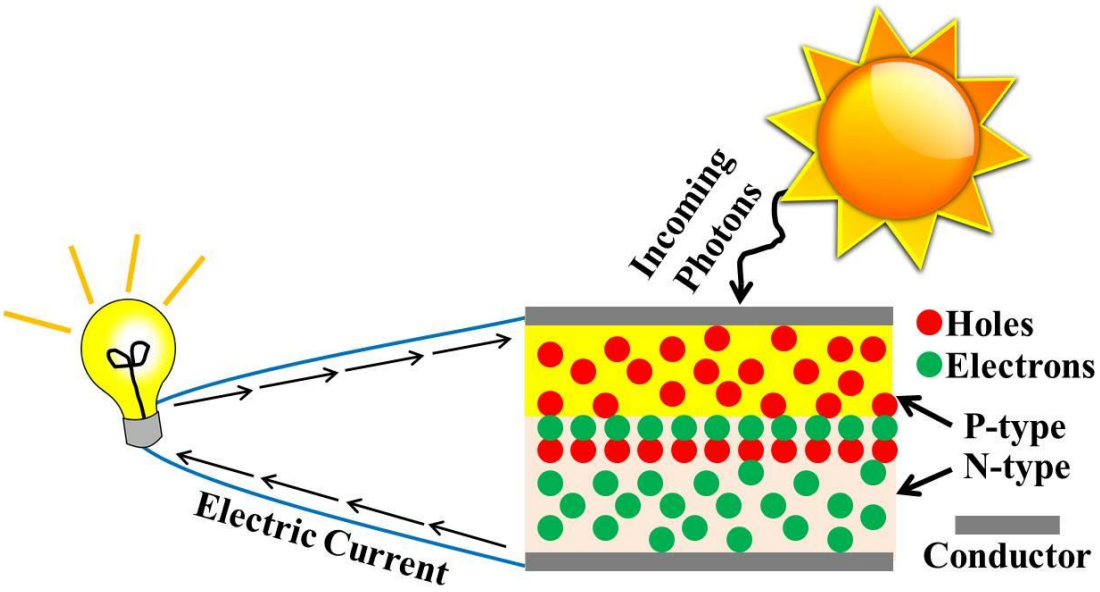

Figure 1.10: Depiction of the photovoltaic effect in a photovoltaic device. 2D model of the basic workings of the photovoltaic cell provided. First absorption of photons occurs, followed by the formation of e/h pairs, e/h pair diffusion to the junction, charge separation, charge transport to the cathode by electrons and the anode by the hole, and lastly, direct current supply for the load. (Adopted from reference 144.)

electron hole pair diffusion to the junction, charge separation, charge transport to the cathode by electrons and to the anode by the holes, and lastly, a direct current supply for the load.[146] (Figure 1.10) This basic understanding of this process is required in order to tailor SNCs to more efficiently undergo the photovoltaic effect and transform sunlight into usable energy, since the excitons must have the same energy as that of the incident rays from the sun.[147] There are three major types of SNC-based photovoltaic devices: (1) polymer hybrid solar cells, (2) metal junction solar cells, and (3) QD-sensitized solar cells.[148-152] The polymer hybrid solar cells utilize blends of conducting polymers and QDs for charge transport and separation. In the second type of solar cell, the metal junction solar cell, charge separation upon visible laser excitation is achieved at the metal-

semiconductor interface. The third type of SNC solar cell, the QD-sensitized solar cell, works by injecting excited electrons from SNCs into a large bandgap semiconductor, such as TiO_2 or ZnO, and the holes are scavenged by a redox couple.[148] SNCs have been used as the intermediate energy level in solar cells to control the size of the bandgap which improves efficiency by providing an intermediate energy level that allows for low energy photons to still generate electron-hole pairs.[41] Additionally, SNCs have been reported to emit linearly polarized light with a large stokes shift, which is the separation between the absorption and emission maxima.[153] The large stokes shift reduces light reabsorption which is important for many optoelectronic and photovoltaic applications. Therefore, SNCs for solar cell application is being actively pursued.

1.6.3 Bioimaging

SNCs can also be used for bioimaging and biosensing applications as they are known to be highly resistant to photobleaching and have a high surface to volume ratio allowing for biofunctionalization.[154] For these reasons, SNCs have been used for cell tracking and multichannel and multimodual imaging such as that reported by Alivisatos, et al. Their group utilized SNCs as fluorescent probes for biological staining and diagnostics in mouse fibroblasts.[155] They stated that ideal probes for multicolor experiments should be able to emit at spectrally resolved energies while having a narrow emission spectrum and furthermore the entire group of probes should be excitable at a single wavelength, which was possible using SNCs. When considering SNCs' biological purposes there are two important factors: (1) colloidal stability in an aqueous environment, and (2) potential toxicity. The first is accomplished using a phase transfer procedure or post-synthetic ligand exchange as described previously. The second,

however, is complicated due to the intrinsic potential toxicity of SNCs themselves. Despite this toxic nature, it was reported that SNCs with <6.0 nm hydrodynamic radii have (1) low toxicity in biological systems, (2) faster diffusion into cells, and (3) faster renal clearance.[121,156] Therefore, proper choice of ligand modification, size and shape, delivery method, and dosage all play a major role in this consideration making overcoming toxicity difficult, yet achievable for ultrasmall SNCs in bioimaging applications.[154]

1.6.4 Advanced Oxidative Processes

SNCs have been applied to recent photocatalytic research using advanced oxidation processes (AOPs) for the decomposition of organic contaminants, conversion of water to hydrogen gas, and decomposition of crude oil or pesticides. AOPs rely on solar energy-driven in-situ generation of reactive radical species such as superoxide ($O^{\bullet -}$) and hydroxide ($HO^{\bullet}$) radicals that facilitate the photodecomposition.[157] For this reason, sunlight conversion efficiency is extremely important, and thus, the choice of photocatalytic material is pivitol.[43,158-161]

1.6.4.1 Photocatalytic Activity of Binary SNCs

A photocatalyst is defined as a chemical substance which is activated by an adsorbed photon and created e/h pairs that increases a chemical reaction rate without being consumed or chemically altered.[162] The photogenerated electron and hole could perform reduction and oxidation reactions, respectively. (Figure 1.11)[163] For example, during catalytic water splitting, the photocatalyst, such as anatase TiO_2, initiates the following reaction: $2H_2O \rightarrow 2H_2 + O_2$. The first application of TiO_2 as a photocatalyst was introduced by Bard et al. in which they demonstrated the oxidation of CN^- and SO_3^{2-}

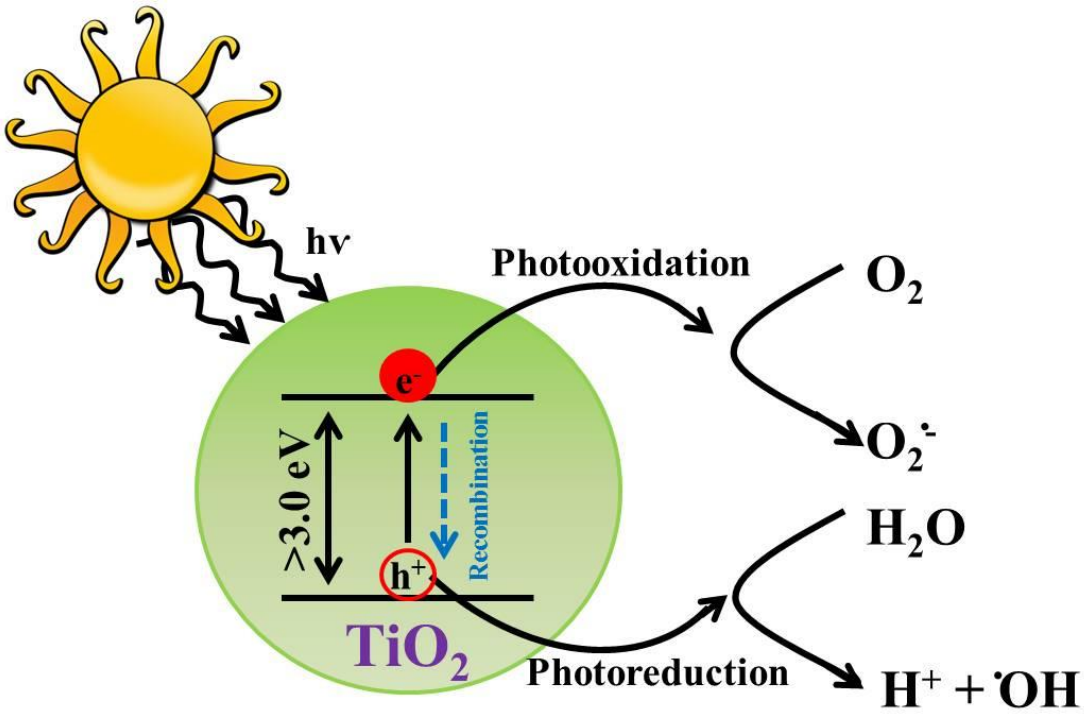

Figure 1.11: Schematic representation of anatase TiO_2 under sunlight illumination. General bandgaps are >3.0 eV. The excited electron can undergo photooxidation whereas the hole can undergo photoreduction as shown above. Recombination (blue) is also possible, but attempts to minimize this process should always be taken. (Adopted from reference 163.)

in an aqueous medium under sunlight.[164] Even today, metal oxides (TiO_2 and ZnO) are the most commonly used materials for various photocatalytic reactions.[137,162,165,166] However, metal oxides lose energy through light reflection and can only absorb ultraviolet light which accounts for less than 5% of the total solar radiation.[157] Therefore, binary SNCs (e.g. CdS and ZnSe) have been used since their bandgaps are more compatible with the solar spectrum.

A bandgap of <3.0 eV is required to effectively utilize sunlight, and as mentioned previously, there is an inverse relationship between diameter of the SNC and the bandgap. [167] Therefore, large band-gap SNCs, such as CdS and ZnS are capable of

effectively absorbing solar energy; however, they undergo photochemical decomposition without the addition of sacrificial electron and hole donors.[168] Additionally, when considering the use of a photocatalyst for AOPs, the idea of green chemistry (non-toxic) plays a critical role as the photocatalyst will be applied to our water supply. Therefore, Cd and many other binary SNCs are inadequate photocatalytic material.[169] Recent developments have aimed at improving these binary photocatalysts through: (i) doping and formation of solid solutions, (ii) introduction of co-catalysts, and (iii) development of a support structure.[157] Additionally, there has been significant interest in using ternary SNCs in order to improve bandgap position, decrease toxicity, and increase overall photocatalytic efficiency.

1.6.4.2 Photocatalytic Behavior of Ternary SNCs

Ternary SNCs provide many advantages over binary SNCs including direct bandgaps, high absorption coefficients, superb stability, and large separation of charges (slowed recombination rates).[170-175] However, composition, size, and surface chemistry determine the overall catalytic efficiency. Semiconductors composed of metal ions with partially filled orbitals show little to no photocatalytic activity due to the ions acting as catalytic centers for electron-hole recombination and therefore do not produce the radicals necessary to generate photocatalysis. However, exceptions to that rule include diamagnetic ions with d^{10} configurations such as Ag^{+}, Zn^{2+}, and Cu^{2+}, as well as those ions with an s^2 configuration such as Pb^{2+} and Bi^{3+}.[168] For these reasons, copper-based ternary SNCs (e.g., $CuInSe_2$,$CuInS_2$, $CuSbS_2$, and $CuSbSe_2$) have long been used for photovoltaic devices to replace environmentally toxic elements (e.g., Cd and Pb), but not until recently have these materials been explored for their potential use in

photocatalysis.[36,139,176-183] Moreover, all reports of ternary SNCs have been used in order to sensitize wide bandgap semiconductors (e.g., ZnS, ZnO, and TiO_2) or in conjunction with a cocatalyst (Pt). [36,138,171,184-186] For instance, Wang et al. used ZnO microspheres sensitized by $CuInSe_2$ (20 nm) and $CuInS_2$ (3.5 nm) SNCs to determine the photodegradation of rhodamine B under irradiation.[171] Results showed that the photocatalytic activity was much higher for the sensitized SNCs versus ZnO microspheres alone most likely due to the large bandgap of the ZnO material (3.37 eV) and fast recombination rate of the photogenerated e/h pairs. ZnO/$CuInS_2$ also produced higher photocatalytic efficiency than ZnO/$CuInSe_2$ as a direct result of a more suitable bandgap to utilize sunlight by $CuInS_2$ SNCs and the large surface area stemming from the SNC size regime. Similarly, Xie et al. demonstrated that $CuInS_2$ in conjunction with Pt as a cocatalyst was able to achieve higher average hydrogen production than previously reported.[138]

However, since all reports of ternary SNCs are in the form of sensitized wide bandgap semiconductors or in combination with a cocatalyst, much remains unexplored as to the significance of the ternary SNCs themselves. Therefore, the principle activity-controlling factors for photocatalysis, as explained by Osterloh[168], have been identified for semiconductor-heterostructures but not for ternary SNCs alone. The dependence of the photocatalytic activity on the structural and electronic features at the surface of the ternary SNCs are unknown. These areas represent significant opportunities for improving AOPs. A better understanding of the quantum size effects can lead to the tailoring of the electronic structure as well as the reactivity of the SNC, thus producing higher efficiency

overall. In this thesis, the effect of size and surface modification of $CuInSe_2$ for the purpose of photocatalytic decomposition of pollutants is explored.

1.7 Purpose and Specific Aims of Dissertation

The purpose of this work is to better understand the electronic and electrochemical properties of colloidal SNCs, specifically those that are in the strong confinement regime. By modulation of surface ligand chemistry and core composition, we can tailor SNC properties to meet their specific application. In the chapters to follow, we explore the following specific aims: (1) investigate the delocalization of exciton wave functions of SNCs into the ligand monolayer, (2) explore ligand-controlled electronic coupling of SNCs both in colloidal and solid states, and (3) characterize solution-state electrochemical properties and photocatalytic activity of ternary SNCs as a function of their size and surface ligand chemistry.

In Chapter 2, we demonstrate the delocalization of the exciton wave function through appropriate selection of surface passivating ligands. We present reversible delocalization of exciton wave functions of molecule-like CdSe SNCs due to attachment of Z-type ligand onto their surface. It was hypothesized that passivation of Se sites of metal chalcogenide SNCs by Z-type ligands (e.g., cadmium benzoate ($Cd(O_2CPh)_2$)), would have a two-fold outcome by (1) facilitating the delocalization of exciton wave functions into ligand monolayers (through appropriate symmetry matching and energy alignment) and (2) increasing fluorescence quantum yield (through passivation of midgap trap states). An ~240 meV red-shift in absorbance was observed upon addition of $Cd(O_2CPh)_2$ as well as a ~260 meV shift in emission with an increase in PL-QY to 73%.

These observations were reversible upon displacement of $Cd(O_2CPh)_2$ complex with *N,N,N',N'*-tetramethylethylene-1,2-diamine. ^{1}H NMR and FTIR characterizations of the SNCs demonstrate that the OLA remained attach to the surface of the SNCs during the reversible exchange of $Cd(O_2CPh)_2$ and based on surface ligand characterization, we propose that these bathochromic shifts are a consequence of the delocalization as opposed to originating from a change in the size or relaxation of the inorganic core. Furthermore, increase in radiative lifetime and PL-QY was proven to be a combination of passivation and delocalization effects. This section has been submitted to Chemistry of Materials (2016).

In Chapter 3, we explored the ligand-controlled electronic coupling of SNCs through the use of PEG-thiolate. PEG chains can impart liquid crystalline characteristics to ligand-coated SNCs, which can improve SNCs packing into thin-films and is imperative for solid state device fabrication. This “solvent-like” nature of PEGs coupled with a low hydrodynamic radii, allow for strong inter-SNC interaction through the entanglement of the excitonic wave function. Here, the inter-SNC electronic coupling through manipulation of exciton delocalization using a systematic variation of size and surface ligation was studied. This strong inter-SNC electronic coupling coupled with high solubility, such as that provided by PEG-thiolate-coated CdSe SNCs, can increase the stability of SNCs during solution-phase electrochemical characterization. This enhanced stability provides quantitative information about the electrochemical oxidation and reduction potentials and enables the control of the generation and transfer of charge carriers for applications such as photovoltaic and photocatalytic applications. The work

presented in this section has been published in *RSC Advances* (2014, 4, 30742-30753) and *Nanoscale* (2015, 7, 11667-11677).

The last section utilizes the previous two sections in order to perform electrochemical analysis of $CuInSe_2$ SNCs and investigate their visible light driven photocatalytic activities. These studies provide some of the most pristine solution phase electrochemistry available and serve as the first reports of the effects of structural parameters of $CuInSe_2$ SNCs on visible light driven photocatalytic degradation of pollutants under homogenous conditions. $CuInSe_2$ SNCs provide: (1) high absorption coefficients, (2) environmentally nontoxic, (3) tunable optical bandgaps in the visible to NIR region of the solar spectrum through size and composition (as stated in previous sections), and (4) low bandgap energy, which will allow more effective generation of electron-hole pairs, and prevent recombination, which are prerequisites for nanomaterials to be used in AOPs. In order to efficiently evaluate the bandgap and for eventual use in an aqueous environment a solution-phase, post-synthetic ligand exchange replacing insulating, bulky OLA with PEG-thiol to prepare PEG_n-thiolate-coated (n=6-150) $CuInSe_2$ SNCs was used to enhance their solubility in water. Electrochemical characterization of our PEG-thiolate-coated SNCs showed that the thermodynamic driving force ($-\Delta G$) for oxygen reduction, which increased with decreasing bandgap, was a major contributor to the overall photocatalytic reaction using $CuInSe_2$ SNCs as a photocatalyst. Additionally, phenol degradation efficiency was monitored and a two-fold increase from 30-60% was achieved by varying the diameter of the $CuInSe_2$ SNCs from 5.3 to 1.8 nm. Surface ligand dependency of the photocatalytic efficiency was also investigated on $CuInSe_2$ SNCs where shorter chain lengths of PEG produced the highest

photocatalytic efficiency. The information provided herein could be used to produce superior SNC photocatalysts for a variety of applications including oxidation of organic contaminants, conversion of water to hydrogen gas, and decomposition of crude oil or pesticides. Therefore, we believe our work will significantly advance quantitative electrochemical characterization of SNCs and allow for the design of highly efficient, sustainable photocatalysts resulting in economic and environmental benefits. This final section has been published in *Chemistry of Materials* (2016, 28, 1107-1120).

1.8 Outlook

The work presented in this thesis has the ability to facilitate the design of bioimaging, solid-state, and photocatalytic materials through appropriate choice of surface ligation without changing the core chemical or structural integrity. This knowledge can further be applied to various SNCs for a myriad of applications including AOPs. While ternary $CuInSe_2$ SNCs provided us with a means to study the structural parameters of SNCs on visible light-driven photocatalysis, the high cost and low earth abundance of indium makes its use in AOPs questionable. On the other hand, ternary copper antimony chalcogenide SNCs ($CuSbE_2$ (E=S or Se)) are emerging as an alternative to many ternary and quaternary indium based SNCs due to their relative abundance and non-toxic composition.[185,187-192] Many promising reports of $CuSbS_2$ and $CuSbSe_2$ SNCs as photovoltaic material are available, however, to date; there are no reports on their photocatalytic activity.[185,187,188,191-193] Additionally, there are no reports in which low-temperature synthesis is utilized for $CuSbE_2$ and very few reports of colloidal synthetic methods[194-197]. Therefore, using our previously gained knowledge, a low temperature synthesis of $CuSbS_{2-x}Se_x$ SNCs could be achieved in which proper ligation

could be utilized in order to perform electrochemical characterization and study their photocatalytic behavior. Furthermore, our knowledge of surface chemistry could be used to produce hybrid NSs[158] between localized surface plasmon resonance (LSPR) active Au nanoprisms (NPs) and our $CuSbS_{2-x}Se_x$ SNCs to further enhance their photocatalytic behavior. Hybrid NSs require (1) plasmonic NSs with defined geometric features that are able to enhance the surrounding medium yet robust enough to withstand treatment with the semiconductor and (2) the ability to easily integrate such structures with a semiconductor material.[198]Au NPs provide extraordinary stability under light, a well-defined prismatic shape, and unique LSPR properties in the 700-900 nm region. Likewise NPs provide strong electromagnetic (EM) field enhancement at their sharp tips and large absorption cross-section.[199-201] This is extremely important for hybrid NSs as it has been reported that emergent photoprocesses are most active in the regions of high EM field strength.[202] Additionally, the second requirement is extremely important as the ability to connect both the Au NPs with the SNCs while still providing adequate electron transfer is vital. The use of PEG-dithiol as the insulating interlayer and covalent bond between the nanoprisms and the ternary structures would provide the necessary connection while allowing for electron transfer from the Au NP to the SNC. Since Au NPs are plasmonically active, a drastic increase in efficiency coming from the sharing of concentrated energy contained in the localized plasmonic oscillations is expected. To the best of our knowledge, there are no reports of the photocatalytic behavior of $CuSbS_{2-x}Se_x$ SNC-Au NP hybrid NSs. We believe that these hybrid NSs would more effectively capture sunlight than SNCs alone, and as such, they offer a unique and environmentally sound solution to current obstacles in AOPs.

1.9 References

(1) Murray, C. B.; Norris, D. J.; Bawendi, M. G. *J. Am. Chem. Soc.* 1993, *115*, 8706-8715.

(2) Dukes, A. D.; McBride, J. R.; Rosenthal, S. J. *Chem. Mater.* 2010, *22*, 6402-6408.

(3) Purdie, N., Brittain, H. G., Eds.; Elsevier: Amsterdam, 1994.

(4) Harrell, S. M.; McBride, J. R.; Rosenthal, S. J. *Chem. Mater.* 2013, *25*, 1199-1210.

(5) Bowers, M. J.; McBride, J. R.; Rosenthal, S. J. *J. Am. Chem. Soc.* 2005, *127*, 15378-15379.

(6) Harrell, S. M.; McBride, J. R.; Rosenthal, S. J. *Chem. Mater.* 2013.

(7) Jiang, Z.-J.; Kelley, D. F. *ACS Nano* 2010, *4*, 1561-1572.

(8) Newton, J. C.; Ramasamy, K.; Mandal, M.; Joshi, G. K.; Kumbhar, A.; Sardar, R. *J. Phys. Chem. C* 2012, *116*, 4380-4389.

(9) Peng, Z. A.; Peng, X. *J. Am. Chem. Soc.* 2001, *123*, 1389-1395.

(10) Landes, C.; Braun, M.; Burda, C.; El-Sayed, M. A. *Nano Lett.* 2001, *1*, 667-670.

(11) Soloviev, V. N.; Eichh√∂fer, A.; Fenske, D.; Banin, U. *J. Am. Chem. Soc.* 2001, *123*, 2354-2364.

(12) Peng, Z. A.; Peng, X. *J. Am. Chem. Soc.* 2000, *123*, 183-184.

(13) Peng, Z. A.; Peng, X. *J. Am. Chem. Soc.* 2002, *124*, 3343-3353.

(14) Qu, L.; Peng, Z. A.; Peng, X. *Nano Lett.* 2001, *1*, 333-337.

(15) Qu, L.; Yu, W. W.; Peng, X. *Nano Lett.* 2004, *4*, 465-469.

(16) Cossairt, B. M.; Owen, J. S. *Chem. Mater.* 2011, *23*, 3114-3119.

(17) Dolai, S.; Nimmala, P. R.; Mandal, M.; Muhoberac, B. B.; Dria, K.; Dass, A.; Sardar, R. *Chem. Mater.* 2013.

(18) Kim, B. H.; Hackett, M. J.; Park, J.; Hyeon, T. S. *Chem. Mater.* 2014, *26*, 59-71.

(19) Long, R.; English, N. J.; Prezhdo, O. V. *J. Am. Chem. Soc.* 2013, *135*, 18892-18900.

(20) Yang, Y.; Rodríguez-Córdoba, W.; Lian, T. *J. Am. Chem. Soc.* 2011, *133*, 9246-9249.

(21) Cossairt, B. M.; Juhas, P.; Billinge, S. J. L.; Owen, J. S. *J. Phys. Chem. Lett.* 2011, *2*, 3075-3080.

(22) Zanella, M.; Abbasi, A. Z.; Schaper, A. K.; Parak, W. J. *J. Phys. Chem. C* 2010, *114*, 6205-6215.

(23) Riehle, F. S.; Bienert, R.; Thomann, R.; Urban, G. A.; Kruger, M. Blue *Nano Lett.* 2009, *9*, 514-518.

(24) Kuçur, E.; Ziegler, J.; Nann, T. *Small* 2008, *4*, 883-887.

(25) Evans, C. M.; Guo, L.; Peterson, J. J.; Maccagnano-Zacher, S.; Krauss, T. D. *Nano Lett.* 2008, *8*, 2896-2899.

(26) Kudera, S.; Zanella, M.; Giannini, C.; Rizzo, A.; Li, Y.; Gigli, G.; Cingolani, R.; Ciccarella, G.; Spahl, W.; Parak, W. J.; Manna, L. *Adv. Mater.* 2007, *19*, 548-552.

(27) Wang, Y.; Zhang, Y.; Wang, F.; Giblin, D. E.; Hoy, J.; Rohrs, H. W.; Loomis, R. A.; Buhro, W. E. *Chem. Mater.* 2014, *26*, 2233-2243.

(28) Beecher, A. N.; Yang, X.; Palmer, J. H.; LaGrassa, A. L.; Juhas, P.; Billinge, S. J. L.; Owen, J. S. *J. Am. Chem. Soc.* 2014, *136*, 10645-10653.

(29) Talapin, D. V.; Rogach, A. L.; Kornowski, A.; Haase, M.; Weller, H. *Nano Lett.* 2001, *1*, 207-211.

(30) Talapin, D. V.; Lee, J.-S.; Kovalenko, M. V.; Shevchenko, E. V. *Chem. Rev.* 2009, *110*, 389-458.

(31) Cao, Y. C.; Wang, J. *J. Am. Chem. Soc.* 2004, *126*, 14336-14337.

(32) Morris-Cohen, A. J.; Frederick, M. T.; Lilly, G. D.; McArthur, E. A.; Weiss, E. A.. *J. Phys. Chem. Lett.* 2010, *1*, 1078–1081.

(33) Yu, K.; Hu, M. Z.; Wang, R.; Piolet, M. L.; Frotey, M.; Zaman, M. B.; Wu, X.; Leek, D. M.; Tao, Y.; Wilkinson, D.; Li, C. *J. Phys. Chem. C* 2010, *114*, 3329.

(34) Siy, J. T.; Brauser, E. M.; Bartl, M. H. *Chem. Commun.* 2011, *47*, 364.

(35) Lees, E. E.; Nguyen, T.-L.; Clayton, A. H. A.; Mulvaney, P. *ACS Nano* 2009, *3*, 1121-1128.

(36) Tvrdy, K.; Frantsuzov, P. A.; Kamat, P. V. *Proc. Natl. Acad. Sci. USA* 2011, *108*, 29-34.

(37) Buckley, J. J.; Couderc, E.; Greaney, M. J.; Munteanu, J.; Riche, C. T.; Bradforth, S. E.; Brutchey, R. L. *ACS Nano* 2014, *8*, 2512-2521.

(38) G. D. Lilly, A. C. W., S. Grunder, C. Valente,; M. T. Frederick, J. F. S. a. E. A. W. *J. Mater. Chem.* 2011, *21*, 11492-11497.

(39) Alexander L. Efros, D. J. L., and Leonid Tsybeskov. Kluwer Academic/Plenum Publishers: New York, New York, 2003.

(40) Gregg, B. A. *J. Phys. Chem. B* 2003, *107*, 4688-4698.

(41) Jennifer A. Hollingsworth, V. I. K., David J. Norris, Alexander L. Efros, Philippe Guyot-Sionnest, Moonsub Shim, Congjun Wang, Ken T. Shimizu, Moungi G. Bawendi, Neil C. Greenham, Uri Banin, Oded Millo, Authur J. Nozik, Olga I. Micic, Hedi Mattoussi, Remi Beaulac, Stefan T. Ochsenbein, and Daniel R. Gamelin: *Nanocrystal Quantum Dots*; 2 ed.; CRC Press, 2010.

(42) Kairdolf, B. A.; Smith, A. M.; Stokes, T. H.; Wang, M. D.; Young, A. N.; Nie, S. *Annu. Rev. Anal. Chem (Palo Alto, Calif.)* 2013, *6*, 143.

(43) Kolny-Olesiak, J.; Weller, H. *ACS Appl. Mater. Interfaces* 2013, *5*, 12221-12237.

(44) Kovalenko, M. V.; Scheele, M.; Talapin, D. V. *Science* 2009, *324*, 1417-1420.

(45) Law, M.; Luther, J. M.; Song, Q.; Hughes, B. K.; Perkins, C. L.; Nozik, *J. Am. Chem. Soc.* 2008, *130*, 5974-5985.

(46) Lee, J.-S.; Kovalenko, M. V.; Huang, J.; Chung, D. S.; Talapin, D. V. *Nat. Nanotechnol.* 2011, *6*, 348-352.

(47) Querner, C.; Reiss, P.; Sadki, S.; Zagorska, M.; Pron, A. *Phys. Chem. Chem. Phys.* 2005, *7*, 3204-3209.

(48) Knowles, K. E.; Tice, D. B.; McArthur, E. A.; Solomon, G. C.; Weiss, E. A. *J. Am. Chem. Soc.* 2009, *132*, 1041-1050.

(49) Tomasulo, A.; Ramakrishna, M. V. *J. Chem. Phys* 1996, *105*, 3612-3626.

(50) Liu, J.; Yang, W.; Li, Y.; Fan, L.; Li, Y. *Phys. Chem. Chem. Phys.* 2014, *16*, 4778-4788.

(51) Riel, B. J. *Am. J. Phys.* 2008, *76*, 750-757.

(52) Anderson, N. C. Columbia University, 2014.

(53) Nirmal, M.; Brus, L. *Acc. Chem. Res.h* 1999, *32*, 407-414.

(54) Rumbles, G. D. S. a. G. *Nat Mater* 2006, *5*, 683-696.

(55) Chamarro, M.; Gourdon, C.; Lavallard, P.; Lublinskaya, O.; Ekimov, A. I. *Phys. Rev. B* 1996, *53*, 1336-1342.

(56) Brus, L. E. *J. Chem. Phys* 1984, *80*, 4403-4409.

(57) Ioannou, D.; Griffin, D. K. 2010.

(58) Chukwuocha, E. O.; Onyeaju, M. C.; Harry, T. S. T. *World Journal of Condensed Matter Physics* 2012, *Vol.02No.02*, 5.

(59) Green, M. *Organomet. Chem.* 1995, *500*, 127-148.

(60) Kamat, P. V.; Tvrdy, K.; Baker, D. R.; Radich, J. G. *Chem. Rev.* 2010, *110*, 6664-6688.

(61) Coe, S.; Woo, W.-K.; Bawendi, M.; Bulovic, V. *Nature* 2002, *420*, 800-803.

(62) Colvin, V. L.; Schlamp, M. C.; Alivisatos, A. P. *Nature* 1994, *370*, 354-357.

(63) Teunis, M. B.; Dolai, S.; Sardar, R. *Langmuir* 2014, *30*, 7851-7858.

(64) Sardar, R.; Lawrence, K.; Johnson, M.; Dolai, S.; Kumbhar, A. *Nanoscale* 2015.

(65) Williams, K. J.; Tisdale, W. A.; Leschkies, K. S.; Haugstad, G.; Norris, D. J.; Aydil, E. S.; Zhu, X. Y. *ACS Nano* 2009, *3*, 1532-1538.

(66) Fafarman, A. T.; Koh, W.-k.; Diroll, B. T.; Kim, D. K.; Ko, D.-K.; Oh, S. J.; Ye, X.; Doan-Nguyen, V.; Crump, M. R.; Reifsnyder, D. C.; Murray, C. B.; Kagan, C. R. *J. Am. Chem. Soc.* 2011, *133*, 15753-15761.

(67) Koole, R.; Liljeroth, P.; de Mello Donegá, C.; Vanmaekelbergh, D.; Meijerink, A. *J. Am. Chem. Soc.* 2006, *128*, 10436-10441.

(68) Zanella, M.; Abbasi, A. Z.; Schaper, A. K.; Parak, W. J. *J. Phys. Chem. C* 2010, *114*, 6205-6215.

(69) Riehle, F. S.; Bienert, R.; Thomann, R.; Urban, G. A.; Krüger, M. *Nano Lett.* 2009, *9*, 514-518.

(70) Park, Y.-S.; Dmytruk, A.; Dmitruk, I.; Kasuya, A.; Takeda, M.; Ohuchi, N.; Okamoto, Y.; Kaji, N.; Tokeshi, M.; Baba, Y. *ACS Nano* 2009, *4*, 121-128.

(71) Luther, J. M.; Law, M.; Song, Q.; Perkins, C. L.; Beard, M. C.; Nozik, A. J. *ACS Nano* 2008, *2*, 271-280.

(72) Yu, D.; Wang, C.; Guyot-Sionnest, P. *Science* 2003, *300*, 1277-1280.

(73) Norman, Z. M.; Anderson, N. C.; Owen, J. S. *ACS Nano* 2014, *8*, 7513-7521.

(74) Nag, A.; Kovalenko, M. V.; Lee, J.-S.; Liu, W.; Spokoyny, B.; Talapin, D. V. *J. Am. Chem. Soc.* 2011, *133*, 10612-10620.

(75) Liu, Y.; Tolentino, J.; Gibbs, M.; Ihly, R.; Perkins, C. L.; Liu, Y.; Crawford, N.; Hemminger, J. C.; Law, M. *Nano Lett.* 2013, *13*, 1578-1587.

(76) Zhou, Y.; Wang, F.; Buhro, W. E. *J. Am. Chem. Soc.* 2015.

(77) Anderson, N. C.; Hendricks, M. P.; Choi, J. J.; Owen, J. S. *J. Am. Chem. Soc.* 2013, *135*, 18536-18548.

(78) Zhang, H.; Hu, B.; Sun, L.; Hovden, R.; Wise, F. W.; Muller, D. A.; Robinson, R. D. *Nano Lett.* 2011, *11*, 5356-5361.

(79) Choi, J.-H.; Fafarman, A. T.; Oh, S. J.; Ko, D.-K.; Kim, D. K.; Diroll, B. T.; Muramoto, S.; Gillen, J. G.; Murray, C. B.; Kagan, C. R. *Nano Lett.* 2012, *12*, 2631-2638.

(80) Kloust, H.; Schmidtke, C.; Merkl, J.-P.; Feld, A.; Schotten, T.; Fittschen, U. E. A.; Gehring, M.; Ostermann, J.; Poselt, E.; Weller, H. *J. Phys. Chem. C* 2013, *117*, 23244-23250.

(81) Yu, W. W.; Chang, E.; Falkner, J. C.; Zhang, J.; Al-Somali, A. M.; Sayes, C. M.; Johns, J.; Drezek, R.; Colvin, V. L. *J. Am. Chem. Soc.* 2007, *129*, 2871-2879.

(82) Carion, O.; Mahler, B.; Pons, T.; Dubertret, B. *Nat Protoc* 2007, *2*, 2383-2390.

(83) Igor L. Medintz, H. T. U., Ellen R. Goldman, Hedi Mattoussi. Quantum Dot Bioconjugates for Imaging, Labelling, and Sensing. *Nat. Mater.* 2005, *4*, 435-446.

(84) Wuister, S. F.; de Mello Donegá, C.; Meijerink, A. *J. Phys. Chem. B* 2004, *108*, 17393-17397.

(85) Frenkel, J. *Phys. Rev.* 1931, *37*, 17-44.

(86) Wannier, G. H. *Phys. Rev.* 1937, *52*, 191-197.

(87) Frederick, M. T.; Weiss, E. A. *ACS Nano* 2010, *4*, 3195-3200.

(88) Koole, R.; Luigjes, B.; Tachiya, M.; Pool, R.; Vlugt, T. J. H.; de Mello Donegá, C.; Meijerink, A.; Vanmaekelbergh, D. *J. Phys. Chem. C* 2007, *111*, 11208-11215.

(89) Brus, L. E. *J. Chem. Phys* 1983, *79*, 5566-5571.

(90) Lippens, P.; Lannoo, M. *Phys. Rev. B* 1990, *41*, 6079.

(91) Wang, L.-W.; Li, J. *Phys. Rev. B* 2004, *69*, 153302.

(92) Wang, L.-W.; Zunger, A. *Phys. Rev. B* 1996, *53*, 9579.

(93) Zhang, P.; Crespi, V. H.; Chang, E.; Louie, S. G.; Cohen, M. L. *Nature* 2001, *409*, 69-71.

(94) Perdew, J. P. *Int. J. Quantum Chem.* 1985, *28*, 497-523.

(95) Bechstedt, F.; Del Sole, R. *Phys. Rev. B* 1988, *38*, 7710-7716.

(96) Grüning, M.; Marini, A.; Rubio, A. *J. Chem. Phys* 2006, *124*, 154108.

(97) Fabien, T.; Peter, B.; Karlheinz, S. *J. Phys. Condens. Matter* 2007, *19*, 196208.

(98) Schlaf, R.; Parkinson, B. A.; Lee, P. A.; Nebesny, K. W.; Armstrong, N. R. *J. Phys. Chem. B* 1999, *103*, 2984-2992.

(99) Liao, L. S.; Fung, M. K.; Lee, C. S.; Lee, S. T.; Inbasekaran, M.; Woo, E. P.; Wu, W. W. *Appl. Phys. Lett.* 2000, *76*, 3582-3584.

(100) Ahmadi, M.; Pramana, S. S.; Batabyal, S. K.; Boothroyd, C.; Mhaisalkar, S. G.; Lam, Y. M. *Inorg. Chem.* 2013, *52*, 1722-1728.

(101) Lesnyak, V.; George, C.; Genovese, A.; Prato, M.; Casu, A.; Ayyappan, S.; Scarpellini, A.; Manna, L. *ACS Nano* 2014, *8*, 8407-8418.

(102) Norako, M. E.; Greaney, M. J.; Brutchey, R. L. *J. Am. Chem. Soc.* 2012, *134*, 23-26.

(103) Zhong, H.; Lo, S. S.; Mirkovic, T.; Li, Y.; Ding, Y.; Li, Y.; Scholes, G. D. *ACS Nano* 2010, *4*, 5253-5262.

(104) Kuçur, E.; Bücking, W.; Arenz, S.; Giernoth, R.; Nann, T. *ChemPhysChem* 2006, *7*, 77-81.

(105) Kucur, E.; Bücking, W.; Giernoth, R.; Nann, T. *J. Phys. Chem. B* 2005, *109*, 20355-20360.

(106) Pradhan, N.; Reifsnyder, D.; Xie, R.; Aldana, J.; Peng, X. *J. Am. Chem. Soc.* 2007, *129*, 9500-9509.

(107) Jasieniak, J.; Califano, M.; Watkins, S. E. *ACS Nano* 2011, *5*, 5888-5902.

(108) Inamdar, S. N.; Ingole, P. P.; Haram, S. K. *ChemPhysChem* 2008, *9*, 2574-2579.

(109) Munro, A. M.; Zacher, B.; Graham, A.; Armstrong, N. R. *ACS Appl. Mater. Interfaces* 2010, *2*, 863-869.

(110) Hwang, J.; Wan, A.; Kahn, A. *Mater. Sci. Eng. R-Rep.* 2009, *64*, 1-31.

(111) Yi, Y.; Lyon, J.; Beerbom, M.; Schlaf, R. *J. Appl. Phys.* 2006, *100*, 093719.

(112) Van Buuren, T.; Dinh, L.; Chase, L.; Siekhaus, W.; Terminello, L. J. *Phys. Rev. Letters* 1998, *80*, 3803.

(113) Bard, A. J. F., L. R. *Fundamentals and Applications*; 2nd ed., 2001.

(114) Kucur, E.; Riegler, J.; Urban, G. A.; Nann, T. *J. Chem. Phys* 2003, *119*, 2333-2337.

(115) Yu, D.; Wang, C.; Guyot-Sionnest, P. *Science* 2003, *300*, 1277-1280.

(116) Haram, S. K.; Quinn, B. M.; Bard, A. J. *J. Am. Chem. Soc.* 2001, *123*, 8860-8861.

(117) Amelia, M.; Lincheneau, C.; Silvi, S.; Credi, A. *Chem. Soc. Rev.* 2012, *41*, 5728-5743.

(118) Haram, S. K.; Quinn, B. M.; Bard, A. J. *J. Am. Chem. Soc.* 2001, *123*, 8860-8861.

(119) Ingole, P. P.; Markad, G. B.; Saraf, D.; Tatikondewar, L.; Nene, O.; Kshirsagar, A.; Haram, S. K. *J. Phys. Chem. C* 2013, *117*, 7376-7383.

(120) Poznyak, S. K.; Osipovich, N. P.; Shavel, A.; Talapin, D. V.; Gao, M.; Eychmüller, A.; Gaponik, N. *J. Phys. Chem. B* 2005, *109*, 1094-1100.

(121) Lawrence, K. N.; Dolai, S.; Lin, Y.-H.; Dass, A.; Sardar, R. *RSC Adv.* 2014, *4*, 30742-30753.

(122) Williams, M. E.; Masui, H.; Long, J. W.; Malik, J.; Murray, R. W. *J. Am. Chem. Soc.* 1997, *119*, 1997-2005.

(123) Williams, M. E.; Murray, R. W. *Chem. Mater.* 1998, *10*, 3603-3610.

(124) Schreuder, M. A.; Xiao, K.; Ivanov, I. N.; Weiss, S. M.; Rosenthal, S. J. *Nano Lett.* 2010, *10*, 573-576.

(125) Dagani, R. O. N. *C&EN* 2001, *79*, 7-8.

(126) Dolai, S.; Dutta, P.; Muhoberac, B. B.; Irving, C. D.; Sardar, R. *Chem. Mater.* 2015, *27*, 1057-1070.

(127) Yang, Y.; Zheng, Y.; Cao, W.; Titov, A.; Hyvonen, J.; MandersJesse, R.; Xue, J.; Holloway, P. H.; Qian, L. *Nat Photon* 2015, *9*, 259-266.

(128) Oertel, D. C.; Bawendi, M. G.; Arango, A. C.; Bulovic, V. *Appl. Phys. Lett.* 2005, *87*, 213505.

(129) Drndic, M.; Jarosz, M. V.; Morgan, N. Y.; Kastner, M. A.; Bawendi, M. G. *J. Appl. Phys.* 2002, *92*, 7498-7503.

(130) Rogalski, A.; Razeghi, M. *Opto-Electron. Rev.* 1996, 13-30.

(131) Monroy, E.; Omnès, F.; Calle, F. *Semicond. Sci. Technol.* 2003, *18*, R33.

(132) Liu, S.; Wang, W. M.; Briseno, A. L.; Mannsfeld, S. C.; Bao, Z. *Adv. Mater.* 2009, *21*, 1217-1232.

(133) Talapin, D. V.; Murray, C. B. PbSe *Science* 2005, *310*, 86-89.

(134) Robel, I. n.; Kuno, M.; Kamat, P. V. *J. Am. Chem. Soc.* 2007, *129*, 4136-4137.

(135) Ahn, S.; Kim, C.; Yun, J. H.; Gwak, J.; Jeong, S.; Ryu, B.-H.; Yoon, K. *J. Phys. Chem. C* 2010, *114*, 8108-8113.

(136) Guo, Q.; Ford, G. M.; Yang, W.-C.; Walker, B. C.; Stach, E. A.; Hillhouse, H. W.; Agrawal, R. *J. Am. Chem. Soc.* 2010, *132*, 17384-17386.

(137) Hoffmann, M. R.; Martin, S. T.; Choi, W.; Bahnemann, D. W. *Chem. Rev.* 1995, *95*, 69-96.

(138) Zheng, L.; Xu, Y.; Song, Y.; Wu, C.; Zhang, M.; Xie, Y. *Inorg. Chem.* 2009, *48*, 4003-4009.

(139) Zhao, J.; Holmes, M. A.; Osterloh, F. E. *ACS nano* 2013, *7*, 4316-4325.

(140) Fraas, L. M., Springer, 2014.

(141) Becquerel, A.-E. *Comptes Rendus* 1839, *9*, 1839.

(142) Energy, U. S. D. o. *Energy Efficiency and Renewable Energy* 2001.

(143) Physics 232 the Photoelectric Effect. http://www.pa.msu.edu/courses/1997spring/phy232/lectures/quantum/photoelectric.html.

(144) What is Solar? http://solarpowerplanetearth.com/index.html (accessed November 5, 2012).

(145) Year of Einstein--Photoelectric Effect. http://www.einsteinyear.org/facts/photoelectric_effect/ (accessed March 21, 2015).

(146) Cho Woo-Suhl, X. W., James E. Moore, Tom Adams. *Solar Cell Technology* [Purdue University]

(147) Solar Cells http://org.ntnu.no/solarcells/index.php. (accessed February 3, 2016)

(148) Bang, J. H.; Kamat, P. V. *ACS Nano* 2009, *3*, 1467-1476.

(149) Lee, H. J.; Yum, J.-H.; Leventis, H. C.; Zakeeruddin, S. M.; Haque, S. A.; Chen, P.; Seok, S. I.; GraÃàtzel, M.; Nazeeruddin, M. K. *J. Phys. Chem. C* 2008, *112*, 11600-11608.

(150) Fuke, N.; Hoch, L. B.; Koposov, A. Y.; Manner, V. W.; Werder, D. J.; Fukui, A.; Koide, N.; Katayama, H.; Sykora, M. *ACS Nano* 2010, *4*, 6377-6386.

(151) Bakulin, A. A.; Neutzner, S.; Bakker, H. J.; Ottaviani, L.; Barakel, D.; Chen, Z. *ACS Nano* 2013.

(152) Mocatta, D.; Cohen, G.; Schattner, J.; Millo, O.; Rabani, E.; Banin, U. *Science* 2011, *332*, 77-81.

(153) Smith, A. M.; Nie, S. *Acc. Chem. Res.h* 2009, *43*, 190-200.

(154) Wang, Y.; Hu, R.; Lin, G.; Roy, I.; Yong, K.-T. *ACS Appl. Mater. Interfaces* 2013, *5*, 2786-2799.

(155) Bruchez, M.; Moronne, M.; Gin, P.; Weiss, S.; Alivisatos, A. P. *Science* 1998, *281*, 2013-2016.

(156) Hak Soo, C.; Wenhao, L.; Preeti, M.; Eiichi, T.; John, P. Z.; Binil Itty, I.; Moungi, G. B.; John, V. F. *Nat. Biotechnol.* 2007, *25*, 1165-1170.

(157) Colmenares, J. C.; Luque, R.; Campelo, J. M.; Colmenares, F.; Karpiński, Z.; Romero, A. A. *Materials* 2009, *2*, 2228-2258.

(158) Cushing, S. K.; Li, J.; Meng, F.; Senty, T. R.; Suri, S.; Zhi, M.; Li, M.; Bristow, A. D.; Wu, N. *J. Am. Chem. Soc.* 2012, *134*, 15033-15041.

(159) Naya, S.-i.; Inoue, A.; Tada, H. *J. Am. Chem. Soc.* 2010, *132*, 6292-6293.

(160) Du, K.; Glogowski, E.; Tuominen, M. T.; Emrick, T.; Russell, T. P.; Dinsmore, A. D. *Langmuir* 2013, *29*, 13640-13646.

(161) Qin, N.; Liu, Y.; Wu, W.; Shen, L.; Chen, X.; Li, Z.; Wu, L. *Langmuir* 2015, *31*, 1203-1209.

(162) M., F.: *Photocatalytic Oxidation of Organic Substances.*; New York Academic Publishers: New York, 1988. pp. 445-467.

(163) Li, C.; Wang, F.; Yu, J. C. S. *Energy & Environmental Science* 2011, *4*, 100-113.

(164) Frank, S. N.; Bard, A. J. *J. Phys. Chem.* 1977, *81*, 1484-1488.

(165) Fujishima, A.; Rao, T. N.; Tryk, D. A. *J. Photochem. Photobiol.* 2000, *1*, 1-21.

(166) Rajaambal, S.; Sivaranjani, K.; Gopinath, C. *J Chem Sci* 2015, *127*, 33-47.

(167) Kogo, K.; Yoneyama, H.; Tamura, H. *J. Phys. Chem.* 1980, *84*, 1705-1710.

(168) Osterloh, F. E. *Chem. Mater.* 2007, *20*, 35-54.

(169) Aragay, G.; Pino, F.; Merkoçi, A. *Chem. Rev.* 2012, *112*, 5317-5338.

(170) Jiang, C.; Lee, J.-S.; Talapin, D. V. *J. Am. Chem. Soc.* 2012, *134*, 5010-5013.

(171) Shen, F.; Que, W.; He, Y.; Yuan, Y.; Yin, X.; Wang, G. *ACS Appl. Mater. Interfaces* 2012, *4*, 4087-4092.

(172) Kamat, P. V. *J. Phys. Chem. Lett.* 2012, *3*, 663-672.

(173) Aldakov, D.; Lefrancois, A.; Reiss, P. *J. Mater. Chem. C* 2013, *1*, 3756-3776.

(174) Guillemoles, J.-F.; Rau, U.; Kronik, L.; Schock, H.-W.; Cahen, D. *Adv. Mater.* 1999, *11*, 957-961.

(175) Rockett, A.; Birkmire, R. *J. Appl. Phys.* 1991, *70*, R81-R97.

(176) Guo, Q.; Kim, S. J.; Kar, M.; Shafarman, W. N.; Birkmire, R. W.; Stach, E. A.; Agrawal, R.; Hillhouse, H. W. *Nano Lett.* 2008, *8*, 2982-2987.

(177) Holmes, M. A.; Townsend, T. K.; Osterloh, F. E. *Chem. Commun* 2012, *48*, 371-373.

(178) Jara, D. H.; Yoon, S. J.; Stamplecoskie, K. G.; Kamat, P. V. *Chem. Mater.* 2014, *26*, 7221-7228.

(179) Liang, Y. N.; Yu, K.; Yan, Q.; Hu, X. *ACS Appl. Mater. Interfaces* 2013, *5*, 4100-4106.

(180) Pan, Z.; Mora-Seró, I. n.; Shen, Q.; Zhang, H.; Li, Y.; Zhao, K.; Wang, J.; Zhong, X.; Bisquert, J. *J. Am. Chem. Soc.* 2014, *136*, 9203-9210.

(181) Panthani, M. G.; Stolle, C. J.; Reid, D. K.; Rhee, D. J.; Harvey, T. B.; Akhavan, V. A.; Yu, Y.; Korgel, B. A. *J. Phys. Chem. Lett.* 2013, *4*, 2030-2034.

(182) Thibert, A.; Frame, F. A.; Busby, E.; Holmes, M. A.; Osterloh, F. E.; Larsen, D. S. *J. Phys. Chem. Lett.* 2011, *2*, 2688-2694.

(183) Wu, N.; Wang, J.; Tafen de, N.; Wang, H.; Zheng, J. G.; Lewis, J. P.; Liu, X.; Leonard, S. S.; Manivannan, A. *J Am Chem Soc* 2010, *132*, 6679-6685.

(184) Ramasamy, K.; Tien, B.; Archana, P. S.; Gupta, A. *Mater. Lett.* 2014, *124*, 227-230.

(185) Choi, Y. C.; Yeom, E. J.; Ahn, T. K.; Seok, S. I. *Angew. Chem., Int. Ed.* 2015, *54*, 4005-4009.

(186) Shen, F.; Que, W.; Liao, Y.; Yin, X. *Ind. Eng. Chem. Res.* 2011, *50*, 9131-9137.

(187) Welch, A. W.; Baranowski, L. L.; Zawadzki, P.; Lany, S.; Wolden, C. A.; Zakutayev, A. *Appl. Phys. Express* 2015, *8*, 1-4.

(188) Suehiro, S.; Horita, K.; Yuasa, M.; Tanaka, T.; Fujita, K.; Ishiwata, Y.; Shimanoe, K.; Kida, T. *Inorg. Chem.* 2015, *54*, 7840-7845.

(189) Liu, S.; Chen, L.; Nie, L.; Wang, X.; Yuan, R. *Chalcogenide Lett.* 2014, *11*, 639-644.

(190) Ramasamy, K.; Gupta, R. K.; Palchoudhury, S.; Ivanov, S.; Gupta, A. *Chem. Mater.* 2015, *27*, 379-386.

(191) Kumar, M.; Persson, C. *J. Renew. Sust. Energ. Rev.* 2013, *5*, 031616/031611-031616/031616.

(192) Yang, B.; Wang, L.; Han, J.; Zhou, Y.; Song, H.; Chen, S.; Zhong, J.; Lv, L.; Niu, D.; Tang, J. *Chem. Mater.* 2014, *26*, 3135-3143.

(193) Rodriguez-Lazcano, Y.; Nair, M. T. S.; Nair, P. K. *J. Electrochem. Soc.* 2005, *152*, G635-G638.

(194) Yan, C.; Su, Z.; Gu, E.; Cao, T.; Yang, J.; Liu, J.; Liu, F.; Lai, Y.; Li, J.; Liu, Y. *RSC Adv.* 2012, *2*, 10481-10484.

(195) Ramasamy, K.; Sims, H.; Butler, W. H.; Gupta, *J. Am. Chem. Soc.* 2014, *136*, 1587-1598.

(196) Ikeda, S.; Sogawa, S.; Tokai, Y.; Septina, W.; Harada, T.; Matsumura, M. *RSC Adv.* 2014, *4*, 40969-40972.

(197) Zou, Y.; Jiang, J. *Mater. Lett.* 2014, *123*, 66-69.

(198) Mangelson, B. F.; Jones, M. R.; Park, D. J.; Shade, C. M.; Schatz, G. C.; Mirkin, C. A. *Chem. Mater.* 2014, *26*, 3818-3824.

(199) Joshi, G. K.; McClory, P. J.; Dolai, S.; Sardar, R. *J. Mater. Chem.* 2012, *22*, 923-931.

(200) Joshi, G. K.; McClory, P. J.; Muhoberac, B. B.; Kumbhar, A.; Smith, K. A.; Sardar, R. *J. Phys. Chem. C* 2012, *116*, 20990-21000.

(201) Joshi, G. K.; Smith, K. A.; Johnson, M. A.; Sardar, R. *J. Phys. Chem. C* 2013, *117*, 26228-26237.

(202) Kazuma, E.; Sakai, N.; Tatsuma, T. *Chem Commun (Camb)* 2011, *47*, 5777-5779.

CHAPTER 2. DUAL ROLE OF METAL-CARBOXYLATE LIGANDS: REVERSIBLE EXCITON DELOCALIZATION AND PASSIVATION OF NONRADIATIVE TRAP-STATES IN MOLECULE-LIKE CDSE NANOCRYSTALS

2.1 Synopsis

This chapter details the dual role of metal-carboxylate ligands and reports large bathochromic shifts up to 240 meV in both the excitonic absorption and emission peaks of oleylamine (OLA)-coated molecule-like $(CdSe)_{34}$ semiconductor nanocrystals (SNCs) caused by post-synthetic treatment with electron accepting $Cd(O_2CPh)_2$ at room temperature. These shifts are found to be reversible upon displacement of $Cd(O_2CPh)_2$ complex with *N,N,N',N'*-tetramethylethylene-1,2-diamine. ^{1}H NMR and FTIR characterizations of the SNCs demonstrate that the OLA remained attached to the surface of the SNCs during the reversible exchange of $Cd(O_2CPh)_2$. Based on surface ligand characterization, X-ray powder diffraction measurements, and additional control experiments, we propose that these red-shifts in peak positions are a consequence of the delocalization of strongly confined exciton holes into the interfacial electronic states that are formed from interaction of the HOMO of the SNCs (electron donors) and the LUMO of the $Cd(O_2CPh)_2$ (electron acceptors) as opposed to originating from a change in the size or relaxation of the inorganic core. Furthermore, attachment of $Cd(O_2CPh)_2$ to the OLA-coated $(CdSe)_{34}$ SNC surface increases the photoluminescence quantum yield from

5% to an unprecedentedly high 73% and causes a three-fold increase in radiative lifetime, which are attributed to both passivation of nonradiative surface trap states and exciton delocalization. Taken together, our work demonstrates the unique aspects of surface ligand chemistry in controlling the excitonic absorption and emission properties of ultrasmall $(CdSe)_{34}$ SNCs, which could expedite their potential applications in solid-state device fabrication.

2.2 Introduction

The surface ligand chemistry of semiconductor nanocrystals (SNCs) has profound influence on their optoelectronic properties.[1-4] Such properties can be successfully tailored by selective manipulation of surface chemistry[1-3,5-7] to achieve large photoluminescence (PL) quantum yields (PL-QY),[8-10] high carrier mobility[6,11], and fast charge transport[3,11,12] to facilitate optoelectronic[13,14] and photovoltaic device fabrication[12,15]. Surface ligands are generally introduced during the colloidal synthesis of SNCs,[9,10,16-20] however most of the ligands, long-chain aliphatic amines and phosphines (neutral 2-electron donating L-type) and long-chain aliphatic carboxylate and phosphonate (1-electron donating X-type) ligands,[16,21-35] are insulating in nature. Therefore, in order to enhance their charge transport properties and their biological imaging detection, post-synthetic surface ligand exchange is routinely carried out. [20,36-42] The ligand exchange reaction strongly affects their emission properties (PL-QY and radiative lifetime)[43,44] and excitonic absorption characteristics.[3,6,34,45-47] Recently Weiss et al.,[43,45] our group,[3] and others[3,6,48-50] have shown that post-synthetic ligand exchange on CdSe and/or CdS SNCs with X-type ligands induces the delocalization of quantum confined holes causing a red-shift in the first excitonic absorption peak, which can be

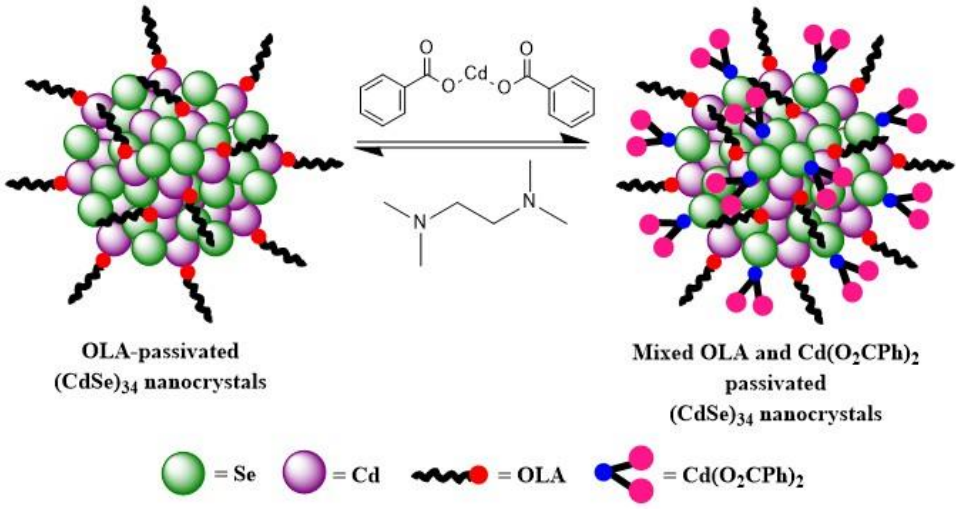

Figure 2.1: Reversible surface modification of OLA-passivated $(CdSe)_{34}$ SNC with $Cd(O_2CPh)_2$. The red circles represent amine head group of OLA, the blue circles and pink dots represent Cd and phenyl rings of $Cd(O_2CPh)_2$.*The illustration of $(CdSe)_{34}$ SNC structure does not correspond to the actual core-cage structure.

characterized as an "increase in the confinement box size".[3,4,6,43,45,48-50] However, such change in the optical properties was found irreversible. In this chapter, we report for the first time that the post-synthetic surface ligand treatment of oleylamine (OLA)-passivated "molecule-like" $(CdSe)_{34}$ SNCs with the Cd(benzoate)$_2$ ($(Cd(O_2CPh)_2)$, a 2-electron accepting Z-type ligand) (1) produces mixed ligand-passivated SNC $Cd(O_2CPh)_2$-OLA-passivated $(CdSe)_{34}$ SNCs, and (2) induces a red-shift of the excitonic absorption and emission peaks that can be restored upon removal of $Cd(O_2CPh)_2$ through *N,N,N',N'*-tetramethylethylene-1,2-diamine (TMEDA) treatment (Figure 2.1) in which the red-shift is caused by delocalization of excitonic holes.

In contrast to X-type ligand exchange where *irreversible* change in the optical spectra has always been observed, Buhro et al. recently reported *reversible* shifts of 140 meV in the absorption and emission peaks of two-dimensional CdSe and CdS quantum

belts upon fully exchanging L-type ligands (octylamine) with the Z-type ligands ($Cd(oleate)_2$).[51] The shift in optical spectra is attributed to a combination of change in strain state (structural relaxation of the inorganic core) and exciton delocalization. The magnitude of change in the confinement dimension is remarkably large considering that only an ~4 meV change is observed in the absorption spectra by Owen et al. for CdSe SNCs quantum dots (QDs) under similar experimental conditions.[52] However, reversible change in the confinement dimension of three-dimensional SNCs solely due to delocalization of excitons upon attachment of metal-complexes without compromising the original surface chemistry of SNCs has yet to be demonstrated. In this chapter, we report that attachment and detachment of $Cd(O_2CPh)_2$ to surface Se sites of $(CdSe)_{34}$ SNCs without displacing the original OLA attached to the surface Cd sites produces a reversible change in the SNC absorption and emission peaks up to 240±12 meV for at least five cycles.

Our experimental results and proposed molecular orbital (MO) theory of SNC-metal complexes demonstrate that the reversible change in the optical spectra of mixed OLA- and $Cd(O_2CPh)_2$- passivated $(CdSe)_{34}$ SNCs is not controlled by change in dimension, crystal, or strain states. It is, however, a consequence of delocalization of hole wave functions into the hybrid MOs that are formed from the interaction between HOMOs of OLA-passivated $(CdSe)_{34}$ SNCs and LUMOs of $Cd(O_2CPh)_2$. The wave function's delocalization process is further supported by a three-fold increase in PL lifetime.[43] Furthermore, our particular surface passivation increased the PL-QY from 5% to 73%, which is the highest PL-QY reported in the literature for such ultrasmall SNCs,[8,9]

therefore, illustrating the dual role of $Cd(O_2CPh)_2$ in both spectral modulation and trap state passivation.

Taken together, our results provide new insights into how optoelectronic properties (absorption and emission spectra, PL-QY, and radiative lifetimes) can be controlled through post-synthetic surface modification without replacing the surface ligand of the original SNCs. Thus, this research provides a rational approach in obtaining the desired optoelectronic properties of SNCs through selective surface passivation without changing their size, shape, or inorganic core composition.

2.3 Materials and Methods

2.3.1 Materials

Cadmium acetate dihydrate ($Cd(OAc)_2•2H_2O$) (98%), cadmium oxide (99.9%), benzoic acid (99.5%), benzoic anhydride (95%), tetrahydrofuran (THF) (99.9%), oleylamine (OLA) (70%), cadmium chloride ($CdCl_2$) (99%), 1-hexanethiol (HT) (95%), toluene (HPLC grade), elemental selenium (99.99%), *N*,*N*,*N*′,*N*′-tetramethylethane-1,2-diamine (98 %) (TMEDA), acetonitrile (MeCN) (HPLC grade), chloroform (HPLC grade), dichloromethane (DCM) (>99%), hexanes (95%), hexadecylamine (HDA) (90 %), and trioctylphosphine (TOP) (90%), oleic acid (OA) (99 %), *n*-nonanoic acid (98%), and 1-octadecene (90%) were purchased from Aldrich and used without further purification. Methanol (99.98%) was purchased from Fisher Scientific. Cadmium stearate (90%) was purchased from STREM Chemicals and used without further purification.

2.3.2 Optical Spectroscopy

UV-vis absorption spectra were collected using a Varian Cary 50 UV-vis spectrophotometer over a range of 800-300 nm. Prior to sample measurements, the

baseline was corrected with pure solvent. The emission spectra were acquired using a Cary Eclipse fluorescence spectrophotometer from Varian Instruments with an excitation of 380 nm. ^{1}H NMR was recorded on a Bruker AVANCE III 500 instrument at 500 MHz frequency. Approximately ~2 mg of sample were dissolved in 0.6 mL of CD_2Cl_2 at room temperature and a minimum of 1000 scans were collected.

The PL-QYs of the synthesized OLA-passivated $(CdSe)_{34}$ SNCs before and after exciton delocalization were calculated via a comparison technique using coumarin-30 as a standard fluorophore. Coumarin-30 exhibits UV-Vis absorption maximum at 407 nm and an emission maximum at 482 nm when excited at 380 nm with a PL-QY of 55.3% in acetonitrile.[53] All samples were prepared in toluene and the optical density of the samples was kept to a similar level (~0.08-0.1). The emission data were collected from 400-700 nm and the area of the PL peak was determined. The following equation was used to calculate the PL-QY of the $(CdSe)_{34}$ NCs:[16]

$$QY_{NC} = \left(\frac{E_{NC} / A_{NC}}{E_{STD} / A_{STD}} \right) \times \left(\frac{\eta_{NC}}{\eta_{STD}} \right)^2 \times QY_{STD} \qquad (2.1)$$

Here QY_{NC}, A_{NC}, and E_{NC} represent the calculated quantum yield, measured absorbance, and integrated emission intensity of the $(CdSe)_{34}$ NCs, respectively. QY_{STD} is the quantum yield of coumarin-30 and the η_s refer to the refractive indices of the two solvents.

2.3.3 Ground State Photoluminescence, Excited State Lifetime, and Absolute Quantum Yield Measurement

PL spectra were acquired using a Cary Eclipse fluorescence spectrophotometer from Varian Instruments. The lifetime measurements were recorded using a Time-correlated single photon counting (TCSPC) experimental set up. The data acquisition card (DAQ) was from Edinburgh Instrument (TCC900). The laser was a 405 nm pulsed laser from PICOQUANT (LDH-D-C-405M, CW-80MHz) with pulse width < 100 ps. The detector was a photomultiplier tube (PMT) from the HAMAMATSU (H7422-40, <250 s). The samples were excited at maximum absorption wavelength and the lifetime decay was measured at the emission wavelength maxima. The following stretch exponential equation was used to determine the excited state lifetime using a TCSPC experimental set up:

$$I(t) = I_0 \quad \exp\left[-\left(\frac{t}{\tau}\right)^{\beta}\right] \qquad (2.2)$$

Here I(t) and I_0 are the PL intensities at time t and zero. β and τ are the dispersion factor and emission decay time, respectively. For the limiting case where $\beta \rightarrow 1$, a single exponential decay was achieved with a characteristic lifetime of τ.

2.3.4 Structural Characterizations

Fourier transform infrared spectroscopy (FTIR) measurements were taken using a Thermo Nicolet IS10 FTIR spectrometer. For FTIR analysis, samples were prepared using a 1:10 ratio of sample to KBr, ground using a mortar and pestle, and pressed into a pellet. A minimum of 300 scans were collected and all data was processed using Omnic FTIR software.

X-Ray Diffraction measurements were obtained using a Bruker D8 Discover X-Ray Diffraction Instrument with a IμS microfocus X-ray source and the operating voltage and current are 50 kV and 1000 mA. The measurements were taken by preparing a thin film, or fine powder, of the material on a clean glass slide.

2.3.5 Synthesis of OLA-passivated $(CdSe)_{34}$ SNCs

SNCs were synthesized using our laboratory's previously published synthesis and purification with minor modifications.[19] In brief, 0.2 g of cadmium acetate dihydrate ($Cd(OAc)_2•2H_2O$) was dissolved in 5 mL of oleylamine in a 100 mL two-neck round bottom under reduced pressure while stirring. The Se-precursor stock solution was prepared by adding 0.12 g of freshly ground selenium in a 5 mL round bottom with 1.57 mL OLA and 0.43 mL of HT under N_2 atmosphere until all the Se has dissolved. Once all Cd salt has dissolved, 5 mL toluene was added to the reaction mixture. Then 1 mL of the prepared Se-precursor was added and the reaction and stirred for 1h under N_2 atmosphere. The reaction was quenched by diluting with 20 mL of toluene and adding a mixture of MeCN/MeOH (1:1 v/v) dropwise until cloudy. The mixture was then centrifuged at 7000 r.p.m. for 5 min. The resulting bright yellow precipitate was redissolved in 20 mL of toluene and stored in the refrigerator for up to 2 weeks.

2.3.6 Synthesis of Cadmium Stearate Passivated $(CdSe)_{34}$ SNCs

SNCs were synthesized using a previously published procedure with minor modifications.[30] Briefly, 0.56 g of cadmium stearate (0.5 mmol) was combined with 9.66 g hexadecylamine (HDA) (40.0 mmol) in a 25 mL Schlenk flask and heated at 100℃ under N_2. When fully dissolved, 1 mL of TOPSe (1 mmol) stock solution was swiftly injected. This reaction was allowed to proceed at this temperature and was monitored by

UV-Vis spectroscopy and PL in chloroform using the above mentioned parameters. Upon completion, the solution was diluted in 25 mL chloroform and ethanol was added dropwise until cloudy. The solution was then centrifuged for 5 min at 7000 rpm. The resulting yellow solid was dissolved in chloroform and used immediately.

2.3.7 Synthesis of Cadmium Benzoate $Cd(O_2CPh)_2$

$Cd(O_2CPh)_2$ was synthesized using a previously published procedure with minor modifications.[54] Briefly, 6.0 g (47 mmol) cadmium oxide, 34.4 g (282 mmol) benzoic acid, and 12.7 g (56 mmol) benzoic anhydride were combined in a Schlenk flask and stirred under N_2 at 180℃ until a colorless melt occurred. The clear solution was allowed to cool to room temperature while stirring and then 100 mL toluene was added over ice. To remove unreacted products, the solid was collected on a fritted filter while washing with toluene (3 x 200 mL) and DCM (3 x 200 mL). The white powder was redissolved in a mixture of 1:3 THF to DCM in a round bottom flask. The solution was concentrated by rotary distillation. The resulting milky white suspension was then filtered again and cleaned with a 1:1 mixture of DCM and toluene (3x 100 mL). The white powder was dried under high vacuum at 100℃ overnight. Yield: 6.52 g (79 %).

2.3.8 Synthesis of Cadmium Nonanoate ($Cd(nonanoate)_2$)

$Cd(nonanoate)_2$ was synthesized using a previously published for $Cd(O_2CPh)_2$ above.[54] Briefly, 3.0 g (23.5 mmol) cadmium oxide, 22.3 g (141 mmol) n-nonanoaic acid, and 6.4 g (28 mmol) benzoic anhydride were combined in a Schlenk flask and stirred under N_2 at 180℃ until a colorless melt occurred. The resulting colorless melt was allowed to cool to room temperature while stirring and then 100 mL toluene was added over ice. The solid was collected on a fritted filter while washing with toluene (3 x 200

mL) and DCM (3 x 200 mL). The white powder was redissolved in a mixture of 1:3 THF to DCM. The colorless solution was then concentrated by rotary distillation. The resulting milky white suspension was then filtered again and cleaned with a 1:1 mixture of DCM and toluene (3x 100 mL). The white powder was dried under high vacuum at 100℃ overnight. Yield: 7.21 g (72 %).

2.3.9 Synthesis of Cadmium Oleate ($Cd(oleate)_2$)

$Cd(oleate)_2$ was synthesized using a previously published procedure with minor modifications.[55] Oleic acid (2.5 mL, 2.8 mmol) and CdO (0.09 g, 0.7 mmol) were combined in a 3-neck r.b. and degassed at 100℃. Next the mixture was heated at 190℃ under N_2 for 20 min until a colorless melt was achieved. Then the solution was cooled to 100℃ and degassed 20 min. The clear product was allowed to cool to room temperature and then was precipitated using dropwise addition of acetone. The gluey white product was centrifuged for 5 min at 7000 rpm and the clear supernatant was discarded. The purified $Cd(oleate)_2$ was washed an additional 2x with a 1:1 mixture of hexane:acetone and dried under vacuum overnight.

2.3.10 Post-synthetic Surface Modification with Z-type Ligand

The molar extinction coefficient was calculated using the literature empirical formula[56] to be $2.33 \times 10^4\ M^{-1}\ cm^{-1}$, a 0.25 mM stock solution of OLA-coated $(CdSe)_{34}$ SNCs was prepared in toluene. To the solution, 0.25 g (0.7 mmol) prepared $Cd(O_2CPh)_2$ was added. The reaction mixture was stirred under N_2 atmosphere for 24 h then centrifuged to remove any unreacted $Cd(O_2CPh)_2$. The exciton delocalization and surface passivation of the yellow solution was monitored using UV-Vis spectrometry and PL

using the above mentioned parameters. Post-synthetic surface modification controls were ran using the same parameters replacing $Cd(O_2CPh)_2$ for Cd(nonanoate)$_2$ or Cd(oleate)$_2$.

2.3.11 Displacement of Z-type Ligand using L-type Ligand Modification

0.25 mM stock solution of the $Cd(O_2CPh)_2$ modified OLA-passivated $(CdSe)_{34}$ SNCs was prepared in 10 mL toluene. To the solution, 524 uL (0.03 mmol) TMEDA was added while stirring under N_2 atmosphere. The solution was allowed to stir for 1 hr. The displacement of the Z-type ligand was monitored using UV-Vis spectrometry, PL, and ^{1}H NMR. Time dependent ^{1}H NMR of the displacement was run using the above mentioned parameters.

2.3.12 Rebinding of Z-type ligand

To the $Cd(O_2CPh)_2$ displaced $(CdSe)_{34}$ SNCs (0.25 mM), 100 uL (0.3 mmol) OLA was added while stirring under N_2. The mixture was allowed to stir 15 minutes. Then 0.35 g (1.0 mmol) was added and allowed to stir overnight. Again the resulting exciton delocalization was monitored using UV-Vis spectrometry and PL using the above mentioned parameters.

2.3.13 Theoretical Calculation of HOMO and LUMO Positions

Orbital energy calculations were performed with QChem 3.1 software using a LANL2DZ effective core potential for Cd^{2+} with the matching basis set of 6-311+G** for C, O, and H atoms and B3LYP functional.

2.4 Results and Discussion

2.4.1 Surface Treatment of OLA-Coated Molecule-like $(CdSe)_{34}$ SNCs with $Cd(O_2CPh)_2$.

We used OLA-coated, molecule-like $(CdSe)_{34}$ SNCs with core-cage structure of $(CdSe)_6(CdSe)_{28}$[57] as a model system for the study of surface ligand chemistry-dependent optoelectronic properties[6,9] for several reasons: (1) These magic-sized SNCs are thermodynamically very stable,[33,57] thus changes in their crystallographic structure during the ligand exchange reaction is unlikely. (2) With SNCs in the ultrasmall size range, the majority of the atoms reside at the surface of the SNCs. Therefore, even a minor variation in their surface ligand chemistry will have profound effects on their optoelectronic properties,[3,6,7] as compared to larger SNCs. (3) The L-type ligand OLA binds to surface Cd sites[6,58] leaving the Se sites unpassivated, which can then be coated with Z-type ligands (e.g., metal-carboxylate complexes) without displacing the OLA but changing the surface chemistry of original SNCs. Afterwards we expect that the Z-type ligands can be removed from the surface of the SNCs via a ligand exchange procedure using a different L-type ligand.[52] (Figure 2.1) (4) We expect that the surface ligand interaction has the potential to dramatically alter SNC electronic structure and dictate SNC function more than ligand interactions with QDs, because SNCs have a larger surface-to-volume ratio that results in a higher density of surface orbitals (e.g., HOMOs and LUMOs), behaving more similar to isolated molecules. SNC surface orbitals readily interact with the MOs of surface ligands in a process called interfacial orbital mixing.[3,59]

The synthesis of OLA-coated, molecule-like $(CdSe)_{34}$ SNCs was performed according to our published procedure.[19] The blue lines in Figure 2.2 show that the lowest energy absorption and band-edge emission peaks are appeared at 416 and 435 nm, respectively. The sharp absorption peak (FWHM ~ 12 nm) at this wavelength confirms the formation of nearly monodispersed $(CdSe)_{34}$ SNCs.[6,9,19] In order to investigate the surface ligand-dependent optical properties, a 0.25 mM toluene solution of OLA-coated

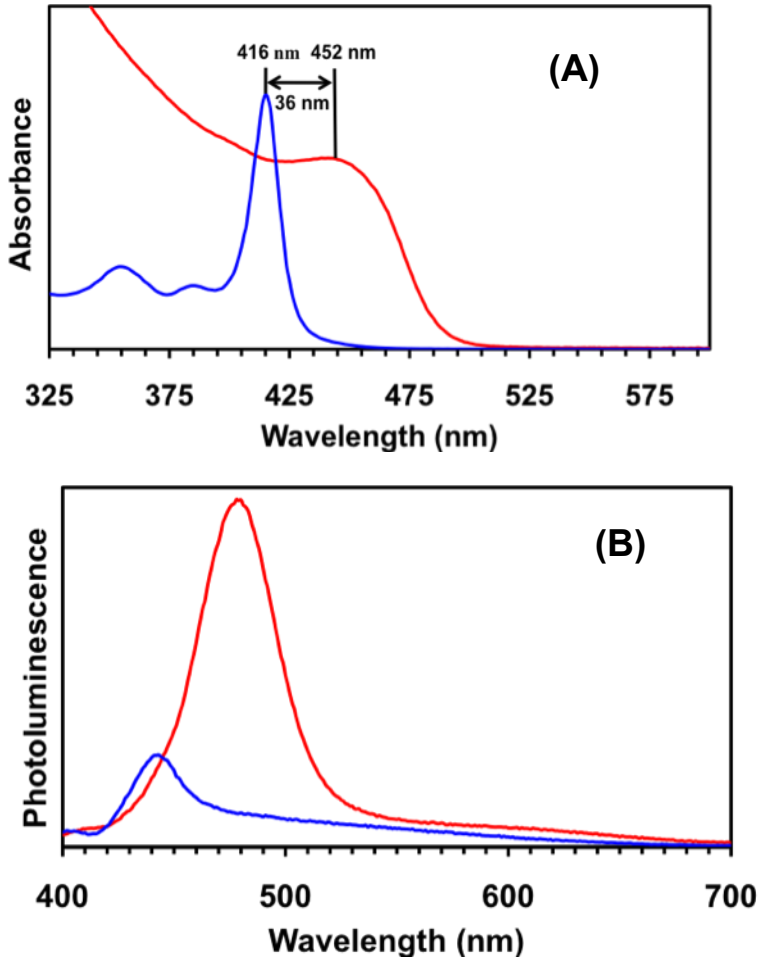

Figure 2.2: Absorption (A) and emission (B) spectra (in toluene) of purified OLA-coated $(CdSe)_{34}$ SNCs prior to (blue lines) and after (red lines) *ex situ* treatment with $Cd(O_2CPh)_2$ at room temperature. The emission spectra were collected at 380 nm excitation wavelength.

purified SNCs was treated with 0.7 mmol of $Cd(O_2CPh)_2$ and stirred under N_2 atmosphere for 24 h at room temperature. The details of the surface modification procedure are provided in the experimental section. The 24 h reaction mixture was centrifuged to remove free $Cd(O_2CPh)_2$ and produced a clear yellow supernatant. The SNCs were purified with solvent-assisted precipitation and then dissolved in toluene which produced a clear yellow solution that displayed a 36 nm (240 ± 12 meV) red shift with FWHM of ~ 30 nm in the lowest energy absorption peak (Figure 1A, red line). The observed shift of 240 meV in the absorption peak upon modification of L-type ligand coated SNCs with this metal-carboxylate complexes is the highest value reported in the literature for SNCs with a Z-type ligand.[51,52] (Appendix A shows the time dependent absorption spectra upon addition of $Cd(O_2CPh)_2$ and increase in ΔR as a function of exchange time.)

Along with changes in the absorption peak, we also observed a 43 nm (260 ± 9 meV) red-shift (Figure 2.2 B, red line) in the band-edge emission peak along with the peak broadening. Importantly, a substantial increase in the band-edge emission peak intensity (14 fold increase in PL-QY) and emission decay lifetime (3.3 fold increase in τ_r) were observed after treatment of $Cd(O_2CPh)_2$, which we believed is due a combination of passivation of nonradiative trap states and delocalization of the exciton wave functions, as discussed later in this chapter. Therefore, we propose that the observed (1) red-shift in the absorption and emission peak, (2) broadened absorption peaks, (3) increased emission peak intensity, and (4) enhanced k_r were caused by delocalization of the hole wave functions of $(CdSe)_{34}$ SNCs from change in the confinement dimension as opposed to the change in size (mechanism-(i)) or strain states (mechanism-(ii))

2.4.2 Binding of Z-Type Ligands

To precisely assess the $Cd(O_2CPh)_2$-induced change in the optical properties of OLA-coated $(CdSe)_{34}$ SNCs, it is important to characterize their surface ligand chemistry. Based on our predicted model of surface structure of these SNCs (Figure 2.1), the L-type ligand OLA is attached to the surface Cd sites while surface Se sites remain unpassivated. Addition of the Z-type ligand $Cd(O_2CPh)_2$ passivates the Se sites without replacing the OLA. Testing our surface model is important in that it is different than recent reports by the Buhro[51] and Owen[52] groups in which these authors have concluded that addition of Z-

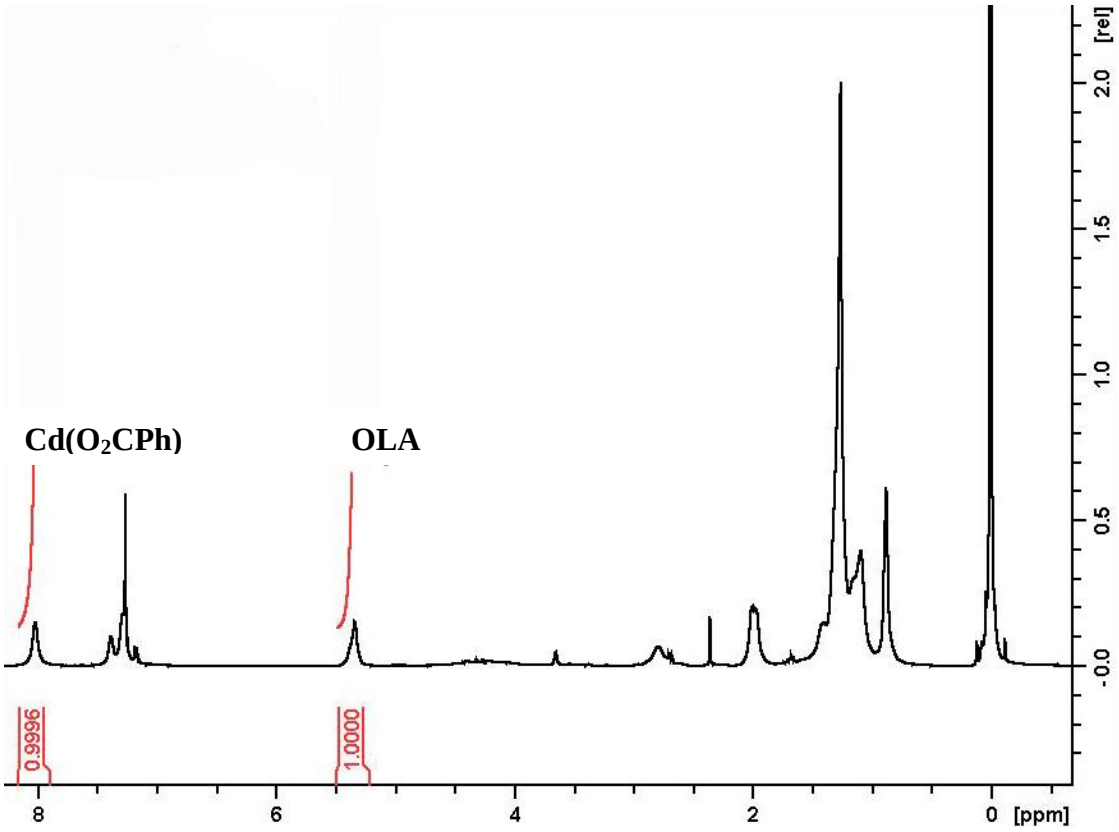

Figure 2.3: ^{1}H NMR of OLA-capped CdSe SNCs after $Cd(O_2CPh)_2$ attachment. Peak at 8.12 ppm corresponds to aromatic (cyclic C-H, ortho) resonance of $Cd(O_2CPh)_2$ and 5.53 ppm corresponds to vinyl proton (-HC=CH-) resonance of OLA. The ratio is 0.99:1.00 thus showing ~50% attachment of $Cd(O_2CPh)_2$after centrifugation.

type ligands completely displaced L-type ligands from the surface of CdSe SNCs. To confirm our hypothesis, $Cd(O_2CPh)_2$-treated, OLA-coated $(CdSe)_{34}$ SNCs were analyzed by ^1H NMR (Figure 2.3 and Appendix B) and FTIR spectroscopy (Appendix C). In the NMR analysis the SNCs displayed broad vinyl proton (-*CH*=*CH*-) and aromatic proton (-*ortho*) signals at 5.53 and 8.12 ppm, which originated from OLA and $Cd(O_2CPh)_2$, respectively. The NMR analysis showed a ratio of 1:1 between vinyl and aromatic protons. Given that 28 surface Cd and Se sites are available with $(CdSe)_{34}$ SNCs and all the Cd sites are occupied by OLA, then NMR analysis suggested that ~14 surface Se sites were passivated by $Cd(O_2CPh)_2$. The FTIR analysis showed carboxylate group ($-COO^-$) stretch modes along with N-H stretches from the primary amine OLA. These analyses unequivocally support the mixed surface ligation of our SNCs and resulting formation of $((CdSe)_{34}(OLA)Cd(O_2CPh)_2)$. As discussed above, the increased emission peak intensity after $Cd(O_2CPh)_2$ treatment indicates its attachment to the surface Se sites while OLA remained bound to surface Cd sites.

2.4.3 Mechanism–(i): Change in the Inorganic Core Size

The observed red-shift of 260 meV in the absorption spectra of OLA-coated $(CdSe)_{34}$ SNCs upon treatment with $Cd(O_2CPh)_2$ could be caused by Ostwald ripening growth of the original SNCs, resulting in an increase in size and thus confinement dimension. Although Ostwald ripening growth of thermodynamically stable $(CdSe)_{34}$ SNCs is unlikely at room temperature, addition of $Cd(O_2CPh)_2$ could trigger such a growth process. Thus we performed transmission electron microscopic (TEM) analysis to determine the diameter of the CdSe SNC before and after $Cd(O_2CPh)_2$ attachment. (Figure 2.4) The original OLA-coated $(CdSe)_{34}$ SNCs were ~1.6 nm in diameter[19,56] and

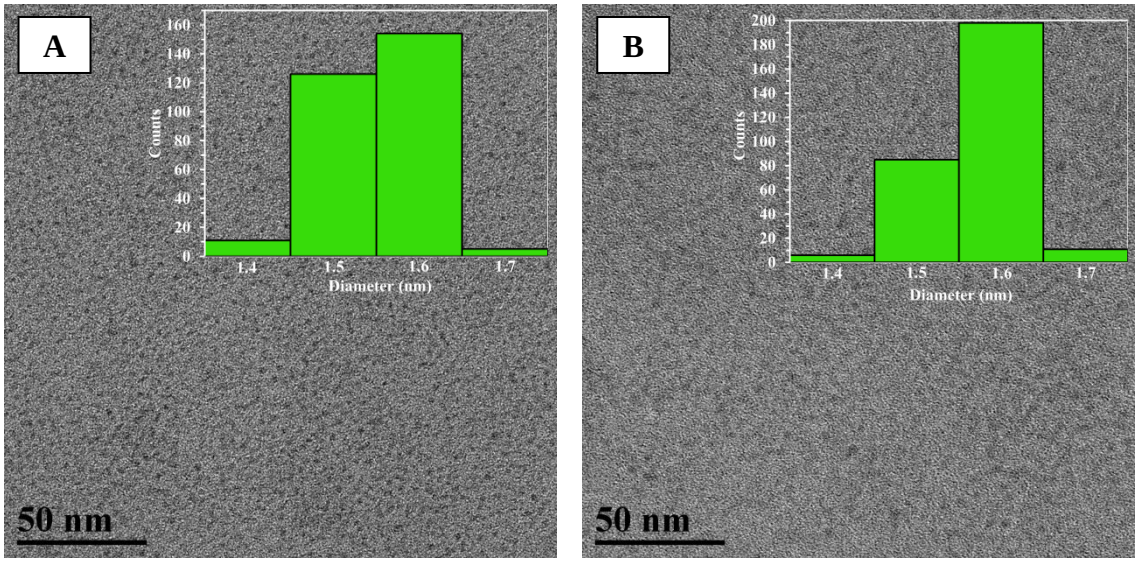

Figure 2.4: HRTEM image of OLA-passivated CdSe SNCs A) before and B) after attachment of $Cd(O_2CPh)_2$. Isolated SNCs have a diameter of 1.6 nm and very little aggregation is observed. Scale bar is 50 nm. Insets show histograms of SNC analysis; 300 SNCs each were counted.

no noticeable change in diameter was observed after $Cd(O_2CPh)_2$ attachment. Moreover, the SNCs remained well dispersed on the TEM grid.

Determination of exact size of ultrasmall CdSe SNCs by TEM however is difficult. In this context the red-shift in the lowest energy absorption peak of $(CdSe)_{34}$ SNCs to 452 nm corresponds to a final diameter of 2.0 nm, based on a generally used empirical formula.[56] Precisely quantifying such a small difference in diameter (0.4 nm) by TEM is extremely challenging, and thus proving our hypothesis that attachment of $Cd(O_2CPh)_2$ to OLA-coated $(CdSe)_{34}$ SNCs did not change the actual core dimension through TEM is difficult. However, an ideal way to prove size retention of $(CdSe)_{34}$ SNCs and that the 36 nm red-shift of the absorption peak was due to attachment of

$Cd(O_2CPh)_2$ resulting in delocalization of hole wave functions is through reversing the absorption peak shift by detaching $Cd(O_2CPh)_2$.

2.4.4 Optical Spectroscopy: Reversible Modulation of the Absorption Peak of $(CdSe)_{34}$ SNCs

We used a similar ligand exchange procedure for displacing $Cd(O_2CPh)_2$ from the surface of CdSe SNCs and replacing it by the L-type ligand, TMEDA, as previously reported by Anderson et al.[52] As mentioned previously, a 36 nm red-shift in the absorption peak of OLA-coated $(CdSe)_{34}$ SNCs was observed after treatment with $Cd(O_2CPh)_2$. Figure 2.5 A illustrates that TMEDA treatment of our mixed ligand-coated SNCs caused an ~35 nm blue-shift in the absorption spectrum. Importantly, the peak retained the spectral shape (FWHM ~13 nm) of the original OLA-coated $(CdSe)_{34}$ SNCs. When the purified $(CdSe)_{34}$ SNCs were again treated with $Cd(O_2CPh)_2$, an average 35 nm red-shift in the absorption peak position was again observed. As shown in Figure 2.5 B and Appendix D, we were able to observe this reversible change in the absorption and emission peak position over at least 5 cycles due to attachment and detachment of $Cd(O_2CPh)_2$ from the surface of the OLA-coated $(CdSe)_{34}$ SNCs.

2.4.5 ^{1}H NMR Spectroscopy: Displacement of $Cd(O_2CPh)_2$

We used *in situ* ^{1}H NMR spectroscopy to monitor the $Cd(O_2CPh)_2$ displacement from the surface of $((CdSe)_{34}(OLA)Cd(O_2CPh)_2))$ SNCs. Figure 2.6 shows the time-dependent ^{1}H NMR spectra of the aromatic proton (-*ortho*) signals of $Cd(O_2CPh)_2$ at 8.12 ppm after TMEDA treatment. The broad aromatic signal, which appears from a combination of spin-spin relaxation and dipole broadening,[60] becomes sharper and increases in intensity. Our experimental result is in agreement with a previous report

demonstrating the displacement of Z-type ligands from the surface of the CdSe SNCs upon treatment with L-type ligands.[52] Importantly, vinyl resonance (-*CH*=*CH*-) signals at 5.53 from OLA remained broad even after TMEDA treatment (Appendix B), suggesting that OLA was still present on the surface of the $(CdSe)_{34}$ SNCs. Therefore, we believe

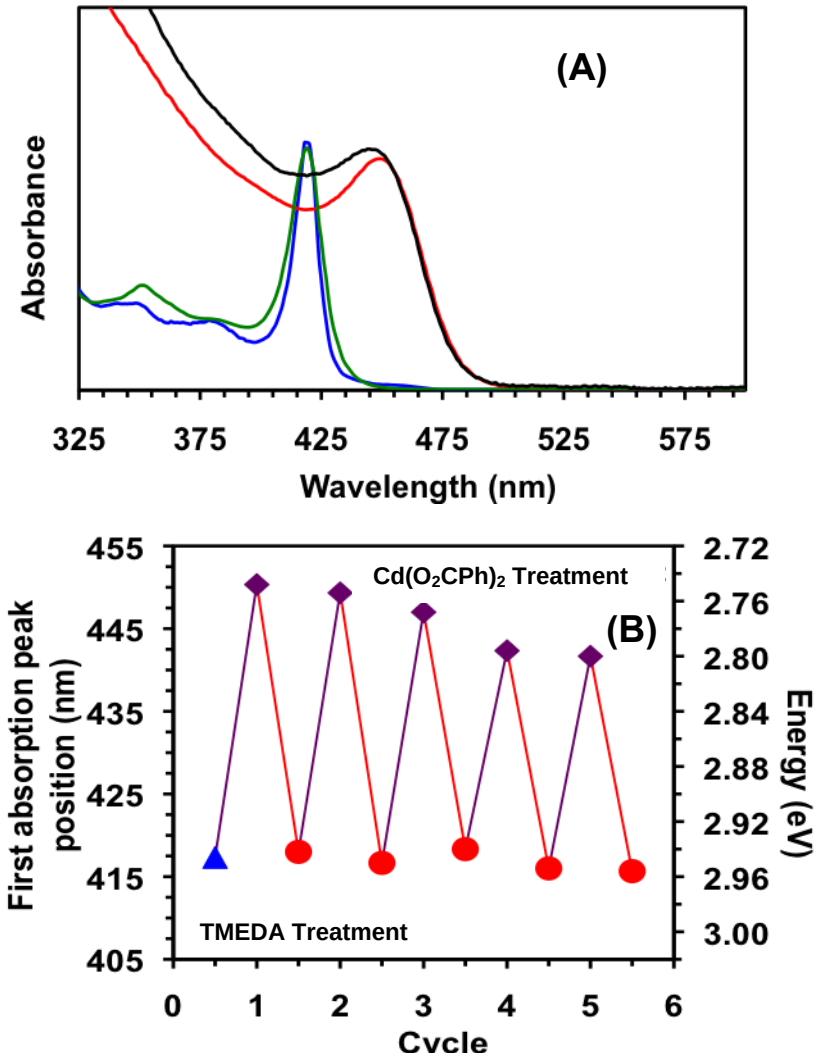

Figure 2.5: (A) Room temperature absorption spectra (in toluene) of purified OLA-coated $(CdSe)_{34}$ SNCs after synthesis (blue line), after binding $Cd(O_2CPh)_2$ (red line), after treatment with TMEDA (green line), and after rebinding $Cd(O_2CPh)_2$ (black line). (B) Reversibility of the lowest energy absorption peak position of purified OLA-coated $(CdSe)_{34}$ SNCs (blue triangle) after repeatedly binding (purple diamonds) and replacing (red dots) $Cd(O_2CPh)_2$. Over the time, the peak position did not fully reverse, which could be due to change in the surface chemistry caused by multiple purifications.

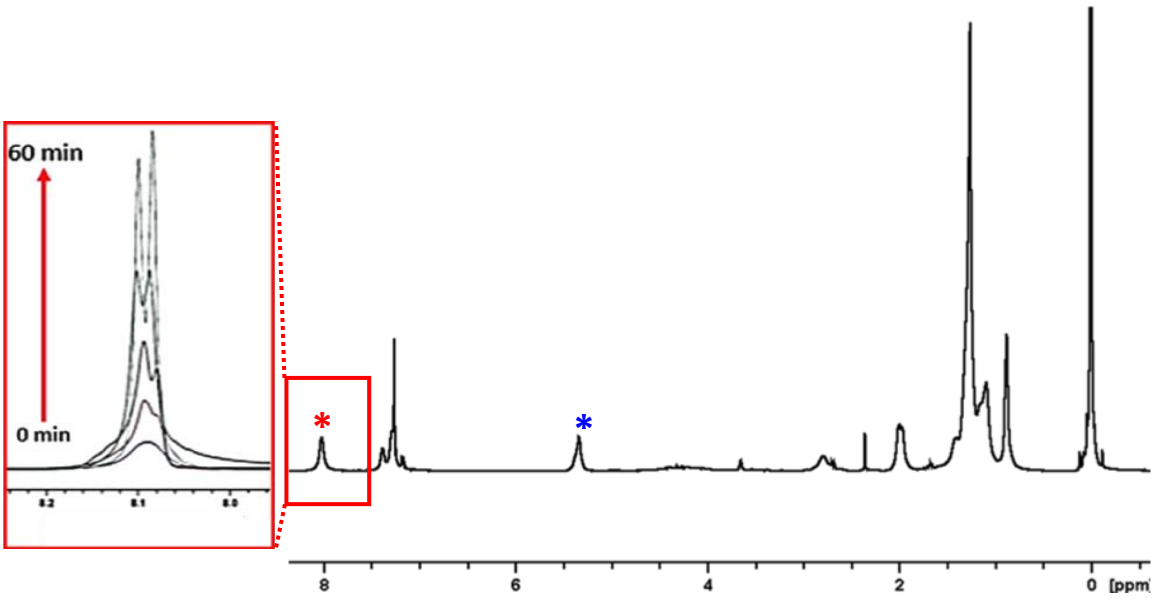

Figure 2.6: ^{1}H NMR spectrum of purified OLA-coated $(CdSe)_{34}$ SNCs after binding of $Cd(O_2CPh)_2$ and insert showing time-dependence from TMEDA treatment. The appearance of broad aromatic (red star) and vinyl (blue star) proton signals from $Cd(O_2CPh)_2$ and OLA, respectively, suggests that the SNC surface is passivated with these two ligands. The expanded spectra in the insert demonstrate temporal evolution of sharp aromatic peaks at ~8.1 ppm after treatment of SNCs that had mixed (OLA) and $Cd(O_2CPh)_2$) passivation with TMEDA for 60 min.

that addition of TMEDA to the $(CdSe)_{34}(OLA)Cd(O_2CPh)_2$ SNCs results in the formation of a TMEDA-$Cd(O_2CPh)_2$) complex, which weakens the interaction between Cd from $Cd(O_2CPh)_2$) and the Se sites of the $(CdSe)_{34}$ SNCs and displaces $Cd(O_2CPh)_2$ from their surface.[52]

2.4.6 FTIR Spectroscopy: Reversible Change in Surface Ligand Chemistry

To further elucidate the mechanism of control of delocalization of exciton confinement by manipulating passivating ligands of molecule-like $(CdSe)_{34}$ SNCs, we used FTIR spectroscopy to characterize surface ligand chemistry and specifically the reversible exchange of $Cd(O_2CPh)_2$. After different ligand treatments and before each spectroscopic measurement, the ligand-coated $(CdSe)_{34}$ SNCs were purified through a

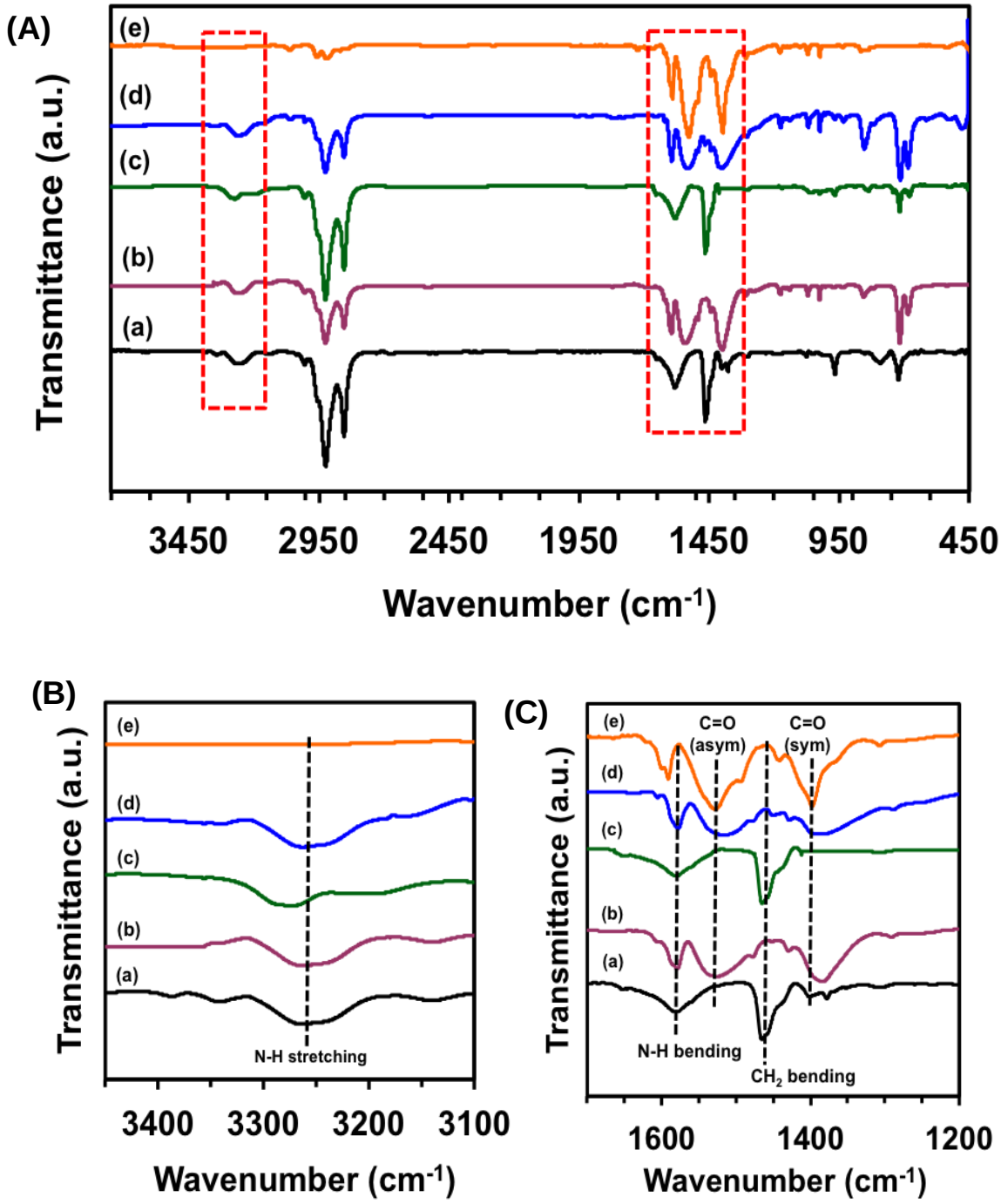

Figure 2.7: (A) FTIR spectra of purified OLA-coated $(CdSe)_{34}$ SNCs (a), and after (b) binding of $Cd(O_2CPh)_2$, (c) displacement of by TMEDA, and (d) the second addition of $Cd(O_2CPh)_2$. Pure $Cd(O_2CPh)_2$ (e). (B) Expanded FTIR of N-H stretch region in the range of 3400-3000 cm^{-1}, and (C) expanded N-H bending mode, asymmetric stretch and symmetric stretch of the carboxylate group ($-COO^-$). Both expanded regions (B and C) are highlighted by dotted red boxes in A.

solvent-assisted precipitation technique to remove bound ligands free and/or loosely. Figure 2.7 A illustrates the FTIR spectra of OLA-coated $(CdSe)_{34}$ SNCs (a, black curve) in which the characteristic N-H stretch in the range of 3400-3000 cm^{-1} and the N-H bending mode at 1581 cm^{-1} (Figure 2.7B) appeared, confirming the presence of the primary amine OLA passivating the SNC surface.[61,62] After the $Cd(O_2CPh)_2$ treatment (b, red curve), new asymmetric (1518 cm^{-1}) and symmetric (1388 cm^{-1}) stretch vibrations from the carboxylate group ($-COO^-$) appeared (Figure 2.7 C). The separation between these two vibration is 130 cm^{-1}, which suggest $-COO^-$ attachment to the Cd^{2+} through a chelating bidentate interaction.[63] Importantly, both the asymmetric and symmetric vibrations red-shifted from 1527 (~9 cm^{-1}, 39 nm) and 1397 cm^{-1} (~9 cm^{-1}, 46 nm), respectively, along with peak broadening of the pure $Cd(O_2CPh)_2$ (e, orange curve), which suggests that the interaction between $-COO^-$ and Cd^{2+} had weakened due to their attached to the surface Se sites.

Furthermore, the presence of N-H stretch and N-H bending modes indicates mixed surface ligation, and the addition of the Z-type ligand $Cd(O_2CPh)_2$ did not replace the L-type ligand OLA, as had been demonstrated in the literature.[51,52] The addition of TMEDA to the $(CdSe)_{34}(OLA)Cd(O_2CPh)_2$ SNCs removed the characteristic $-COO^-$ vibration modes (c, green curve), which reappeared after the addition of $Cd(O_2CPh)_2$ to the SNCs. Moreover, no noticeable change in the position of the N-H bending mode (Figure 2.7B) is indicative of the attachment of $Cd(O_2CPh)_2$ to the inorganic core of the SNC, not with the $–NH_2$ group of OLA, but through hydrogen bonding. [51,63]

We tested our other hypothesis that a reversible change in the optical spectra is allowed if the $Cd(O_2CPh)_2$ complex is attached to unpassivated Se sites of OLA-coated

$(CdSe)_{34}$ SNCs. We prepared mixed Cd(stearate)$_2$-, hexadecylamine (HDA)-, and trioctylphosphine (TOP)-coated $(CdSe)_{34}$ SNCs,[30] which displayed a characteristic absorption peak at 415 nm. (Appendix E) According to the literature, the SNC surface would be coated with a mixture of all three ligands, and in particular, HDA and TOP would be attached to surface Cd and Se sites, respectively.[30,64] Negligible change (~14 meV red-shift) in the lowest energy absorption peak position was observed over 24 h at room temperature after addition of $Cd(O_2CPh)_2$. Replacement of TOP at the surface Se sites by $Cd(O_2CPh)_2$ and formation of new Se-$Cd(O_2CPh)_2$ attachment on $(CdSe)_{34}$ SNCs is very unlikely due to strength of TOP-Se interaction, which in addition result in no major change in the confinement dimension.

Taken together, based on our observed reversible change in the absorption peak position and surface ligand chemistry of the $(CdSe)_{34}$ SNCs, we predict that the red-shift in the lowest energy absorption peak of OLA-coated $(CdSe)_{34}$ SNCs when $Cd(O_2CPh)_2$ becomes attached to the unpassivated Se sites is a consequence of decreased exciton confinement (increased delocalization). Moreover, increase in SNC size and/or structural reconstruction[51,65,66] due to *ex situ* ligand exchange can be ruled out because under such circumstances, the absorption peak would not return to its original position. Our experimental results are significant and suggested that our proposed mechanism is a valid explanation for the observed red-shift in the absorption spectrum of OLA-coated $(CdSe)_{34}$ SNCs upon the treatment with $Cd(O_2CPh)_2$ at room temperature.

2.4.7 Mechanism–(ii): Changes in the Strain States

Strongly quantum confined ultrasmall $(CdSe)_{34}$ SNCs have very large surface area and radius of curvature. Therefore, small changes in their surface ligand chemistry will

have significant influence in the strain states, resulting in spectral shifts during the Z-type ligand exchange, as opposed to weakly confined CdSe quantum dots.[3,5,6,19] To further validate our hypothesis that attachment of $Cd(O_2CPh)_2$ to OLA-coated $(CdSe)_{34}$ SNCs causes a red-shift in the absorption peak position due to exciton wave functions delocalization rather than change in strain states, we performed a control experiment in which $Cd(nonanoate)_2$ was used in an *ex situ* ligand exchange reaction. We used $Cd(nonanoate)_2$ as the Z-type ligand instead of the widely used $Cd(oleate)_2$[51] so that the identity of the surface bound ligands can be investigated by ^1H NMR spectroscopy without overlapping -*CH=CH*- proton signal of OLA and oleic acid. Furthermore, both $Cd(nonanoate)_2$ and $Cd(O_2CPh)_2$ are insoluble in the exchange solvent toluene, thus allowing us to mimic the ligand exchange condition.

Appendix F illustrates the almost identical UV-visible absorption spectra of OLA-coated $(CdSe)_{34}$ SNCs before and after treatment with $Cd(nonanoate)_2$ and shows there was no shift in the peak position. The ^1H NMR spectrum showed the presence of a broad -*CH=CH*- proton signal at 5.53 ppm from OLA and of *CO*-CH_2- proton at 2.38 ppm from nonanoate (Appendix G), implying the SNC surface was passivated by these two ligands. The NMR analysis also indicated a 2:1 ratio of OLA:$Cd(nonanoate)_2$ present on the surface of $(CdSe)_{34}$ SNCs similar to our mixed OLA- and $Cd(O_2CPh)_2$-coated SNCs. Furthermore, FTIR analysis (Appendix H) of the same sample also demonstrated the formation of mixed OLA- and $Cd(nonanoate)_2$-coated $(CdSe)_{34}$ SNCs. Upon $Cd(nonanoate)_2$ treatment, a significant increase in PL-QY of 46% was observed, which together with the NMR and FTIR data strongly support the binding to surface Se sites by $Cd(nonanoate)_2$ and thus passivation of nonradiative trap states.[52,67] Our PL-QY data are

in agreement with the work by Rosenthal and coworkers in which post-synthetic surface ligand treatment of ultrasmall CdSe SNCs resulted in increased in PL-QY ~8% to 45%.[8] The authors stated that such a dramatic increase in PL-QY is a consequence of passivation of nonradiative surface trap states. Nevertheless, the PL-QY of our mixed OLA- and Cd(nonanoate)$_2$-coated $(CdSe)_{34}$ SNCs is nearly 25% lower than we found with the OLA- and Cd$(O_2CPh)_2$ SNCs. Although the chemical structure of nonanoate and benzoate is different, their mode of binding to Cd^{2+} and the interaction of Cd(nonanoate)$_2$ and Cd$(O_2CPh)_2$ with the surface Se sites of CdSe SNCs are expected to be similar. The ratio of these two Cd complexes to OLA onto CdSe SNC surface was also found to be same as determined from the NMR analysis. Therefore, the higher PL-QY for Cd$(O_2CPh)_2$ is considered to stem from the passivation of nonradiative surface trap states and the delocalization of exciton wave functions, as will be discussed shortly.

At present, we are not certain of the explanation why CdSe quantum belts display an ~50 meV absorption peak shift caused by Cd(oleate)$_2$ attachment[51] but our ultrasmall $(CdSe)_{34}$ SNCs that have a large surface area a similar to quantum belts showed no change in their lowest energy absorption peak with Cd(nonanoate)$_2$ attachment, even though both of them are Z-type ligands. One possible explanation is that in the case of CdSe quantum belts, octylamine was fully exchanged by Cd(oleate)$_2$ causing the inorganic crystal lattice to undergo a significant contraction process. In our investigation, Cd(nonanoate)$_2$ was attached onto the $(CdSe)_{34}$ SNCs surface without replacing the bound OLA, and thus such a lattice contraction like nanobelts might not take place. Furthermore, X-ray diffraction (XRD) analysis of OLA-coated $(CdSe)_{34}$ SNCs showed three peaks along the (100), (002), and (101) reflections (Figure 2.8), which represent the

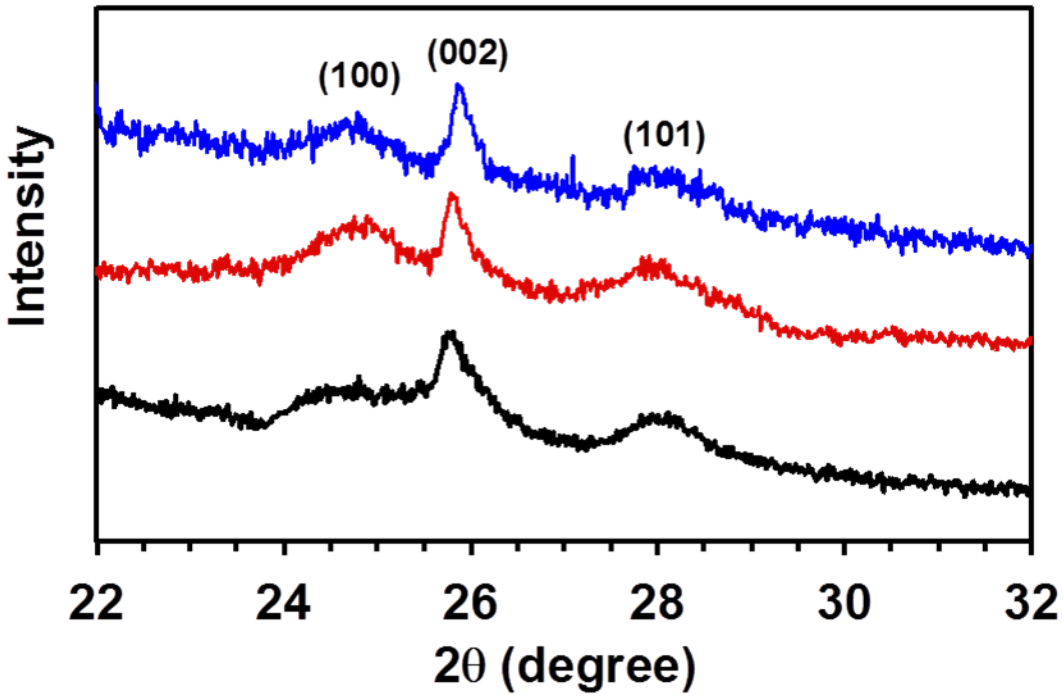

Figure 2.8: XRD pattern of purified OLA-coated $(CdSe)_{34}$ SNCs (black line), and after (red line) binding of $Cd(O_2CPh)_2$, (blue line) displacement of by TMEDA.

wurtzite crystals structure in agreement with the literature.[51] After $Cd(O_2CPh)_2$ treatment, no noticeable change in the position of these three reflection were observed. XRD analysis therefore suggests no changes in the crystal strain state caused by the attachment of $Cd(O_2CPh)_2$ to the surface of $(CdSe)_{34}$ SNCs.

The delocalization of exciton wave functions of the CdSe quantum belts into the $Cd(oleate)_2$ monolayer resulted in an ~90 meV red-shifts in the lowest energy absorption peak.[51] We did not observe a shift for our OLA-coated $(CdSe)_{34}$ SNCs after $Cd(nonanoate)_2$ treatment, indicating no wave function delocalization. We believe that an appropriate energetic alignment between the Z-type ligand and SNC MOs is critical for the delocalization of the exciton wave functions as discuss below. No noticeable changes

in the absorption and XRD peak positions were observed for the OLA-coated $(CdSe)_{34}$ SNCs upon Cd(nonanoate)$_2$ and $Cd(O_2CPh)_2$ treatment, which taken together suggests that the mechanism (ii) did not play a role in the shift of the lowest energy absorption peak (Figure 2.2 A) when the OLA-coated SNCs were treated with $Cd(O_2CPh)_2$.

2.4.8 Mechanism–(iii): Delocalization of Exciton Confinement

The various experimental approaches described above suggest that delocalization of exciton wave functions of the OLA-coated $(CdSe)_{34}$ SNCs beyond the inorganic core boundary does occur upon $Cd(O_2CPh)_2$ attachment. In the case of strong confinement (ultrasmall size) SNCs, the Coulombic interaction energy of the electron-hole pair is lower than the kinetic energy of electron and hole..[6,68,69] Thus, strongly confined exciton wave functions potentially leak through the SNC core boundary into the ligand monolayer, which results in an expansion of the confinement boundary. [3,6,47] The HOMOs of OLA-coated $(CdSe)_{34}$ SNCs are Se^{2-} character and behave as electron donors that can interact with LUMOs of the electron acceptor $Cd(O_2CPh)_2$. In the case of ultrasmall SNCs, a larger number of surface occupied orbitals are available, making the cumulative electronic interaction with ligands MOs very strong. Though several HOMOs and LUMOs of a SNC and ligand could interaction, for simplicity we describe only a single HOMO-LUMO interaction. The HOMO energy value of -6.16 eV (vs vacuum) for 1.6 nm diameter CdSe SNCs from literature reports of electrochemical measurements and an effective mass approximation calculation.[70] We determined the HOMO (-7.34 eV) and LUMO (-1.70 eV) energies of $Cd(O_2CPh)_2$ from geometry optimized density functional theory (DFT) calculation (LANL2DZ effective core potential for Cd^{2+} with the matching 6-311G** basis set and the B3LYP functional).

The interaction at the SNC- $Cd(O_2CPh)_2$ interface creates new hybrid bonding and antibonding MOs in which electrons from the SNC HOMO occupy newly formed hybrid bonding MO. As reported in the literature, in the steady state, the wave function of the excitonic hole can delocalize into the HOMOs of $Cd(O_2CPh)_2$ because of energetic alignment that facilitate an increase in the effective confinement boundary, which in turn results in a red-shift in the lowest energy absorption and band-edge emission peak.[43,71] We further believe that delocalization of the excitonic hole wave functions from hybrid bonding MOs of ligand-coated $(CdSe)_{34}$ SNCs into HOMOs of $Cd(O_2CPh)_2$ can be facilitated by the extended π-conjugated electronic structure of $Cd(O_2CPh)_2$. Although the SNC- $Cd(nonanoate)_2$ interaction potentially creates new hybrid bonding and antibonding MOs, the HOMOs of $Cd(nonanoate)_2$ are thought to be much lower in energy than those of $Cd(O_2CPh)_2$. Thus the energetic alignment between the hybrid bonding MOs of ligand-coated $(CdSe)_{34}$ SNCs and these particular HOMOs was not present for hole wave function delocalization. In addition, π-conjugation is not available for $Cd(nonanoate)_2$ to enable the delocalization of hole wave functions. We believe that a more detailed computational study is needed to accurately model both the SNC and ligands simultaneously. However, this level of quantitative energy level calculation requires complex computational modeling and sophisticated DFT calculations, which are beyond our expertise.

Finally, we also investigated the photophysical properties of OLA-coated $(CdSe)_{34}$ SNCs upon treatment with $Cd(oleate)_2$ to determine its effect on the hole delocalization process. We used very similar experimental conditions to those described for the other two Cd-carboxylate complexes to bind $Cd(oleate)_2$. Within 5 min we

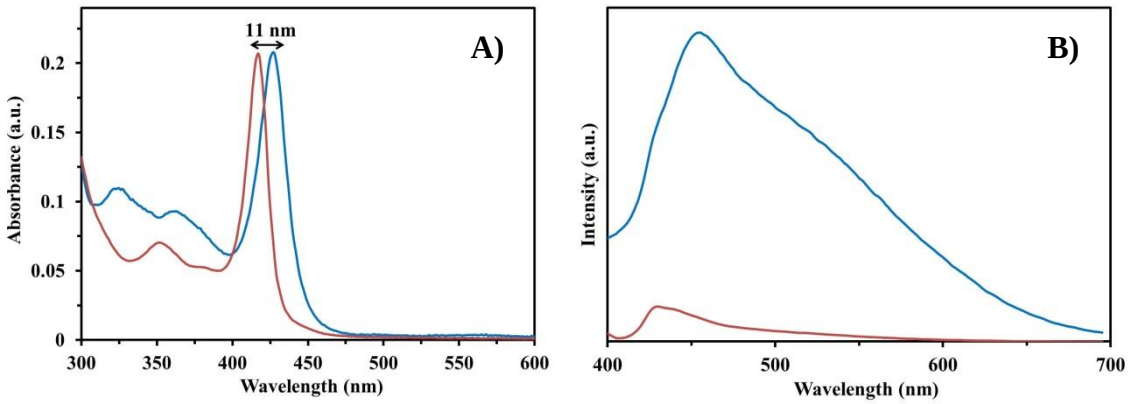

Figure 2.9: A) absorbance and B) emission spectra of as-synthesized OLA-passivated $(CdSe)_{34}$ SNCs (red) and after addition of $Cd(oleate)_2$ (blue). PL-QY was increased from 5% to 18% upon addition of $Cd(oleate)_2$ and the effective radius increased 0.04 nm.

observed an 11 nm (77 ± 4 meV) red-shift in the lowest energy absorption peak and a 16 nm (101 ± 12 meV) red-shift in the band-edge emission peak (Figure 2.9). The PL-QY was 18%, which is much lower than what we observed with either $Cd(nonanoate)_2$- or $Cd(O_2CPh)_2$-treated $(CdSe)_{34}$ SNCs. Table 2.1 provides a detail comparison of the photophysical properties of three different $Cd(carboxylate)_2$ complexes. Importantly, the emission spectrum of $Cd(oleate)_2$-treated OLA-coated $(CdSe)_{34}$ SNCs contained both band-edge and broad-band features, which implies the presence of nonradiative trap states. The FTIR analysis (Appendix I) showed that the original OLA ligand was nearly completely replaced by $Cd(oleate)_2$ similar to the previous reports by the Buhro and Owen groups.[51,52] In addition, the literature reports that magic-sized $(CdSe)_{34}$ SNCs are thermodynamically very stable, thus changes in the crystal structure and/or strain state are unlikely to occur, which further supports our $Cd(nonanoate)_2$ data in which no change in the lowest energy absorption peak was observed. Therefore, we believe that the red-shift in the absorption and band-edge emission peaks after treatment of $Cd(oleate)_2$ is due

to the delocalization of the hole wave function, which is facilitated by energetic alignment of the MOs.

2.4.9 Dual Role of Z-Type Ligands: Passivation of Trap States and Exciton Delocalization

The experimental emission data provided above show that binding of $Cd(O_2CPh)_2$ to OLA-coated $(CdSe)_{34}$ SNCs (1) red-shifted the band-edge emission peak, (2) increased the PL-QY up to 14 fold, (3) increased the τ_r by 3.3 fold (Figure 2.10), and (4) increased k_r (calculated from the PL-QY and τ_r) by 4.2 fold. The increased τ_r for $Cd(nonanoate)_2$ and $Cd(oleate)_2$ SNCs were due to passivation of nonradiative trap states and delocalization of hole wave functions, respectively. We believe for $Cd(O_2CPh)_2$-treated SNCs that with the exception of the red-shift of the band-edge emission peak, which resulted solely from delocalization of hole wave functions, the other three emission

Table 2.1: Shifts in the Lowest energy Absorption and Emission Peak Position, Emission Quantum Yields, and Radiative Lifetime of OLA-coated $(CdSe)_{34}$ SNCs after Treatment with Various Z-Type Ligands

ligand	absorption peak shift (nm)[a]	absorption peak shift (meV)	emission peak shift (nm)[b]	emission peak shift (meV)	quantum yield (%)[c]	radiative lifetime (ns)[d,e]
$Cd(benzoate)_2$	36 ±4	240 ± 12	43 ±2	260 ± 9	70 ± 3	45.5 ± 7
$Cd(nonanoate)_2$	0	0	0	0	46 ± 6	39.1 ± 4.5
$Cd(oleate)_2$	11 ± 2	77 ± 4	16 ± 3	101 ± 12	18 ± 4	17.4 ± 2.3

[a,b]OLA-coated $(CdSe)_{34}$ SNCs displayed lowest energy absorption and emission peaks at 416 and 435 nm, respectively. [c,d]The PL-QY and radiative lifetime OLA-coated $(CdSe)_{34}$ SNCs were 5% and 13.7 ns, respectively. [e]A stretch exponential function was used to determine the excited state lifetime (see Experimental Section). For each case, three different batches of OLA-coated $(CdSe)_{34}$ SNCs were characterized after surface treatment with metal-carboxylate to determine the average value and statistical deviation.

components were controlled by a combination of nonradiative trap states passivation and hole wave function delocalization. Specifically, it is reported in the literature that delocalization of exciton (electron and/or hole) wave functions increases the PL-QY and τ_r.[43] OLA is a neutral 2-electron donating L-type ligand, which passivates the surface Cd sites. The unpassivated Se sites, therefore, result in formation of mid-gap trap states, which enable capture of photogenerated electrons before they can radiatively recombine with holes at the edge of HOMO, consequently causing low PL-QY and τ_r. In the case of ultrasmall semiconductor SNCs, the majority of the atoms (~90%) are at the surface, and thus large number of surface occupied orbitals are available to capture the electrons (act

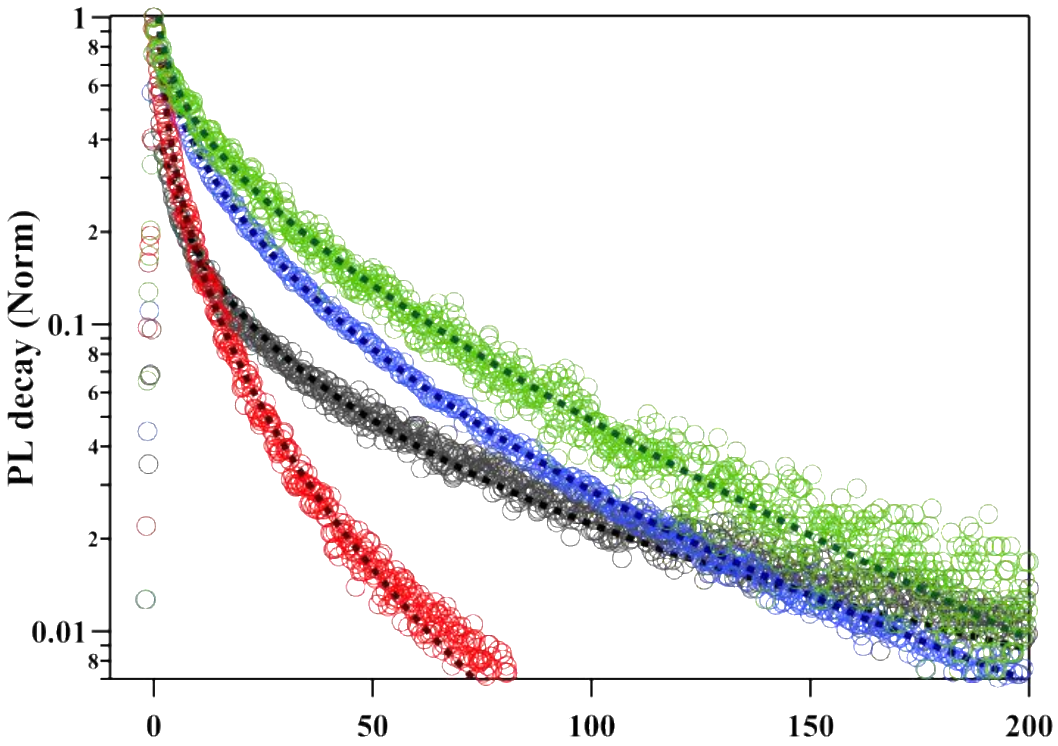

Figure 2.10: Radiative decay of purified OLA-coated $(CdSe)_{34}$ SNCs (red circles), after treatment with $Cd(oleate)_2$ (purple circles), $Cd(nonanoate)_2$, and $Cd(O_2CPh)_2$, (green circles). A stretch exponential function (dotted black lines) was used to fit the decay curves.

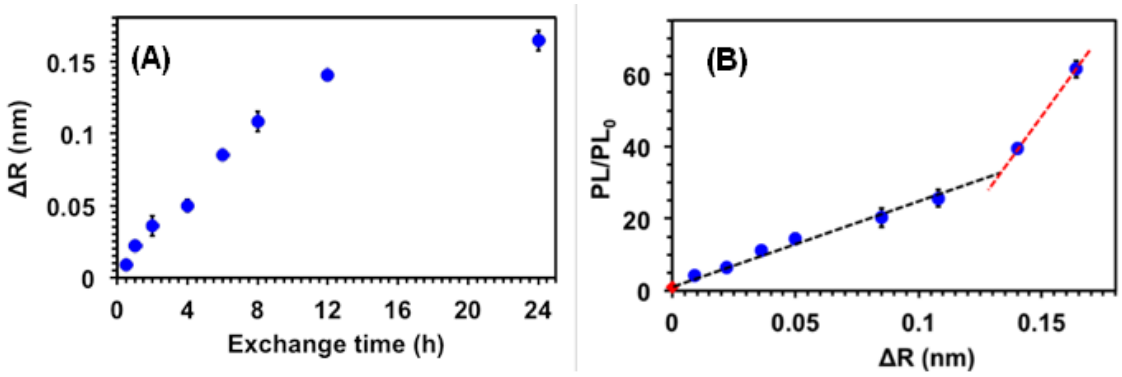

Figure 2.11: (A) Plot of the apparent increase of the excitonic radius (ΔR) of OLA-coated $(CdSe)_{34}$ SNCs with time after exposure to $Cd(O_2CPh)_2$ at room temperature. The R values were determined using an empirical equation.[56] (B) Plot of enhancement of band-edge PL peak intensity of OLA-coated $(CdSe)_{34}$ SNCs with $Cd(O_2CPh)_2$ treated as a function of calculated delocalization radius. Optical density of the SNC solution at the excitation wavelength (380 nm) was kept constant.

as nonradiative trap states) if they are not fully passivated.[72-75] This is a potential pitfall for ultrasmall CdSe SNCs causing their weak emission properties. Passivation of Se sites by 2-electron accepting Z-type ligands (e.g., metal-carboxylates) prevents the formation of nonradiative trap states. Therefore, fully-passivated CdSe SNCs (with the surface Cd and Se sites passivated by L-type and Z-type ligands, respectively) are expected to demonstrate much improved emission properties, as shown for our OLA-coated $(CdSe)_{34}$ SNCs after binding of metal-carboxylate complexes, see Table 2.1.

To determine the contribution of delocalization of hole wave function- versus passivation of mid-gap trap state-related PL-QY in $Cd(O_2CPh)_2$, we used our $Cd(nonanoate)_2$ values for reference because it lacks exciton delocalization. Thus, we believe that ~25% of the increase in PL-QY by treatment with $Cd(O_2CPh)_2$ was associated with excitonic wave function delocalization. Moreover, mixed OLA- and $Cd(O_2CPh)_2$-coated $(CdSe)_{34}$ SNCs displayed a k_r of 15.6 x 10^6 s^{-1} in comparison to 3.7 x

10^6 s^{-1} found with of only OLA-coated SNCs. Furthermore, the nonradiative rate constant (k_{nr}) of OLA-coated $(CdSe)_{34}$ SNCs before and after $Cd(O_2CPh)_2$ treatment was determined to be 69.5 x 10^6 s^{-1} and 6.4 x 10^6 s^{-1}, respectively. Therefore, passivation of Se sites on $(CdSe)_{34}$ SNCs not only enhances the k_r but also reduces k_{nr} by 10 fold. Table 2.1 summarizes the various emission properties of $(CdSe)_{34}$ SNCs upon treatment of various $Cd(carboxylate)_2$ complexes.

The dual role of $Cd(O_2CPh)_2$ was further investigated through determination of the apparent increase in the excitonic radius ("delocalization radius", ΔR) of $(CdSe)_{34}$ SNCs and the relationship with their emission property. The ΔR values were determined from the limiting time-dependent absorption spectra of OLA-coated $(CdSe)_{34}$ SNCs after their treatment with $Cd(O_2CPh)_2$ at room temperature (see Figure 2.11 A and Appendix A). As illustrated in Figure 2.11 B, the PL/PL_0 ratio (with PL the limiting time-dependent integrated band-edge emission intensity of the OLA-coated $(CdSe)_{34}$ SNCs after treatment of $Cd(O_2CPh)_2$ and PL_0 is the emission intensity before treatment) is directly related to the ΔR up to a value of ~30. This value is in agreement with the extent of enhancement of PL-QY as discussed above. Therefore, we believe that the remaining enhancement in the band-edge peak position intensity was caused by the passivation of nonradiative trap states. A similar relationship (PL/PL_0 vs. ΔR) was reported in the literature for X-type ligand functionalization of CdSe quantum dots, in which the changes in emission properties were correlated with the delocalization of excitonic wave functions.[43] However, the effects of exciton wave function delocalization on emission properties of ultrasmall CdSe SNCs are more dramatic than that found with quantum dots.

Taken together, enhancement of PL-QY and increase of k_r resulting from the attachment of $Cd(O_2CPh)_2$ onto the surface of $(CdSe)_{34}$ SNCs induces delocalization of hole wave functions and passivation of nonradiative trap states, thus demonstrating the dual role of $Cd(O_2CPh)_2$ uncovered in this present investigation. Perhaps such ligand attachment and dual passivation of the surface of the SNC can be compared to *core-shell* SNC with high emission efficiencies,[76] in which here the semiconducting inorganic shell (e.g., CdS or ZnS) is replaced by the metal-carboxylate complex. Thus, from our work one would expect to be able to achieve an unprecedented modulation of photophysical properties of semiconductor SNCs through appropriate selection of surface ligand chemistry in which energetic alignment between MOs of the SNC and surface ligand would allow delocalization of excitonic wave functions from SNC to ligand monolayer. Furthermore, the electron and/or hole delocalization into the ligand monolayer depends strongly on the energetic coupling of interfacial orbitals between the SNC and surface passivating ligands, that in turn, is influenced by the definable (synthesizable) ligand structural parameters of the metal(carboxylate)$_2$ complex. Further investigation of the effects of the organic ligand chemical structure and group II metal identity is currently underway.

2.5 Conclusion

An unprecedentedly large bathochromic shift of the lowest energy absorption and emission peaks of molecule-like $(CdSe)_{34}$ SNCs was observed upon treatment with $Cd(O_2CPh)_2$ without changing the surface ligand chemistry and crystallographic structure of original SNCs. The shift has been found to be reversible for at least five cycles of attachment and detachment of $Cd(O_2CPh)_2$. Based on several control experiments,

additional structural characterizations, and energy levels calculation of three different Cd(carboxylate) complexes via DFT calculation, we propose a MO diagram, which shows delocalization of excitonic hole wave functions from SNCs into ligand monolayers. Such delocalization is facilitated by the high kinetic energy of the hole in the strong confinement region. Moreover, we have also shown that the Z-type ligands are responsible for substantially enhancement of the emission properties of ultrasmall semiconductor SNCs through simultaneous nonradiative trap states passivation and hole wave function delocalization, demonstrating that $Cd(O_2CPh)_2$ has a dual role in this process. The intrinsic simplicity of their crystal structure,[51] their large surface-to-volume ratio, and their potential ability to provide electronic information at the molecular level, coupled with our finding of the simultaneous delocalization of exciton confinement and enhancement of emission properties will allow the study of more complex photophysical properties (biexciton generation, Auger recombination, exciton fine structure dynamics)[77-79] which are found to be extremely challenging in the larger quantum dot systems. We believe that the large band-gap tuning of ultrasmall CdSe SNCs will be applicable to other ultrasmall semiconductor SNCs (e.g., CdS, ZnS, and ZnSe) over the range of ultraviolet to the mid visible region in the solar spectrum. Thus through manipulation of surface chemistry and SNC composition, the potential application of ultrasmall SNCs to solar energy production will be enhanced.

2.6 References

(1) Hines, D. A.; Kamat, P. V. *ACS Appl. Mater. Interfaces* 2014, *6*, 3041-3057.

(2) Peterson, M. D.; Cass, L. C.; Harris, R. D.; Edme, K.; Sung, K.; Weiss, E. A. *Annu. Rev. Phys. Chem.* 2014, *65*, 317-339.

(3) Teunis, M. B.; Dolai, S.; Sardar, R. *Langmuir* 2014, *30*, 7851-7858.

(4) Knowles, K. E.; Frederick, M. T.; Tice, D. B.; Morris-Cohen, A. J.; Weiss, E. A. *J. Phys. Chem. Lett.* 2012, *3*, 18-26.

(5) Xie, Y.; Teunis, M. B.; Pandit, B.; Sardar, R.; Liu, J. *J. Phys. Chem. C* 2015, *119*, 2813-2821.

(6) Sardar, R.; Lawrence, K.; Johnson, M.; Dolai, S.; Kumbhar, A. *Nanoscale* 2015.

(7) Lawrence, K. N.; Dolai, S.; Lin, Y.-H.; Dass, A.; Sardar, R. *RSC Adv.* 2014, *4*, 30742-30753.

(8) Rosson, T. E.; Claiborne, S. M.; McBride, J. R.; Stratton, B. S.; Rosenthal, S. J. *J. Am. Chem. Soc.* 2012, *134*, 8006-8009.

(9) Dolai, S.; Dutta, P.; Muhoberac, B. B.; Irving, C. D.; Sardar, R. *Chem. Mater.* 2015, *27*, 1057-1070.

(10) Ouyang, J.; Kuijper, J.; Brot, S.; Kingston, D.; Wu, X.; Leek, D. M.; Hu, M. Z.; Ripmeester, J. A.; Yu, K. *J. Phys. Chem. C* 2009, *113*, 7579-7593.

(11) Lee, J.-S.; Kovalenko, M. V.; Huang, J.; Chung, D. S.; Talapin, D. V. *Nat. Nanotechnol.* 2011, *6*, 348-352.

(12) Kamat, P. V.; Tvrdy, K.; Baker, D. R.; Radich, J. G. *Chem. Rev.* 2010, *110*, 6664-6688.

(13) Colvin, V. L.; Schlamp, M. C.; Alivisatos, A. P. *Nature* 1994, *370*, 354-357.

(14) Schlamp, M. C.; Peng, X.; Alivisatos, A. P. *J. Appl. Phys.* 1997, *82*, 5837-5842.

(15) Kamat, P. V. *J. Phys. Chem. C* 2008, *112*, 18737-18753.

(16) Newton, J. C.; Ramasamy, K.; Mandal, M.; Joshi, G. K.; Kumbhar, A.; Sardar, R. *J. Phys. Chem. C* 2012, *116*, 4380-4389.

(17) Rogach, A. L.; Kornowski, A.; Gao, M.; Eychm√ºller, A.; Weller, H. *J. Phys. Chem. B* 1999, *103*, 3065-3069.

(18) Wang, X.; Zhuang, J.; Peng, Q.; Li, Y. *Langmuir* 2006, *22*, 7364-7368.

(19) Dolai, S.; Nimmala, P. R.; Mandal, M.; Muhoberac, B. B.; Dria, K.; Dass, A.; Sardar, R. *Chem. Mater.* 2013.

(20) Fafarman, A. T.; Koh, W.-k.; Diroll, B. T.; Kim, D. K.; Ko, D.-K.; Oh, S. J.; Ye, X.; Doan-Nguyen, V.; Crump, M. R.; Reifsnyder, D. C.; Murray, C. B.; Kagan, C. R. *J. Am. Chem. Soc.* 2011, *133*, 15753-15761.

(21) Talapin, D. V.; Rogach, A. L.; Kornowski, A.; Haase, M.; Weller, H. *Nano Lett.* 2001, *1*, 207-211.

(22) Talapin, D. V.; Lee, J.-S.; Kovalenko, M. V.; Shevchenko, E. V. *Chem. Rev.* 2009, *110*, 389-458.

(23) Peng, Z. A.; Peng, X. *J. Am. Chem. Soc.* 2000, *123*, 183-184.

(24) Cao, Y. C.; Wang, J. *J. Am. Chem. Soc.* 2004, *126*, 14336-14337.

(25) Morris-Cohen, A. J.; Frederick, M. T.; Lilly, G. D.; McArthur, E. A.; Weiss, E. A. *J. Phys. Chem. Lett.* 2010, *1*, 1078–1081.

(26) Yu, K.; Hu, M. Z.; Wang, R.; Piolet, M. L.; Frotey, M.; Zaman, M. B.; Wu, X.; Leek, D. M.; Tao, Y.; Wilkinson, D.; Li, C. *J. Phys. Chem. C* 2010, *114*, 3329.

(27) Siy, J. T.; Brauser, E. M.; Bartl, M. H. *Chem. Commun.* 2011, *47*, 364.

(28) Lees, E. E.; Nguyen, T.-L.; Clayton, A. H. A.; Mulvaney, P. *ACS Nano* 2009, *3*, 1121-1128.

(29) Kudera, S.; Zanella, M.; Giannini, C.; Rizzo, A.; Li, Y.; Gigli, G.; Cingolani, R.; Ciccarella, G.; Spahl, W.; Parak, W. J.; Manna, L. *Adv. Mater.* 2007, *19*, 548-552.

(30) Kuçur, E.; Ziegler, J.; Nann, T. *Small* 2008, *4*, 883-887.

(31) Riehle, F. S.; Bienert, R.; Thomann, R.; Urban, G. A.; Kruger, M. *Nano Lett.* 2009, *9*, 514-518.

(32) Zanella, M.; Abbasi, A. Z.; Schaper, A. K.; Parak, W. J. *J. Phys. Chem. C* 2010, *114*, 6205-6215.

(33) Cossairt, B. M.; Owen, J. S. *Chem. Mater.* 2011, *23*, 3114-3119.

(34) Cossairt, B. M.; Juhas, P.; Billinge, S. J. L.; Owen, J. S. *J. Phys. Chem. Lett.* 2011, *2*, 3075-3080.

(35) Tvrdy, K.; Frantsuzov, P. A.; Kamat, P. V. *Proc. Natl. Acad. Sci. USA* 2011, *108*, 29-34.

(36) Law, M.; Luther, J. M.; Song, Q.; Hughes, B. K.; Perkins, C. L.; Nozik, A. J. *J. Am. Chem. Soc.* 2008, *130*, 5974-5985.

(37) Luther, J. M.; Law, M.; Song, Q.; Perkins, C. L.; Beard, M. C.; Nozik, A. J. *ACS Nano* 2008, *2*, 271-280.

(38) Yu, D.; Wang, C.; Guyot-Sionnest, P. *Science* 2003, *300*, 1277-1280.

(39) Norman, Z. M.; Anderson, N. C.; Owen, J. S. *ACS Nano* 2014, *8*, 7513-7521.

(40) Nag, A.; Kovalenko, M. V.; Lee, J.-S.; Liu, W.; Spokoyny, B.; Talapin, D. V. *J. Am. Chem. Soc.* 2011, *133*, 10612-10620.

(41) Liu, Y.; Tolentino, J.; Gibbs, M.; Ihly, R.; Perkins, C. L.; Liu, Y.; Crawford, N.; Hemminger, J. C.; Law, M. *Nano Lett.* 2013, *13*, 1578-1587.

(42) Kovalenko, M. V.; Scheele, M.; Talapin, D. V. *Science* 2009, *324*, 1417-1420.

(43) Jin, S.; Harris, R. D.; Lau, B.; Aruda, K. O.; Amin, V. A.; Weiss, E. A. *Nano Lett.* 2014, *14*, 5323-5328.

(44) Liu, I.-S.; Lo, H.-H.; Chien, C.-T.; Lin, Y.-Y.; Chen, C.-W.; Chen, Y.-F.; Su, W.-F.; Liou, S.-C. *J. Mater. Chem.* 2008, *18*, 675-682.

(45) Frederick, M. T.; Weiss, E. A. *ACS Nano* 2010, *4*, 3195-3200.

(46) Frederick, M. T.; Amin, V. A.; Weiss, E. A. *J. Phys. Chem. Lett.* 2013, *4*, 634-640.

(47) Knowles, K. E.; Tice, D. B.; McArthur, E. A.; Solomon, G. C.; Weiss, E. A. *J. Am. Chem. Soc.* 2009, *132*, 1041-1050.

(48) Koole, R.; Liljeroth, P.; de Mello Donegá, C.; Vanmaekelbergh, D.; Meijerink, A. *J. Am. Chem. Soc.* 2006, *128*, 10436-10441.

(49) Koole, R.; Luigjes, B.; Tachiya, M.; Pool, R.; Vlugt, T. J. H.; de Mello Donegá, C.; Meijerink, A.; Vanmaekelbergh, D. *J. Phys. Chem. C* 2007, *111*, 11208-11215.

(50) Buckley, J. J.; Couderc, E.; Greaney, M. J.; Munteanu, J.; Riche, C. T.; Bradforth, S. E.; Brutchey, R. L. *ACS Nano* 2014, *8*, 2512-2521.

(51) Zhou, Y.; Wang, F.; Buhro, W. E. *J. Am. Chem. Soc.* 2015.

(52) Anderson, N. C.; Hendricks, M. P.; Choi, J. J.; Owen, J. S. *J. Am. Chem. Soc.* 2013, *135*, 18536-18548.

(53) Senthilkumar, S.; Nath, S.; Pal, H. *Photochem. Photobiol.* 2004, *80*, 104-111.

(54) Beecher, A. N.; Yang, X.; Palmer, J. H.; LaGrassa, A. L.; Juhas, P.; Billinge, S. J. L.; Owen, J. S. *J. Am. Chem. Soc.* 2014, *136*, 10645-10653.

(55) Garcia-Rodriguez, R.; Liu, H. *Chem. Commun* 2013, *49*, 7857-7859.

(56) Jasieniak, J.; Smith, L.; Embden, J. v.; Mulvaney, P.; Califano, M. *J. Phys. Chem. C* 2009, *113*, 19468-19474.

(57) Battaglia, D.; Blackman, B.; Peng, X. *J. Am. Chem. Soc.* 2005, *127*, 10889-10897.

(58) Kasuya, A.; Sivamohan, R.; Barnakov, Y. A.; Dmitruk, I. M.; Nirasawa, T.; Romanyuk, V. R.; Kumar, V.; Mamykin, S. V.; Tohji, K.; Jeyadevan, B.; Shinoda, K.; Kudo, T.; Terasaki, O.; Liu, Z.; Belosludov, R. V.; Sundararajan, V.; Kawazoe, Y. *Nat Mater* 2004, *3*, 99-102.

(59) Hens, Z.; Martins, J. C. *Chem. Mater.* 2013, *25*, 1211-1221.

(60) Moreels, I.; Lambert, K.; Smeets, D.; De Muynck, D.; Nollet, T.; Martins, J. C.; Vanhaecke, F.; Vantomme, A.; Delerue, C.; Allan, G.; Hens, Z. *ACS Nano* 2009, *3*, 3023-3030.

(61) Knowles, K. E.; Tice, D. B.; McArthur, E. A.; Solomon, G. C.; Weiss, E. A. *J. Am. Chem. Soc.* 2010, *132*, 1041-1050.

(62) Kim, B. H.; Hackett, M. J.; Park, J.; Hyeon, T. *Chem. Mater.* 2014, *26*, 59-71.

(63) Cooper, J. K.; Franco, A. M.; Gul, S.; Corrado, C.; Zhang, J. Z. *Langmuir* 2011, *27*, 8486-8493.

(64) Mourdikoudis, S.; Liz-Marzán, L. M. *Chem. Mater.* 2013, *25*, 1465-1476.

(65) Papageorgiou, S. K.; Kouvelos, E. P.; Favvas, E. P.; Sapalidis, A. A.; Romanos, G. E.; Katsaros, F. K. *Carbohydr. Res.* 2010, *345*, 469-473.

(66) Bowers Ii, M. J.; McBride, J. R.; Garrett, M. D.; Sammons, J. A.; Dukes Iii, A. D.; Schreuder, M. A.; Watt, T. L.; Lupini, A. R.; Pennycook, S. J.; Rosenthal, S. J. *J. Am. Chem. Soc.* 2009, *131*, 5730-5731.

(67) Steigerwald, M. L.; Brus, L. E. *Acc. Chem. Res.h* 1990, *23*, 183–188.

(68) Banin, U.; Cao, Y.; Katz, D.; Millo, O. *Nature* 1999, *400*, 542-544.

(69) Brus, L. *J. Phys. Chem.* 1986, *90*, 2555-2560.

(70) Kambhampati, P. *Acc. Chem. Res.h* 2011, *44*, 1-13.

(71) Kilina, S.; Velizhanin, K. A.; Ivanov, S.; Prezhdo, O. V.; Tretiak, S. *ACS Nano* 2012, *6*, 6515-6524.

(72) Dolai, S.; Dass, A.; Sardar, R. *Langmuir* 2013, *29*, 6187-6193.

(73) Bowers, M. J.; McBride, J. R.; Rosenthal, S. J. *J. Am. Chem. Soc.* 2005, *127*, 15378.

(74) Anderson, N. C. Thesis. Columbia University, 2014.

(75) Wasielewski, M. R. *Chem. Rev.* 1992, *92*, 435-461.

(76) Gust, D.; Moore, T. A.; Moore, A. L. *Acc. Chem. Res.h* 2001, *34*, 40-48.

(77) Weinberg, D. J.; Khademi, Z.; Malicki, M.; Marder, S. R.; Weiss, E. A. *Optics InfoBase Conference Papers* 2014.

(78) Frederick, M. T.; Amin, V. A.; Cass, L. C.; Weiss, E. A. *Nano Lett.* 2011, *11*, 5455-5460.

(79) Brus, L. E. *J. Chem. Phys.* 1983, *79*, 5566-5571.

(80) Coe, S.; Woo, W.-K.; Bawendi, M.; Bulovic, V. *Nature* 2002, *420*, 800-803.

2.7 Appendices

Appendix A: Fitted time dependent absorption spectra and increase in ΔR as a function of exchange time

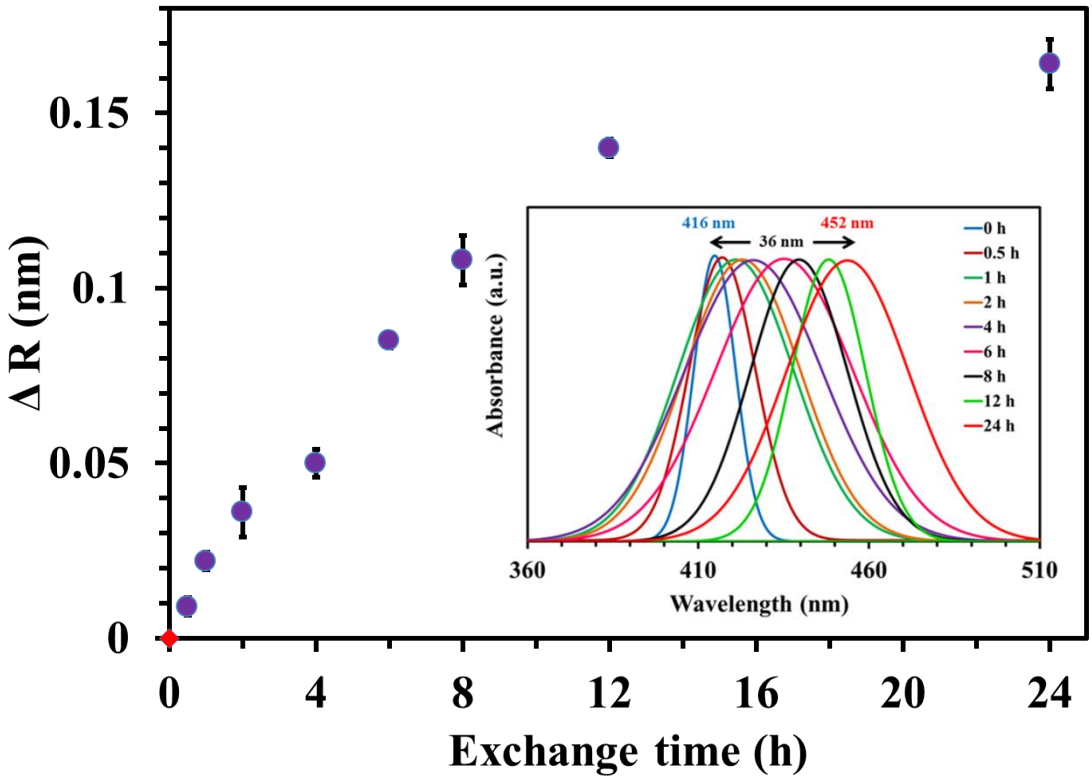

Plot of change in effective radius (ΔR) after addition of $Cd(O_2CPh)_2$ over 24 h. Inset: fitted first absorption peak UV-Vis spectra over 24 h.

Appendix B: ^{1}H NMR OLA-passivated $(CdSe)_{34}$ SNCs, $Cd(O_2CPh)_2$ – amine complex, and addition of $Cd(O_2CPh)_2$ to OLA-passivated $(CdSe)_{34}$ SNCs

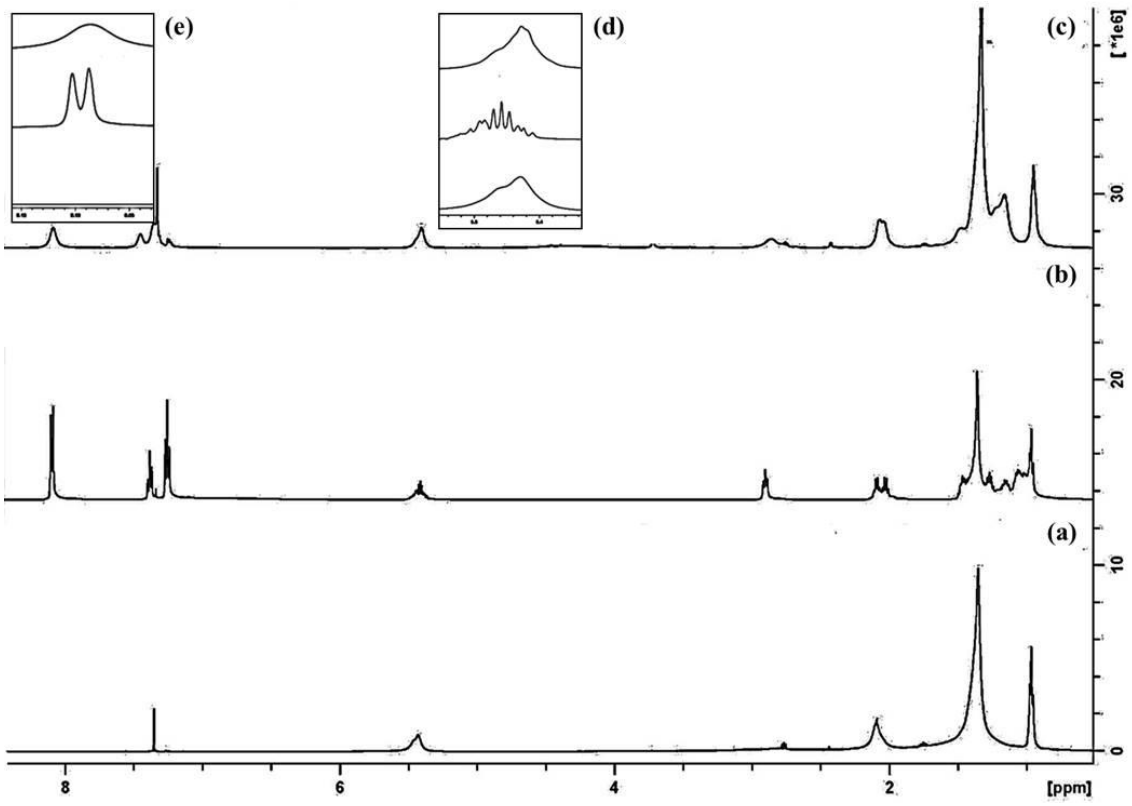

^{1}H NMR of (a) OLA-passivated $(CdSe)_{34}$ NCs (b) amine-benzoate complex, and (c) after attachment of $Cd(O_2CPh)_2$. Aromatic CH of benzoate at 8.1 ppm (e) is distinct from that of OLA. When comparing this peak to HC=CH of OLA at 5.5 ppm (d), integration is ~1:1. Broad peaks are indicative of bonding to the core attributed to the transversal interproton dipolar relaxation mechanism which restricts rotational mobility of ligands attached to the surface, and thus, they tumble more slowly than their free counterparts creating broadening in the spectra.[1-3] These peaks are sharp as seen for free amine-benzoate complex (b).

Appendix C: FTIR spectra of $Cd(O_2CPh)_2$-OLA-passivated $(CdSe)_{34}$ SNCs

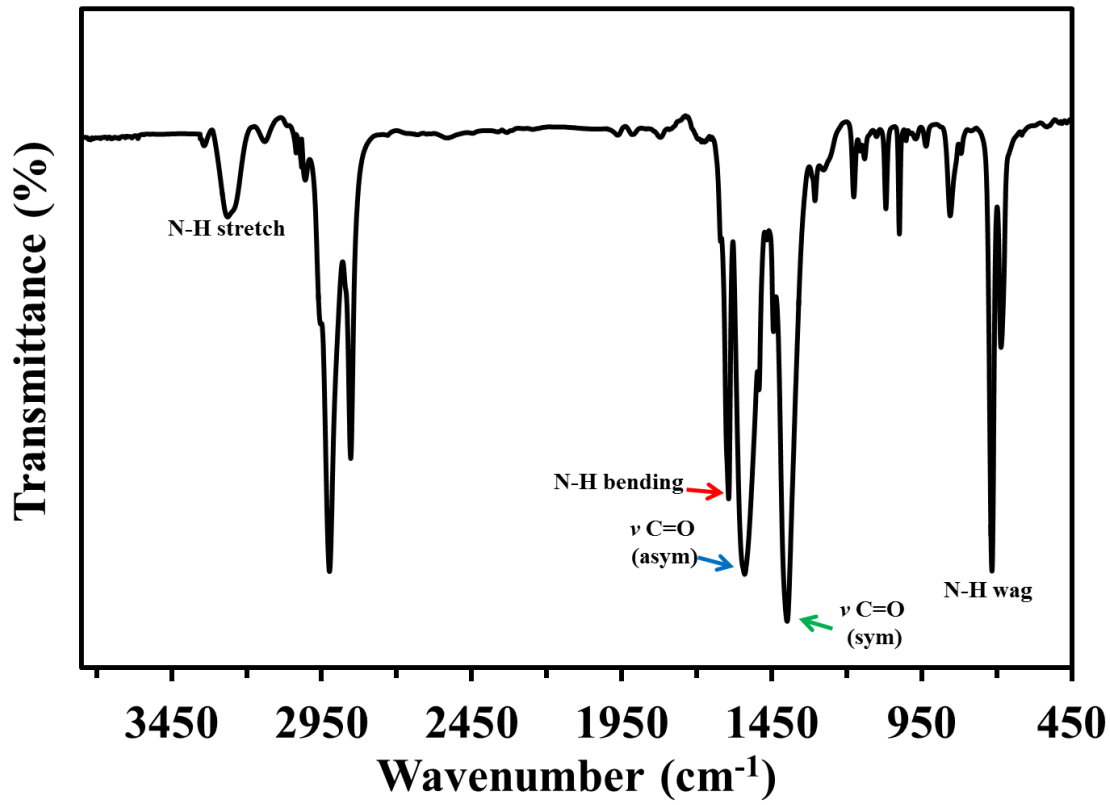

FTIR spectrum of purified OLA-passivated $(CdSe)_{34}$ SNCs after binding with $Cd(O_2CPh)_2$. Characteristic N-H stretching vibrations in the range of 3400-3300 cm^{-1}, N-H bending mode (red arrow) at 1581 cm^{-1}, and N-H wag at 721 cm^{-1} were present after the addition of $Cd(O_2CPh)_2$ confirming the attachment of primary OLA on the SNC surface.[2,3] Additionally, new asymmetric (1518 cm^{-1}) (blue arrow) and symmetric (1388 cm^{-1}) (green arrow) stretching vibrations of the carboxylate group (C=O) appeared. The separation between these two stretching vibrations is 130 cm^{-1}, suggesting $-COO^-$ attached to the Cd^{2+} through a chelating bidentate interaction. Importantly, presence of both N-H and C=O after the addition of $Cd(O_2CPh)_2$ suggest mixed surface ligation rather than commonly demonstrated surface exchange.

Appendix D: Multiple cycles of exciton delocalization as measured by absorption spectroscopy

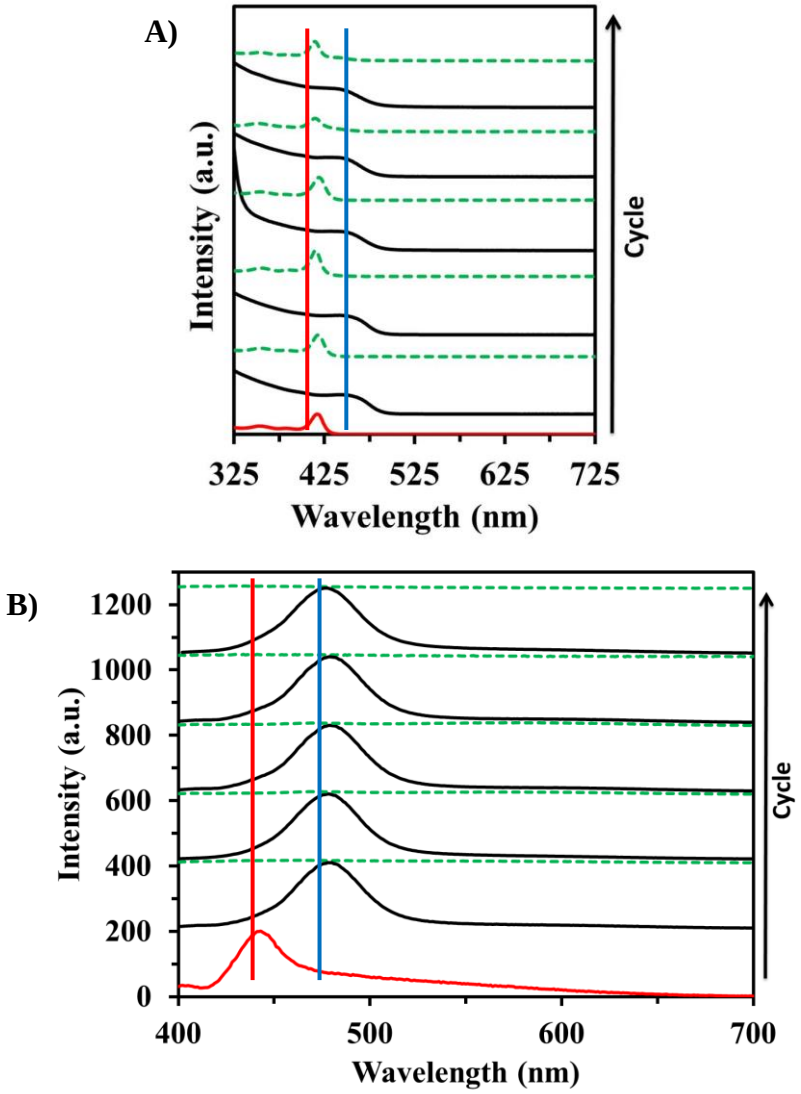

A) Normalized UV-vis absorption and B) emission of OLA-passivated $(CdSe)_{34}$ SNCs during multiple cycles of attachment of $Cd(O_2CPh)_2$ and displacement by TMEDA. The solid red line depicts the as-synthesized OLA-passivated $(CdSe)_{34}$ SNCs, solid black lines depict attachment of $Cd(O_2CPh)_2$, and dashed green lines represent ligand displacement via TMEDA. The number of cycles increases as you move up the graph. Blue and red lines are a focal point for the eye.

Appendix E: HDA- and TOPO-passivated $(CdSe)_{34}$ SNCs

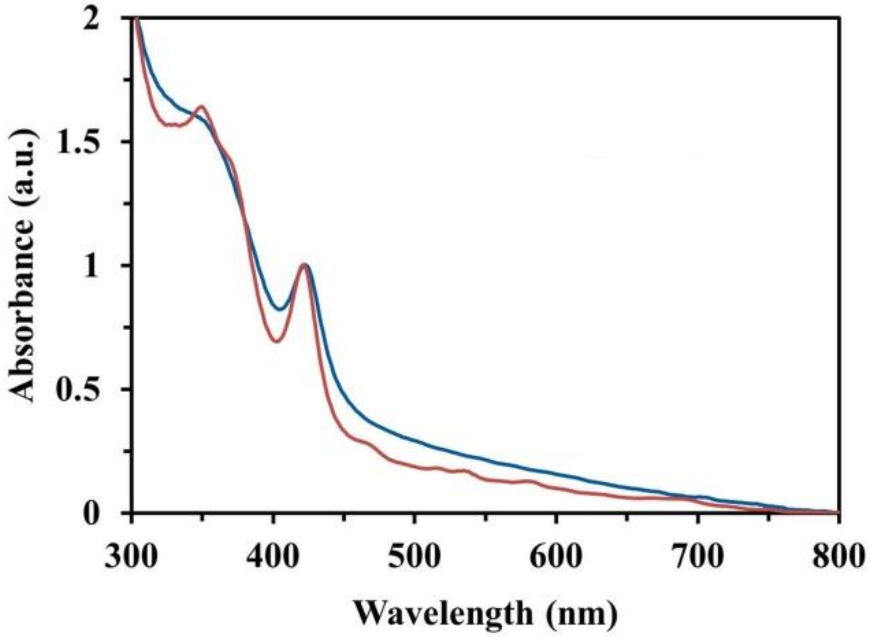

Absorption spectra (in toluene) of purified mixed HDA- and TOP-passivated $(CdSe)_{34}$ nanocrystals (blue lines) synthesized according to literature procedure[30] and after ex situ treatment with $Cd(O_2CPh)_2$ at room temperature. The nanocrystals displayed lowest energy absorption peak position at 415 and 417 nm before and after $Cd(O_2CPh)_2$ treatment, respectively. This ~14 eV shift of lowest energy absorption peak could result from the negligible delocalization of exciton wave functions.

Appendix F: UV-visible absorption and emission spectra of Cd(nonanoate)$_2$-OLA-coated $(CdSe)_{34}$ SNCs

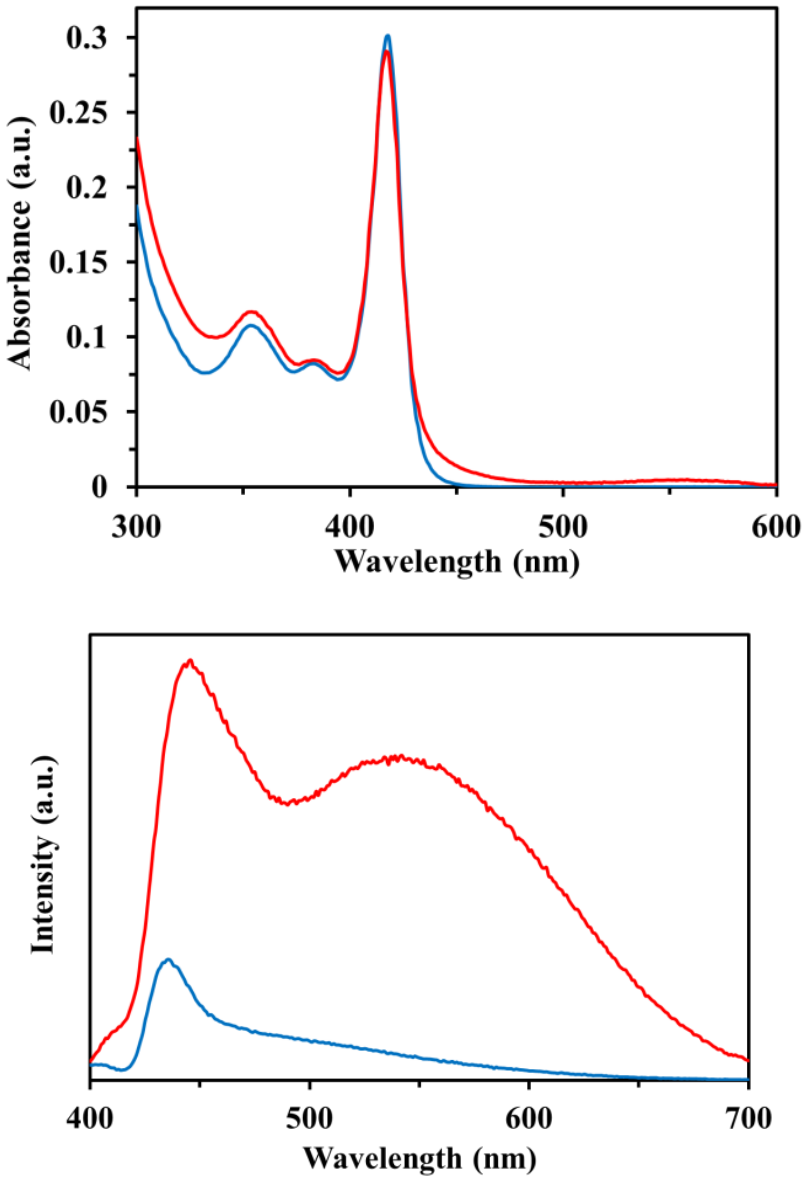

Absorbance (A) and emission (B) spectra of as-synthesized OLA-passivated $(CdSe)_{34}$ SNCs (blue) and after addition of Cd(nonanoate)$_2$ (red).

Appendix G: ^{1}H NMR OLA-passivated $(CdSe)_{34}$ SNCs after attachment of cadmium nonanoate

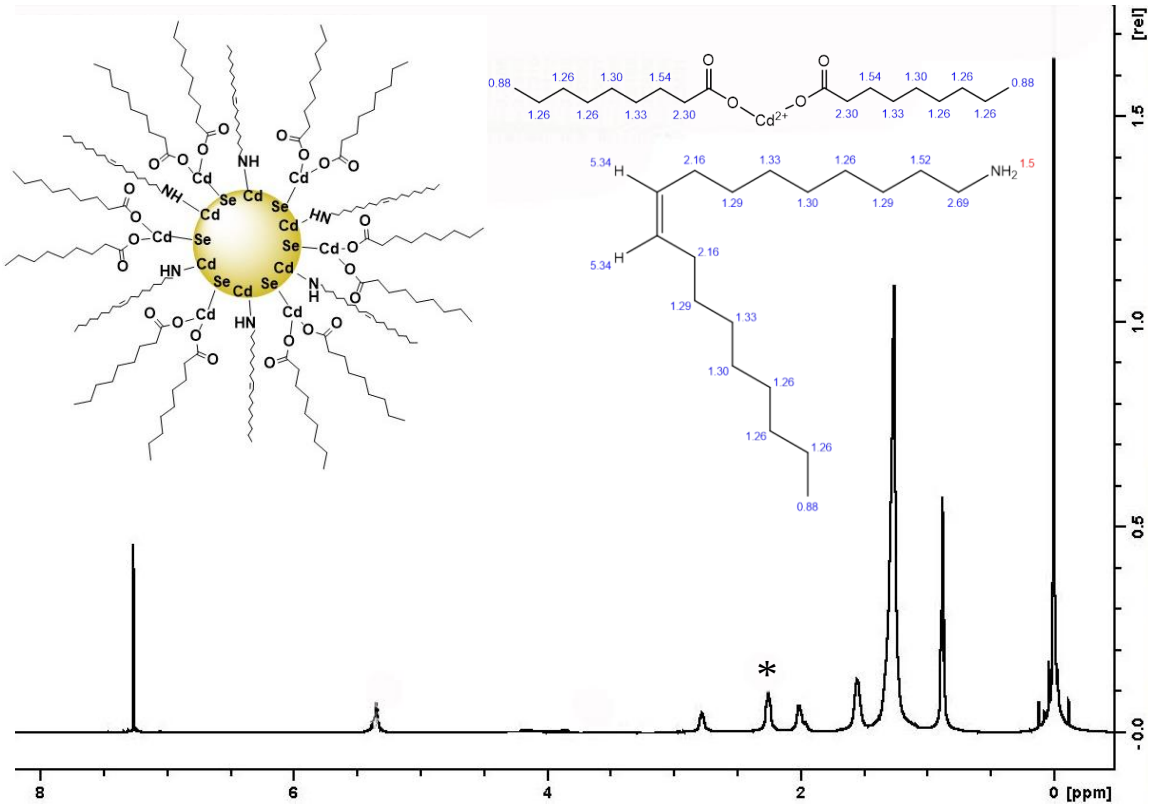

^{1}H NMR of OLA-passivated $(CdSe)_{34}$ SNCs after attachment of cadmium nonanoate. (Image does not represent true core-cage structure.) Cd(nonanoate)$_2$ –CH peak at 2.32 ppm (*) is distinct from that of OLA. When comparing this peak to HC=CH of OLA at 5.53 ppm, integration is ~1:1. Broad peaks are indicative of bonding to the core attributed to the transversal interproton dipolar relaxation mechanism which restricts rotational mobility of ligands attached to the surface, and thus, they tumble more slowly than their free counterparts creating broadening in the spectra.[1-3] *Structures and ^{1}H NMR approximations via ChemDraw Professional.

Appendix H: FTIR spectra of OLA-passivated $(CdSe)_{34}$ SNCs upon addition of $Cd(nonanoate)_2$

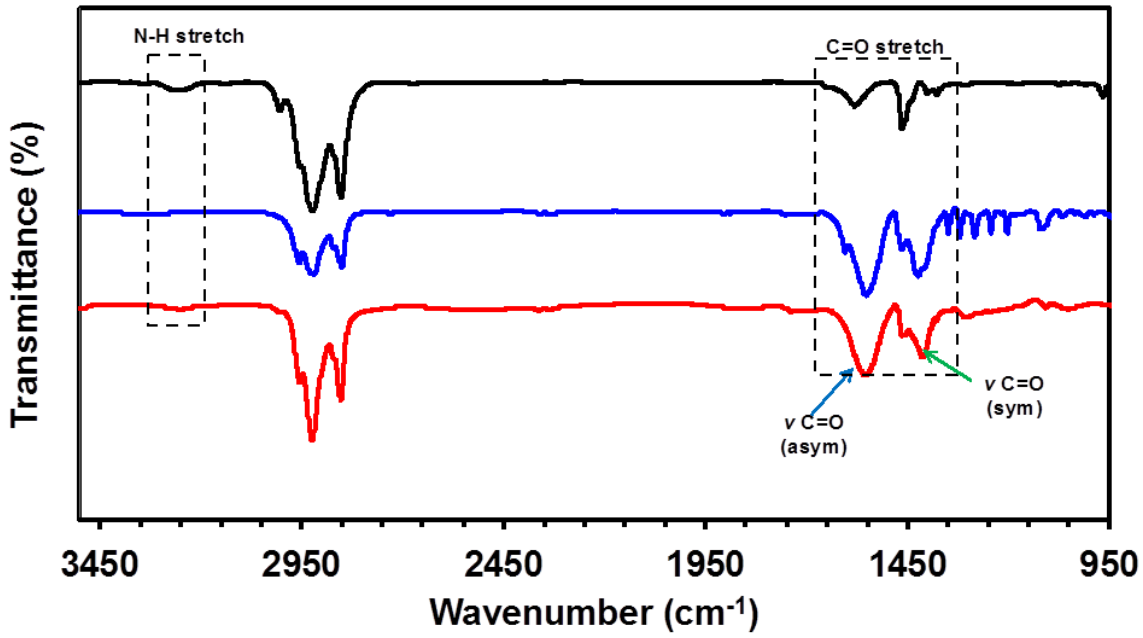

FTIR spectra of OLA-passivated $(CdSe)_{34}$ nanocrystals (black curve) in which characteristic N-H stretching vibrations in the range of 3400-3000 cm^{-1} appeared, confirming the presence of primary amine OLA passivates the nanocrystals surface. After $Cd(nonanoate)_2$ treatment (red curve) new asymmetric (1546 cm^{-1}) and symmetric (1406 cm^{-1}) stretching vibrations of the carboxylate group ($-COO^-$) appeared. The separation between these two stretching vibration is 141 cm^{-1}, suggesting $-COO^-$ attached to the Cd^{2+} through a chelating bidentate interaction. Most importantly, both the asymmetric and symmetric vibration red-shifted from 1552 (~6 cm^{-1}, 26 nm) and 1411 cm^{-1} (~5 cm^{-1}, 25 nm), respectively, along with peak broadening of the pure $Cd(nonanoate)_2$ (blue), suggesting the interaction between $-COO^-$ and Cd^{2+} weakened due to their attached to the surface Se sites. Beside, presence of N-H stretching N-H bending vibration modes indicate the mixed surface ligation, and addition of Z-type ligand $Cd(nonanoate)_2$ did not replace L-type ligand OLA, as demonstrated in the literature.

Appendix I: FTIR spectra of OLA-passivated $(CdSe)_{34}$ SNCs upon addition of $Cd(oleate)_2$

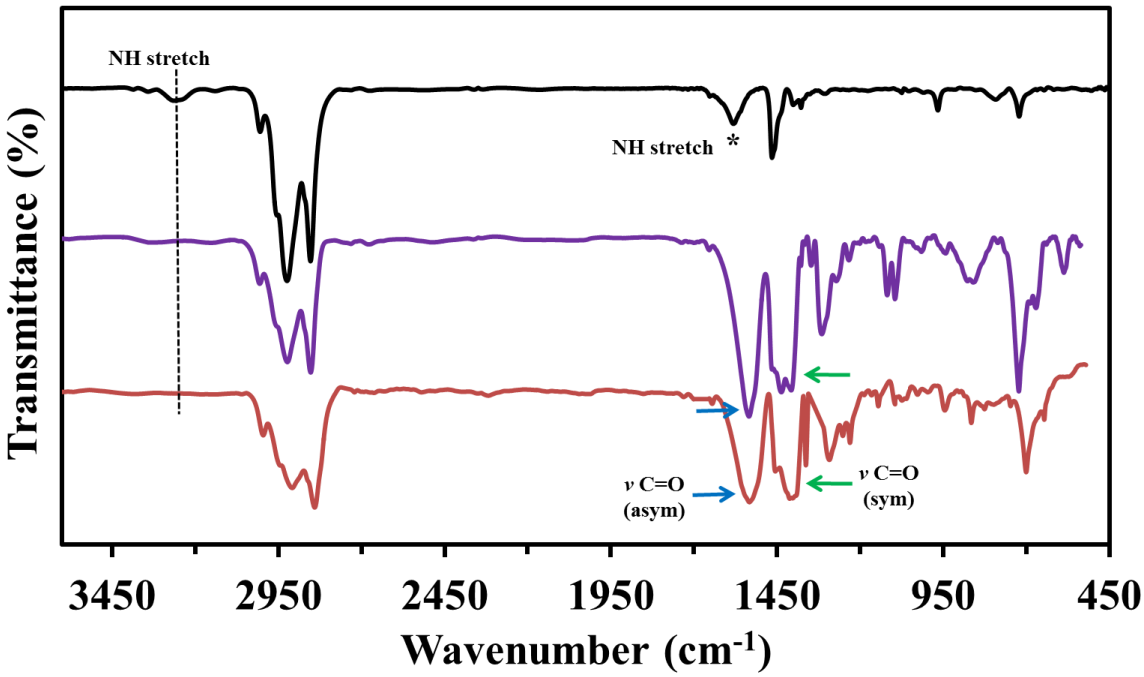

Solid FTIR spectra of OLA-passivated $(CdSe)_{34}$ nanocrystals (black), pure $Cd(oleate)_2$ (purple), OLA-passivated $(CdSe)_{34}$ SNCs after addition of $Cd(oleate)_2$ (red). FTIR shows distinct differences between OLA-passivated $(CdSe)_{34}$ SNCs and pure $Cd(oleate)_2$ and bound and unbound $Cd(oleate)_2$. Broad N-H stretching is present at ~3250 cm^{-1} for OLA-passivated $(CdSe)_{34}$ SNCs (black) and absent for pure $Cd(oleate)_2$ and after addition of $Cd(oleate)_2$ to $(CdSe)_{34}$ SNCs (red). Additional peaks present in OLA-capped CdSe include N-H bending at 1581 cm^{-1}, CH_2 bending at 1464 cm^{-1}, C-N stretching at 965 cm^{-1}, and N-H wag at 721 cm^{-1}.[cite] On the other hand, pure $Cd(nonanoate)_2$ (purple) displays two peaks at 1535 and 1406cm^{-1} corresponding to the asymmetric and symmetric carbonyl stretching; whereas, the bound carbonyl has two peaks at 1531 and 1396 cm^{-1}, respectively. The broadening in peak shape and shift to lower wavenumbers is indicative of bound ligands.

Appendices References

(1) Anderson, N. C.; Hendricks, M. P.; Choi, J. J.; Owen, J. S. *J. Am. Chem. Soc.* 2013, *135*, 18536-18548.

(2) Hens, Z.; Martins, J. C. *Chem. Mater.* 2013, *25*, 1211-1221.

(3) Moreels, I.; Lambert, K.; Smeets, D.; De Muynck, D.; Nollet, T.; Martins, J. C.; Vanhaecke, F.; Vantomme, A.; Delerue, C.; Allan, G.; Hens, Z. *ACS Nano* 2009, *3*, 3023-3030.

(4) Cooper, J. K.; Franco, A. M.; Gul, S.; Corrado, C.; Zhang, J. Z. *Langmuir* 2011, *27*, 8486-8493.

(5) Mourdikoudis, S.; Liz-Marzán, L. M. *Chem. Mater.* 2013, *25*, 1465-1476.

CHAPTER 3. ENHANCING THE SOLUBILITY AND ELECTRONIC COUPLING OF SEMICONDUCTOR NANOCRYSTALS THROUGH SOLVENT-LIKE LIGAND PASSIVATION

3.1 Synopsis

The chemical properties of surface passivating ligands that surround semiconductor nanocrystals (SNCs) are extremely important for controlling their structural, physiochemical, and photophysical properties. However, to investigate these properties under various environments, it is important to be able to dissolve the ligand-coated SNCs in a wide range of polar and nonpolar solvents. We have developed a direct synthesis and purification procedure for poly(ethylene glycol) (PEG) thiolate-coated ultra-small (<3.0 nm diameter) CdSe SNCs, which have such solubility characteristics. The SNCs were synthesized in aqueous medium and purified using a simple solvent extraction method. The organic phase-extracted CdSe SNCs were readily soluble in a wide range of polar and nonpolar organic solvents including acetonitrile, ethanol, chlorobenzene, dichloromethane, and chloroform, as well as in water. The diverse solubility property of PEG-thiolate-coated CdSe SNCs allowed us to perform a post-synthetic surface ligand treatment with triphenylphosphine in an organic solvent, which resulted in an ~8 fold increase in photoluminescence quantum yield (PL-QY). This significant improvement of photophysical property is vital for many applications ranging

from biological imaging to light emitting diodes. However, for many other solid state applications, high conductivity stemming from strong inter-SNC electronic coupling must also occur. Interestingly, our unique short chain PEG- thiolate provided not only stability and solubility, but that much needed inter-SNC electronic interaction. We were able to manipulate this interaction of PEG-thiolate-coated CdSe SNCs to achieve 170 meV electronic coupling energy. Cryo-transmission electron microscopy analysis showed the formation of a *pearl-necklace* assembly of SNCs in solution with regular inter-SNC spacing. The electronic coupling was studied as a function of CdSe SNC size where the smallest SNCs exhibited the largest coupling energy and the shortest chain displayed the most effective electronic coupling. The electronic coupling in spin-cast thin-film (<200 nm in thickness) was also studied as a function of annealing temperature, where an unprecedentedly large, ~400 meV coupling energy was observed for 1.6 nm diameter SNCs, which were coated with a thin layer of PEG-thiolates. Small-angle X-ray scattering (SAXS) measurements showed that CdSe SNCs maintained an order array inside the films. Therefore, through a simple ligand modification with PEG-thiolate, we were able to enhance CdSe SNCs' solubility, stability, and electronic coupling which is vital for a myriad of applications ranging from bionanotechnology to solid state devices such as the large-scale production of highly efficient electronic materials for advanced optoelectronic devices.

3.2 Introduction

Synthesis and isolation of quantum dots (QDs) of different size, shape, and composition have been of tremendous interest in modern nanotechnology-based research.[2-10] Due to their unique photophysical and physicochemical properties, these

QDs have successfully been used in the fabrication of efficient photovoltaic devices,[6, 11-13] light-emitting diodes, [14-19] and photodetectors. [20-23] In this context, ultra-small SNCs (< 3 nm) are a special type of semiconductor nanomaterial, because they display sharp absorption peaks as well as broad band[24-26] or a combination of broad band and band-edge photoluminescence (PL).[14, 27-30] Furthermore, ultra-small SNCs bridge the divide between molecules and QDs by displaying distinct energy levels with molecule-like highest occupied (HOMO) and lowest unoccupied (LUMO) molecular orbitals as discussed in detail in chapter 1. Additionally, at this ultra-small size, the large majority of atoms comprising the SNC reside at the surface; therefore, fundamentally new photophysical properties originate at the SNC core-surface ligand interface. Several synthetic methods have been developed to prepare ultra-small group II-VI[14, 24, 25, 27-36] and IV-VI[37] SNCs; the most widely utilized being long-chain hydrocarbon-containing aliphatic amines, phosphine, phosphine oxide, and/or phosphonic acids.[6, 11, 24-26, 28-30, 32, 38-46]

These ligand-passivated SNCs have shown promise in the fabrication of solid-state light-emitting devices,[14, 15] but lack the versatility needed for other applications. For example, SNCs passivated by long hydrocarbon chain-containing ligands are only soluble in organic solvents. In order for these SNCs to be of use in nanobiotechnology, their surface structure must be altered. One such way of doing this is through encapsulation of hydrophobic ligand-coated SNCs with phospholipids or PEGylated polymers.[38, 47-50] However, this process comes at a cost of increasing the hydrodynamic radius which can inhibit the SNCs ability to inter cells during cellular imaging. [64] Conversely, post-synthetic ligand exchange reactions in which various thiolate ligands replace the

hydrophobic ligand has also widely been used to enhance the solubility of ligand-coated SNCs for biological imaging.[8, 50, 51] Thiol forms a strong metal-thiolate bond, thereby increases the stability of QDs in various solvents. However, thiols are notorious for quenching the PL quantum yield (PL-QY) of SNCs due to trapping of photogenerated holes which prevents radiative recombination of excitons.[52] This results in extremely low PL-QYs as apparent in previous reports of aqueous phase synthesis and characterization of ultra-small CdSe SNCs[31, 33, 53] in which PL-QYs have not been reported, most likely due to these extremely low values. Additionally, thiols only bind with surface metals (e.g., Cd) leaving the surface Se sites free, which creates trap states resulting in faster electron-hole recombination and low PL-QY as described in detail in chapter 2.

On the other hand, SNCs synthesized using long-chain aliphatic ligands, for solid state devices (which do not require solubility in an aqueous media) also suffer from poor choice of surface ligation. Meager carrier mobilities and conductivities are a direct result of electrically insulating ligands, which have deleterious effects on thin-film-based optoelectronic devices. The conductivity in SNC films can be improved by increasing inter-SNC electronic coupling by reducing the thickness of the insulating ligand shell, because when two SNCs are brought into close vicinity, their exciton (bound electron-hole pair) wave functions can expand beyond the SNC boundary, overlap, and entangle. Use of this property of the SNC films would open a new frontier of scientific research by enabling the preparation of "artificial solids" with unprecedented high conductivity.[54]

A number of methods have been developed to enhance the electronic coupling between SNCs in colloidal dispersions and/or solid films by exchanging the native bulky, hydrocarbon ligands with small organic ligands,[55-58] inorganic ions,[59-65] and metal

chalcogenide complexes.[5, 40, 66, 67] However, solid phase ligand exchange reaction can cause a dramatic structural rearrangement of SNCs, which results in the appearance of cracks and voids in the solid films or irreversible aggregation of SNCs inside films.[56, 68] In contrast, a solution phase exchange reactions enable preservation of the solution dispersibility, which allows for better solution processing for more efficient film preparation. Various ligands such as chloride,[59] thiocyanate,[62] sulfide,[63-65] metal chalcogenide complexes,[5, 40, 66, 67] tetrafluoroborate,[60, 61] hydrazine,[68, 69] and pyridine[56] have most commonly been used to perform these solution phase exchange reactions. However, the newly formed ligand-coated SNCs lack electronic coupling, which would be represented as a red-shift of the excitonic peaks in the absorption spectrum.[70-72] Additionally, ligand exchange reactions with small ligand molecules often create trap states causing the emission to take an altered path, meaning direct recombination is lowered, which results in a diminished PL-QY. Thus, similar to the above mentioned thiols, these ligand properties nullify the advantage of strong electronic coupling in the film.[40, 64] Lastly, small molecules and various other ions used as passivating ligands are unstable, meaning they are susceptible to undergoing fast oxidation even at ambient conditions,[56] and they are only soluble in high boiling solvents,[5, 56, 62, 65, 67, 73] which makes device fabrication using these materials problematic.

The above-mentioned difficulties of solid phase exchange reactions can be avoided through solution phase exchange reactions with moderately long chain ligands. Under ambient conditions, these ligands remain stable; therefore, SNCs will not only retain their solution dispersibility but also enable facile thin-film preparation with strong electronic coupling. Short chain length organic molecules such as 1,2-ethanedithiol,[55]1,6-

hexanedithiol,[74] and mercaptobenzoic acid[75] have been used to replace native insulating ligands. However, these ligand-coated large SNCs (>3.0 nm in diameter) displayed weak electronic coupling.[55, 74, 75] As described in chapter 1, it is well known that coupling increases as the size of the SNCs decreases due to the expansion and entanglement of the SNC's wavefunction.[70, 74, 76-78] Therefore, we hypothesized that ultrasmall SNCs with <3.0 nm in diameter would display strong electronic coupling in solution through ordered arrays and/or reduction of inter-SNC distance with appropriate selection of surface passivating ligands. Moreover, such ligand choice would allow SNCs to maintain stability, have versatile solubility, and display strong electronic coupling.

A systematic manipulation of surface ligand chemistry of ultra-small SNCs is required in order to fully exploit the many advantages awarded by this size regime (< 3.0 nm), which we hypothesized to provide the following advantages: (1) long-term stability in both aqueous and organic solvents, (2) solubility in organic solvent that facilitates an organically soluble ligand treatment to minimize trap states and an increase in PL-QY without removing the original ligands, (3) solubility in aqueous medium for applications such as biological imaging, (4) conductivity through increased electronic coupling. Taken together, the enrichment of above-mentioned photophysical and physicochemical properties of ligand passivated ultra-small SNCs will facilitate their potential application in the field of nanotechnology and nanobiotechnology.

This chapter describes a new method of preparation and isolation of ultra-small (< 3.0 nm in diameter) poly(ethylene glycol) (PEG)-thiolate-coated CdSe SNCs with substantially enhanced solubility and fluorescence properties, which display all the above mentioned characteristics. The SNCs displayed a sharp absorption peak that resembled

the so-called "magic-sized" CdSe SNCs.[24, 33, 79-81] These organic phase-extracted and purified CdSe SNCs were readily soluble in a wide range of polar and nonpolar organic solvents as well as in water. Such unique solubility of the PEG-thiolate-coated CdSe SNCs allowed us to perform post-synthetic ligand treatment and modification with triphenylphosphine (TPP) to further enhance their PL-QY up to 8-fold, which resulted in a bright yellow PL making the material suitable for bioimaging. Moreover, the "*solvent-like"* character of PEGs, along with their low hydrodynamic radii,[82] allowed for strong inter-SNC interaction which allowed for a thorough investigation of electronic coupling as a function of not only SNC size, but ligand chain length to occur. We observed up to 170 meV change in coupling energy in solution which was the highest value reported in the literature in the case of dissolved SNCs. The solution-phase organization of PEG-thiolate-coated SNCs was further investigated with Cryo-transmission electron microscopy (TEM), which showed formation of *"pearl-necklace"* assemblies. The SNC size effects in electronic coupling were also investigated. Finally, we explored the electronic coupling of SNCs in spin-casted thin-films on solid surfaces as a function of annealing temperature. An ~400 meV decrease in excitonic peak energy was observed for PEG_6-thiolate-coated CdSe SNCs film upon annealing at 175 ^{o}C. Structural properties of thin-films were characterized by small-angle X-ray scattering (SAXS) to unravel the strong electronic coupling. Precise manipulation of electronic interactions due to delocalization of strongly confined excitons of ultrasmall SNCs, which are also capable of donating and accepting multiple charges, PEG-thiolate-coated SNCs can be considered as ionically conductive *hybrid redox polyethers*[83] with potential for future applications in solid-state device fabrication. Therefore, through simple ligand modification using PEG-

thiolate we were able to tailor the solubility, stability, and electronic coupling energy of ultra-small SNCs to use as potential materials not only for solid state device fabrication, but also biological applications such as cellular imaging.

3.3 Experimental Methods

3.3.1 Materials

$CdSO_4 \cdot 8/3\ H_2O$ (>99%), selenium metal (99.99%), triphenylphosphine (99%), different chain length poly(ethylene glycol) methyl ethers (PEG_n, n = glycol unit = 6-150), *p*-toluene sulfonyl chloride (>99%), thiourea (>99%), anhydrous acetonitrile (CH_3CN, >99.8%), hexanes (99%), ethanol (98.5%), methanol (98.5%), chloroform (>99%), oleylamine (OLA, >70%), 1-hexanethiol (>95%), toluene (>99%), and dichloromethane (DCM, >99%) were purchased from Aldrich and used without further purification. Organic solvents were purged with N_2 for 30 min prior to use. All water was purified using a Thermo Scientific Barnstead Nanopure system. A 0.25 M aqueous solution of Na_2SeSO_3 was prepared according to the literature.[33] PEG_n-thiols were synthesized following a published procedure (see Appendix A).[84]

3.3.2 Optical Spectroscopy, Electron Microscopy, and Mass Spectrometry Measurements

UV-vis absorption spectra were collected using a Varian Cary 50 UV-vis spectrophotometer over a range of 800-300 nm. Prior to the sample measurements, the baseline was corrected with pure solvent. The emission spectra were acquired using a Cary Eclipse fluorescence spectrophotometer from Varian Instruments. ^1H NMR was recorded on a Bruker AVANCE III 500 instrument at 500 MHz. Typically ~2 mg of sample were dissolved in 0.6 mL of CD_2Cl_2 at room temperature and a minimum of 1000

scans were collected. HRTEM analysis was performed using a JEOL 3200FS-JEM instrument at 300 kV beam energy. The sample was prepared inside a glovebox by placing a drop of CdSe SNCs in CH_3CN onto a lacey carbon-coated copper grid (Electron Microscopy Science), and excess solution was removed by wicking with a Kimwipe to avoid particle aggregation. Cryo-TEM analysis was conducted using a JEOL-3200FS-JEM instrument at 200 kV beam energy. The aqueous solution of the samples was frozen using liquid nitrogen. SEM micrographs were acquired using a Hitachi S-4700 FESEM at 20 kV. Matrix-assisted laser desorption ionization time of flight mass spectrometry (MALDI-TOF MS) measurements were performed using a Bruker Autoflex equipped with a nitrogen laser.

The PL-QYs of the synthesized PEG-thiolate-coated CdSe SNCs before and after TPP treatment were calculated via a comparison technique using coumarin-30 as a standard fluorophore. Coumarin-30 exhibits UV-Vis absorption maximum at 407 nm and an emission maximum at 482 nm when excited at 380 nm with a QY of 55.3% in acetonitrile.[85] All samples were prepared in DCM and the optical density of the samples was kept to a similar level (~0.08-0.1). The emission data were collected from 350-750 nm and the area of the PL peak was determined between 400-700 nm. The following equation was used to calculate the QY of the CdSe SNCs:[25]

$$QY_{NC} = \left(\frac{E_{NC}/A_{NC}}{E_{STD}/A_{STD}}\right) \times \left(\frac{\eta_{NC}}{\eta_{STD}}\right)^2 \times QY_{STD} \qquad (3.1)$$

Here QY_{NC}, A_{NC}, and E_{NC} represent the calculated quantum yield, measured absorbance, and integrated emission intensity of the CdSe SNCs, respectively. QY_{STD} is

the quantum yield of coumarin-30 and the η_s refer to the refractive indices of the two solvents.

Matrix-assisted laser desorption ionization time of flight mass spectrometry (MALDI-TOF MS) measurements were performed using a Bruker Autoflex equipped with a nitrogen laser. 2-[(2E)-3-(4-tert-butylphenyl)-2-methylprop-2-enylidene]malononitrile (DCTB) was used as the matrix. CdSe nanoclusters were dissolved in DCM and mixed with DCTB in THF (20 nM). Five μL of the freshly prepared matrix solution was mixed with 1 μL of sample, vortexed, and then 2 μL of the mixture was applied to the target and air dried.

3.3.3 Synthesis of PEG_n-Thiolate-Coated CdSe SNCs

Briefly, stock solutions of $CdSO_4$•8/3 H_2O (1M) and Na_2SeSO_3 (0.25 M) were prepared in water. In a 100 mL two-neck round bottom flask 30 mL of nitrogen-purged water was mixed with 0.120 mL $CdSO_4$•8/3 H_2O and the required amount of PEG_n-SH. The reaction mixture was stirred at room temperature under nitrogen for 30 min. Next, 1.0 M NaOH was added dropwise to the reaction mixture under gentle stirring until a stable pH of 11.5 was achieved. The solution was then heated to 30 °C for 5 min with stirring. 0.36 mL of Na_2SeSO_3 was quickly injected and the formation of CdSe SNCs was followed by UV-vis spectroscopy. For PEG_6-thiolate-coated CdSe SNCs final concentrations of the reactants were calculated to be 4 mM $CdSO_4$, 32 mM PEG_6-thiols, and 3 mM Na_2SeSO_3. To prepare different PEG_n-thiolate-coated CdSe SNCs, concentration of Cd and Se precursors was kept identical but amount of PEG_n-thiols were varied: for n = 4, 18, 60, and 150 the amount of PEG_n-thiols used was 32, 32, 48, and 60 mM, respectively.

3.3.4 Purification of PEG_n-thiolate-Coated CdSe SNCs

The PEG_6-thiolate-coated CdSe SNCs were purified by solvent extraction and precipitation. The prepared aqueous nanocluster solution was transferred to a 500 mL separatory funnel. A mixture of DCM and isopropanol (ratio 1.0:0.5) was added to the nanocluster solution and was shaken vigorously. The solution was then allowed to stand in the dark until two distinct layers appeared where the top layer was completely clear and the bottom layer was yellow. The yellow solution was collected and then brought to dryness using a rotary evaporator. The resulting yellow material was then redissolved in a minimum volume of DCM and precipitated by adding hexane. The hexane precipitation was performed at least three times. The solid was then collected by centrifugation, dried under high vacuum, and stored under N_2 in the dark. The dried samples were redissolved in various N_2-purged solvents prior to study. The similar strategy was adopted to purify PEG_n-thiolate-passivated (n= 4-150) CdSe SNCs.

3.3.5 Post-synthetic Surface Modification of PEG_n-thiolate-Coated CdSe SNCs (n = 6 and 18)

The PEG_n-thiolate-coated CdSe SNCs were purified by solvent extraction and precipitation techniques.[86] An aqueous solution of prepared CdSe SNCs was transferred to a 500 mL separatory funnel followed by addition of a mixture of CH_2Cl_2 and isopropanol (1.0:0.5 of CH_2Cl_2 : isopropanaol). The SNCs solution was shaken vigorously and then allowed to stand in the dark until two distinct layers appeared where the top layer was clear and the bottom layer was yellow. The yellow solution was collected and brought to dryness using a rotary evaporator. The resulting yellow material was then redissolved in a minimum volume of CH_2Cl_2 and precipitated with hexane. The

hexane precipitation was performed a minimum of two times. The yellow solid was then collected by centrifugation, dried under high vacuum, and stored under nitrogen in dark.

3.3.6 Synthesis of OLA-capped CdSe SNCs

For 1.6 nm diameter CdSe SNCs synthesis 0.14 g of $CdCl_2$ was added to a 100 mL two-neck round-bottom flask and dissolved in 5 mL of OLA under nitrogen with stirring at 70 ^{0}C. Se-precursor stock solution was prepared by reacting 0.12 g of freshly ground selenium in a 25 mL two-neck round-bottom flask containing 1.57 mL OLA and 430 μL of 1-hexanethiol under nitrogen atmosphere until all selenium dissolved. The Cd-precursor was diluted with 10 mL toluene before addition of Se-precursor. After addition of Se-precursor, the reaction was allowed to stir at 70 ^{0}C for 4 h. The SNC growth was quenched by diluting with 20 mL of toluene. To synthesize larger CdSe SNCs (1.7-2.3 nm diameter) the Se-precursor was injected to Cd-OLA precursor at 100 ^{0}C and the aliquots were removed at specific time points and immediately diluted with toluene to obtain desirable sizes.

3.3.7 Purification of OLA-capped CdSe SNCs

The SNCs were immediately precipitated by dropwise addition of CH_3CN until the solution become cloudy. The SNCs were collected through centrifugation at 7000 rpm for 5 min. This precipitation step was repeated once more and then the resultant bright yellow solid was dissolved in chloroform and centrifuged for a final time to remove insoluble materials, decanted, and the yellow solution containing the OLA-coated CdSe SNCs was evaporated under reduced pressure.

3.3.8 Ligand Exchange Reaction

Purified OLA-capped CdSe SNCs (1.6-2.5 nm diameter) were dissolved in 5.0 mL of nitrogen-purged chloroform to obtain a concentration of 0.25 mM. A 0.3 g of PEG_6-SH was added to OLA-coated CdSe SNCs at room temperature and stirred (~6 h) until a stable band-edge excitonic peak was obtained. The solution was then brought to dryness and the solid was redissolved in a minimum amount of CH_2Cl_2 and precipitated with hexane. The resulting solid was collected by centrifugation. The precipitation step was performed once more to remove excess PEG_6-SH. The soluble PEG_6-thiol-coated CdSe SNCs were characterized by ^1H NMR, MALDI-TOF-MS, and PL analyses to determine the structural properties.

3.4 Results and Discussion

3.4.1 Synthesis and Photophysical Properties of PEG_6-Thiolate-Coated CdSe SNCs

The formation of PEG_6-thiolate-passivated ultra-small CdSe SNCs was monitored through UV-vis absorption spectroscopy over a period of 7 h as illustrated in Figure 3.1 A. Immediately after the addition of freshly prepared Na_2SeSO_3 (1 min), the spectrum showed two broad features, which were a shoulder at ~350 nm and a peak near 390 nm. The intensity of the lowest energy (first absorption) peak continued to grow quickly with concurrent shifting towards higher wavelength. After 30 min, a well-defined absorption peak near 425 nm had developed. Over the course of the next 6.5 h, the 425 nm peak continued to grow and red-shift to 429 nm while improving in sharpness. Over the same 7 h the peak at 350 nm also grew. However, the increase in its intensity was comparably slower than that of the peak at 429 nm. The growth of the SNCs was completed over 7 h,

and after this, no detectable changes in peak intensity and position were observed over a 24 h period.

The aqueous solution of PEG_6-thiolate-coated CdSe SNCs, which displayed a stable absorption peak at 429 nm after 7 h, was analyzed by PL spectroscopy (Figure 3.1 B). The spectrum displayed a broad emission band centered at 550 nm attributable to surface trapped electrons and holes.[14,24] The broad emission property of these PEG_6-thiolate-passivated CdSe SNCs is in agreement with previous literature, where stabilizing ligands such as TOP,[87] TOPO,[25] or a mixture of aliphatic amines and phenyl carboxylate[24] were used as surface passivating ligands.

In order to compare the optical properties with the size of the SNCs obtained at the end of the synthesis, the crude CdSe SNC solution was deposited on a TEM grid and analyzed. Figure 3.2 illustrates a representative TEM image of the SNCs which appear to be aggregated on the TEM grid. This aggregation could be due to the viscous nature of

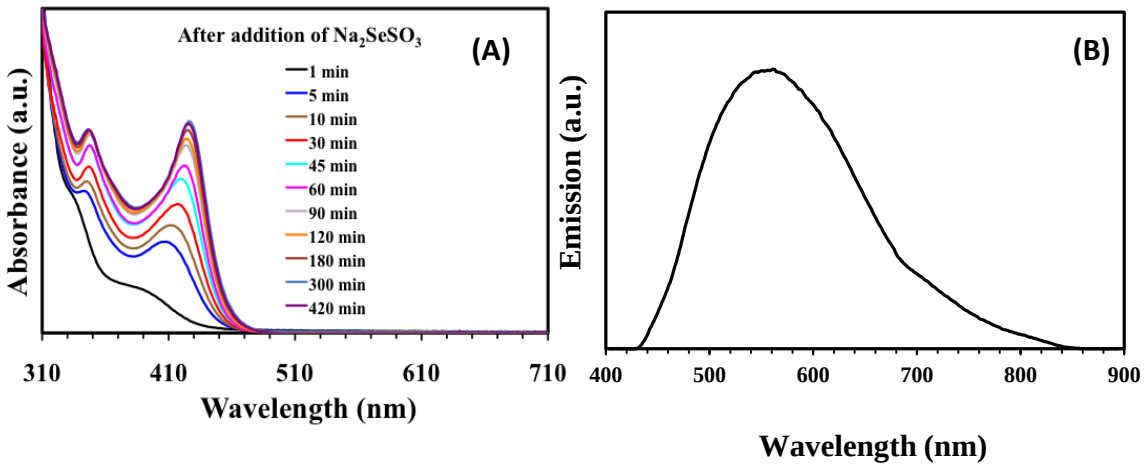

Figure 3.1: (A) Time-dependent absorption spectra following formation of PEG_6-thiolate-coated CdSe SNCs. The maximum intensity of the lowest energy absorption peak was observed ~7 h after Na_2SeSO_3 addition. (B) The emission spectra of the crude reaction mixture after 7 h of reaction. The excitation wavelength was 365 nm.

the PEGs and/or the drying process on the TEM grid. The diameter of the SNCs determined from TEM analysis was 2.0 ± 0.7 nm, which is slightly higher than the size calculated by an empirical formula (1.7 nm) based on the lowest energy absorption peak of the CdSe SNCs.[88] The difference in size could be due to skewing from the aggregation of SNCs as mentioned above.

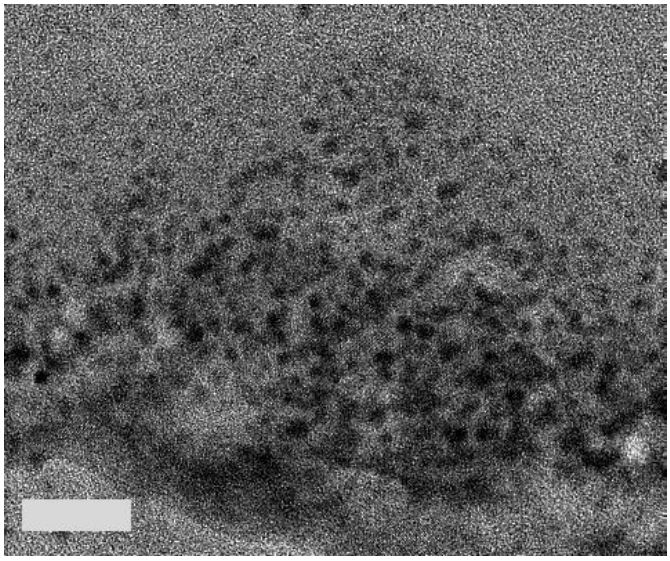

Figure 3.2: TEM image of PEG_6-thiolate-coated CdSe SNCs with lowest energy absorption peak at 429 nm. The NCs are 1.7 nm in diameter. Scale bar is 10 nm.

3.4.2 Purification and Analytical Characterization of PEG_6-thiolate-Coated CdSe SNCs

PEGs are soluble in a wide range of polar and nonpolar organic solvents. Because of their diverse solubility properties it is extremely difficult to remove unbound ligands (e.g., PEG-thiol in solution) from the ligand-coated SNCs (e.g., PEG-thiolate-coated SNCs). However, it is critical to obtain pure SNCs for quantitative characterization of photophysical properties and future applications. Previously, it was shown that ω-functionalized alkylthiolate-coated CdSe QDs can be purified by addition of isopropanol into an aqueous solution of QDs.[53] Following the same protocol we were unable to precipitate our PEG_6-thiolate-coated CdSe SNCs from the aqueous solution. This is likely because PEG_6-thiolate-coated CdSe SNCs are also significantly soluble in isopropanol.

Thus we deduced and demonstrated a unique approach to purify the SNCs, namely a solvent-induced phase transfer followed by an additional precipitation step.

The experimental section outlines in detail the purification procedure of PEG_6-thiolate-coated CdSe SNCs. It is also important to mention that once the SNCs are transferred into organic solvent, further purification steps via solvent-induced precipitation can be performed without causing aggregation of the SNCs. Additionally; the aqueous solution of the solvent-extracted SNCs had a pH of 7.4, whereas the crude reaction mixture had a pH of 11.5. This experimental result suggested that the purified

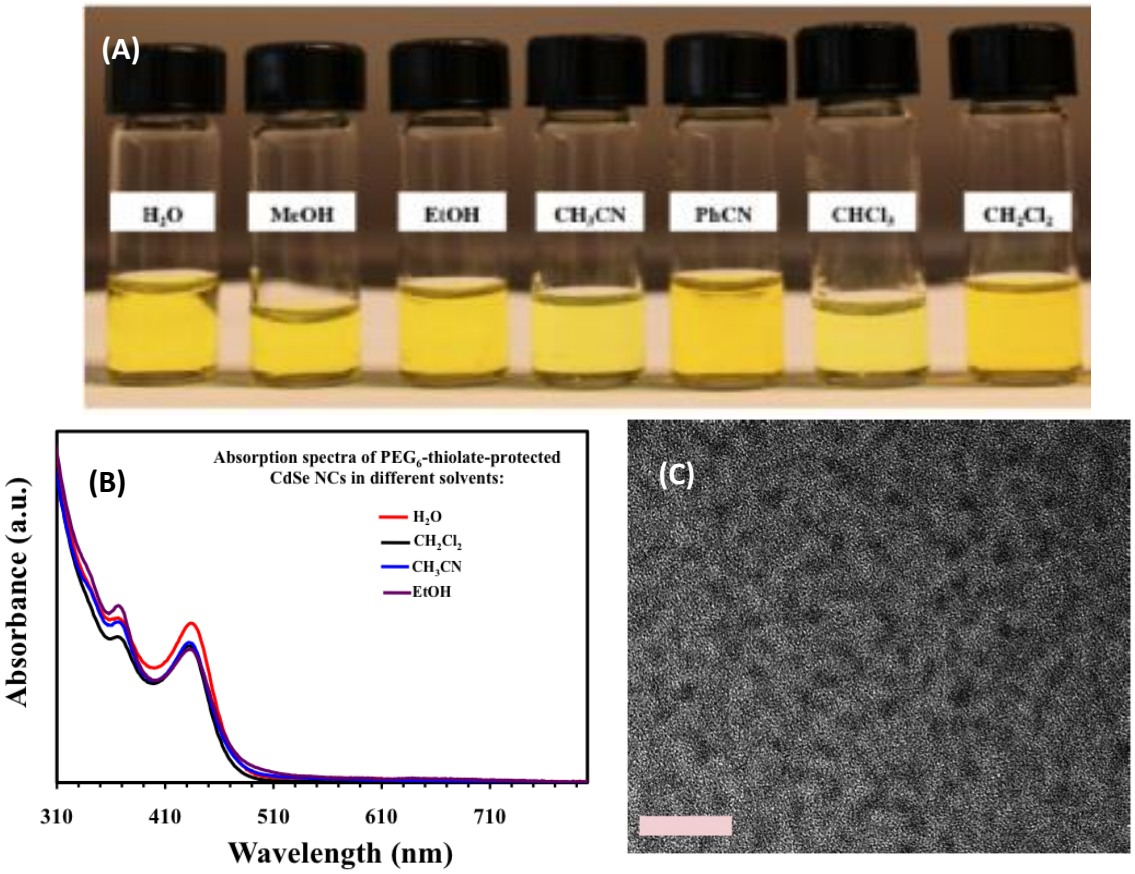

Figure 3.3: (A) Photograph of PEG_6-thiolate-coated CdSe SNCs dissolved in different solvents. (B) Absorption spectra of PEG_6-thiolate-coated CdSe SNCs in different solvents. The lowest energy absorption peak was at 430 nm. (C) TEM image of purified PEG_6-thiolate-coated CdSe SNCs. The SNCs are ~1.6 nm in diameter. Scale bar is 10 nm.

SNCs were free from excess salts and stabilizing ligand. This result is significant in the context of previously reported solvent-induced precipitation techniques where both SNCs and inorganic salt precipitated simultaneously. Our purified PEG_6-thiolate-coated CdSe SNCs are soluble in a wide range of organic solvent as well as in water. Figure 3.3 A shows a photograph of dissolved PEG_6-thiolate coated CdSe SNCs in different solvents taken under normal laboratory light.

The absorption spectra of purified PEG_6-thiolate-coated CdSe SNCs in few selected solvents are shown in Figure 3.3 B. Importantly, no noticeable differences in either peak position or peak shape were observed. For example, the crude PEG_6-thiolate-coated CdSe SNCs (before solvent extraction and purification) displayed a first absorption peak at 429 nm in water and after purification the position of the peak was 430

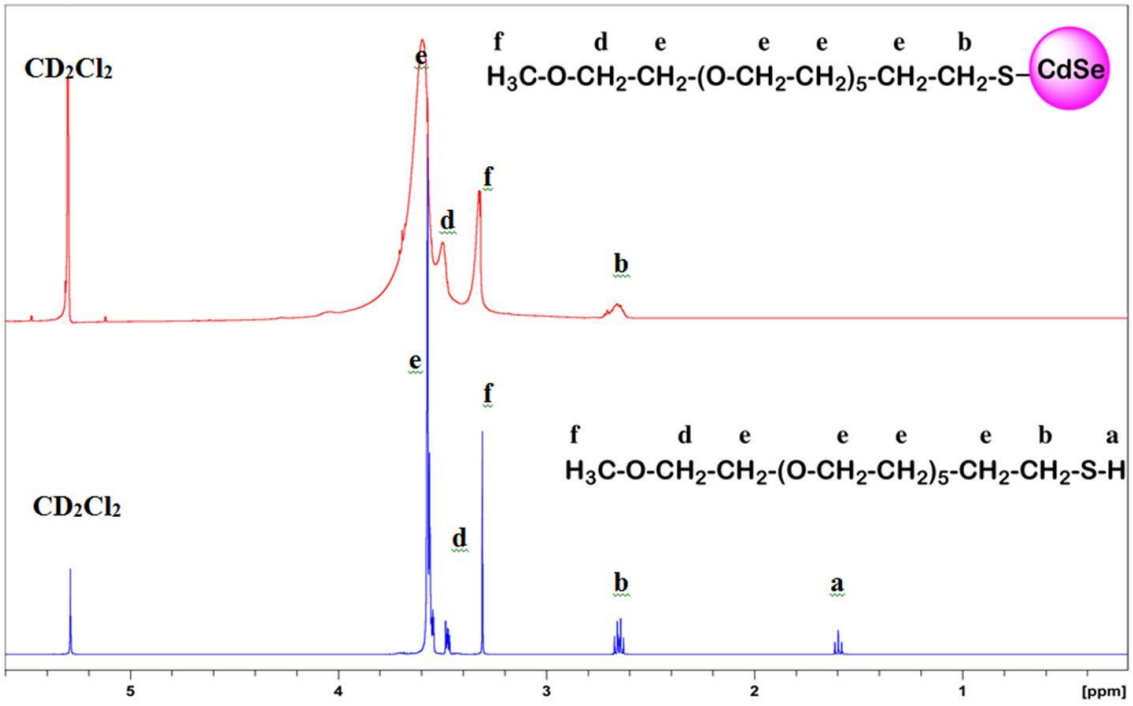

Figure 3.4: Comparison of ^1H NMR of pure PEG_6-thiol (lower panel) and purified PEG_6-thiolate-coated CdSe SNCs (upper panel). The spectra were recorded in CD_2Cl_2.

nm. The purified PEG_6-thiolate-coated CdSe SNCs were dissolved in CH_3CN, drop-casted on a TEM grid, and analyzed. Figure 3.3 C illustrates a representative image of the well-dispersed nanoclusters with size of 1.6 ± 0.2 nm and is in good agreement with the size calculated by the empirical formula of 1.7 nm.[70]

As we mentioned before, it is extremely important to obtain pure SNCs in order to properly assess their photophysical properties. Purified PEG_6-thiolate-coated CdSe SNCs were analyzed by ^1H NMR, and the spectrum showed broad peaks in terminal methyl (-CH_3: 3.30 ppm), glycol (-O-CH_2-CH_2: 3.71-3.46 ppm), and methylene protons attached to the sulfur (-S-CH_2: 2.65 ppm) of the PEG_6-thiolate (Figure 3.4). The broad peaks can be attributed to a combination of spin-spin relaxation broadening, dipole broadening, and a distribution of chemical shifts,[89, 90] which is commonly observed for long-chain aliphatic ligands used for surface passivation of SNCs.[24, 91] Additionally, the purified CdSe SNCs were also analyzed by powder X-ray diffraction (XRD). (Appendix B) The diffraction features at 25.4° and 45.7° appeared broad, which indicated the presence of ultra-small CdSe SNCs.[24, 53] The SNC size was 1.7 nm by calculation from the full width at half maximum of the 25.4° peak by the Scherrer formula. Thus the calculated diameter from XRD data is in agreement with the high-resolution TEM analysis of 1.6 nm.

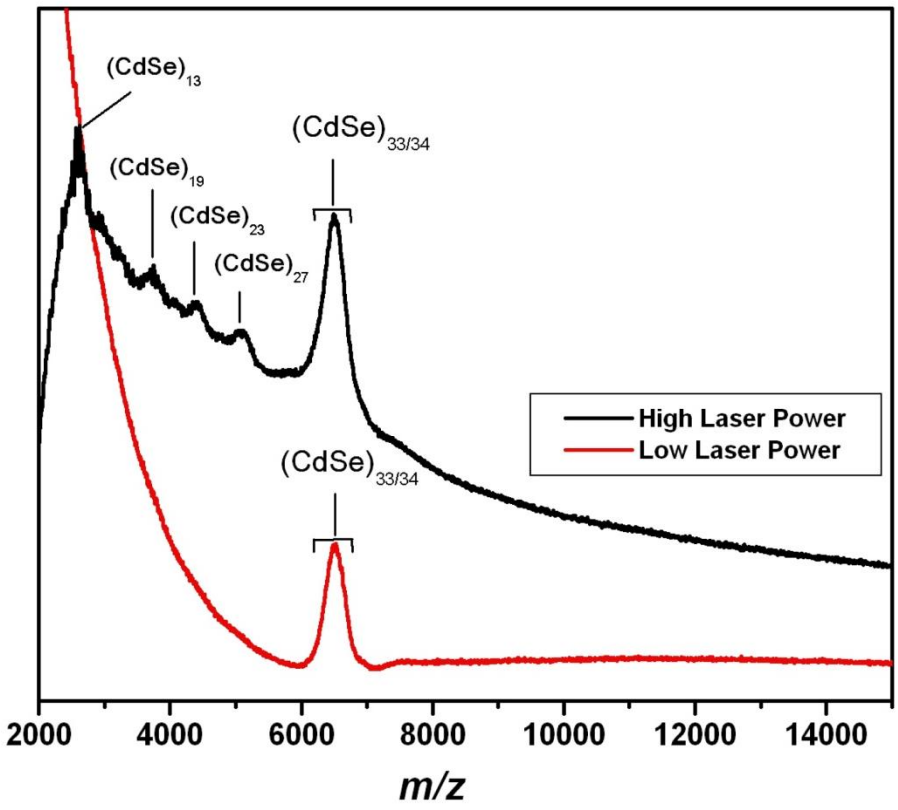

Figure 3.5: MALDI-TOF MS spectra of PEG_6-thiolate-coated CdSe SNCs at two different laser powers. CdSe SNCs were dissolved in DCM and mixed with DCTB matrix in THF with ~ 1:1000 NCs:matrix ratio.

The PEG-thiolate-coated CdSe SNCs were analyzed by MALDI-TOF MS using a DCTB matrix to determine their core composition. DCTB matrix is routinely used for MS analysis of thiolate-coated gold nanoparticles to determine their composition.[92, 93] The mass spectra in Figure 3.5 show detailed information about the core composition of purified PEG_6-thiolate-coated CdSe SNCs. The spectra obtained at low laser power exhibited a sharp peak centered at m/z 6505.1 which corresponds to the $(CdSe)_{34}$ crystalline core (calculated m/z = 6506.6). The slight broadness of the peak likely indicates the presence of a contribution from a $(CdSe)_{33}$ core along with the $(CdSe)_{34}$ core.

At higher laser power the peak at m/z 6505.1 became more intense along with the appearance of few other low-mass peaks. The positions of the these peaks corresponds to $(CdSe)_{27}$, $(CdSe)_{23}$, $(CdSe)_{19}$, and $(CdSe)_{13}$ cores. This suggests that the $(CdSe)_{33}$ and $(CdSe)_{34}$ cores underwent fragmentation at high laser power.[79] The presence of $(CdSe)_{19}$ and $(CdSe)_{13}$ cores also suggested that CdSe nanoclusters with specific core compositions of $(CdSe)_{13}$, $(CdSe)_{19}$, $(CdSe)_{33}$, and $(CdSe)_{34}$ possess high stability.[81] Beside fragmentation to $(CdSe)_{19}$ and $(CdSe)_{13}$ cores at high laser power and increased peak sharpness at m/z 6505.1, no low intensity higher-mass peaks were observed. Therefore, it is clearly evident from MALDI-TOF MS analysis that our samples contained predominantly $(CdSe)_{33/34}$ cores. Since thiolate is a X-type ligand and only binds with Cd-sites,[94] one would expect that this ligand capped SNC should have stoichiometry core with Cd-rich surface to maintain the overall charge balance. The XPS analysis indeed confirmed that the Cd:Se ratio is 1.35:1.0. However, in the MALDI-TOF-MS analysis we were unable to determine the total mass of the ligand-coated CdSe SNC. This could be due to fragmentation of the Cd-bound thiolate-ligand leaving a core mass of ~6.5 kDa.

Using identical molar ratio of reagents, we also synthesized the longer PEG chain length PEG_{18}-thiolate-coated CdSe SNCs to investigate the ligand effects on the physicochemical and photophysical properties of ultra-small SNCs. Appendix C illustrates the UV-vis and PL spectra, and the TEM image of purified PEG_{18}-thiolate-coated CdSe SNCs. The CdSe SNCs displayed an UV-vis absorption maxima at 424 nm with an average size of 1.6 ± 0.3 nm. Interestingly, even though the TEM analysis showed both PEG_6- and PEG_{18}-thiolate-coated CdSe SNCs were similar in size (1.6 nm in diameter), their corresponding lowest energy UV-vis absorption maxima were 430 and

424 nm, respectively. This 42 meV difference in the energy was hypothesized to be due to the difference in the electronic coupling between SNCs, which is facilitated by the "solvent-like" properties of PEGs, and is explored in great detail in section 3.4.4 of this chapter. Nevertheless, both PEG_6- and PEG_{18} -thiolate-coated CdSe SNCs were used to further investigate the influence of surface ligand chemistry on their emission properties as discussed below.

3.4.3 Modulating the Emission Properties of PEG-Thiolate-Coated CdSe SNCs

In the case of ultrasmall (<2.0 nm diameter) SNCs, most of the atoms are present on the surface. Therefore, any unpassivated surface Cd or Se sites could result in surface trap states, and the SNCs could potentially display trap state emission, as discussed in chapters 1 and 2 of this body of work. Depending on the physicochemical nature of the surface passivating ligands, ultrasmall CdSe SNCs can display either trap state[24, 25] or a combination of band-edge and trap state emission.[14, 24, 25] Even though the PL-QY of long aliphatic ligand-coated CdSe can be as large as 10%, as described above, they are only soluble in organic solvent and therefore incompatible with biological systems. One of the advantages of our PEG-thiolate-coated CdSe SNCs is that they are soluble in aqueous medium, which is ideal for nanobiotechnology applications. However, as mentioned, thiolate not only binds to surface Cd sites leaving Se sites unpassivated, but also significantly quenches the CdSe SNC's PL properties. The quenching of PL emission is expected to be more prominent for SNCs of ultra-small size, because most of their atoms are at the surface and resulting PL properties (broad deep trap) are dominated by surface occupied atoms. In this context, no previous reports of PL-QY of thiolate ligand-coated <2.0 nm CdSe SNCs were available in the literature.[31, 33, 53] Therefore, an additional

modification of the surface of thiolate ligand-coated SNCs through appropriate surface ligand chemistry was hypothesized to produce fluorescent SNCs that could be used for applications such as bioimaging.

Recently, it was reported that PL-QY of 1.5 nm CdSe SNCs passivated with mixed long aliphatic chain containing acids and amines can be enhanced up to 45% from a QY of ~5% through post synthetic treatment with formic acid.[95] In our initial investigation, a similar surface ligand treatment resulted in immediate aggregation of our PEG_6-thiolate-coated CdSe SNCs. This could be due to the presence of formic acid in the reaction mixture that protonates the surface-attached thiolates to thiols, which would detach from the SNC surface resulting in fast aggregation of unpassivated CdSe SNCs.

However, Dolai et al. reported that passivation of surface Se sites of octylamine-coated ~1.6 nm CdSe SNCs with TPP enhanced the PL quantum yield nearly 400%.[79] Through various spectroscopic analyses it was determined that TPP and octylamine were

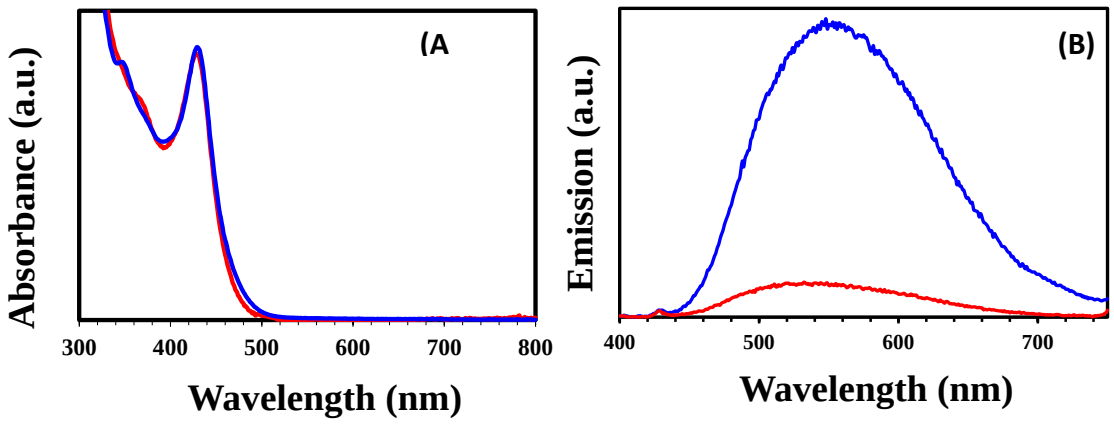

Figure 3.6: The optical properties of PEG_6-thiolate-coated CdSe NCs before (red) and after (blue) TPP treatment: (A) UV-visible absorption and (B) emission spectra. The spectra were taken by dissolving the NCs in DCM. The excitation wavelength for the PL spectra was 365 nm.

attached to surface Se and Cd sites, respectively, similar to the cadmium benzoate discussed in chapter two of this thesis. These resulting mixed ligand-coated CdSe SNCs were only soluble in organic solvents, which hindered their biological application, but we hypothesized that such limitations should not apply to our PEG-coated SNCs. Because of the restriction of TPP solubility to organic solvents, the post-synthetic surface modification of PEG_n-thiolate-coated CdSe SNCs can only be performed in such solvents. Therefore, we performed the TPP treatment of PEG_n-thiolate-coated CdSe SNCs in DCM (see experimental section for details) where both SNCs and TPP are completely soluble. Additionally, mixed TPP- and PEG_n-thiolate-coated CdSe SNCs produced a homogenous solution, which prevented aggregation while the mixed ligand-coated SNCs formed. Figure 3.6 A compares the UV-visible absorption spectrum of purified PEG_6-thiolate-coated CdSe SNCs before and after TPP treatment. No noticeable change in the lower energy absorption peak position or shape was observed. Figure 3.6 B

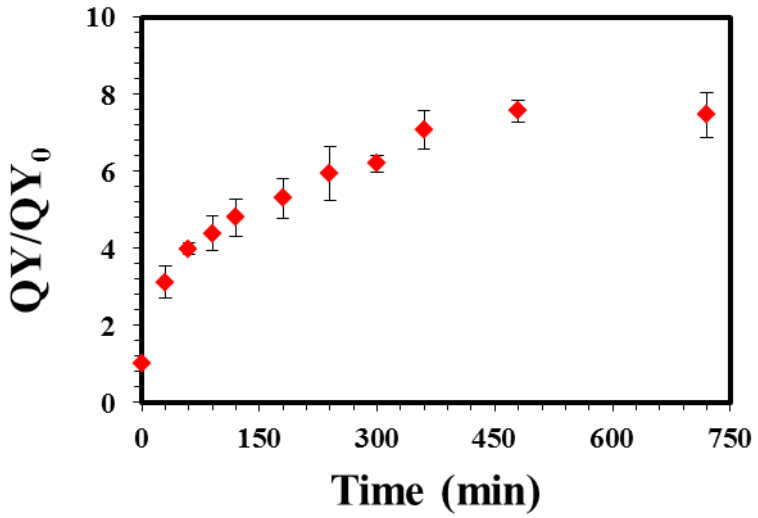

Figure 3.7: Normalized PL-QY of PEG_6-thiolate-coated ultra-small CdSe SNCs in DCM after addition of TPP relative to the initial yield (QY_0).

shows the PL spectra of PEG_6-thiolate-coated and TPP treated PEG_6-thiolate-coated CdSe SNCs, which displayed PL-QYs of ~0.7% and 6.3%, respectively. Although this substantial increase in PL intensity was observed after TPP treatment (Figure 3.6 B) no significant change in the full width at half maximum of the peak was detected.

We also measured the PL-QY of PEG_6-thiolate-coated ultra-small CdSe SNCs after addition of TPP as a function of time, and Figure 3.7 shows that the PL-QY of the SNCs increased monotonically. We hypothesize that the increase of PL-QY is due to the stabilization of nonradiative surface trap states by passivating the surface Se sites as described in chapter 2. Importantly, within 2 h of TPP addition, the PL-QY had increased nearly 500% with a total eight fold increase over 10 h. We believe this could be because initially all Se sites are empty and over the time some sites become capped by TPP, which increases steric hindrance for additional incoming TPP and prevents the adsorption of more ligands on neighboring surface Se sites. Furthermore, TPP binding likely reduced the flexibility of the PEG chains and hindered the TPP entering through the existing PEG-thiolate layer. Therefore, it is suggested that only a modest number of Se sites were passivated with TPP molecules, which did passivate the nonradiative trap states to a certain and increased quantum yield. The purified PEG_6-thiolate-coated CdSe SNCs displayed a PL peak maximum at 547 nm in DCM and after TPP treatment the trap state emission peak of the SNCs shifted to shorter wavelength by ~3 nm over the time of our experiment. Taken together, the increase of PL-QY and slight shift of peak position suggest that the chemical environment at the SNC surface changes upon TPP addition. After the SNCs displayed stable PL intensity, they were purified and no change in the PL peak position or PL-QY was observed. Importantly, the purified SNCs displayed bright

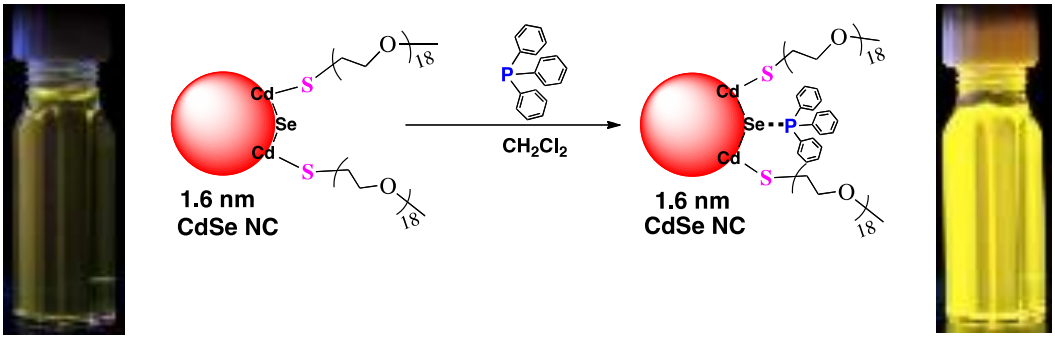

Figure 3.8: Schematic representation of surface modification and emission property of ultra-small CdSe SNCs. The Cd sites were ligated through the sulfur of the PEG-thiolate and the Se sites through the phosphorus of TPP. Both photographs of the UV cell were taken under identical illumination with a 365 nm UV light source. The PEG_6-thiolate-coated CdSe SNCs displayed almost no light emission whereas after TPP treatment they displayed bright yellow color.

yellow color upon illumination with 365 nm UV light (Figure 3.8). The post-synthetic TPP treatment was also performed under identical reaction conditions on the longer PEG_{18}-thiolate-coated CdSe SNCs. These SNCs displayed similar PL-QY enhancement as observed for PEG_6-thiolate-coated CdSe SNCs. Appendix D shows the PL-QY of PEG_{18}-thiolate-coated ultra-small CdSe SNCs after addition of TPP as a function of time.

To test our hypothesis that TPP treatment of PEG_6-thiolate-coated ultra-small CdSe SNCs would result in mixed surface passivation in which TPP was bound to surface Se sites, the TPP-treated purified sample was analyzed by X-ray photoelectron spectroscopy (XPS) (Figure 3.9). The XPS data exhibited peaks at 129.1, 134.2 and 162.1 eV, which are due to P 2p free and CdSe surface-bound TPP, respectively. The peak at 134.2 eV is ~5.1 eV higher than free P and this large difference is because P is datively bound to Se sites.[96] Since TPP forms an L-type of bond with Se atoms, it has the ability to undergo dynamic equilibrium (i.e., an adsorption-desorption process) in solution.

Additionally, the S 2s peak at 162.3 eV was detected. The XPS data suggest that the post synthetic ligand treatment did not displace the original surface passivating ligand (PEG-thiolate) from the CdSe SNC surface. Phosphorous coordinates to surface Se sites of the SNCs, and therefore we would not expect detachment of thiolates because they bind strongly to Cd surface sites. Additionally, Cd $3d_{5/2}$, Cd $3d_{3/2}$, and Se 3d peaks were centered at 404.5, 411.4, and 53.1 eV, respectively. The sharp peak observed in the Cd 3d region and the absence of a peak at ~60 eV indicated that the CdSe SNCs did not contain CdO or SeO_2 on their surface.[96] These XPS data are also important in the context of the

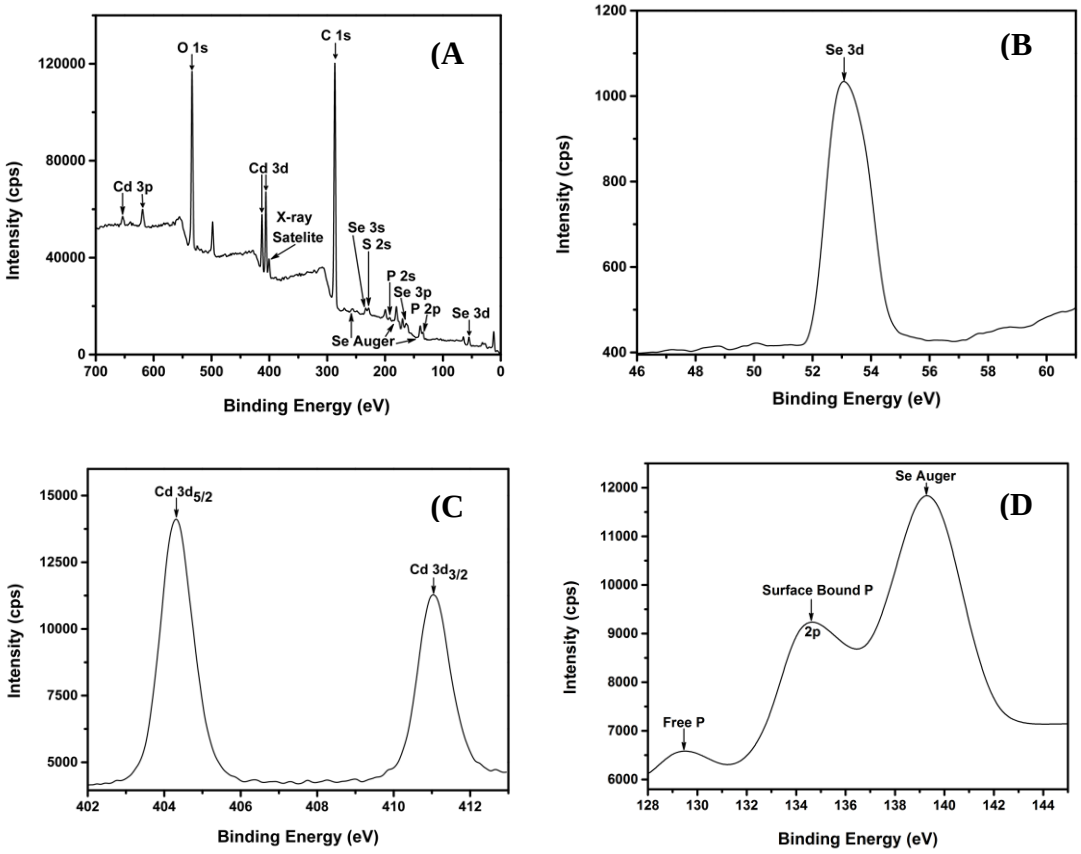

Figure 3.9: (A) XPS survey scan of TPP-treated PEG_6-thiolate-coated CdSe SNCs. High resolution scan of (B) Se 3d region, (C) Cd 3d region, (D) P 2p region. Two P 2p peaks at 129.1 and 134.2 eV are observed due to free TPP and CdSe SNC surface bound TPP, respectively.

post synthetic ligand treatment and purification steps that we have adopted in our synthesis to enhance PL-QY, and they suggest that our procedure is very efficient and the SNCs did not undergo photooxidation.

3.4.4 Importance of Hydrodynamic Radii

Although our SNCs displayed substantial PL-QY and were stable in an aqueous media, the importance of hydrodynamic radii came into question for their future application in nanobiotechnology. Attaching organic fluorophores or fluorescent proteins to biomolecules is commonly used for cellular imaging.[97, 98] These organic dyes and fluorescent proteins have narrow excitation spectral windows and generally undergo fast chemical and photodegradation, which limits their applications in biotechnology. All the above-mentioned drawbacks have been substantially eliminated by using QDs.[8, 50, 99, 100] It was reported that QDs with <6.0 nm hydrodynamic radii have (1) low toxicity in biological systems, (2) faster diffusion into cells, and (3) faster renal clearance.[101] As determined from our TEM analysis the diameter of our CdSe SNC core was ~1.6 nm and the hydrodynamic radii of PEG-ligand is ~0.4 nm as reported in the literature.[82, 102] Therefore, the overall hydrodynamic diameter of the PEG-thiolate-coated CdSe SNCs is ~2.4 nm. This value is much lower than recently reported QDs of ~12 nm[64] which caused increased cytotoxicity and slower renal clearance. Therefore, our TPP-treated PEG_n-thiolate-coated CdSe SNCs are not only soluble in an aqueous medium but are also expected to have all the above-mentioned beneficial characteristics. Furthermore, it is also known that passivated QDs with PEGylated ligands can reduce nonspecific interactions making them a suitable candidate for cellular imaging.[103] Therefore, we have shown as a proof-of-concept that ultrasmall CdSe SNCs can be applied to cellular

imaging by enhancing their physicochemical and photophysical properties, and they could be an alternative for organic fluorophores, fluorescent proteins, or QDs. (cellular imaging data available in Appendix E)

3.4.5 Ligand-mediated Inter-SNC electronic coupling

As shown above, we were able to enhance the solubility and PL-QY of ultra-small (<3.0 nm) CdSe SNCs through surface modification using PEG-thiolate for possible bionanotechnology applications. However, during the course of this study we observed that the transmission electronic microscopy (TEM) analysis showed PEG_6- and PEG_{18}-thiolate-coated CdSe SNCs were 1.6 nm in diameter but their first excitonic peaks were 429 and 424 nm, respectively. The hydrodynamic radii of PEG_6-thiolate-coated CdSe SNCs, determined from dynamic light scattering (DLS) technique, indicated more than two SNCs were connected together in solution. The DLS measurements also suggested

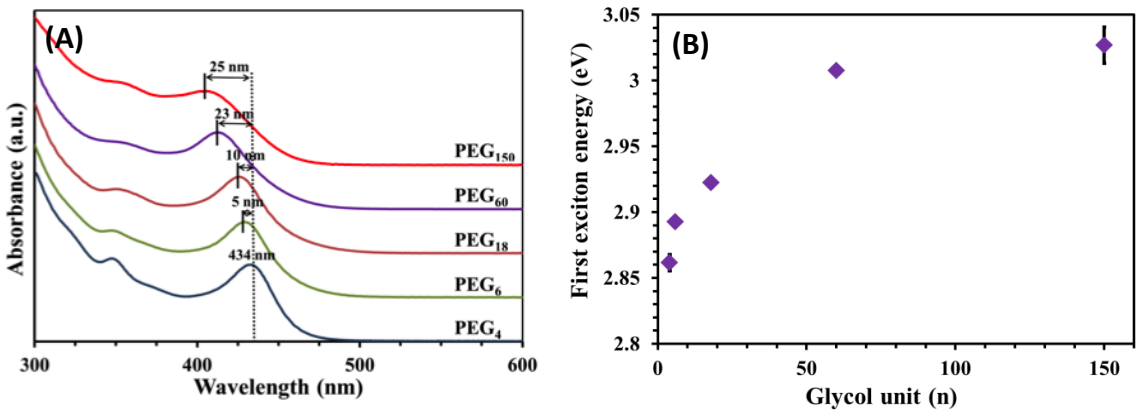

Figure 3.10: (A) Room temperature UV-visible absorption spectra of purified samples of different chain length PEG_n-thiolate-coated CdSe SNCs in CH_2Cl_2. The HRTEM analysis demonstrated that the average size for each-type of PEG_n-thiolate-coated CdSe SNCs were 1.6 nm. The blue shifting of the band-gap excitonic peak position from PEG_4 to PEG_{150} suggested inter-SNC electronic coupling. (B) Excitonic peak energy of different chain length PEG_n-thiolate-coated CdSe SNCs. An ~170 meV difference between first exciton energy of PEG_4 and PEG_{150} was observed in solution, which is defined as coupling energy.

that the PEG_n chains were not fully extended in the solution. Based on these analyses we hypothesized that the 5 nm (30 meV) difference in the excitonic peak position between PEG_6- and PEG_{18}-thiolate-coated CdSe SNCs was controlled by differences in the inter-SNC distance, resulting in better electronic coupling. In order to prove our hypothesis, 1.6 nm diameter CdSe SNCs were synthesized using various chain length PEG_n-thiolates as capping ligands (n = 4, 60, and 150).

3.4.6 PEG-Chain Length Dependent Inter-SNC Coupling.

Various PEG_n-thiolate-coated CdSe SNCs were synthesized and a detailed protocol is provided in the experimental section. Figure 3.10 A illustrates the solution state UV-vis absorption spectra of different chain length PEG-thiolate-coated CdSe SNCs dissolved in CH_2Cl_2. The band-edge excitonic peak was 5 nm blue-shifted as glycol units in the PEG chain was reduced from four to six. By increasing glycol units to 150, a total 20 nm blue shift of the excitonic peak was observed. Therefore a total 25 nm (170 meV) difference in peak position was detected between PEG_4- and PEG_{150}-thiolate-coated CdSe SNCs. We believe this red-shift in the first excitonic peak is due to inter-SNC electronic coupling.

Figure 3.10 B shows the position of the first excitonic energy as a function of glycol unit. We assume no apparent inter-SNC electronic coupling has taken place in solution for PEG_{150}-thiolate-coated CdSe SNCs because the thick dielectric shell of PEG_{150}-thiolate is a good insulator, therefore, the wave function is unable to extend past the long chain PEG-thiolate. Hence, we hypothesize that the change in coupling energy that is observed (up to 170 meV) was solely due to electronic coupling, which was controlled by the inter-SNC spacing. To the best of our knowledge, this is the highest

value reported in literature for an electronic coupling of SNCs in solution.[74, 75] In order for the SNCs to participate in strong electronic coupling, their electron and/or hole wavefunctions are required to expand outside the boundary of the isolated SNC, overlap, and entangle to form a delocalized state which reduces the excitonic band gap (red-shift of the peak position), as discussed in chapters 1 and 2. It is also know that the delocalization kinetic energy of the excitons is higher in strongly confined ultrasmall SNCs than intermediate or weakly confined larger SNCs.[104, 105] Therefore, unlike larger SNCs (>3.0 nm) [5, 55, 62, 63, 67, 70, 74, 75, 106] , at the ultrasmall size regime, the quantum-confined electron and/or hole wave functions could fill the entire SNC core volume more effectively and delocalize to the adjacent SNCs.

Besides inter-SNC electronic coupling, which controls the excitonic peak position for different PEG_n-thiolate-coated CdSe SNCs, other parameters such as SNC core diameter and variable dielectric constant of the PEG-thiolate shell could potentially modulate the peak position. We investigated the potential contribution of these parameters to the dramatic shift of excitonic peak of CdSe SNCs in solution. First, different PEG_n-thiolate-coated CdSe SNCs were analyzed by high-resolution TEM (HRTEM), just as depicted for PEG_6-thiolate-coated CdSe SNCs in Figure 3.2, to determine the core diameter as shown in Figure 3.11. Again, in most cases, we observed aggregation on the TEM grid (because of the drying process), but individual SNCs of both PEG_4- and PEG_{150}-thiolate coating were 1.6 ± 0.2 nm in diameter, which is in agreement with the values we determined previously for either PEG_6- or PEG_{18}-thiolate-coated CdSe SNCs.[86] Interestingly, PEG_4-thiolate-coated CdSe SNCs were present in aggregated states consisting averagely three to four individual SNC (Figure 3.11 A)

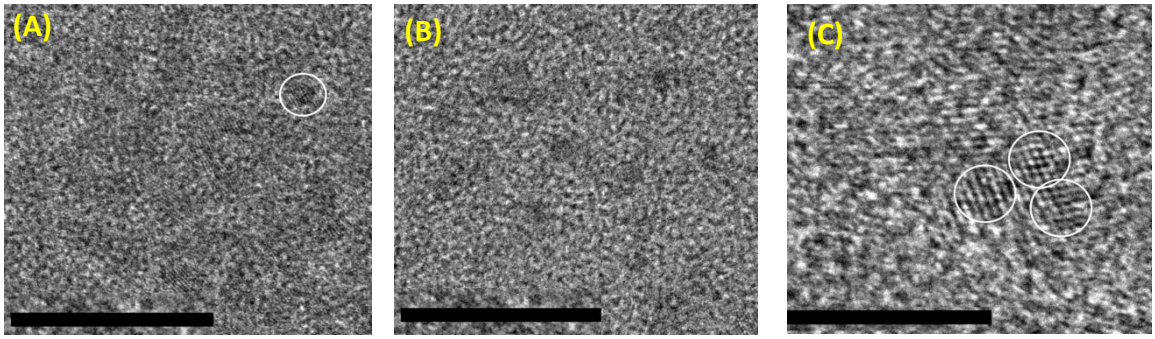

Figure 3.11: HRTEM images of PEG_4- (A) and PEG_{150}- (B) thiolate-coated CdSe SNCs. The circle in (A) shows an isolated SNC with diameter ~1.6 nm. The scale bars are 10 nm. (C) Selected area HRTEM image of PEG_4-thiolate-coated CdSe SNCs demonstrating three individual SNCs were self-assembled. The scale bar is 5 nm.

whereas PEG_{150}-thiolate-coated CdSe SNCs were present as isolated SNCs. Precise determination of the size of these ultrasmall SNCs by conventional TEM is extremely challenging. Therefore, we again attempted the use of matrix-assisted laser desorption ionization time-of-flight mass spectrometry (MALDI-TOF-MS) for further determination of the core mass of PEG_4- and PEG_{18}-thiolate-coated CdSe SNCs using a DCTB matrix. Appendix F illustrates the MALDI-TOF-MS spectra of three different chain length PEG-thiolate-coated CdSe SNCs. The peak at m/z 6505, seen in Figure 3.5 and Appendix F, is evident in all of the samples, corresponds to a stoichiometric $(CdSe)_{34}$ core as described previously. Also, the energy dispersive X-ray spectroscopy (EDS) analysis of PEG_4-thiolate-coated CdSe SNCs confirmed the Cd:Se ratio of 1.33:1.0 (Appendix G) which is consistent with the value of 1.35:1.0 as determined for PEG_6-thiolate-coated CdSe SNCs in Figure 3.9. Therefore, we assume that the overall compositions of the CdSe SNCs coated with different PEG_n-thiolates were nearly identical. As previously mentioned, thiolate is an X-type ligand, and therefore, to maintain the overall charge neutrality of the thiolate-ligand-coated SNCs, the stoichiometrically inorganic core [e.g., $(CdSe)_{34}$] should

be passivated with $Cd(S\text{-}PEG)_2$, which can be referred as a Z-type ligand that attaches to the surface Se ions, similar to cadmium benzoate discussed in chapter 2.[94] Thus, PEG-thiolate-ligand coated CdSe SNCs are expected to be Cd rich. Unfortunately, in the MALDI-TOF-MS analysis we were unable to determine the complete mass of the PEG_n-thiolate-coated CdSe SNCs because of the detachment of the $Cd(S\text{-}PEG)_2$ from the $(CdSe)_{34}$ core. This type of ligand detachment has been observed for thiolate-ligand-coated metal nanocrystals and SNCs during MALDI-TOF-MS analysis.[93, 107] Nevertheless, both structural and compositional analyses suggest that the size and composition of the inorganic core in PEG_n-thioltate-coated CdSe SNCs (n = 4 -150) were identical and therefore blue-shifting of the excitonic peak from n = 4 to 150 cannot be attributed to change in core size, but instead suggests a decrease in inter-SNC electronic coupling.

Though our conventional TEM analysis strongly supports electronic coupling of PEG_4- or PEG_{150}-thiolate-coated CdSe SNCs in solution due to their spatial organization, this analysis is inadequate to determine existence of ordered assembly in solution. We performed Cryo-TEM of PEG_4- or PEG_{150}-thiolate-coated CdSe SNCs as shown in Figure 3.12. The micrograph showed appearance of pearl-necklace type assembly of CdSe SNCs, which are coated with PEG_4-thiolate. An average 0.6 nm inter-SNC spacing was observed in pearl-necklace assembly. This spacing is shorter than twice the length of fully stretched PEG_4-thiols (1.0 nm), but corresponds reasonably well to the expected radius of gyration for PEG polymers in a good solvent.[82] Therefore it is reasonable to propose that SNCs were present in close proximity and this induced strong electronic coupling. The exact nature of the driving force responsible for pearl-necklace assembly in

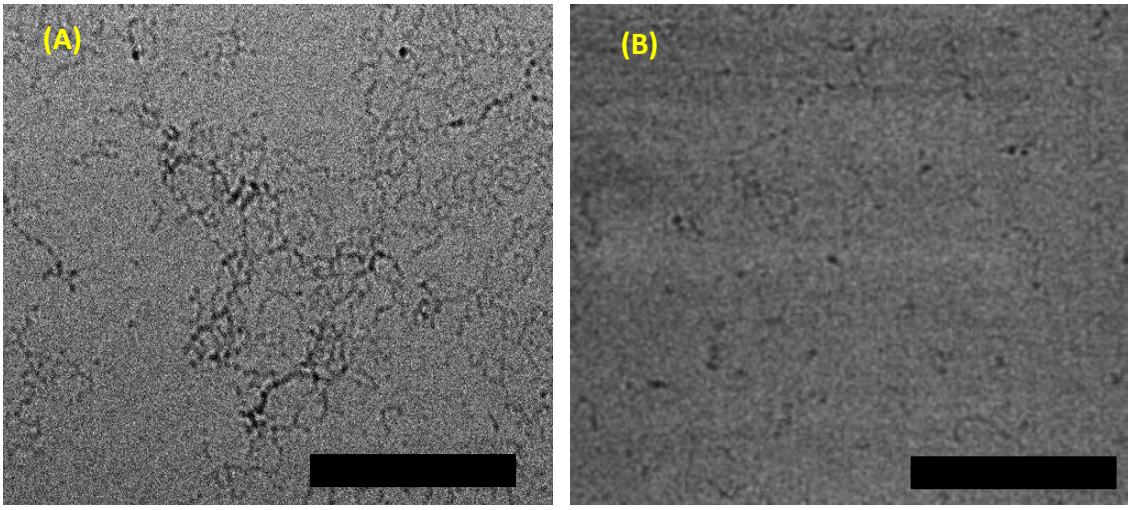

Figure 3.12: Cryo-TEM images of PEG_4- (A) and PEG_{150}- (B) thiolate-coated CdSe SNCs. The aqueous solution of SNCs was frozen by liquid nitrogen inside the cell. The dark black dots are the CdSe SNCs. The images were taken at 200 kV operating voltage. Scale bars are 20 nm.

solution is unknown to us, but is thought to have originated due to the van der Waals forces and dipole-dipole attraction between SNC cores, as observed for thioglycolic acid-capped CdTe SNCs.[108]

Beside the electronic coupling and exciton delocalization inducing red-shift of band-gap exciton peak, an increase in the dielectric constant of the surrounding media could also influence the exciton peak energy (bathochromic shift).[109] Therefore for quantitative determination of the coupling energy, contribution of dielectric constant with a suitable model must be taken into account,[109] which is not within the scope of thesis. However, for a qualitative estimation, absorption spectra of dissolved PEG_6-thiolate-coated CdSe SNCs were collected in three different solvents with varying dielectric constant (ε), dichloromethane (ε = 8.93), ethanol (ε = 24.5), and acetonitrile (ε = 37.5), as shown in Figure 3.13. Importantly, no noticeable change in the peak position was observed. Moreover, a PEG_{150} ligand layer would impose a higher dielectric constant

compared to a PEG_4 ligand layer and under such circumstances we would expect lower energy first exciton peak for PEG_{150}-thiolate-coated CdSe SNCs than PEG_4-thiolate-coated SNCs, however we observed an opposite spectral response (Figure 3.10). Together our experimental data suggest that the dielectric constant has negligible effects on the red-shifts observed for different chain length PEG_n-thiolate-coated CdSe SNCs.

We performed additional experiments to further test our hypothesis that the small hydrodynamic radii and solvent-like properties of the PEG chain facilitate the inter-SNC electronic coupling. It was observed that PEG_6-thiolate-coated CdSe SNCs displayed excellent solution stability and therefore all our remaining investigation is focused on CdSe SNCs that were coated with either PEG_6-thiol or thiolate. Recently Dolai et. al.,[79] reported a synthetic method producing single-sized (1.6 nm in diameter) $(CdSe)_{34}$ SNCs, which were coated with OLA. The long hydrocarbon chain of OLA is insulating in nature, thus no electronic coupling is expected to take place in solution. However, we

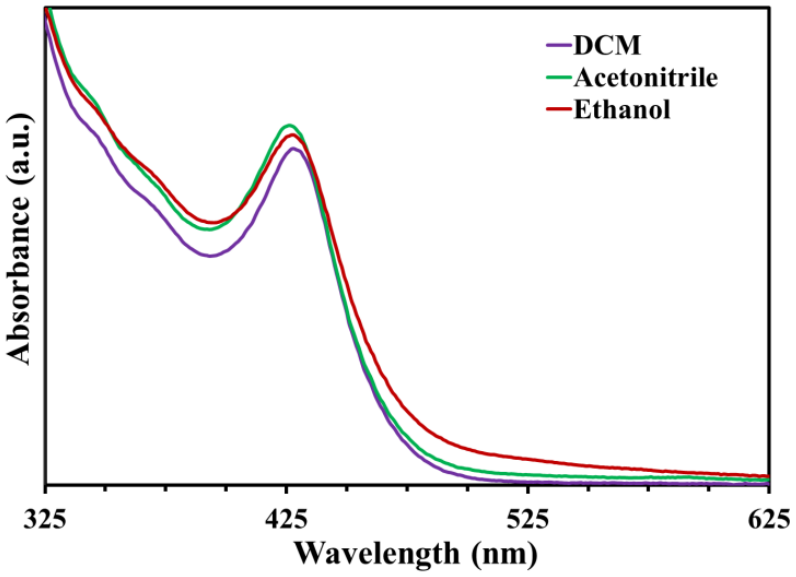

Figure 3.13: Room temperature UV-visible absorption spectra of PEG_6-thiolate-coated CdSe SNCs in different solvent.

hypothesized that if OLAs from the SNC surface were to be replaced by PEG_6-thiols, the spacing between the SNCs will decrease and the solvent-like properties of PEG_6 chain would facilitate electronic coupling. The coupling phenomena can be studied by monitoring the band-edge excitonic peak position using UV-vis absorption spectroscopy, as demonstrated previously in Figure 3.10. The synthesis of OLA-coated 1.6 nm CdSe SNCs, solution phase ligand exchange reaction with PEG_6-thiols, and purification procedure are provided in the experimental section.

Figure 3.14 A illustrates the UV-vis absorption spectra of OLA- and PEG_6-thiol-coated 1.6 nm CdSe SNCs. OLA-coated CdSe SNCs displayed band-edge excitonic peak at 416 nm (2.98 eV), which was 13 nm red-shifted to 429 nm (2.89 eV) upon ligand exchange. An ~90 meV change in the exciton peak energy is feasible when the SNCs participate in electronic coupling, but first it must be confirmed that the ligand exchange

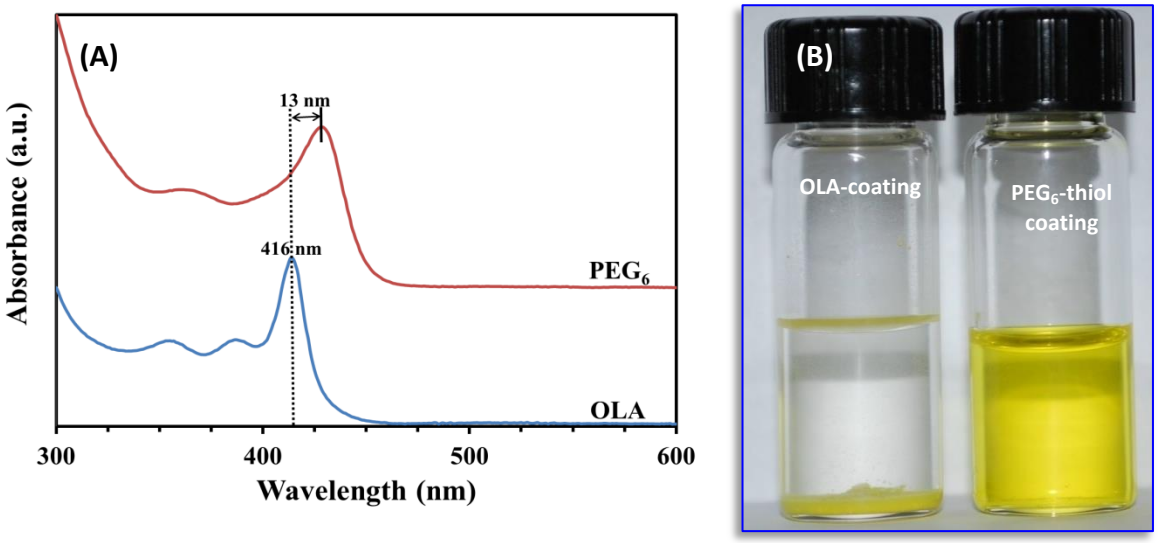

Figure 3.14: (A) UV-visible absorption spectra of OLA-coated 1.6 nm diameter $(CdSe)_{34}$ SNCs (blue) and after ligand exchange reaction with PEG_6-thiols (red). An ~13 nm (90 meV) red shift of the first exciton peak was predominantly due to the increase in the electronic coupling. (B) Variable solubility properties of undissolved OLA-coated CdSe SNCs and dissolved PEG_6-thiol-coated CdSe SNCs in acetonitrile.

procedure was successful and the PEG_6-thiols successfully replaced the OLA ligands, and the change is not simply due to changes of the local dielectric environment caused by the ligand exchange reaction. First, OLA-coated CdSe SNCs are not soluble in acetonitrile whereas after ligand exchange reaction the CdSe SNCs were completely soluble in acetonitrile, suggesting attachment of PEG-thiol to CdSe SNC core surface (Figure 3.14 B). Previously we demonstrated the unique solubility properties of PEG_6-thiolate-coated CdSe SNCs (Figure 3.3 A). Second, the ^{1}H NMR analysis of the purified PEG_6-thiols exchange product indeed confirmed that ~95% of the surface was coated with PEG_6-thiols with some residual OLA present (Figure 3.15) Third, the broadness of the peaks associated to PEG_6-thiols and presence of H-S- proton at ~2.0 ppm suggest that the

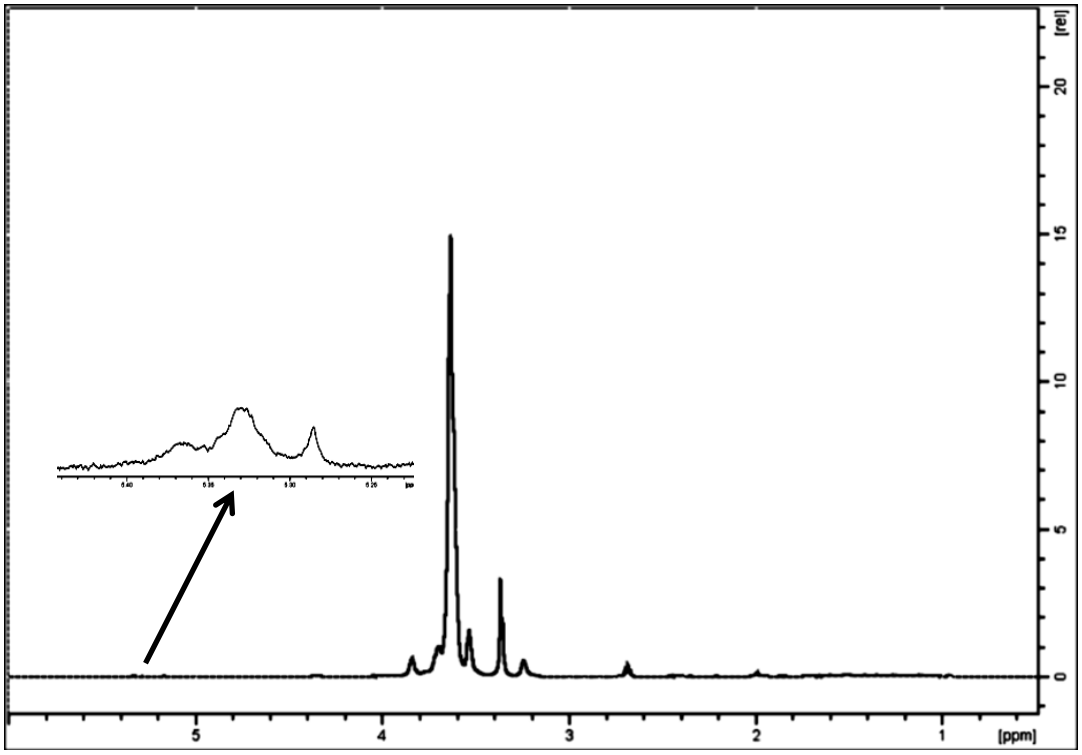

Figure 3.15: ^{1}H spectrum of PEG_6-thiol-coated CdSe SNCs. The ligand exchange reaction on OLA-coated SNCs was conducted with PEG_6-SH. The insert shows zoom OLA double bond region. The spectrum indicates that 95% of the original surface bound OLA ligand was replaced by PEG_6-SH.

PEG_6-thiol was attached to the $(CdSe)_{34}$ SNCs surface as a neutral two electron donor ligand like OLA. Finally, our MALDI-TOF-MS analysis of both OLA- and PEG_6-thiol-coated CdSe SNCs showed similar core mass (Appendix F). This is important in the context of ligand exchange reaction, which could induce the change in the core composition resulting in red-shifting of the band-edge excitonic peak position. Attachment of PEG_6-thiol as a neutral ligand onto the stoichiometric $(CdSe)_{34}$ core also supports the overall charge neutrality of the ligand-coated SNCs.

Lastly, we performed photoluminescence (PL) measurements of the PEG_6-thiol ligand exchange product to confirm our hypothesis that the CdSe SNCs surface was coated with two electrons donor neutral thiols (H-S-PEG_6) and not anionic thiolates (-S-PEG_6). The exchange product showed no change in the band-edge PL intensity as compared to OLA-coated CdSe SNCs (data not shown). Since our exchange reaction was conducted in organic solvent, therefore we would expect that thiol remains protonated and attaches onto CdSe SNCs surface as a neutral ligand rather an anionic ligand. The attachment of thiolate to surface Cd sites should lead to quenching of PL because of the formation of hole traps that prevent radiative recombination of excitons, however, this was not observed in our investigation. All of the above data support the hypothesis that the addition of PEG_6-thiols to an organic solvent solution of OLA-coated CdSe SNCs result in PEG_6-thiol-coated SNCs. The solvent-like properties of PEG lead to strong inter-SNC electronic coupling and display ~90 meV change in the exciton peak energy.

3.4.7 Size Dependent Excitonic Coupling Energy

To investigate size dependent electronic coupling, OLA-coated 1.8 nm to 2.5 nm CdSe SNCs were synthesized according to the procedure described for 1.6 nm SNCs with

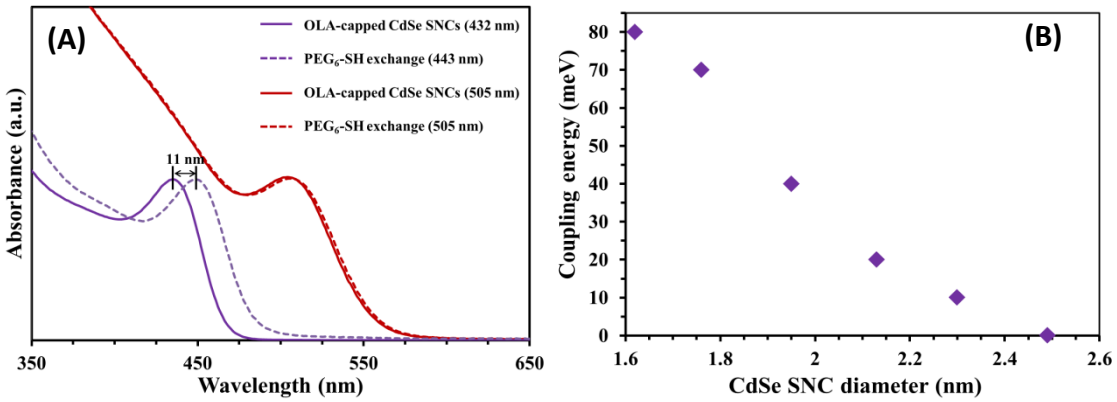

Figure 3.16: (A) UV-visible absorption spectra of OLA-coated 1.8 (purple) and 2.5 nm (red) diameter CdSe SNCs before and after ligand exchange reaction with PEG_6-thiols. An ~11 nm (70 meV) red shift of the first exciton peak for 1.8 nm CdSe SNCs suggested electronic coupling where as such interaction was nearly negligible for 2.5 nm SNCs. (B) Experimentally determined coupling energy as a function of SNC diameter. The coupling energy was measured from UV-visible absorption spectra (Figure 5A and 6A) whereas diameter was calculated from an empirical sizing equation.[1]

slight modification (see experimental section). Ligand exchange reactions were performed in solution to replace original insulating OLA ligands with PEG_6-thiol to reduce the inter-SNC distance and increase the electronic coupling. Figure 3.16 A illustrates the UV-visible absorption spectra of 1.8 and 2.5 nm CdSe SNCs before and after PEG_6-thiol exchange. In the case of the largest CdSe SNC size (2.5 nm in diameter) no noticeable change in the peak position was observed whereas 1.8 and 2.3 nm diameter SNCs displayed 70 and 10 meV coupling energy, respectively (Figure 3.16 B).

According to the mathematic model proposed by Efros and coworkers, the carrier mobility of a SNC solid increases with decreasing SNC size.[110] The mobility of the charge carrier is directly related to the electronic coupling between neighboring SNCs where higher coupling would result in faster mobility. In the case of smaller SNCs, the kinetic energy of the exciton [either electron or hole] is higher than the columbic

interaction energy of an electron-hole pair.[104, 105] Therefore, for smaller SNCs, the exciton wave functions could easily fill the inorganic core volume and leak outside the core boundary compared to larger SNCs. A strong electronic coupling is expected to happen when a large fraction of excitons wavefunctions expand beyond the core boundary, overlap, and entangle with wavefunctions from adjacent SNCs, as discussed in detail in chapters 1 and 2. Previous theoretical reports strongly support our experimental data that stronger electronic coupling would be observed for smaller size SNCs. Therefore, through the use of PEGn-thiolate (n=4-150) and various size OLA-capped CdSe SNCs, we were able to impart solubility, stability, and enhance electronic coupling of SNCs for potential use as crack-free, highly conductive thin-film materials in solid state device fabrication.

3.4.8 Electronic Coupling of CdSe SNC Thin-Films

The ability to display strong electronic coupling of colloidal SNCs has been utilized to design optoelectronic devices. In this context, a solid support is required to assemble the colloidal SNCs in well-ordered thin-films where strong electronic coupling will remain active. In this chapter, we have already demonstrated dissolved PEG_n-thiolate-coated CdSe SNCs in solution displayed electronic coupling because of their pearl-necklace type assembly. In this section we explore the electronic coupling of PEG_n-thiolate-coated CdSe SNCs spin-cast as thin-films (200 nm in thickens) onto glass supports as possible crack-free, highly conductive thin-film materials for solid state device fabrication. In our first investigation, the electronic coupling was studied as a function of annealing temperature using PEG_6-thiolate-coated CdSe SNCs. Even though CdSe SNCs coated with PEG_4-thiolate displayed the highest electronic coupling, the low

boiling point (~150 ^{o}C)[53] of the ligand could volatilize during high temperature annealing, and distort the film morphology including cracking, and also create multiple trap states.[26] To avoid these undesirable structural and electronic changes, we used CdSe SNCs coated with PEG_6-thiolate, which has a higher boiling point (~250 ^{o}C).

Figure 3.17 A illustrates the temperature dependent absorption spectra of CdSe SNC thin-films. Annealing the film caused red-shift of the band-edge excitonic peak. An ~13 nm red-shift was detected at 100 ^{o}C annealing temperature. The change is dramatic as the temperature was raised to 175 ^{o}C where ~70 nm (400 meV) shift observed along with broadening of the band-edge excitonic peak. The broadness of the peak was due to the electronic coupling as reported previously.[30, 32, 34] Increasing the annealing temperature likely caused the trapped solvent molecules inside the film to evaporate and the film to become more compact, leading to decreased inter-SNC spacing and the formation of close-packed solids of CdSe SNCs ("superlattices"). Importantly, the

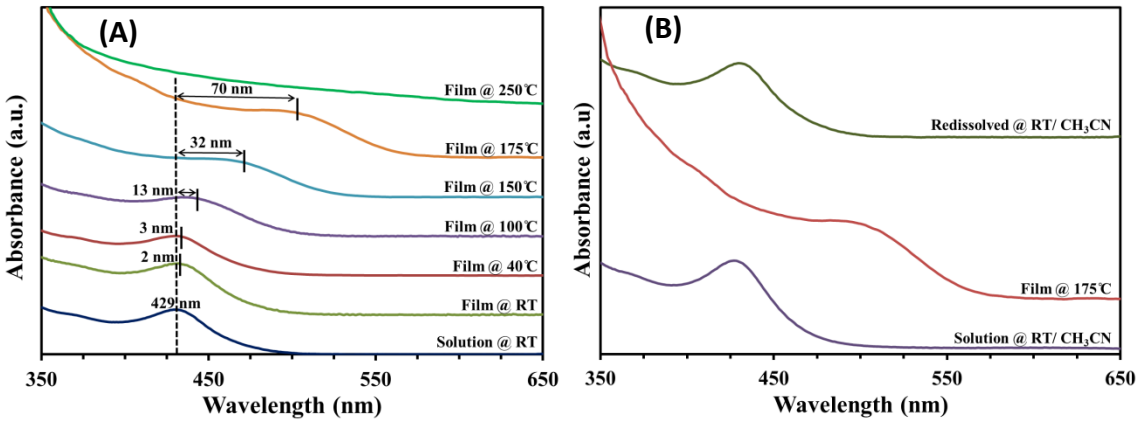

Figure 3.17: (A) UV-visible absorption spectra of (A) PEG_6-thiolate-coated 1.6 nm CdSe SNC films on glass substrates as a function of annealing temperature. (B) UV-visible absorption spectra of PEG_6-thiolate-coated 1.6 nm CdSe SNCs at different physiological conditions: Dissolved SNCs in CH_3CN before film preparation at room temperature (blue), thin-film on glass substrate annealed at 175 ^{o}C (red), and redissolved film in CH_3CN at room temperature (green).

solution phase absorption property of the CdSe SNCs can be regained when the film was redissolved in CH_3CN by sonicating the 175 ^oC-annealed film (Figure 3.17 B). The PEG chains collapse in the dry films, but SNCs maintained their structural integrity. Based on this observation, we overruled the possibility of PEG_6-thiolate desorption from the SNC surface that may influence the inter-SNC interaction as demonstrated before for small molecule or ion coated SNCs.[15, 16, 19, 22, 25-27, 29, 33] In contrast, 100 ^oC annealed film of OLA-coated CdSe SNCs did not display any electronic coupling (Figure 3.18). This experimental result confirms that the long chain aliphatic amines (e.g., OLA) are insulating in nature and do not allow wave functions of neighboring SNC to couple and form an extended delocalize state.

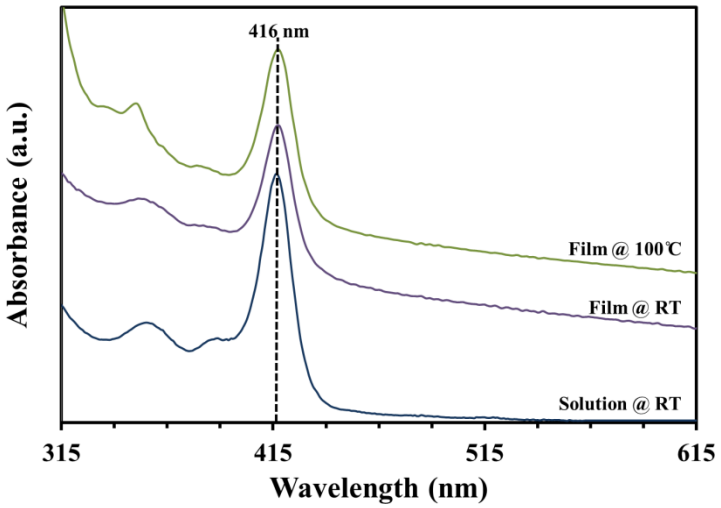

Figure 3.18: UV-visible absorption spectra of OLA-coated 1.6 nm CdSe SNC films on a glass substrate. CdSe SNCs did not display any electronic coupling when they were assembled onto solid surface as a dry film. The electronic coupling was not observed even after annealing at 100 ^oC.

Annealing the film >200 ^oC resulted in the complete disappearance of the band-edge excitonic peak features as similar to bulk CdSe. We believe at higher temperature a permanent structural change occurred where PEG_6-thiolates completely detached from CdSe SNC surface and these ultrasmall SNCs were fused together to form a bulk structure. Therefore, red-shifting and broadening of the excitonic peak <175 ^oC was a

result of strong electronic coupling between SNCs and was not due to any structural changes. Therefore, better ordering of SNCs and a lower potential barrier are critical for stronger quantum mechanical coupling. Additionally we would expect the formation of delocalized and extended states (minibands) in strongly coupled SNCs as similar to one-dimensional superlattice of quantum wells.

The SEM analysis (Figure 3.19) of PEG_6-thiolate-coated 1.6 nm CdSe SNCs films after temperature treatment (175 ^{o}C) showed no apparent change in the morphology

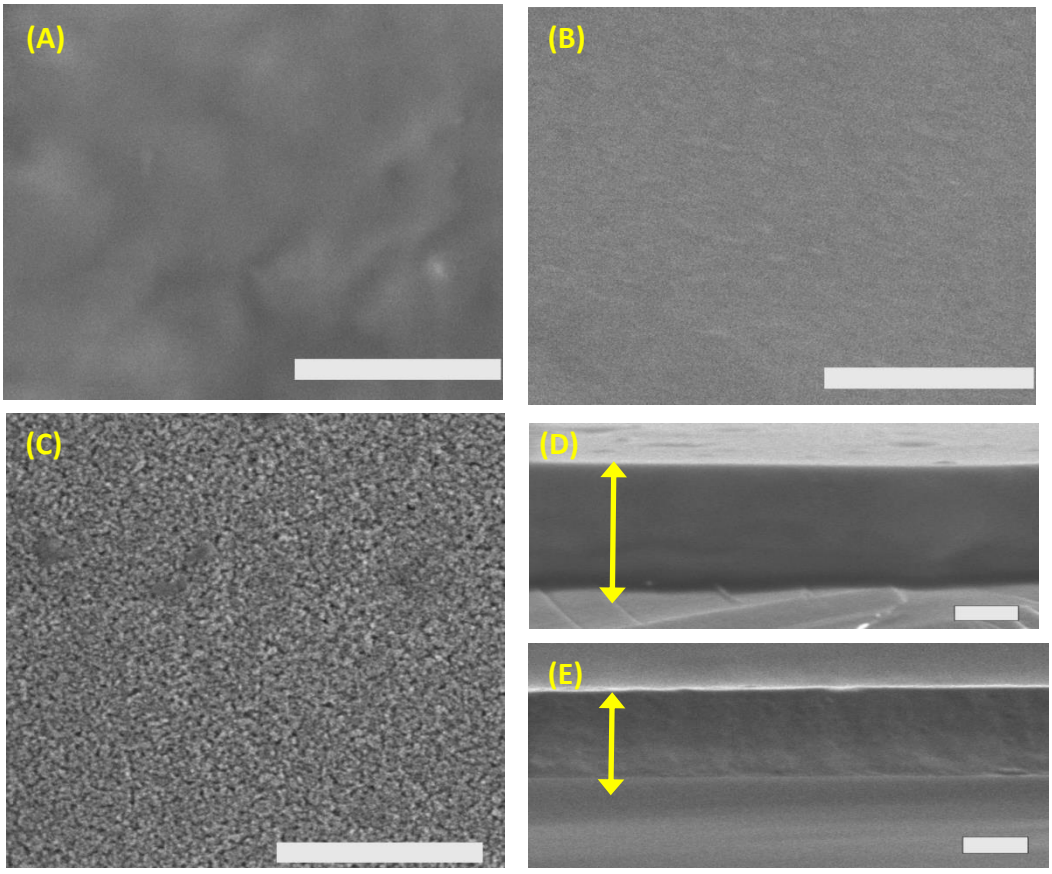

Figure 3.19: SEM images of PEG_6-thiolate-coated 1.6 nm CdSe SNC films as a function of annealing temperature. (A) As prepared film as room temperature, (B) annealing at 175 ^{o}C and annealing at 250 ^{o}C. Scale bars are 500 nm. The thickness (double headed arrow) of SNC films at (D) room temperature and (E) after annealing at 175 ^{o}C. The scale bars are 100 nm.

compared to as prepared films at room temperature. Interestingly, the films were smooth and crack free, similar to structural features that are generally observed in *charged* polymeric thin-films.[54] We also observed that film thickness decreases with heat treatment. The 250 ^{o}C annealed film showed small grain growth. We used the SAXS technique to investigate structural changes such as ordering and average inter-SNC spacing of the PEG_6-thiolate-coated 1.6 nm CdSe SNC films as a function of annealing temperature. Figure 3.20 shows the SAXS profile as a function of annealing temperature. Interestingly, the SAXS peak becomes narrower as the temperature was increased, which suggests that there was either an increase of SNC size or higher ordering of SNCs inside the film.[55] We hypothesize that no change in SNC size took place because the 175 ^{o}C annealed film retained the excitonic band-gap property of 1.6 CdSe SNCs after redissolving in solvent (see Figure 3.17 B). The SEM analysis (Figure 3.19) clearly showed decreased film thickness, therefore we believe that evaporation of trapped solvent inside the film and collapse of the PEG chain, together densify the films

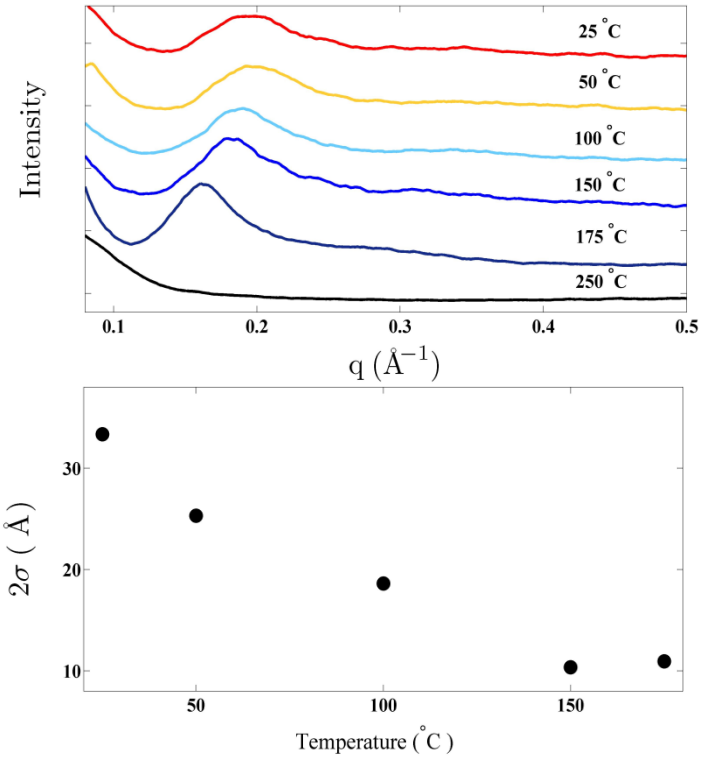

Figure 3.20: (A) SAXS patterns of PEG_6-thiolate-coated 1.6 nm CdSe SNC films as a function of annealing temperature. (B) Relation between SAXS peak width with annealing temperature.

and increase the short-range ordering of SNCs inside the film. Additionally, with increased annealing temperature, the PEG chain could form some ordered structure that would result in an ordered array or periodic SNCs.[56] At 250 ^{o}C annealing temperature, the SAXS peak completely disappeared, which could be due to melting and desorption of the PEG-thiolate ligand from the surface of the CdSe SNCs that resulting in degradation of SNCs.

The strong electronic coupling between PEG-thiolate-coated CdSe SNCs in their solid films demonstrated here has provided several important advantages over existing SNC-based thin-film materials. First, there is no need to perform a solid phase ligand exchange reaction to replace insulating ligands, a process that typically leads to a dramatic structural rearrangement of SNCs and results in the appearance of cracks and voids in the solid films or fusion of SNCs in such films.[16, 29] Second, we can prevent formation of trap states and recombination sites while maintaining strong electronic coupling by using nonvolatile PEG-thiolate ligands instead of using chloride,[19] thiocyanate,[22]sulfide,[23-25] metal chalcogenide complexes,[10, 26-28] tetrafluoroborate,[20, 21] hydrazine,[11, 29] or pyridine.[16] Third, SNCs coated with either small molecules or various ions are susceptible to undergoing fast oxidation even at ambient conditions[16] making processing during device fabrication very difficult. All of these drawbacks can be avoided using our ligand-coated SNCs where the thin-film was almost defect free (cracks or sintering).

3.5 Conclusion

In summary, a simple synthetic and purification procedure has been developed for the synthesis of PEG_n-thiolated-coated ultra-small CdSe SNCs (n=4-150). Along with

optical spectroscopy, high-resolution MALDI-TOF MS analysis has demonstrated the formation of a stoichiometry core of possible composition $(CdSe)_{33/34}$. These PEG_n-thiolate-coated CdSe SNCs showed unusual solubility properties, being readily soluble in a wide array of organic solvents including acetonitrile, ethanol, chlorobenzene, dichloromethane, and chloroform. This unique solubility allowed us to prepare bright yellow light emitting CdSe SNCs through a post synthetic ligand treatment with TPP on PEG_n-thiolated-coated SNCs. The XPS analysis unequivocally proved that the SNC surface is coated with TPP and PEG-thiolate ligands. TPP preferentially bound to the surface Se sites through a dative bond, which reduced the formation of nonradiative trap state formation and enhanced the PL-QY. Because of their aqueous solubility and bright emission properties, the mixed ligand-coated ultra-small CdSe SNCs have the potential to be the next generation of bioimaging materials. In addition, we have also demonstrated that surface ligation with PEG_n-thiolate ligands allowed for controlled band gap tailoring through inter-SNC electronic coupling. This ligand-controlled strong electronic coupling has several potential benefits: (1) The PEG-thiolate-coated CdSe SNCs possess diverse solubility character. Appropriate selection of solvent will allow the preparation of large-scale thin-films with better structural properties such as enhanced homogeneity and less void space, thus eliminating the need to use additional conductive materials to backfill the voids through atomic-layer deposition techniques.[64] Therefore, we could eliminate energy disorder while maintaining strong electronic coupling between SNCs for use in high-performance light-emitting diodes and field-effect transistor fabrication. (2) PEG chains can impart liquid crystalline characteristics to ligand-coated SNCs, which improve the SNCs packing in thin-film. Because of the strong electronic coupling between -

thiolate-coated SNCs, and physical and electrochemical properties of hybrid redox polyethers enable hopping-mediated faster charge transport which enhance their applicability toward electrochromic devices. (3) Current knowledge of electrochemical properties of ligand-coated SNCs is very limited due to fast decomposition during measurement[111] caused by the insulating nature of existing surface ligand coatings. However, strong inter-SNC electronic coupling in organic solvent such as CH_2Cl_2 and CH_3CN would increase the stability of PEG-thiolate-coated CdSe SNCs during the solution-phase electrochemical characterization since the extra charge can delocalize to neighboring SNCs through solvent-like ligand shell and/or be stabilized by "*outer-sphere"* reorganization. Enhanced stability will provide quantitative information about the electrochemical oxidation and reduction potentials of ligand-coated SNCs and therefore enabling the control of the generation and transfer of charge carriers, which should facilitate the design of efficient electronic materials for photovoltaic applications. The latter is the focus of chapter 4.

3.6 References

1. W. W. Yu, L. Qu, W. Guo and X. Peng, *Chem. Mater.*, 2003, 15, 2854-2860.

2. M. L. Steigerwald and L. E. Brus, *Acc. Chem. Res.h*, 1990, 23, 183–188.

3. J. H. Bang and P. V. Kamat, *ACS Nano*, 2009, 3, 1467-1476.

4. J. H. Yu, X. Liu, K. E. Kweon, J. Joo, J. Park, K.-T. Ko, D. W. Lee, S. Shen, K. Tivakornsasithorn, J. S. Son, J.-H. Park, Y.-W. Kim, G. S. Hwang, M. Dobrowolska, J. K. Furdyna and T. Hyeon, *Nat. Mater.*, 2010, 9, 47-53.

5. J.-S. Lee, M. V. Kovalenko, J. Huang, D. S. Chung and D. V. Talapin, *Nat. Nanotechnol.*, 2011, 6, 348-352.

6. K. Tvrdy, P. A. Frantsuzov and P. V. Kamat, *Proc. Natl. Acad. Sci. USA*, 2011, 108, 29-34.

7. A. P. Alivisatos, *Science*, 1996, 271, 933-937.

8. M. Bruchez, M. Moronne, P. Gin, S. Weiss and A. P. Alivisatos, *Science*, 1998, 281, 2013-2016.

9. V. I. Klimov, A. A. Mikhailovsky, S. Xu, A. Malko, J. A. Hollingsworth, C. A. Leatherdale, H.-J. Eisler and M. G. Bawendi, *Science*, 2000, 290, 314-317.

10. C. B. Murray, C. R. Kagan and M. G. Bawendi, *Science*, 1995, 270, 1335-1338.

11. I. n. Robel, M. Kuno and P. V. Kamat, *J. Am. Chem. Soc.*, 2007, 129, 4136-4137.

12. S. Ahn, C. Kim, J. H. Yun, J. Gwak, S. Jeong, B.-H. Ryu and K. Yoon, *J. Phys. Chem. C*, 2010, 114, 8108-8113.

13. Q. Guo, G. M. Ford, W.-C. Yang, B. C. Walker, E. A. Stach, H. W. Hillhouse and R. Agrawal, *J. Am. Chem. Soc.*, 2010, 132, 17384-17386.

14. M. J. Bowers, J. R. McBride and S. J. Rosenthal, *J. Am. Chem. Soc.*, 2005, 127, 15378-15379.

15. M. A. Schreuder, K. Xiao, I. N. Ivanov, S. M. Weiss and S. J. Rosenthal, *Nano Lett.*, 2010, 10, 573-576.

16. R. O. N. Dagani, *C&EN*, 2001, 79, 7-8.

17. S. Dolai, P. Dutta, B. B. Muhoberac, C. D. Irving and R. Sardar, *Chem. Mater.*, 2015, 27, 1057-1070.

18. S. Dolai, P. R. Nimmala, M. Mandal, B. B. Muhoberac, K. Dria, A. Dass and R. Sardar, *Chem. Mater.*, 2013.

19. Y. Yang, Y. Zheng, W. Cao, A. Titov, J. Hyvonen, R. MandersJesse, J. Xue, P. H. Holloway and L. Qian, *Nat Photon*, 2015, 9, 259-266.

20. D. C. Oertel, M. G. Bawendi, A. C. Arango and V. Bulovic, *Appl. Phys. Lett.*, 2005, 87, 213505.

21. M. Drndic, M. V. Jarosz, N. Y. Morgan, M. A. Kastner and M. G. Bawendi, *J. Appl. Phys.*, 2002, 92, 7498-7503.

22. A. Rogalski and M. Razeghi, *OPTO-ELECTRON. REV.*, 1996, 13-30.

23. E. Monroy, F. Omnès and F. Calle, *Semicond. Sci. Technol.*, 2003, 18, R33.

24. B. M. Cossairt and J. S. Owen, *Chem. Mater.*, 2011, 23, 3114-3119.

25. J. C. Newton, K. Ramasamy, M. Mandal, G. K. Joshi, A. Kumbhar and R. Sardar, *J. Phys. Chem. C*, 2012, 116, 4380-4389.

26. B. M. Cossairt, P. Juhas, S. J. L. Billinge and J. S. Owen, *J. Phys. Chem. Lett.*, 2011, 2, 3075-3080.

27. A. D. Dukes, J. R. McBride and S. J. Rosenthal, *Chem. Mater.*, 2010, 22, 6402-6408.

28. M. Zanella, A. Z. Abbasi, A. K. Schaper and W. J. Parak, *J. Phys. Chem. C*, 2010, 114, 6205-6215.

29. F. S. Riehle, R. Bienert, R. Thomann, G. A. Urban and M. Kruger, *Nano Lett.*, 2009, 9, 514-518.

30. E. Kuçur, J. Ziegler and T. Nann, *Small*, 2008, 4, 883-887.

31. Y.-S. Park, A. Dmytruk, I. Dmitruk, A. Kasuya, M. Takeda, N. Ohuchi, Y. Okamoto, N. Kaji, M. Tokeshi and Y. Baba, *ACS Nano*, 2009, 4, 121-128.

32. S. Kudera, M. Zanella, C. Giannini, A. Rizzo, Y. Li, G. Gigli, R. Cingolani, G. Ciccarella, W. Spahl, W. J. Parak and L. Manna, *Adv. Mater.*, 2007, 19, 548-552.

33. Y.-S. Park, A. Dmytruk, I. Dmitruk, A. Kasuya, Y. Okamoto, N. Kaji, M. Tokeshi and Y. Baba, *J. Phys. Chem. C*, 2010, 114, 18834-18840.

34. Q. Yu and C.-Y. Liu, *J. Phys. Chem. C*, 2009, 113, 12766-12771.

35. C. M. Evans, A. M. Love and E. A. Weiss, *J. Am. Chem. Soc.*, 2012, 134, 17298-17305.

36. C. Landes, M. Braun, C. Burda and M. A. El-Sayed, *Nano Lett.*, 2001, 1, 667-670.

37. C. M. Evans, L. Guo, J. J. Peterson, S. Maccagnano-Zacher and T. D. Krauss, *Nano Lett.*, 2008, 8, 2896-2899.

38. E. E. Lees, T.-L. Nguyen, A. H. A. Clayton and P. Mulvaney, *ACS Nano*, 2009, 3, 1121-1128.

39. J. T. Siy, E. M. Brauser and M. H. Bartl, *Chem. Commun*, 2011, 47, 364-366.

40. D. V. Talapin, J.-S. Lee, M. V. Kovalenko and E. V. Shevchenko, *Chem. Rev.* , 2009, 110, 389-458.

41. K. Yu, M. Z. Hu, R. Wang, M. L. Piolet, M. Frotey, M. B. Zaman, X. Wu, D. M. Leek, Y. Tao, D. Wilkinson and C. Li, *J. Phys. Chem. C*, 2010, 114, 3329-3339.

42. A. J. Morris-Cohen, M. T. Frederick, G. D. Lilly, E. A. McArthur and E. A. Weiss, *J. Phys. Chem. Lett.*, 2010, 1, 1078–1081.

43. Y. C. Cao and J. Wang, *J. Am. Chem. Soc.*, 2004, 126, 14336-14337.

44. Z. A. Peng and X. Peng, *J. Am. Chem. Soc.*, 2000, 123, 183-184.

45. F. Wang, R. Tang, J. L. F. Kao, S. D. Dingman and W. E. Buhro, *J. Am. Chem. Soc.*, 2009, 131, 4983-4994.

46. D. V. Talapin, A. L. Rogach, A. Kornowski, M. Haase and H. Weller, *Nano Lett.*, 2001, 1, 207-211.

47. H. Kloust, C. Schmidtke, J.-P. Merkl, A. Feld, T. Schotten, U. E. A. Fittschen, M. Gehring, J. Ostermann, E. Poselt and H. Weller, *J. Phys. Chem. C*, 2013, 117, 23244-23250.

48. W. W. Yu, E. Chang, J. C. Falkner, J. Zhang, A. M. Al-Somali, C. M. Sayes, J. Johns, R. Drezek and V. L. Colvin, *J. Am. Chem. Soc.*, 2007, 129, 2871-2879.

49. O. Carion, B. Mahler, T. Pons and B. Dubertret, *Nat. Protocols*, 2007, 2, 2383-2390.

50. I. L. Medintz, H. T. Uyeda, E. R. Goldman and H. Mattoussi, *Nat. Mater.*, 2005, 4, 435-446.

51. A. Chakraborty, A. R. Maity and N. R. Jana, *RSC Adv.*, 2014, 4, 10434-10438.

52. S. F. Wuister, C. de Mello Doneg√° and A. Meijerink, *J. Phys. Chem. B*, 2004, 108, 17393-17397.

53. A. L. Rogach, A. Kornowski, M. Gao, A. Eychmueller and H. Weller, *J. Phys. Chem. B*, 1999, 103, 3065-3069.

54. C. L. Choi and A. P. Alivisatos, *Annu. Rev. Phys. Chem.*, 2010, 61, 369-389.

55. J. M. Luther, M. Law, Q. Song, C. L. Perkins, M. C. Beard and A. J. Nozik, *ACS Nano*, 2008, 2, 271-280.

56. M. Law, J. M. Luther, Q. Song, B. K. Hughes, C. L. Perkins and A. J. Nozik, *J. Am. Chem. Soc.*, 2008, 130, 5974-5985.

57. D. H. Webber and R. L. Brutchey, *J. Am. Chem. Soc.*, 2011, 134, 1085-1092.

58. D. Yu, C. Wang and P. Guyot-Sionnest, *Science*, 2003, 300, 1277-1280.

59. Z. M. Norman, N. C. Anderson and J. S. Owen, *ACS Nano*, 2014, 8, 7513-7521.

60. E. L. Rosen, R. Buonsanti, A. Llordes, A. M. Sawvel, D. J. Milliron and B. A. Helms, *Angew. Chem. Int.*, 2012, 51, 684-689.

61. A. Dong, X. Ye, J. Chen, Y. Kang, T. Gordon, J. M. Kikkawa and C. B. Murray, *J. Am. Chem. Soc.*, 2010, 133, 998-1006.

62. A. T. Fafarman, W.-k. Koh, B. T. Diroll, D. K. Kim, D.-K. Ko, S. J. Oh, X. Ye, V. Doan-Nguyen, M. R. Crump, D. C. Reifsnyder, C. B. Murray and C. R. Kagan, *J. Am. Chem. Soc.*, 2011, 133, 15753-15761.

63. A. Nag, M. V. Kovalenko, J.-S. Lee, W. Liu, B. Spokoyny and D. V. Talapin, *J. Am. Chem. Soc.*, 2011, 133, 10612-10620.

64. Y. Liu, J. Tolentino, M. Gibbs, R. Ihly, C. L. Perkins, Y. Liu, N. Crawford, J. C. Hemminger and M. Law, *Nano Lett.*, 2013, 13, 1578-1587.

65. H. Zhang, B. Hu, L. Sun, R. Hovden, F. W. Wise, D. A. Muller and R. D. Robinson, *Nano Lett.*, 2011, 11, 5356-5361.

66. R. W. Crisp, J. N. Schrauben, M. C. Beard, J. M. Luther and J. C. Johnson, *Nano Lett.*, 2013, 13, 4862-4869.

67. M. V. Kovalenko, M. Scheele and D. V. Talapin, *Science*, 2009, 324, 1417-1420.

68. K. J. Williams, W. A. Tisdale, K. S. Leschkies, G. Haugstad, D. J. Norris, E. S. Aydil and X. Y. Zhu, *ACS Nano*, 2009, 3, 1532-1538.

69. D. V. Talapin and C. B. Murray, *Science*, 2005, 310, 86-89.

70. O. I. Micic, S. P. Ahrenkiel and A. J. Nozik, *Appl. Phys. Lett.*, 2001, 78, 4022-4024.

71. M. C. Beard, G. M. Turner, J. E. Murphy, O. I. Micic, M. C. Hanna, A. J. Nozik and C. A. Schmuttenmaer, *Nano Lett.*, 2003, 3, 1695-1699.

72. G. W. Bryant and W. Jaskolski, *Phys. E*, 2002, 13, 293-296.

73. J.-H. Choi, A. T. Fafarman, S. J. Oh, D.-K. Ko, D. K. Kim, B. T. Diroll, S. Muramoto, J. G. Gillen, C. B. Murray and C. R. Kagan, *Nano Lett.*, 2012, 12, 2631-2638.

74. R. Koole, P. Liljeroth, C. de Mello Donegá, D. Vanmaekelbergh and A. Meijerink, *J. Am. Chem. Soc.*, 2006, 128, 10436-10441.

75. Y. Liang, J. E. Thorne and B. A. Parkinson, *Langmuir*, 2012, 28, 11072-11077.

76. M. B. Teunis, S. Dolai and R. Sardar, *Langmuir*, 2014, 30, 7851-7858.

77. R. Sardar, K. Lawrence, M. Johnson, S. Dolai and A. Kumbhar, *Nanoscale*, 2015.

78. K. E. Knowles, D. B. Tice, E. A. McArthur, G. C. Solomon and E. A. Weiss, *J. Am. Chem. Soc.*, 2009, 132, 1041-1050.

79. S. Dolai, P. R. Nimmala, M. Mandal, B. B. Muhoberac, K. Dria, A. Dass and R. Sardar, *Chem. Mater.*, 2014, 26, 1278-1285.

80. S. M. Harrell, J. R. McBride and S. J. Rosenthal, *Chem. Mater.*, 2013, 25, 1199-1210.

81. A. Kasuya, R. Sivamohan, Y. A. Barnakov, I. M. Dmitruk, T. Nirasawa, V. R. Romanyuk, V. Kumar, S. V. Mamykin, K. Tohji, B. Jeyadevan, K. Shinoda, T. Kudo, O. Terasaki, Z. Liu, R. V. Belosludov, V. Sundararajan and Y. Kawazoe, *Nat. Mater.*, 2004, 3, 99-102.

82. M. E. Williams, H. Masui, J. W. Long, J. Malik and R. W. Murray, *J. Am. Chem. Soc.*, 1997, 119, 1997-2005.

83. J. W. Long, I. K. Kim and R. W. Murray, *J. Am. Chem. Soc.*, 1997, 119, 11510-11515.

84. A. W. Snow and E. E. Foos, *Synthesis*, 2003, 4, 509-512.

85. S. Senthilkumar, S. Nath and H. Pal, *Photochem. Photobiol.*, 2004, 80, 104-111.

86. K. Lawrence, S. Dolai, Y.-H. Lin, A. Dass and R. Sardar, *RSC Adv.*, 2014, 4, 30742-30753.

87. R. Jose, Z. Zhelev, R. Bakalova, Y. Baba and M. Ishikawa, *Appl. Phys. Lett.*, 2006, 89, 013115-013113.

88. J. Jasieniak, L. Smith, J. v. Embden, P. Mulvaney and M. Califano, *J. Phys. Chem. C*, 2009, 113, 19468-19474.

89. A. Badia, L. Demers, L. Dickinson, F. G. Morin, R. B. Lennox and L. Reven, *J. Am. Chem. Soc.*, 1997, 119, 11104-11105.

90. M. J. Hostetler, J. E. Wingate, C.-J. Zhong, J. E. Harris, R. W. Vachet, M. R. Clark, J. D. Londono, S. J. Green, J. J. Stokes, G. D. Wignall, G. L. Glish, M. D. Porter, N. D. Evans and R. W. Murray, *Langmuir*, 1998, 14, 17-30.

91. Q. Dai, N. Xiao, J. Ning, C. Li, D. Li, B. Zou, W. W. Yu, S. Kan, H. Chen, B. Liu and G. Zou, *J. Phys. Chem. C*, 2008, 112, 7567-7571.

92. A. Dass, *J. Am. Chem. Soc.*, 2009, 131, 11666-11667.

93. A. Dass, A. Stevenson, G. R. Dubay, J. B. Tracy and R. W. Murray, *J. Am. Chem. Soc.*, 2008, 130, 5940-5946.

94. N. C. Anderson, M. P. Hendricks, J. J. Choi and J. S. Owen, *J. Am. Chem. Soc.*, 2013, 135, 18536-18548.

95. T. E. Rosson, S. M. Claiborne, J. R. McBride, B. S. Stratton and S. J. Rosenthal, *J. Am. Chem. Soc.*, 2012, 134, 8006-8009.

96. J. E. B. Katari, V. L. Colvin and A. P. Alivisatos, *J. Phys. Chem.* 1994, 98, 4109–4117.

97. T. Ried, A. Baldini, T. C. Rand and D. C. Ward, *Proc. Natl. Acad. Sci. USA*, 1992, 89, 1388-1392.

98. E. Schrock, S. d. Manoir, T. Veldman, B. Schoell, J. Wienberg, M. A. Ferguson-Smith, Y. Ning, D. H. Ledbetter, I. Bar-Am, D. Soenksen, Y. Garini and T. Ried, *Science*, 1996, 273, 494-497.

99. W. C. W. Chan and S. Nie, *Science*, 1998, 281, 2016-2018.

100. X. Michalet, F. F. Pinaud, L. A. Bentolila, J. M. Tsay, S. Doose, J. J. Li, G. Sundaresan, A. M. Wu, S. S. Gambhir and S. Weiss, *Science*, 2005, 307, 538-544.

101. H. Soo Choi, W. Liu, P. Misra, E. Tanaka, J. P. Zimmer, B. Itty Ipe, M. G. Bawendi and J. V. Frangioni, *Nat. Biotechnol.*, 2007, 25, 1165-1170.

102. M. E. Williams and R. W. Murray, *Chem. Mater.*, 1998, 10, 3603-3610.

103. E. L. Bentzen, I. D. Tomlinson, J. Mason, P. Gresch, M. R. Warnement, D. Wright, E. Sanders-Bush, R. Blakely and S. J. Rosenthal, *Bioconjugate Chem.*, 2005, 16, 1488-1494.

104. L. E. Brus, *J. Chem. Phys*, 1983, 79, 5566-5571.

105. M. T. Frederick, V. A. Amin, L. C. Cass and E. A. Weiss, *Nano Lett.*, 2011, 11, 5455-5460.

106. C. A. Leatherdale, C. R. Kagan, N. Y. Morgan, S. A. Empedocles, M. A. Kastner and M. G. Bawendi, *Phys. Rev. B*, 2000, 62, 2669-2680.

107. J. J. Gaumet, G. A. Khitrov and G. F. Strouse, *Nano Lett.*, 2002, 2, 375-379.

108. Z. Tang, N. A. Kotov and M. Giersig, *Science*, 2002, 297, 237-240.

109. C. A. Leatherdale and M. G. Bawendi, *Phys. Rev. B*, 2001, 63, 165315-165316.

110. A. Shabaev, A. L. Efros and A. L. Efros, *Nano Lett.*, 2013, 13, 5454-5461.

111. M. Amelia, C. Lincheneau, S. Silvi and A. Credi, *Chem. Soc. Rev.*, 2012, 41, 5728-5743.

3.7 Appendices

Appendix A: Synthesis of PEGn-thiols

Synthesis of PEG-thiols. Different chain length PEG_n-thiols (n = 6 and 18) were synthesized according to the literature procedure[1] with modification.

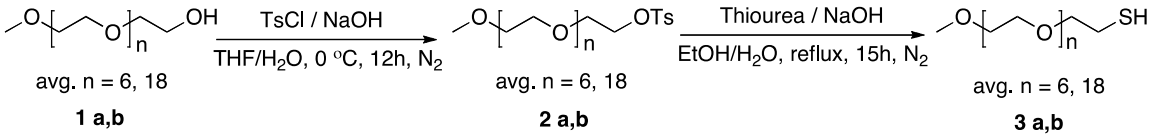

1. Synthesis of Poly(ethylene glycol)-methyl ether-*p*-toluene sulfonate (MeO-PEG_6-OTs) 2a. In a 250 mL two-neck round bottom flask, 20 g (67.48 mmol) of Poly(ethylene glycol)-monomethyl ether (MeO-PEG_6-OH, M_n = 350, **1a**) was dissolved in 25 mL THF and stirred for 20 min under ice-cold condition. In another flask, 3.42 g (85.5 mmol) of NaOH was dissolved in 25 mL distilled water. The NaOH solution was slowly added to **1a** under ice-cold condition. Separately, *p*-Toluene sulfonyl chloride (13 g, 68.18 mmol) was dissolved in 50 mL THF and added drop-wise via a dropping funnel to the reaction mixture at ice-cold condition for a time period of 30 min under N_2 atmosphere. The temperature of the reaction mixture was maintained between 0-10 ^{0}C for an additional 30 min and then left to warm up slowly to room temperature while stirring. After stirring at room temperature for 12 h, the crude reaction mixture was transferred to a separatory funnel and washed with EtOAc (3 X 100 mL). Organic layers were collected and washed with distilled water and brine solution, and then dried over anhydrous Na_2SO_4. Solvent was then removed by rotatory evaporator to yield the product **2a** as colorless viscous liquid. Yield: ~24 g (79 %). ^{1}H NMR (500 MHz, $CDCl_3$) δ ppm: 2.43 (3H, s); 3.36 (3H,

s); 3.52-3.68 (22H, m); 4.13-4.15 (2H, t); 7.32-7.34 (2H, d); 7.77-7.79 (2H, d). ^{13}C NMR (125 MHz, $CDCl_3$) δ ppm: 21.62, 59.0, 68.65, 69.25, 70.50, 70.55, 70.59, 70.72, 71.92, 127.96, 129.81, 133.01, 144.77. ESI-MS (m/z): 336 (n=3), 380.2 (n=4), 424.3 (n=5), 468.3 (n=6), 512.3 (n=7), 556.3 (n=8), 597.3 (n=9), 641.3 (n=10), 685.5 (n=11); where n = number of $–CH_2$-CH_2-O- repeat unit. Under identical molar ratios of reagents and exactly similar reaction conditions, **2b** was synthesized from **1b**.

2. Synthesis of Poly(ethylene glycol)-methyl ether-thiol (MeO-PEG$_6$-SH) 3a. In a 250 mL two-neck round bottom flask, 10 g (22.2 mmol) of MeO-PEG$_6$-OTs and 2.5 g (33.3 mmol) thiourea were dissolved in 100 mL anhydrous EtOH and the reaction mixture was allowed to reflux under N_2 atmosphere for 12 h. Next, 1.4 g (35 mmol) of NaOH was dissolved in 20 mL distilled water and added to the reaction mixture. The reaction mixture was then cycled with vacuum and argon for three times and refluxed for 3h. After cooling down the reaction mixture to room temperature, ethanol was evaporated using a rotary evaporator then diluted with 100 mL of distilled water, and acidified with 0.5 (M) HCl to pH ~3. The product was collected using DCM (3 X 50 mL), which was again washed with water, dried over anhydrous Na_2SO_4, and solvent was evaporated to yield the MeO-PEG$_6$-thiol (**3a**) as colorless viscous liquid. Yield: 7.95 g (86%). ^{1}H NMR (500 MHz, $CDCl_3$) δ ppm: 1.16-1.58 (1H, t); 2.64-2.68 (2H, m); 3.34 (3H, s); 3.48-3.65 (22H, m). ^{13}C NMR (125 MHz, $CDCl_3$) δ ppm: 24.24, 58.99, 70.2, 70.48, 70.50, 70.55, 70.60, 71.90, 72.84. ESI-MS (m/z): 267.1 (n=3), 311.3 (n=4), 355.2 (n=5), 399.3 (n=6), 443.3 (n=7), 487.2 (n=8), 531.3 (n=9), 575.3 (n=10); where n = number of $–CH_2$-CH_2-O- repeat unit. Under identical molar ratios of reagents and exactly similar reaction conditions, **3b** was synthesized from **2b**.

Appendix B: Powder XRD of Purified PEG_6-Thiolate-Coated CdSe SNCs

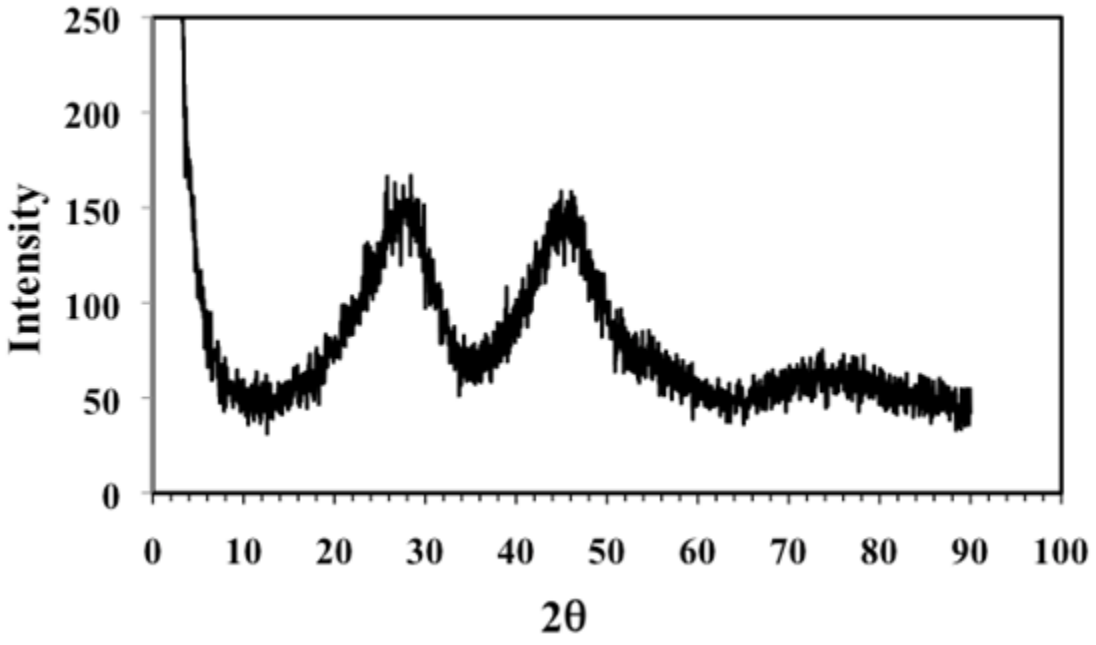

The diffraction features at 25.4° and 45.7° appeared broad, which indicated the presence of ultra-small CdSe0 SNCs.[2,3]

Appendix C: Optical Spectroscopy and TEM Analysis of PEG_{18}-Thiolate-Coated CdSe SNCs

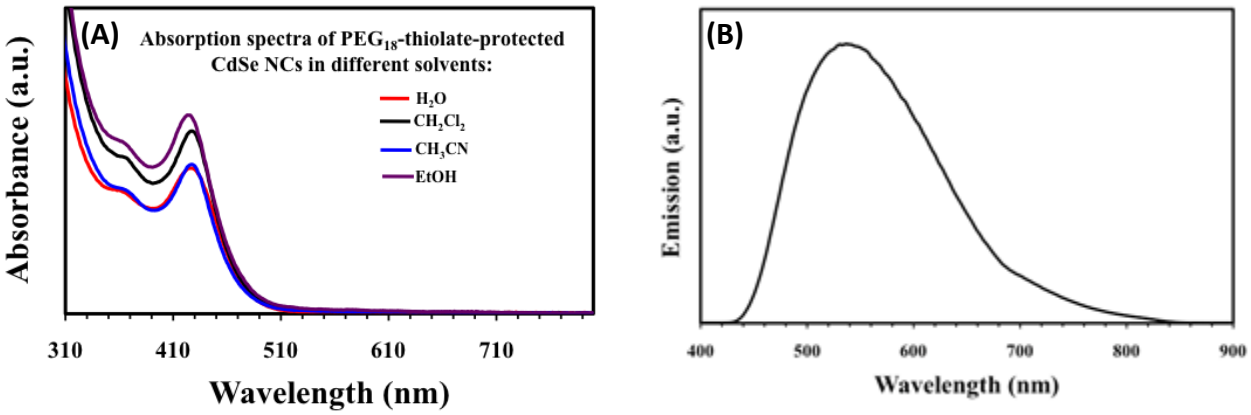

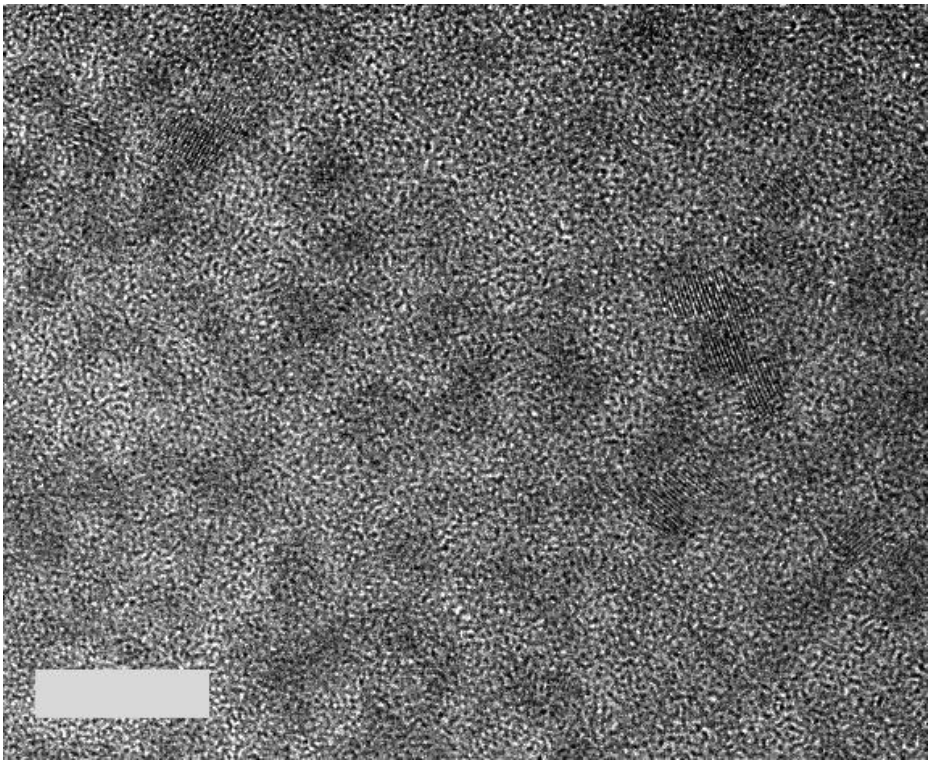

A) Absorption spectra of purified PEG_{18}-thiolate-coated CdSe SNCs in different solvent. (B) PL spectrum of purified PEG_{18}-thiolate-coated CdSe SNCs in CH_2Cl_2, and (C) TEM images of PEG_{18}-thiolate-coated CdSe NCs after phase transfer and purification. Scale bar is 10 nm.

Appendix D: Normalized PL QY of PEG_{18}-Thiolate-Coated CdSe SNCs

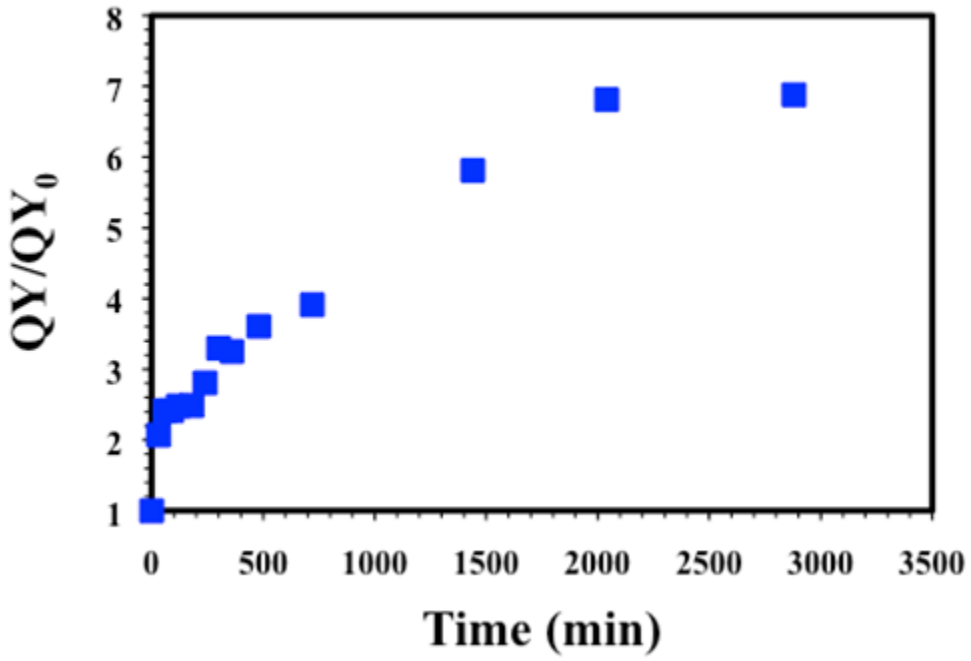

Normalized PL QY of PEG_{18}-thiolate-coated CdSe SNCs in DCM after addition of TPP.

Appendix E: Cellular Imaging

In our initial *in vitro* investigation, the shorter chain length (PEG_6) thiolate ligand-coated bright yellow CdSe SNCs were used for imaging studies. We used green fluorescent protein-transfected fibroblast cells, which displayed green PL highlighting cellular structures upon light excitation. Differential interference contrast (DIC) micrographs showed that the SNCs aggregated around the cell membranes (Figure below) and no SNC fluorescence emission was observed outlining specific internal cellular structures. This could be because the high hydrophobicity of TPP did not allow SNC penetration through the cell membranes even though the SNC surface was coated with PEG-thiolate ligands. The small fraction of SNCs entered inside the cell lost their fluorescent properties either due to aggregation or detachment of TPP during the diffusion through cell membranes. TPP extends out from the SNC surface nearly 0.6 nm (ChemBioDraw 3D) and the PEG_6 shell thickness is approximately 0.4 nm.[4,5] Thus, the hydrophobic character of TPP dominated the hydrophilic character of the PEG-thiolate resulting in a high probability of TPP detachment.

In order to further investigate potential cell membrane penetration, the longer chain length PEG_{18}-thiolate was used to overcome the hydrophobic character imposed by TPP on the mixed ligand-coated CdSe SNCs. The PL properties of TPP-treated PEG_{18}-thiolate-coated CdSe SNCs exhibited the same QY as those coated with PEG_6 thiolate. Thus we investigated the cellular uptake ability of the fibroblast cells for TPP-treated PEG_{18}-thiolate-coated CdSe SNCs. The figure below illustrates the DIC image in which SNCs were asymmetrically aggregated around the cell nucleus as reported by

others in the literature.[6,7] However, individual non-aggregated CdSe SNCs inside the cell were not observed in the DIC analysis due to the limitations in magnification and resolution of the confocal microscope. Nevertheless, the fluorescence image shows that the CdSe SNCs were well dispersed inside the fibroblast cell. We also used these transfected cells to monitor survival for a period of up to 5 days in the presence of NCs. Most importantly, the fluorescence properties of TPP-treated PEG_{18}-thiolate-coated CdSe SNCs inside the cell did not degrade for a period of five days. The green fluorescent protein-transfected fibroblast cells after incubated with mixed TPP- and PEG_{18}-thiolate-coated CdSe SNCs for five days were further incubated with 200 µL of LIVE/DEAD viability stock solution (Invitrogen Co, USA) for 40 min at 30 ^{o}C. The cells were then rinsed with PBS buffer followed by imaging with a Confocal EPI microscopy. After counting cells displayed green and red fluorescent, which represented live and dead cells, respectively. These experimental data are very significant and suggest that more than 95% cells were alive upon incubation with our mixed ligand-coated CdSe SNCs even after 5 days of incubation. This result is important in the context of the enhanced stability of CdSe SNCs versus other fluorescent labels as well as the specific stability of the metal-thiolate bond inside the cell. We believe two factors played an important role in the cell survival when the PEG_{18}-thiolate-coated CdSe SNCs were used for intracellular imaging studies: (1) the moderately long chain PEG-thiolate coating was able to reduce the cytotoxicity of CdSe SNCs by preventing leakage of toxic metal ions (i.e., Cd^{2+}), and (2) only ~ 34 Cd are present per SNCs reducing leakage of ions into their cellular surroundings in comparison with traditionally used QDs which contained hundreds of metal ions in their core.

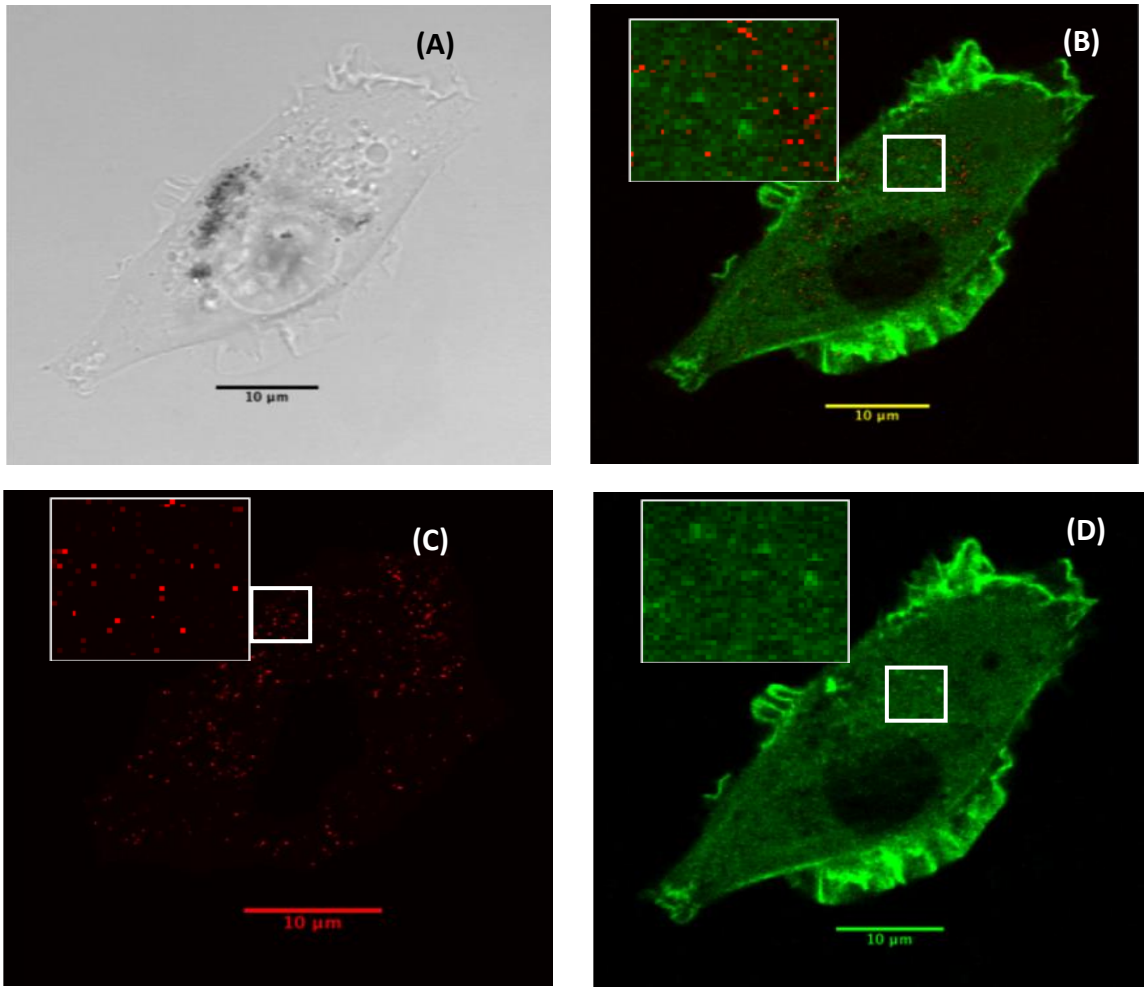

(A) Representative DIC image of a green fluorescence protein transfected fibroblast cell incubated with ~100 nM TPP-treated PEG_{18}-thiolate-coated CdSe SNCs as described in the experimental section, (B) merged SNCs and green fluorescence protein transfected cell (C) SNCs with green fluorescent background removed, and (D) transfected cell before SNC treatment. The inserts in B-D show expanded regions of the cell as marked by the white square box. Close examination of the fluorescence in C shows that the SNCs penetrate the outer cell membranes, but not the nuclear membrane, which totally lacks fluorescence from SNC. The SNCs are red not yellow because of the wavelength filter used. A coverslip was placed on top of the disk to restrict the cell movement during the addition of the CdSe SNC solution.

Appendix F: MALDI-TOF-MS Spectra

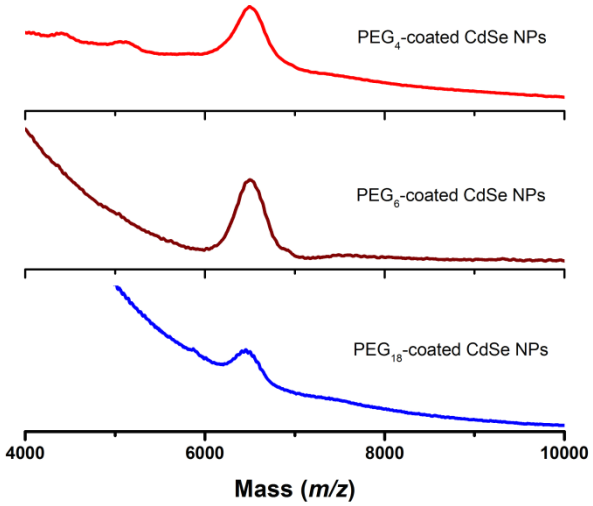

MALDI-TOF-MS spectra of PEG_4- (red) PEG_6- (red), and PEG_{150}- (green) thiolate-coated CdSe SNCs. CdSe SNCs were dissolved in CH_2Cl_2 and mixed with DCTB matrix in THF with 1:1000 SNCs : matrix ratio.

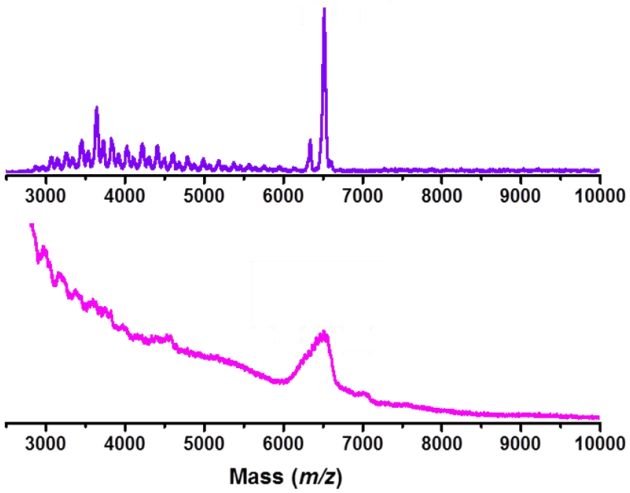

MALDI-TOF-MS spectra of OLA-(blue) and PEG_6-thiol (purple) -coated 1.6 nm CdSe SNCs. The highest intensity peak at m/z 6505 indicate $(CdSe)_{34}$ core composition.

Appendix G: EDS Spectrum of 1.6 nm diameter, PEG_4-thiolate-coated CdSe SNCs

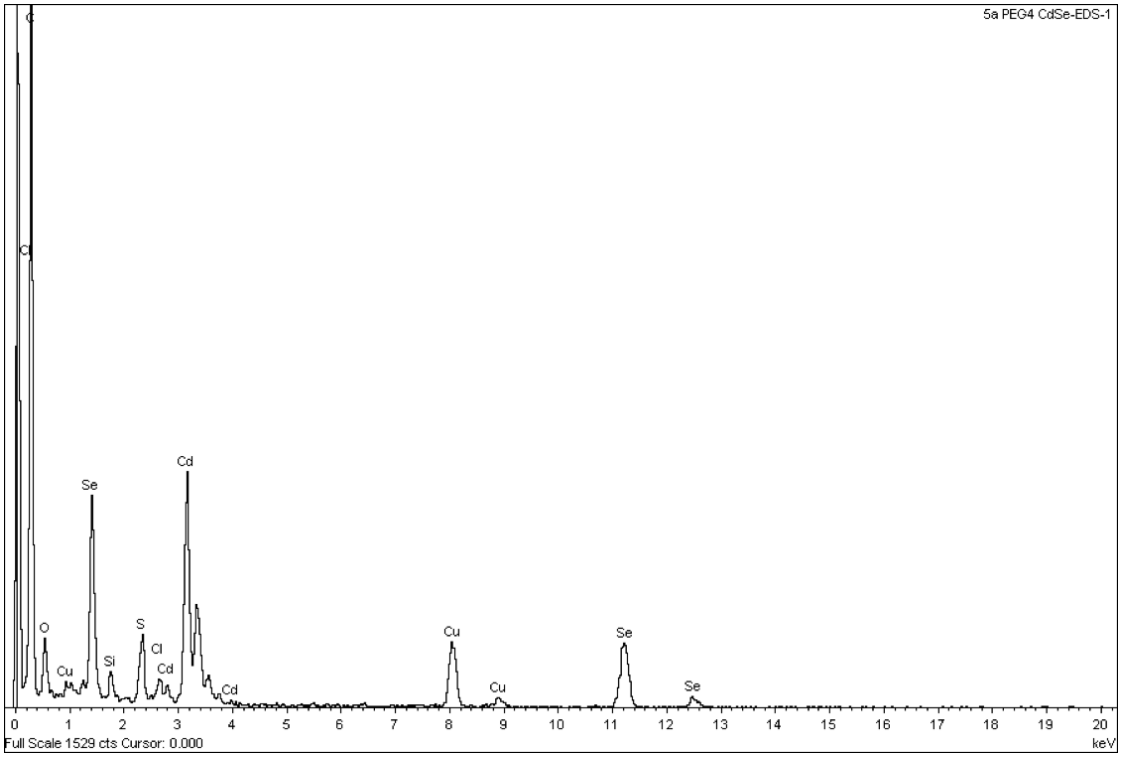

EDS spectrum of PEG_4-thiolate-coated 1.6 nm CdSe SNCs. The spectrum was collected in the TEM instrument with the same sample as shown in Figure 2A. The atomic percentage of Cd:Se was 3.79:2.85. Considering the CdSe SNC contains a stoichiometric core, therefore 0.94 atomic percent of Cd^{2+} was present on the surface in the form of Z-type of ligand. Therefore, theoretically 1.88 atomic percent of sulfur from PEG_4-thiolate should be present in the purified sample. The EDS analysis showed the atomic percentage of sulfur present in the sample was 1.97. Presence of slightly higher percentage of sulfur could be due to presence of free PEG_4-thiols in the sample.

CHAPTER 4. INVESTIGATING THE CONTROL OF QUANTUM CONFINEMENT AND SURFACE LIGAND COATING ON PHOTOCATALYTIC EFFICIENCY OF CHALCOPYRITE COPPER INDIUM DISELENIDE SEMICONDUCTOR NANOCRYSTALS

4.1 Synopsis

Recently, sustainable photocatalysts composed of semiconductor nanocrystals (SNCs) have been of immense interest due to their advantages including direct bandgaps, high absorption coefficients, and large separation of charges. In this chapter, we report for the first time, the effects of structural parameters (size and surface chemistry) of copper indium diselenide ($CuInSe_2$) SNCs on visible light driven photocatalysis. Ligand exchange reactions using PEG_n-thiolate (n=6-150) replace insulating oleylamine (OLA) which enhance the solubility and conductivity of 1.8-5.3 nm diameter $CuInSe_2$ SNCs. Due to the unique solubility provided by PEG-thiolate, inner-sphere electron transfer reactions (O_2 to $O_2^{\bullet -}$) at the SNC surface occurred allowing for sustainable photocatalytic decomposition of pollutants. Solution phase electrochemical characterization of our PEG-thiolate-coated $CuInSe_2$ SNCs showed that the thermodynamic driving force ($-\Delta G$) for oxygen reduction, which increased with decreased SNC size, was the dominate contributor to the photocatalytic process when compared to the light absorption and

coulombic interaction energies of electron hole pair ($J_{e/h}$) contributions. Therefore, the overall photocatalytic activity was highly dependent on SNC size where the smaller SNCs showed the most efficiency. Lastly, the conductivity provided by PEG-thiolate-coated $CuInSe_2$ SNCs caused a two-fold (from 30-60%) increase in degradation efficiency over the native insulating ligand, OLA. Thus, the ligand chain length had a profound effect on the pollutant degradation which could be applied to a variety of pollutants including: phenol, N, N-dimethyl-4-phenlyenediame, methylene blue, and thiourea.

4.2 Introduction

Colloidal SNCs have been used for a variety of applications including optoelectronics, biolabeling, photocatalysis, and photovoltaics as described in previous chapters. These SNCs are typically comprised of cadmium and lead-based metal chalcogenides (CdS, CdSe, CdTe, PbS, PbSe, etc.) due to their extensively studied syntheses. However, as the world becomes more environmentally conscious, the use of heavy and toxic materials becomes less appealing and the search for more benign elements becomes all-pervading. Ternary copper chalcogenide semiconductors have been of particular interested due to their less toxic nature and many advantages over binary SNCs including direct bandgaps, high absorption coefficients ($>10^4$ cm^{-1} for $\lambda<1000$ nm), superb stability, and large separation of charges (slowed recombination rates).[1, 2] For these reasons, ternary SNCs are already making an impact in solar harvesting, biomedicines, and catalysis and recently, advanced oxidative processes (AOPs).[3]

The need for simple, cost-effective decomposition of toxic pollutants, has led to a increased interest in AOPs. Sunlight, the cheapest and most abundant energy source, can

be harnessed by SNCs in order to perform photocatalytic decomposition of these pollutants. [4-9] There are three requirements when designing a SNC photocatalyst: (1) suitable bandgap, (2) high crystallinity to facilitate migration of e/h pairs to the surface (3) large surface area for redox reactions to take place.[10] Assuming constant crystallinity and composition, the SNCs size and surface ligation dictate light absorption, enhance photogenerated charge separation, and reduce charge recombination; all of which are prerequisites for efficient photocatalysis. [1, 2, 11-18]

Semiconductors containing metal ions with partially filled orbitals show little to no photocatalytic activity due to the ions acting as catalytic centers for electron-hole recombination and, therefore, do not produce the radicals necessary to generate photocatalysis. Exceptions include diamagnetic ions with d^{10} configurations such as Ag^{+}, Zn^{2+}, and Cu^{2+}, as well as those ions with an s^2 configuration such as Pb^{2+} and Bi^{3+}.[19] These exceptions such as copper-based ternary SNCs (e.g., $CuInSe_2$, $CuInS_2$, $CuSbS_2$, and $CuSbSe_2$) have long been used for photovoltaic devices to replace environmentally toxic elements (e.g., Cd and Pb), but not until recently have these materials been explored for their potential use in photocatalysis and in all cases, they were used in order to sensitize wide bandgap semiconductors (e.g., ZnS, ZnO, and TiO_2) or in conjunction with a cocatalyst (Pt).[2, 18, 20-23] Therefore, anatase TiO_2 is still considered to be the most efficient and environmentally friendly photocatalyst, however, its large band gap (~3.4 eV) allows for only ultraviolet light absorption. Therefore, a large band gap hinders the potential photocatalytic applications and commercialization. In order to overcome large band gaps and utilize these SNCs unaccompanied, a simple synthesis that allows for high control of composition, size, and surface ligation is imperative.

In addition, quantitative information about (1) energy levels of the highest occupied (HOMO) and lowest occupied (LUMO) molecular orbitals and (2) coulombic interaction energy of photogenerated electron hole-pair (Je/h) in SNCs is crucial to facilitate interfacial (e.g., solid-liquid) charge transfer and design materials for AOPs. However, this information is currently insufficient in literature. In this chapter, we report for the first time, a correlation between the SNC diameter and the thermodynamic driving force ($-\Delta G$) for molecular oxygen reduction, which controlled the photocatlytic efficiency of chalcopyrite copper indium diselenide ($CuInSe_2$) SNCs under homogeneous reaction conditions. To the best of our knowledge, this study provided the first report of quantum confinement-controlled photocatalytic degradation of pollutants, including: phenol, N, N-dimethyl-4-phenylenediamine (DMPD), methylene blue, and thiourea. In order to understand the effects of size and surface chemistry of $CuInSe_2$ SNCs on photocatalytic efficiency, we developed a phosphine-free, low temperature synthetic method to prepare 1.8-5.3 nm oleylamine (OLA)-passivated SNCs. Due to the insulating, hydrophobic nature of OLA, we performed ligand exchange reactions using polyethylene glycol (PEG)n-thiols (n=6, 18, 60, and 150) to replace OLA in order to provide much needed solubility and facilitate inner-sphere electron transfer. Due to these unique solubility properties, we investigated, for the first time, the size-dependent electrochemical properties of fully diffused $CuInSe_2$ SNCs, through cyclic voltammetry (CV). Through electrochemical and optical analysis, we demonstrated that the smallest diameter $CuInSe_2$ SNC exhibited the most efficient interfacial electron transfer which enhanced phenol degradation efficiency by 2-fold (from 30-60%). Additionally, a nearly 4-fold higher

efficiency was achieved using PEG_6-thiolate-passivated $CuInSe_2$ SNCs versus those coated in a more insulating ligand monolayer (OLA or PEG_{150}-thiolate).

Due to the uniqueness and novelty of this study, we believe our results will provide insight into how size and surface ligation affect the use of SNCs as photocatalysis. Thus this information could facilitate the use of ternary SNCs for solar energy conversion eliminating the need for large band gap metal oxides. Moreover, our low-temperature, phosphine-free synthetic method allows for a greener approach to SNC synthesis. Lastly, both the synthetic method and the unique solubility properties of PEGn-thiolate ligand can be applied to a variety of SNCs to provide detailed information on charge transfer dynamics which will enhance our fundamental understanding of electronic properties for faster more efficient AOPs.

4.3 Experimental Methods

4.3.1 Materials

Copper (I) chloride (CuCl, 99.99%), indium (III) chloride ($InCl_3$, 98%), selenium pellets (99.99%), triphenylphosphine (TPP, 99%), different chain length poly(ethylene glycol) methyl ethers (PEG_n, n = glycol unit = 6-150), *p*-toluene sulfonyl chloride (>99%), thiourea (>99%), anhydrous acetonitrile (CH_3CN, >99.8%), hexanes (99%), ethanol (98.5%), methanol (98.5%), chloroform (>99%), oleylamine (OLA, >70%), 1-hexanethiol (>95%), toluene (>99%), dichloromethane (DCM, >99%), phenol (99%), N,N-dimethyl-p-phenylenediamine (DMPD, 97%), methylene blue (MB), toluene (HPLC grade), ethyl acetate (99.5%), tetrahydrofuran (THF, 99.9%) were purchased from Aldrich and used without further purification. Organic solvents were purged with N_2 for 30 min prior to use. All water was purified using a Thermo Scientific Barnstead

Nanopure system. A 0.25 M aqueous solution of Na_2SeSO_3 was prepared according to the literature.[24] PEG_n-thiols were synthesized following a published procedure (see chapter 3 Appendix A).[25]

4.3.2 Optical Spectroscopy

For $CuInSe_2$ SNCs, UV-vis absorption spectra were collected using a Varian Cary 50 UV-vis spectrophotometer over a range of 1100-300 nm. Prior to the sample measurements, the baseline was corrected with pure solvent. The photoluminescence emission (PL) spectra were recorded using a Cary Eclipse fluorescence spectrophotometer from Varian Instruments using 600 nm excitation.

4.3.3 Structural Characterization by ^{1}H NMR, TEM, and XRD

[1] For high-resolution TEM analysis, samples were prepared by placing 10 □L of dissolved $CuInSe_2$ NCs in toluene onto a formver coated copper grid (Electron Microscopy Science). The sample was allowed to sit for 30 sec and any excess solution was removed by wicking with a Kimwipe to avoid particle aggregation. Images were obtained using a JEOL-3200FS-JEM instrument at 200 kV beam energy. The diameter of $CuInSe_2$ SNCs was determined using ImageJ software. At least 300 SNCs were counted to determine the average size. Wide-angle XRD was recorded on a Rigaku MiniFlex™ II (Cu Kα) instrument. Dry samples (typically ~2-4 mg) were placed in a hole of the sample holder and secured on both sides using Kapton tape. ^{1}H NMR was recorded on a Bruker AVANCE III 500 instrument at 500 MHz. Typically 6 mg of sample were dissolved in 0.6 mL of $CDCl_3$ at room temperature and a minimum of 1000 scans were collected.

4.3.4 Elemental Analysis

A field-emission scanning electron microscopy (FE-SEM) system, which was equipped with an energy dispersive X-ray (EDS) was used to determine the composition of the SNCs.

4.3.5 Electrochemical Characterization

Voltammetry was done with a CH Instruments (Austin, TX) model 760D electrochemical analyzer in a conventional three electrodes set-up, which was constructed of a 3.0 mm glassy carbon disk working electrode, a Pt wire counter electrode, and a 0.6 mm diameter Ag wire quasi-reference electrode (QRE). Prior to use, the working electrode was polished with a diamond polishing compound (Buehler), washed with nanopure water, sonicated for 10 min in nanopure water, washed with DCM, and finally dried with N_2. All electrochemical measurements were conducted under a N_2 environment, and sureseal solvents were used for the analysis. A 3.0 ml solution of 0.1 M Bu_4NPF_6, containing 0.02 mmol SNCs was used for CV analysis. The scan rate for all samples was 0.1 V/s. The potential of the Ag QRE was calibrated using Fc/Fc+ redox couple in acetonitrile vs. Ag/AgCl/3 M KCl (aq) and then converted versus absolute scale (eV) or normal hydrogen electrode (NHE).

4.3.6 Photocatalytic Activity Measurement

The photocatalytic studies were carried out using a 350 W xenon arc lamp (Oriel, Newport Corporation), which was fitted with a 450 nm cut-off filter. Irradiation was carried out via side-on illumination onto a 20 mL glass vowel placed 9.0 cm away from the lens adapter. Phenol was chosen as standard substrate to investigate the photocatalytic performance of PEGn-thiolate coated SNCs. In a typical experimental setup, the

photocatalyst (1.2 x10^{-7} M) and phenol (5 x 10^{-3} M) were dissolved in water in a 20 mL glass vial with a total volume of 10mL. The homogeneous solution was stirred for 20 minute under dark with closed capped and then irradiated with light source. To monitor the reaction progress, 70 µl of the reaction mixture was diluted with 3 mL of water and then the concentration of the phenol was determined by measuring the maximum absorbance at 268 nm considering $C/C_0 = A/A_0$. The degradation efficiency of the SNCs was then determined using the following equation:

$$Decomposition\ efficiency\ (\%) = \frac{C_0 - C}{C_0} \times 100\% \quad (4.1)$$

Where C_0 and C are the concentration of phenol before and after light irradiation, respectively, during the photocatalytic reaction. The same protocol was followed to study the degradation of thiourea, N,N-Dimethyl-p-phenylenediamine, and methylene blue, monitoring the absorption maximum at 235 nm, 242 nm and 664 nm, respectively For OLA-coated $CuInSe_2$ SNCs, prior to measure UV-visible absorbance, the aliquot was centrifuged at 7000 rpm for 2 minute, and then supernatant was diluted with 3 ml water.

4.3.7 Synthesis of OLA-Coated $CuInSe_2$ SNCs

In a N_2-filled glove box, CuCl (0.033 g, 0.33 mmol) $InCl_3$ (0.273 g, 1.23 mmol), and 7.5 mL degassed OLA were loaded into a 25 mL two-neck flask. The flask was sealed, removed from glove box, and attached to a Schlenk line. The reaction mixture was heated at desired growth temperature (see Table 4.1) under vacuum with stirring for 2 h and then transferred to N_2 and heated for additional 1 h. The Se-precursor was separately prepared by dissolving 0.240 g of freshly ground Se powder in a mixture of 3.14 mL OLA and 0.860 mL HT at room temperature and stirred for 90 min. under N_2 atmosphere at room temperature. A 0.8 mL Se-precursor (0.608 mmol) was injected in

the metal precursor and the reaction was allowed to proceed for 2 h. The SNCs growth was quenched by injecting 20 mL of toluene. The SNCs were purified by drop wise addition of ethanol (~20 mL) and centrifuged at 5000 rpm for 5 min) to yield a brown solid. The solid then redispersed in toluene (10 mL) and precipitated with ethanol (5 mL). This purification technique was followed once more and then $CuInSe_2$ SNCs were dried by blowing N_2 and stored inside the glovebox for further characterization.

4.3.8 Ligand Exchange Reaction with PEGn-thiols (n=6, 18, 60, 150)

Purified OLA-capped SNCs were dissolved in 5 mL of nitrogen-purged chloroform to obtain a concentration of 1 mM. PEG_6-SH (0.1 mmol) was added to the OLA-coated SNCs at room temperature and stirred (~12 h) under N_2. To remove excess PEG_6-SH, the solution was then brought to dryness and the solid was redissolved in a minimum amount of chloroform and precipitated with hexane. The resulting solid was collected by centrifugation (7000 rpm, 5 min). The same process was repeated when exchanging native OLA for PEGn-thiol (n= 15, 60, and 150) for OLA-capped $CuInSe_2$ SNCs.

4.4 Results and Discussion

4.4.1 Synthesis and Characterization of $CuInSe_2$ SNCs

In order meet the need for greener synthetic procedures and study the quantum confinement effects of ternary SNCs on photocatalytic efficiency, we developed a low-temperature, phosphine-free synthetic method to prepare 1.8-5.3 nm $CuInSe_2$ SNCs. Briefly, CuCl, $InCl_3$, and OLA were added to a two-neck r.b. at 130℃ and stirred for 2h under vacuum and then additional 1 h under N_2 to produce a faint yellow solution. In a separate two-neck r.b., Se powder, OLA, and HT were stirred for 90 min under N_2 at

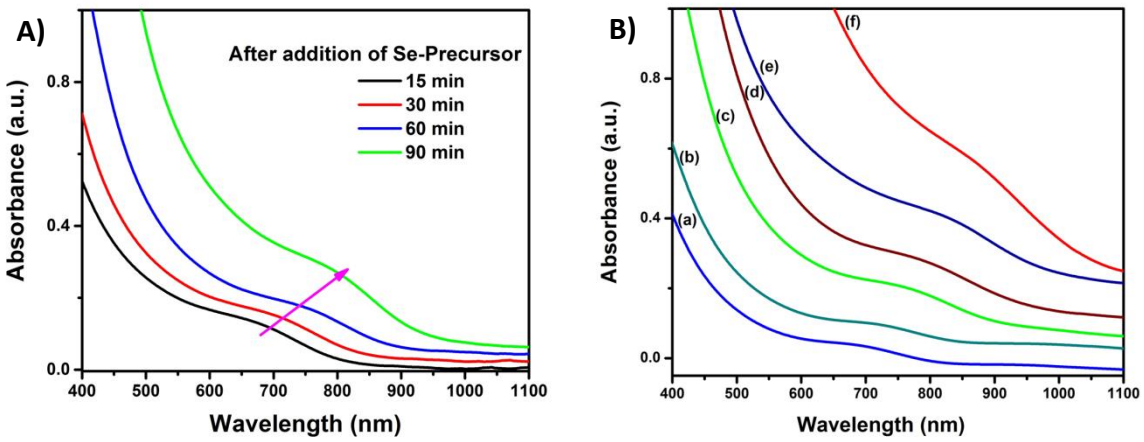

Figure 4.1: UV-visible absorption spectra of CuInSe2 SNCs (A) at different time points of the synthesis after addition of Se-precursor at 130℃ and (B) upon stable growth formation ran at (a) 100, (b) 110, (c) 120, (d) 130, (e) 140, and (f) 150 ℃. Each sample was purified by solvent arrested precipitation before optical analysis. All spectra were collected in toluene.

room temperature. The Se-precursor was then quickly degassed and injected into the metal precursor to form $CuInSe_2$ SNCs. A time dependent UV-visible spectroscopy can be seen in Figure 4.1 A where a continuous red-shifting is observed suggesting an increase in SNC diameter as time progressed. The detailed growth mechanism of $CuInSe_2$ SNCs has been previously reported by Hillhouse, et al. [26] Briefly, upon addition of the Se-precursor, binary metal selenides form which eventually fuse together to form $CuInSe_2$ SNCs. In our synthetic procedure, this stable formation took ~90 min as marked by a stable absorption peak at ~800 nm with no additional shift occurring after a subsequent 30 min period. The fully formed $CuInSe_2$ SNCs were then purified using a solvent arrested precipitation technique which is detailed in the Experimental Methods section of this chapter. Additional sizes of $CuInSe_2$ followed similar synthetic protocol with minor systematic changes as detailed in Table 4.1. The UV-visible absorption spectra of different-sized OLA-passivated $CuInSe_2$ SNCs were collected and an evident

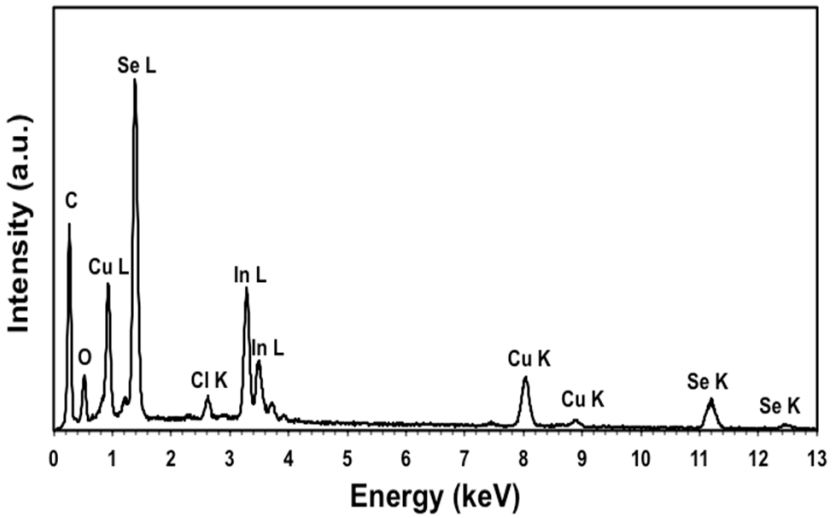

Figure 4.2: Representative EDS spectrum of purified $CuInSe_2$ SNCs.

red-shift (decrease in energy) occurred due to the increase in SNC diameter attributable to quantum confinement effects. [27, 28] (Figure 4.1 B)

To ensure the chemical composition of our SNCs was that of $CuInSe_2$ SNCs, we performed energy dispersive X-ray (EDS) analysis. EDS spectrum of OLA-passivated $CuInSe_2$ can be found in Figure 4.2. Analysis of five randomly selected areas provided an average Cu:In:Se composition of 0.94:0.79:2.00 therefore our SNCs were slightly Cu- (Cu/In = 1.19) and Se- [Se/Cu+In)=1.16] rich. The formation of Se-rich $CuInSe_2$ SNCs is supported by a broad, low-intensity PL stemming from unpassivated Se-sites. [29] (Appendix A) As discussed in previous chapters, OLA is an L-type ligand and as such can only bind to the surface metal sites. [30-32] This leaves the Se-sites unpassivated, thus defect sites act as trap states resulting in poor recombination and decreased PL emission properties in our Se-rich $CuInSe_2$ SNCs.

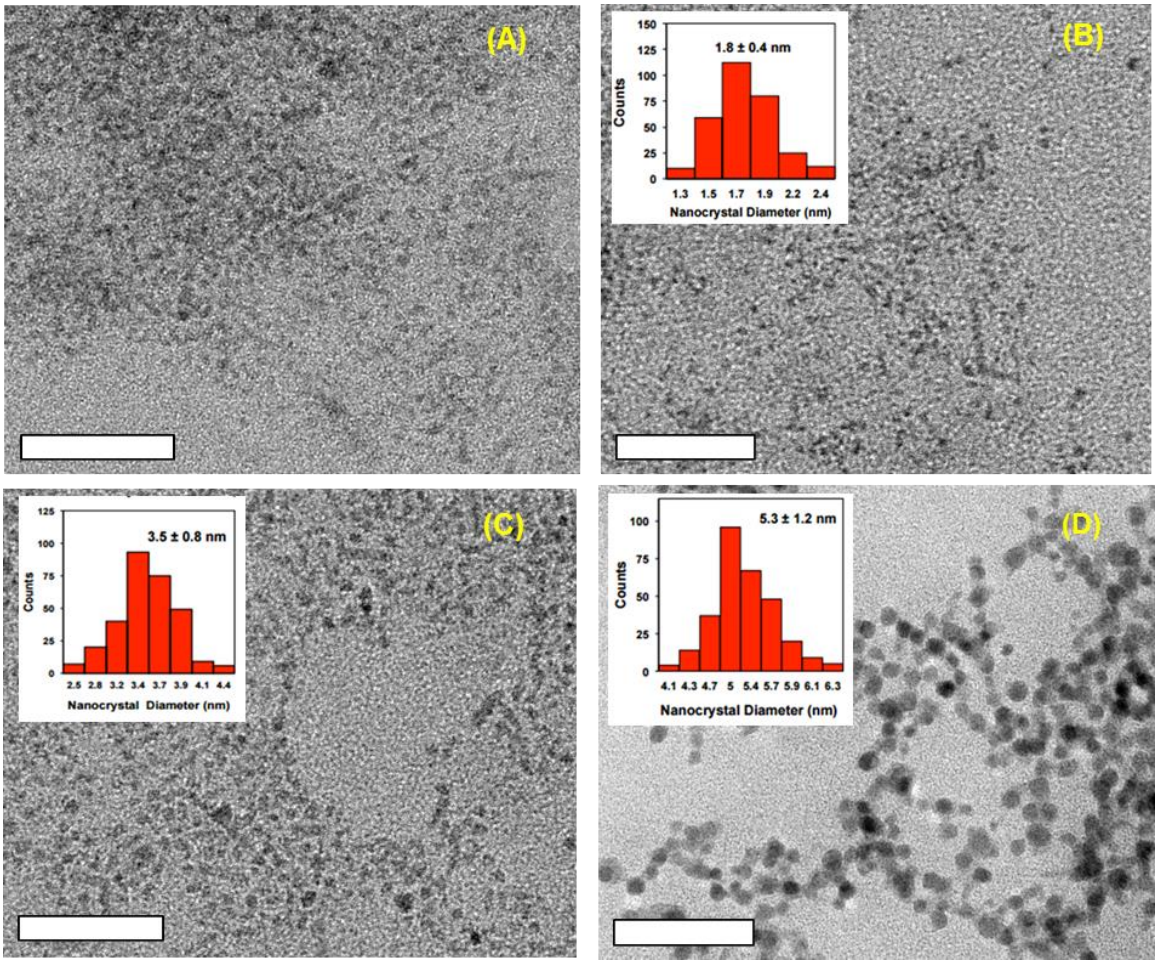

Figure 4.3: TEM images of $CuInSe_2$ SNCs at different UV-visible absorption peak positions: (A) 705, (B) 740, (C) 800, and (D) 915 nm. Scale bars are 100 nm. Insets represent the corresponding histograms, in which 300 SNCs were counted. TEM of 705 nm $CuInSe_2$ SNC resulted in too low of resolution for accurate diameter calculation.

In order to determine the size and shape of the $CuInSe_2$ SNCs formed by our synthetic method, we performed transmission electron microscopy (TEM) of our purified samples. Figure 4.3 depicts $CuInSe_2$ SNCs with UV-visible absorption peak positions of (A) 705, (B) 740, (C) 800, and (D) 900 nm. Through the use of TEM, we can clearly see that shape of our SNCs is spherical in nature. (Appendix B) Additionally, through the use of ImageJ software, we were able to calculate the diameter of each sample. In each case,

Table 4.1: Comprehensive look at OLA-passivated, 1.8-5.3 nm $CuInSe_2$ SNCs.

Growth Temperature (°C)	Time (min)	Absorption Peak Position (nm)	Optical Band Gap (eV)	SNC Diameter (nm)[b,c]
100	150	705	1.76	-[d]
110	90	740	1.67	1.8 (0.4)
120	90	765	1.62	2.4 (0.5)
130	90	800	1.55	3.5 (0.8)
140	120	845	1.47	4.1 (0.9)
150	180	915[a]	1.35	5.3 (1.2)

[a]Synthesis was conducted using (0.825 mL, 0.627 mmol) of Se-precursor and all other reaction conditions were identical. [b]300 SNCs were counted to determine size and size dispersion. [c]Diameter was too small (~1.0 nm) to determine using TEM. [d]Number in parenthesis indicates standard deviation.

300 SNCs were counted to determine the size and size dispersion. A histogram is present as an inset in each TEM image, except (A). For 705 nm (~1.0 nm) $CuInSe_2$ SNCs (A), we were unable to calculate the size and size dispersion due to low contrast in the TEM image. Additional histograms can be found in Appendix C. Table 4.1 provides the results of these calculations. Through TEM, it is evident that our low-temperature, phosphine-free synthesis allowed for a high degree of control leading to very monodispersed $CuInSe_2$ SNCs.

To further structurally classify our SNCs, we performed X-ray diffraction (XRD) analysis. Figure 4.4 depicts the XRD patterns of different-sized $CuInSe_2$ SNCs. In each case, the XRD pattern matched the diffraction pattern of chalcopyrite (vs. sphalerite) [33] phase $CuInSe_2$ SNCs as previously reported[34, 35]. Appendix D provides an expanded XRD pattern of 1.8 nm diameter $CuInSe_2$ SNCs which show the characteristic chalcopyrite peak (211) at 35.68°. These patterns also matched the JCPDS database

(JCPDS no. 75-0107). It should be noted that the diffraction peaks became sharper as the size increased which is indicative of enhanced crystallinity character.

Our newly developed synthetic approach to highly monodispersed, different-sized $CuInSe_2$ SNCs offers many advantageous over current literature procedures. First, we demonstrated a reasonably low temperature (100-150℃) synthesis when compared to other non-phosphonated methods which use temperatures in excess of 240-290℃. [1, 33, 36-39] Secondly, our OLA-passivated $CuInSe_2$ SNCs were highly monodispersed, spherical in nature, and small in diameter (<6.0 nm) which is in contrast to reports of large (~30 nm diameter), polydispersed, anisotropic $CuInSe_2$ SNCs. [40-42] Lastly, we provided a phosphine-free synthesis that utilizes a highly reactive Se-precursor[43-45] which is relatively benign when compared to other methods which use toxic trioctylphosphine, tributylphosphine, and diphenylphosphine to dissolve elemental Se. [34, 35, 46-48] Additionally, the use of OLA as a surface passivating ligand during our synthesis

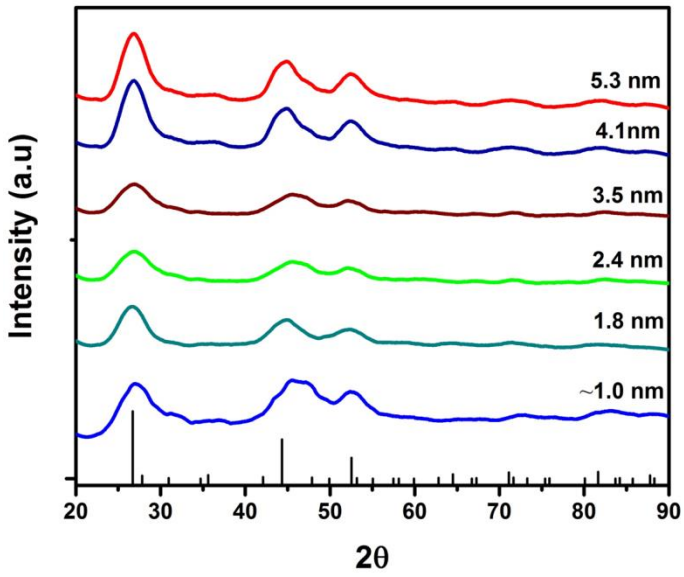

Figure 4.4: XRD patterns of different sized $CuInSe_2$ SNCs. As a reference, bulk tetragonal chalcopyrite $CuInSe_2$ (JCPDS#75-0107) is represented by the bottom stick pattern.

provided us the unique opportunity to systematically modify the surface of the SNC with PEGn-thiols (n= 6-150) which provided enhanced solubility properties for electrochemical analysis and facilitated charge transfer processes for sustainable photocatalysis, as discussed later.

4.4.2 Size Dependent Electrochemical Properties

Electrochemistry, as discussed in Chapter 1, can provide vital information about our $CuInSe_2$ SNCs that optical absorption measurements cannot; such as, their energy level (i.e. HOMO and LUMO) positions, coulombic interaction ($J_{e/h}$), and flat-band potential (potential at zero charge). This information is imperative for application in solar cells and photocatalysis as it is used to extract the maximum number of charge carriers (increased material efficiency). While many techniques have been used to estimate this information ranging from density functional theory (DFT) to the combination of X-ray photoelectron (XPS) and ultraviolet photoemission (UPS) spectroscopy, to date these methods still grossly underestimate the SNC band gap.[49-54] Therefore, electrochemistry proves to be the most precise method for obtaining the necessary information needed for solar cell and photocatalytic applications; however, sample preparation is still a limitation of this electrochemistry. For example, previous reports of copper-based ternary SNCs utilized cyclic voltammetry (CV) where the SNC was deposited as a film on the electrode surface and therefore presented in their aggregated state.[55-57] This aggregation causes the SNCs to act as a bulk material and; therefore, distinct orbitals no longer exist. [58] Additionally, use of insulating ligands such as OLA or dodecanethiol (DDT) on the SNC surface causes a dramatically slowed electron transfer which could trigger chemical byproduct reactions inside the film causing an overall change in morphology and

degradation of the sample. Therefore, accurate quantitative information using solid-phase electrochemistry is scarce.

However, using dispersed SNCs can overcome many of the limitations mentioned above. Using this technique, SNCs are dispersed in a solvent/electrolyte solution in order to prevent aggregation. However, these measurements are most commonly used in an electrochemically unfriendly (toluene, DMF, etc.) solvent which prevents the large potential window scan needed for small SNCs (large band gap).[58] Size-dependent electrochemical band-gaps have been reported for dispersed CdS , CdSe[59-64], CdTe[59, 65, 66], CdS_xSe_{1-x}[65], and $CdSe_xTe_{1-x}$[67] in hopes of gaining a higher understanding of SNCs electrochemical properties, although, in all cases, multiple peaks in the CV were observed, which could be due to poorly purified or poorly passivated SNCs.[59, 68] Highly purified and monodispersed nanoclusters are required for such analysis in order to achieve pristine voltammograms.[58, 60, 69] Lastly, and most likely due to the lack of solubility in the solvent/electrolyte media causing slow charge transfer kinetics, previous

Table 4.2: Size-dependent optical and electrochemical band gaps, and coulombic interaction energies of e/h pairs of OLA-passivated $CuInSe_2$ SNCs.

SNC Diameter (nm)[a]	Absorption Peak Position (nm)	Optical Band Gap (eV)[b]	Electrochemical Band Gap (V)[c]	Coulombic Interaction Energy of Electron-Hole Pair ($J_{e/h}$) (meV)
1.8 (0.4)	740	1.67	1.75	80
3.5 (0.8)	800	1.55	1.58	30
4.1 (0.9)	845	1.47	1.47	10

[a]300 SNCs were counted to determine size and size dispersion. [b]UV-visible absorption peak was used to determine the optical band gap. [c]Cyclic voltammetry using dispersed SNCs in toluene/DCM/Bu4NPF6 solution was used to determine the electrochemical band gap. Coulombic Interaction energy of e/h pair was calculated using: $J_{e/h} = E_{gap}^{el} - E_{gap}^{opt}$.

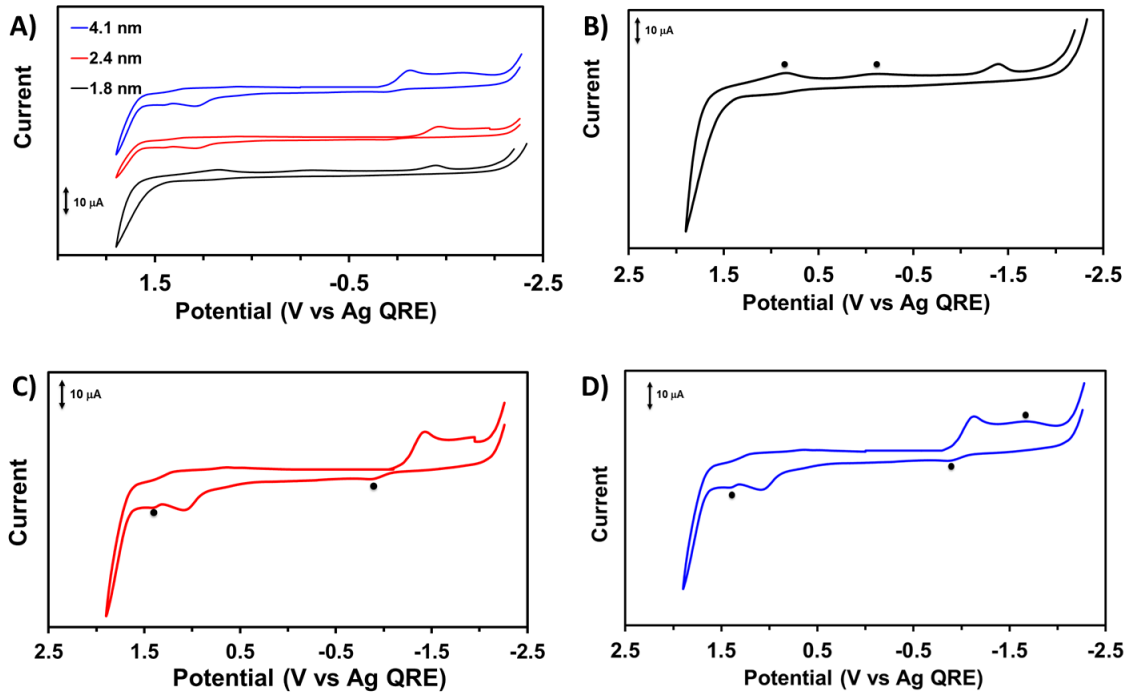

Figure 4.5: (A) stacked cyclic voltammograms of OLA-passivated, 1.8 nm (black, (B)), 2.4 nm (red, (C)), and 4.1 nm (blue, (D)) diameter $CuInSe_2$ SNCs. Black dots represent additional peaks other than those corresponding to HOMO and LUMO.

accounts have reported higher optical band-gaps $\left(E_{gap}^{opt}\right)$ than electrochemical band-gaps $\left(E_{gap}^{el}\right)$ which contradicts quantum confinement effects. (See Chapter 1 Equation 1.4) Therefore, to overcome the above-mentioned limitations in electrochemical analysis, we developed $CuInSe_2$ SNCs with unique solubility that allowed us to perform electrochemistry of diffused SNCs in an electrochemically friendly solvent (e.g., acetonitrile) and consequently the first size-dependent electrochemistry of $CuInSe_2$ SNCs.

Initially, we performed electrochemistry of our OLA-passivated, 1.8-5.3 nm $CuInSe_2$ SNCs dispersed in a toluene/DCM/Bu_4NPF_6 solution. Briefly, 0.02 mmol OLA-coated $CuInSe_2$ SNCs were suspended in 3.0 mL (1:5 mixture of toluene:DCM), 0.1 M

Bu_4NPF_6 electrolyte solution and run using CV. Onset potentials of oxidation (removal of electrons from HOMO) and reduction (addition of electrons to LUMO) waves were used to calculate the E_{gap}^{el} *and* $J_{e/h}$ values. (Table 4.2) Figure 4.5 shows the CV of different-sizes of OLA-passivated $CuInSe_2$ SNCs. Importantly, despite the appearance of additional peaks, the E_{gap}^{el} is higher than the E_{gap}^{opt} (See Eq 1.4), which is in agreement with the theoretical calculations.[59] Additionally, higher E_{gap}^{el} and $J_{e/h}$ for smaller diameter SNCs was observed which follows size-dependent quantum confinement effects.[28] However, appearance of additional peaks appeared in our voltammograms as previously demonstrated in dispersed SNC electrochemical reports.[59-68] Figure 4.5 depicts the size-dependent voltammograms in which, the black dots represents the additional peaks that do not correspond to the SNC's HOMO or LUMO. These features were thought to be due to the presence of trap states, which has previously been reported in electrochemical characterization of CdSe SNCs. [62, 68] Additionally, a large oxidation peak current was observed at higher potential (after the band-gap). It is well known that OLA often undergoes dynamic exchange in solution, meaning that it can be present as either bound or unbound OLA.[70, 71] Therefore, we believe that unbound OLA is undergoing oxidation and that is causing this observed peak. This oxidation of OLA also causes the surface to be less coated resulting in decomposition of our SNCs. For example, a brown precipitate at the bottom of the electrochemical cell after two potential cycle scans (+1.8 to -2.5 V) was observed indicating the decomposition of OLA-passivated $CuInSe_2$ SNCs. For the above mentioned reasons, electrochemical data of our OLA-passivated $CuInSe_2$ may not accurately represent the of E_{gap}^{el} and $J_{e/h}$. However, post-synthetic exchange of insulating

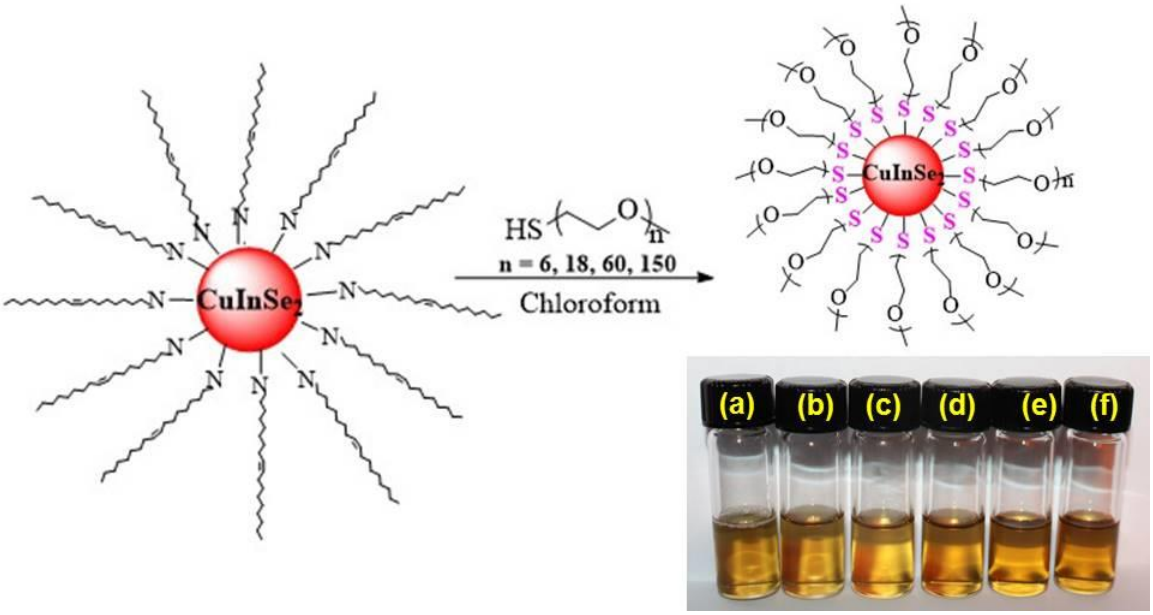

Figure 4.6: Schematic representation of post-synthetic ligand exchange. Insulating, native OLA ligands are replaced by solvent-like PEG_n-thiolate ligands. Ligand exchange allows for unique solubility in a variety of solvents: (a) water, (b) ethanol, (c) acetonitrile, (d) benzonitrile, (e) chloroform, and (f) dichloromethane.

OLA with PEG_n-thiols may provide adequate solubility, stability, and conductivity to our SNCs which is needed to accurately perform electrochemical analysis.

In Chapters 2 and 3, we have shown the unique solubility, stability, and conductivity provided by PEGn-thiols (n= 6-150) through direct synthesis and also post-synthetic ligand exchange. Here we apply a post-synthetic ligand exchange in which PEG-thiol replaces the insulating, hydrophobic ligand, OLA, from the surface of $CuInSe_2$ SNCs. (Figure 4.6) ^{1}H NMR of this ligand exchange shows the disappearance of the broad vinyl proton (-CH=CH-) resonance of OLA at 5.53 ppm, confirming the $CuInSe_2$ SNCs were passivated by PEG_6-thiolate. (Appendix E) Furthermore, UV-Visible spectroscopic (Figure 4.7) and TEM (Appendix E) analysis showed no distinct difference in the optical property and size of $CuInSe_2$ SNCs before and after PEG_6-thiolate

exchange, suggesting that the SNCs maintained their electronic and structural properties. This is similar to our previous ligand exchange report of OLA- to PEG-thoiolate coated CdSe SNCs in Chapter 3. Lastly, as shown in Figure 4.6, PEG_6-thiolate-coated $CuInSe_2$ SNCs were soluble in a diverse range of solvents such as water, ethanol, and acetonitrile that they were not soluble in when OLA passivated the surface of the SNC. This matches our unique solubility of PEG-thiolate coated CdSe SNCs provided in Chapters 3. Due to this unique solubility, we were able to perform electrochemical analysis in a large potential window (soluble in electrochemically friendly solvents), which is imperative to accurately portray the E_{gap}^{el} and $J_{e/h}$ for smaller SNCs.[60] Additionally, as described in detail in Chapter 3, polyether chains such as PEG display "solvent-like" properties which enable fast charge transport through the polymer layers which is highly beneficial for electrochemical analysis. [72-75]

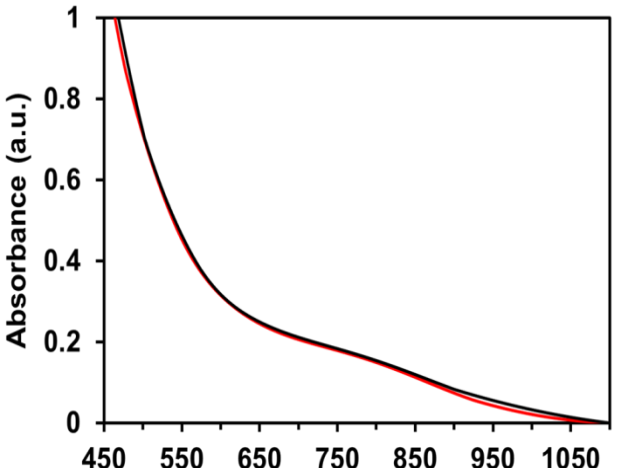

Figure 4.7: UV-Visible absorption spectra of 1.8 nm diameter $CuInSe_2$ before (black) and after (red) native OLA is exchanged with PEG_6-thiolate.

Electrochemical procedural details can be found in the experimental section. Briefly, 0.02 mmol PEG_6-thiolate coated $CuInSe_2$ SNCs were dissolved in 3.0 mL, 0.1 M Bu_4NPF_6/CH_3CN solution. Figure 4.8 A depicts the CV of PEG_6-thiolate coated $CuInSe_2$ SNCs in which the HOMO and LUMO positions and E_{gap}^{el} were determined (Figure 4.8 B). Unlike OLA-passivated $CuInSe_2$ SNCs, PEG-thiolate coated $CuInSe_2$ SNC voltammograms were void of additional peaks. Although there are clean CVs of Au NPs

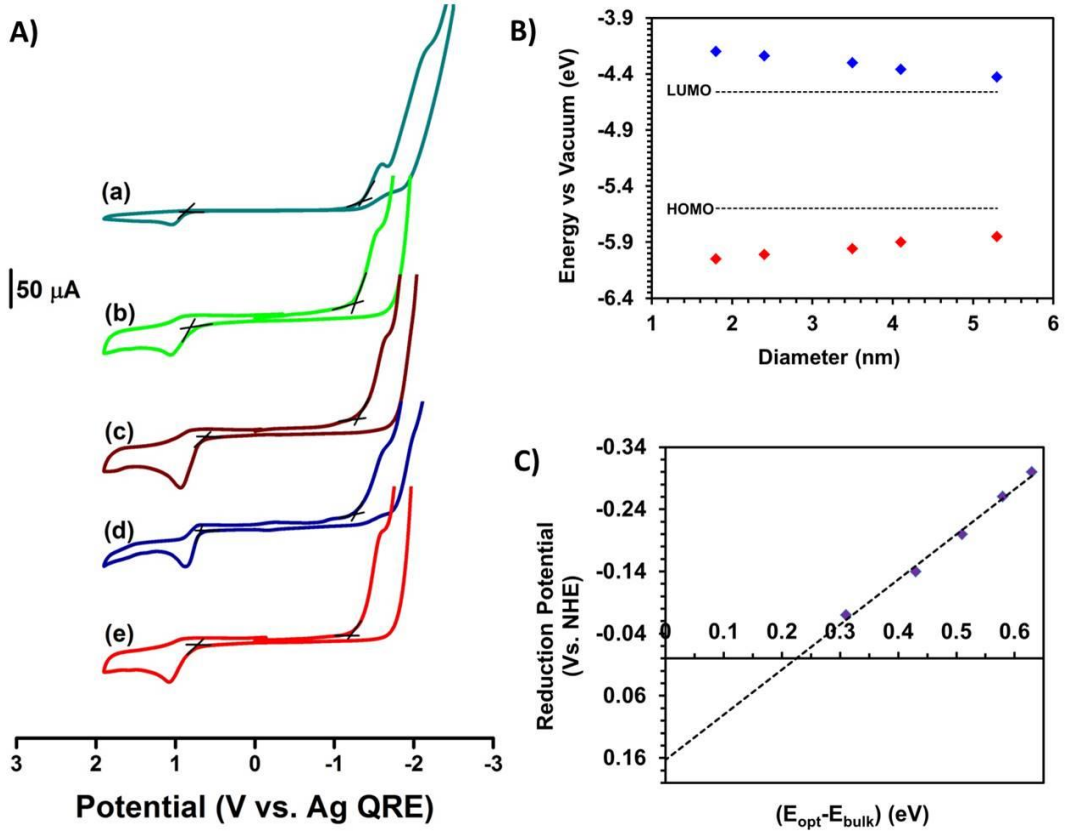

Figure 4.8: (A) Size dependent CV of PEG_6-thiolate coated CuInSe2 SNCs. (a) 1.8, (b) 2.4, (c) 3.5, (d) 4.1, and (e) 5.3 nm in diameter. CV was ran in a Bu_4NPF_6/CH_3CN solution at a potential scan rate of 0.1 V/s with a 3.0 mm glass carbon working electrode, Pt wire electrode, and Ag wire quasi-reference electrode (QRE). (B) Different sizes of $CuInSe_2$ SNCs HOMO and LUMO positions as determined by (A). Bulk $CuInSe_2$ HOMO and LUMO positions are represented by the dotted line. (C) Relationship between reduction potential of $CuInSe_2$ SNCs and confinement energy (vs. NHE), $R^2 = 0.993$. A direct band-gap of 1.04 eV for bulk $CuInSe_2$ was used for the confinement energy calculation.[25, 26]

present in literature[76, 77], to the best of our knowledge, these are the most pristine voltammograms reported for ligand-passivated SNCs. From Figure 4.8, it can be seen that the position of the HOMO (oxidation potential) became more positive and LUMO (reduction potential) became more negative (vs. NHE) as the size of the SNC decreased. Figure 4.8 C shows the linear relationship between the reduction potential (vs. NHE) and

confinement energy (E_{gap}^{opt} minus bulk band gap (E_{gap}^{bulk}, 1.04 eV)). The flat band potential (bulk reduction potential) was then calculated from the extrapolation to zero confinement energy (as define above) and determined to be 0.16 V (vs. NHE). This value is comparable to previously reported $CuInSe_2$ flat band potential of 0.15 V determined from Mott-Shottky plot.[78] Additionally, and most importantly, the $E_{gap}^{el} > E_{gap}^{opt}$ therefore following quantum confinement effects. (Figure 4.8 A)

Using the E_{gap}^{el} determined for PEG_6-thiolate coated $CuInSe_2$ SNCs above, we can calculate the charging energy, $J_{e/h}$, which is the difference between the E_{gap}^{el} and the E_{gap}^{opt}. It can be seen from Figure 4.9 A that $J_{e/h}$ reduces with decreasing SNC diameter. Not surprisingly, the $J_{e/h}$ is ~90 meV higher for PEG_6-thiolate- versus OLA-passivated $CuInSe_2$ SNCs due to the LUMO shift towards more negative (vs. NHE) upon ligand exchange causing an increase in E_{gap}^{el}. It has been previously reported that the interaction between electron donating ligands, such as thiols, with bulk CdSe electrodes could shift the reduction potential (LUMO) more than 500 mV in the negative direction (vs. NHE). [79] Thus PEG-thiolate is more electron donating than OLA causing a shift in reduction potential. This is similar to previous reports of trioctylphosphine oxide (TOPO)- and DDT-coated CdSe SNCs in which the reduction potential was found to be more negative for DDT than TOPO (vs. NHE). [80] As seen in Figure 4.9 B, a linear relationship between $J_{e/h}$ and SNC diameter exists up to 4.1 nm. However, as the diameter approaches 5.3 nm, deviation from linearity occurs. It was thought that for our larger diameter $CuInSe_2$ SNCs, the electrons were injected into trap states near the LUMO of the SNC causing the true reduction potential not to be observed. Nevertheless, we were able to accurately use

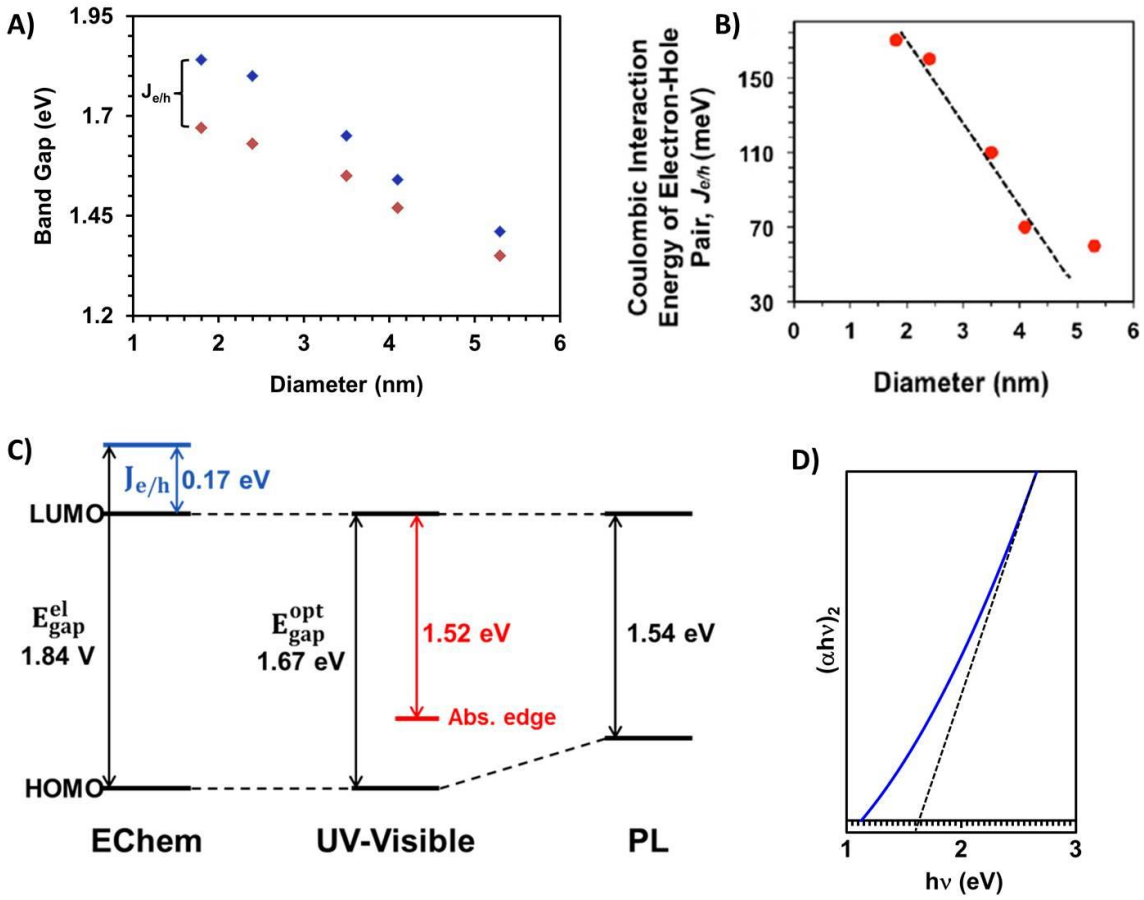

Figure 4.9: (A) Comparison of size-dependent electrochemical (red) and optical (blue) band gaps of PEG_6-tholate coated $CuInSe_2$ SNCs. (B) Coulombic interaction energy of electron-hole pairs ($J_{e/h}$) as a function of SNC diameter. (C) Schematic diagram representing approximate energy levels of PEG_6-thiolate coated, 1.8 nm diameter $CuInSe_2$ SNCs. For simplicity, solvent effects were considered negligible. *Image not drawn to scale. The absorption edge was determined from the (D)Tauc plot.

electrochemical analysis to determine the HOMO and LUMO position of different-sized $CuInSe_2$ as well as their E_{gap}^{el} and $J_{e/h}$. Furthermore, we established a basic energy level diagram of PEG_6-thiolate coated, 1.8 nm diameter $CuInSe_2$ SNCs from UV-visible and PL spectroscopy as well as CV analyses similar to those presented using thiolate-coated Au NPs[77] and CdSe[81] and InAs[82] SNCs (Figure 4.9 C), in which the absorption edge was calculated using a Tauc plot (Figure 4.9 D).

We have shown that electrochemical analysis for the determination of E_{gap}^{el} and $J_{e/h}$, as well as the HOMO and LUMO position is a viable analytical characterization method that could provide more accurate results than those presently used. This work demonstrates the importance of appropriate surface ligation which enables voltammetry to be carried out in an electrochemically suitable solvent/electrolyte system such as that shown in our investigation. Additionally, electrochemical techniques shown here could thwart the need for inaccurate approximations and costly spectroscopic techniques commonly used to determine the band gap of HOMO and LUMO positions of SNCs. [49-54, 83, 84] Thus, electrochemical techniques could provide the information needed to extract the maximum number of charge carriers which is critical for AOPs such as photocatalysis.

4.4.3 Size-Dependent Photocatalysis

Ternary SNCs are commonly used in conjunction with metal oxide heterostructures in order to investigate SNC-induced photocatalytic transformation of various substrates under *heterogeneous* reaction conditions. As demonstrated above, PEG_6-thiolate coated $CuInSe_2$ SNCs have unique solubility properties; therefore, using our ligand-exchanged $CuInSe_2$ SNCs we were able to study the size-dependent photocatalytic activity in *homogenous* reaction conditions (water) making our system fully sustainable. Moreover, PEG_6-thiolate coated $CuInSe_2$ SNCs were used to study the degradation efficiency of not one, but four different pollutants under visible light irradiation (<450 nm) hence showing the versatility of our system. We hypothesized that large interfacial charge transfer would dictate the efficiency of our SNCs, and as such, the highest photocatalytic degradation efficiency (%) would bestowed upon the smallest

diameter (largest band-gap) SNC. To test our hypothesis, we used the photodegradation of phenol as a model system as it is not only water soluble, but commonly found pollutant in petroleum products.[85]

To monitor the photodegradation of phenol as a function of SNC diameter, we first dissolved PEG_6-thiolate coated $CuInSe_2$ SNCs and phenol in water, stirred for 30 min under dark conditions and then illuminated the sample with a 350 W xenon arc lamp fitted with a 450 nm cut-off filter for 2 h. A detailed procedure is provided in the Experimental Section. Time-dependent phenol decomposition was measured using UV-visible spectroscopy of peak intensity at 268 nm. (Figure 4.10 A) Nearly 2-fold difference was observed using 1.6 nm (60 %) versus 5.3 nm (30%) diameter PEG_6-thiolate coated $CuInSe_2$ SNCs as seen in Figure 4.10 B. Additionally, photocatalytic efficiency was found to be a direct function of the E_{gap}^{el} of $CuInSe_2$ SNCs in the range of 1.84 to 1.41 eV. One might expect that the smallest diameter $CuInSe_2$ SNCs would absorb less light than larger SNCs and therefore display the lowest catalytic activity.

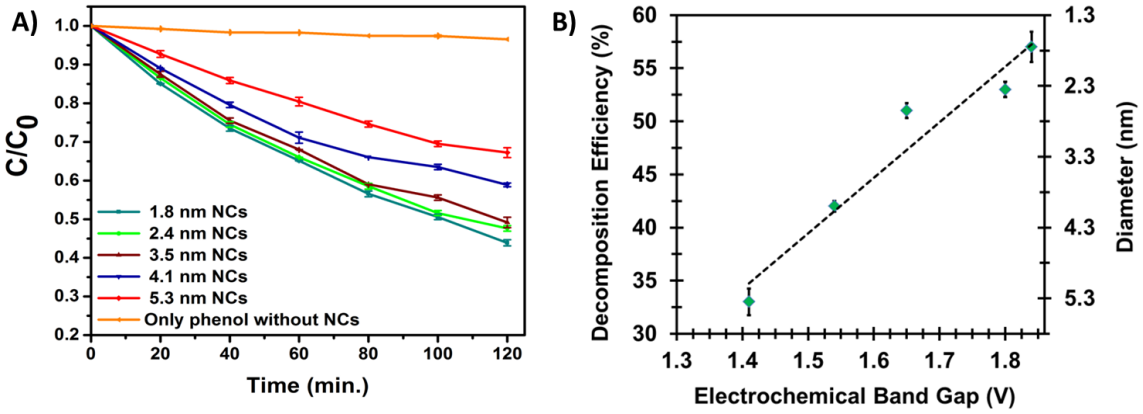

Figure 4.10: (A) Photodecomposition efficiency of phenol using 1.8-5.3 nm diameter, PEG_6-thiolate coated $CuInSe_2$ under visible light irradiation (<450 nm). (B) Decomposition efficiency as a function of electrochemical band gap and diameter, showing a linear relationship, R^2= 0.957.

However, we believe that the large surface area of the smaller SNCs actually allows for more interfacial charge transfer.[5] Kamat et al. states that manipulation of interfacial charge transfer is the most important factor that can assist in improving the photocatalytic conversion efficiency and efforts need to be made to manipulate this process by surface and structural modification.[15] Therefore, through Marcus-Gerischer theory, it is expected that as we modify our SNCs to have a smaller diameter, we would increase the bandgap and effectively shift the LUMO to more reducing and the HOMO to more oxidizing potentials. This in turn would increase the thermodynamic driving force which would then increase the interfacial charge transfer, allowing for the most photocatalytic activity by the smallest diameter SNCs.[5] It is clear that our size-dependent photocatalytic activity corroborates with literature reports, where the highest rate of photocatalytic hydrogen evolution (water splitting) was observed for the smallest diameter CdSe SNCs[86] and also in agreement with the theoretical prediction.[87]

We propose that our observed photocatalytic decomposition of phenol is initiated by the oxygen radical ($O_2^{\bullet-}$) as shown in Figure 4.11 A. During this process, the photoexcited electrons undergo thermodynamically-controlled interfacial charge transfer (as explained above) and react with dissolved O_2. Our first order rate (min^{-1}) of phenol decomposition, calculated using equation 4.2, with respect to E_{gap}^{el} is small. (Appendix F) Here, C_0 and C is the absorption intensity of the pollutant before and after degradation, respectively.

$$\ln(C_0/C)=kt \qquad (4.2)$$

Since our photocatalytic reaction was performed under homogeneous conditions, the interfacial kinetics (reduction of O_2 to $O_2^{\bullet-}$) could be the rate-limiting step, not the

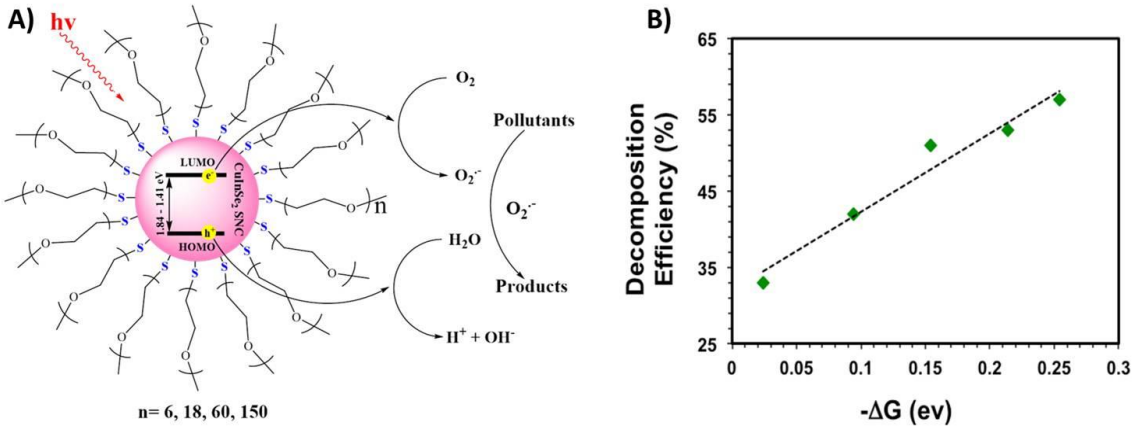

Figure 4.11: (A) Schematic representation of photoexcitation to generate electrons and holes followed by reduction of O_2 and oxidation of H_2O. Photogenerated $O_2^{\bullet-}$ performs photodegradation of pollutants. (B) Decomposition efficiency as a function of thermodynamic driving force (-ΔG) for electron transfer, $R^2 = 0.961$.

mass transport of the reactants to the $CuInSe_2$ SNC surface. [88] Additionally, oxygen reduction in water is an inner-sphere electron transfer reaction which suggests that our system also follows an inner- electron transfer mechanism sphere (strong electronic interaction between the oxidant and reactant) to reduce O_2 to $O_2^{\bullet-}$. This is similar to the reported mechanism of mettalloenzyme, Cu-amine oxidase.[89] The inner-sphere electron transfer mechanism is very complicated, and as such a detailed explanation of this process is outside of our expertise. However, according to Marcus theory[5, 90, 91], under these conditions, the electron transfer rate constant from $CuInSe_2$ SNCs to O_2 would depend on the -ΔG as shown in equation 4.3. [86, 87]

$$k_{red} \propto exp\left(-\frac{(\Delta G-\lambda)^2}{4kT\lambda}\right) \qquad (4.3)$$

Where, k_{red} is the electron transfer rate constant, and λ and k are the reorganization energy and Boltzmann constant, respectively. Thermodynamic driving force, ΔG, is the difference of between the quasi Fermi level in the SNCs[92] (most commonly estimated as

the LUMO of the SNC)[86] and the oxygen reduction potential oxygen reduction potential (E_{red}^{0}, -0.046 vs. NHE).[93] ΔG was calculated using equation 4.4, where E_{LUMO} represents the LUMO position of different sizes of PEG_6-thiolate coated $CuInSe_2$ SNCS.

$$\Delta G = -e(E_{LUMO} - E_{red}^{0}) \qquad (4.4)$$

Figure 4.11 B depicts the linear relationship between decomposition efficiency and -ΔG where the highest decomposition efficiency (smallest size) was observed to have the strongest driving force (more negative). As discussed above, Marcus-Gerischer theory states that as the size of the SNC decreases, the LUMO of the SNC shifts toward more negative (vs. NHE) potential, thus making the ΔG more negative.[5] Therefore, our data stongly corroborates with theory, as well as, previous studies of size-dependent electron

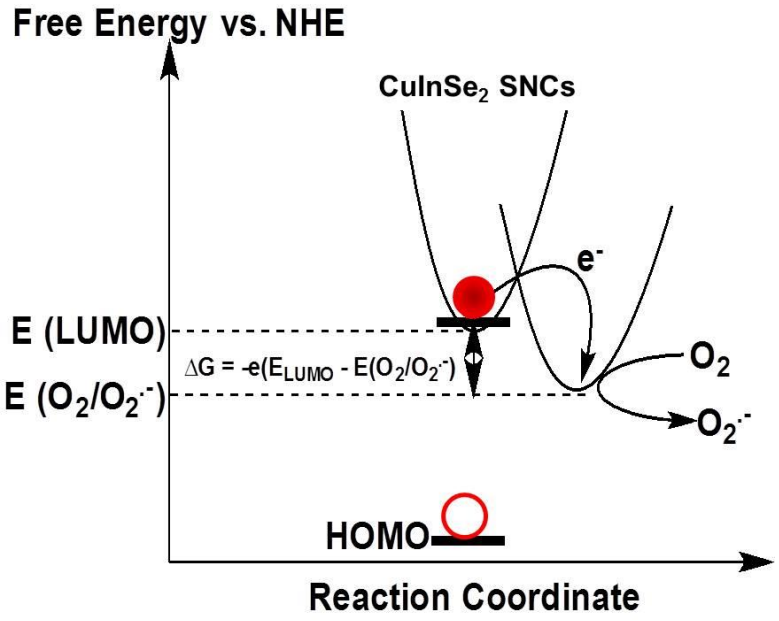

Figure 4.12: Change in free energy as a function of reaction coordinates for $O_2 \rightarrow O_2^{\bullet -}$ reduction (cite 16) under homogeneous conditions in which O_2 reacts at the surface of $CuInSe_2$ SNCs. The electron (red dot)-hole (open circle) pair is formed during illumination via visible light. For simplification, the effect of solvent molecules in activation energy was not considered.

transfer processes in solid-solid interface, where the smallest size displayed the highest transfer rate constant. [16, 18] Thus we conclude that the position of the SNC LUMO is critical for solid-liquid charge transfer which controls the rate of O_2 reduction. Figure 4.12 represents a qualitative free-energy versus reaction coordinate diagram for the electron transfer reaction described above and the subsequent reduction of O_2 to $O_2^{\bullet-}$.[94]

Since we hypothesized that interfacial charge transfer, not size dictates the decomposition efficiency, we also compared the $J_{e/h}$ to the decomposition efficiency. Figure 4.9 B showed an inverse relationship between $J_{e/h}$and SNC diameter, where the smallest diameter has the highest $J_{e/h}$. Despite what one might expect (higher $J_{e/h}$ values suppress charge separation resulting in slow interfacial charge transfer and therefore low catalytic activity), we observed a nearly linear relationship between $J_{e/h}$ and decomposition efficiency (diameter ≤4.1 nm). (Figure 4.13) This is in further contrast to computational studies in which the probability of electron-hole recombination increases with increasing Je/h (decreased SNC size) causing decreased interfacial charge transfer. However, theoretical calculations have shown that the kinetic energy of electrons and/or holes is

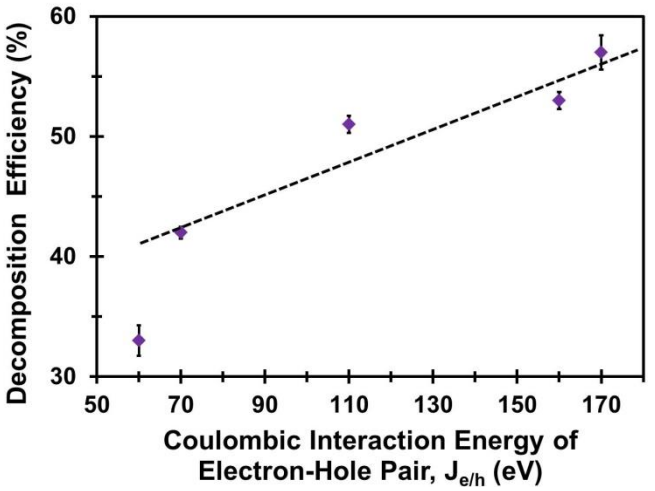

Figure 4.13: Phenol decomposition as a function of Coulombic interaction energy of e/h pair as determined from the difference between electrochemical- and optical- band gaps of different-sized PEG_6-thiolate coated $CuInSe_2$ SNCs.

higher than the $J_{e/h}$ for highly quantum-confined (smaller) SNCs. [28] Therefore, as described in previous chapters, the increased kinetic energy would facilitate the expansion of the exciton wave function which would promote charge transfer processes at the solid-liquid interface.

Thus, the small size, allowing for the strongest driving force, allowed for more solid-liquid charge transfer, which in turn, produced the highest photocatalytic efficiency. This system is the first of its kind in that it produced adequate charge transfer without coupling with large-band gap semiconductors such as TiO_2 which act as electron collectors in order to perform catalytic reactions. [2, 22, 95] Furthermore, the unique surface passivation provided by PEG-thiolate allows for stable, homogeneous photocatalytic reactions without the use of sacrificial agents, thus making the system sustainable. Unlike many reported photocatalytic reactions, the use of sacrificial hole scavengers is not needed due to the excellent solubility properties of PEG_6-thiolate coated $CuInSe_2$ SNCs in water allowing the photogenerated holes to oxidize water to H^+ and $OH^\bullet$ without undergoing SNC decomposition. (See Figure 4.11 A) These properties are unlike those provided by long-chain hydrophobic ligands such as OLA which inhibit charge transport. Therefore, it is important to fully investigate the effects of surface passivating ligands on the photocatalytic activity of $CuInSe_2$ SNCs.

4.4.4 Surface Ligand-Dependent Photocatalysis

As discussed previously, surface ligation affects not only solubility and stability, but also charge transport properties of the SNC. Long-chain insulating ligands, such as OLA for example, obstruct transport of charge carriers. We hypothesized that although we saw remarkable charge transport leading to high photocatalytic efficiency of PEG_6-

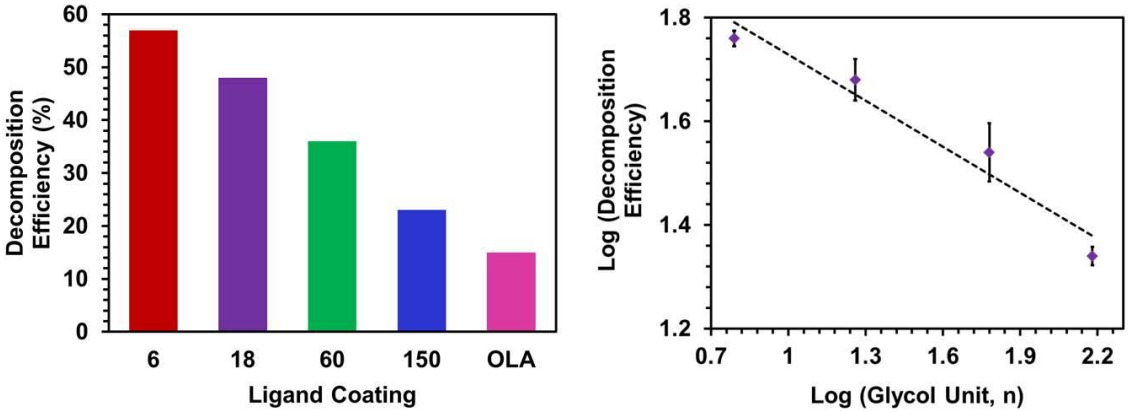

Figure 4.14: (A) Photocatalytic decomposition efficiency of 1.8 nm diameter $CuInSe_2$ SNCs as a function of ligand chain length PEGn-thiolate and OLA. Decomposition efficiency was measured using visible light illumination (<450 nm) for 2h. (B) Log-Log plot of decomposition efficiency as a function of glycol unit.

thiolate coated $CuInSe_2$ SNCs, increased chain length PEGs would produce insulating barriers similar to OLA. Therefore, through a systematic modulation of PEGn-thiolate (n= 6, 18, 60, and 15) chain length on 1.8 nm diameter $CuInSe_2$ SNCs and comparison with OLA-passivated SNCs, we were able to study the effect of surface ligand chemistry on charge transport and ultimately photocatalytic efficiency.

Figure 4.14 A depicts the photocatalytic decomposition efficiency of PEG-thiolate coated $CuInSe_2$ as a function of PEG chain length. As expected, the SNC coated with the shortest PEG_n chain (n=6) displayed the highest photocatalytic efficiency (~60%) , whereas the longest PEG_n chain (n=150) provided the lowest (~25 %). According to our calculations (ChemBioDraw 14.0), the fully stretched length of PEG_6- and PEG_{18}-thiolate is ~2.2 and 6.2 nm, respectively. Thus a mere 4.4 nm difference in chain length resulted in drastically different photocatalytic activity. When compared to OLA-passivated $CuInSe_2$ SNCs, a near 4-fold increase (~15 % to 60%) in efficiency for PEG_6-thiolate coated $CuInSe_2$ SNCs was observed. Whereas, PEG_{150}-thiolate- had comparable

efficiency to OLA-passivated $CuInSe_2$ SNCs with only 10% higher photocatalytic activity observed using PEG_{150}-thiolate. Moreover, Figure 4.14 B demonstrates a log-log plot of decomposition efficiency versus glycol unit (n) in which the decomposition efficiency follows a negative power of n function. Therefore, by increasing the ligand thickness and overall insulating properties of the ligand monolayer, ineffective charge transport of photogenerated charge carriers causing decreased photocatalytic activity. Thus, by modulating the ligand chemistry, we confirmed our hypothesis that long chain

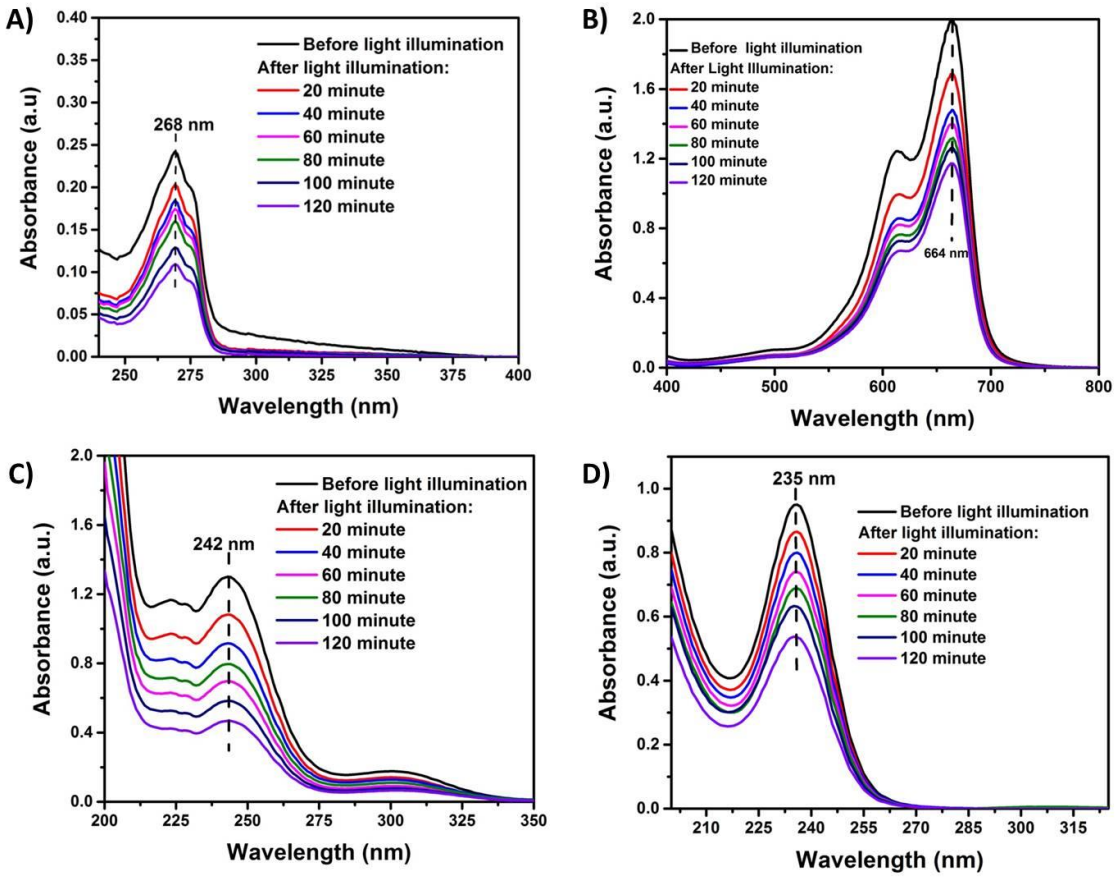

Figure 4.15: Time-dependent UV-visible absorption spectra of (A) phenol, (B) methylene blue, (C) DMPD, (D) thiourea during visible light illumination in the presence of 1.8 nm diameter, PEG_6-thiolate coated $CuInSe_2$ SNCs. Illumination used a 350 W xenon arc lamp with 450 nm cutoff filter.

length ligands become insulating in nature, which hinders the charge transport processes and overall photocatalytic activity. Therefore shorter, more conductive ligands are ideal for photocatalysis.

Lastly, we investigated the effectiveness of our photocatalyst for pollutant degradation using a diverse range of pollutants including those that are colorless. (Figure 4.15) Colorless pollutants do not display photoexcitation like dyes do because of the band gap in the UV region of the solar spectrum. Therefore, unlike most commonly studied dye degradation, it is more difficult to perform photodegradation of colorless pollutants under illumination of visible light. Diversity of our system is important for its future use in AOPs. Details of the experimental design can be found in the Experimental Section and followed similar parameters as those used for phenol, described above. PEG_6-thiolate passivated, 1.8 nm diameter $CuInSe_2$ SNCs were used for all pollutants studied. From Figure 4.16, it can be observed that photocatalytic efficiencies above 35% were achieved

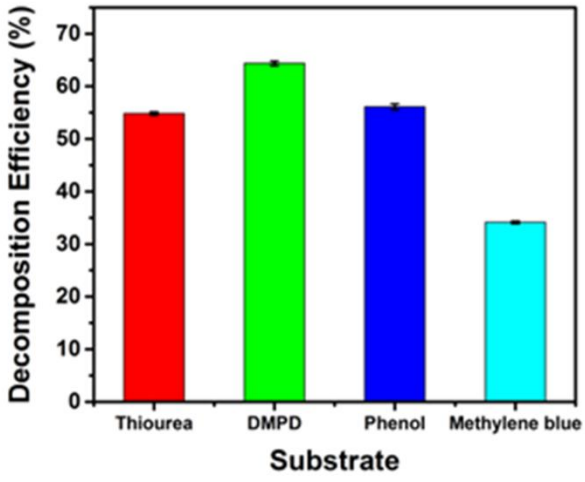

Figure 4.16: Comparison of photocatalytic decomposition efficiency of various water-soluble pollutants using 1.8 nm diameter, PEG_6-thiolate coated $CuInSe_2$ SNCs. Decomposition efficiency was measured after 2h using visible light illumination (<450 nm).

for all pollutants studied (phenol, DMPD, and thiourea, and methylene blue) with the highest efficiency observed for DMPD (65%) demonstrating the unique and versatile catalytic behavior of our system.

Therefore, both size and surface ligand chemistry played a vital role in our enhanced photocatalytic activity of $CuInSe_2$ SNCs. By combining small (<6.0 nm) SNCs with their appropriate ligation (PEG-thiolate) we were able to provide adequate solubility and charge transfer allowing for AOPs without the use of large band gap metal oxides, which are commonly needed to extract photogenerated charges from SNCs. However, using our PEG-thiolate passivated $CuInSe_2$ SNCs; we observed a low degradation rate constant. (Appendix F) This could be due to the unpassivated Se sites, as discussed previously, causing surface defect sites that hinder the effective interfacial charge transfer. Therefore, it is possible that our system could benefit from mixed surface ligation such as that provided in chapter 2 of this dissertation. Appropriate choice of mixed ligation could provide nearly complete surface passivation thus preventing nonradiative trap states as well as the expansion of the wave function into the ligand monolayer which would further facilitate the electron transfer process. Therefore, we believe our unique system coupled with mixed ligation will allow for the preparation of SNCs with unprecedented photocatalytic activity for a variety of AOPs including H_2 evolution and decomposition of pollutants.

4.5 Conclusion

In this chapter, we have presented the first study of $CuInSe_2$ SNCs size and ligand dependent photocatalytic efficiency under homogeneous conditions. It was found that the smallest SNCs displayed the highest decomposition efficiency of pollutants in water.

Surface ligation made this study possible by providing solubility and conductivity through the exchange of the native insulating OLA by PEG-thiolate. These unique solubility properties also allowed us to perform solution-phase electrochemical analysis thus providing quantitative information about HOMO and LUMO position of our SNC, $J_{e/h}$, and ΔG. This analysis demonstrated the vital role of interfacial charge transfer on light-driven AOPs such as photocatalytic decomposition of pollutants using SNCs. Lastly, this photocatalysis was found to be strongly ligand dependent with shorter chain length PEG-thiolate providing the highest photocatalytic efficiency. It was found that appropriate choice of surface ligation is imperative in order to provide the necessary charge transport efficiency through the ligand monolayers while maintaining stability and dispersibility of the SNC. Interestingly, it was found that our PEG_6-thiolate coated $CuInSe_2$ SNCs were stable during photocatalytic reactions which we attribute to the covalent nature of the sulfur bound (Cu-S and In-S). Therefore, we believe this comprehensive study will expedite quantitative electrochemical characterization and provide new insight into the design of highly efficient, sustainable photocatalysts without the use of large band-gap metal oxides or sacrificial agents.

4.6 References

1. C. Jiang, J.-S. Lee and D. V. Talapin, *J. Am. Chem. Soc.*, 2012, 134, 5010-5013.

2. F. Shen, W. Que, Y. He, Y. Yuan, X. Yin and G. Wang, *ACS Appl. Mater. Interfaces*, 2012, 4, 4087-4092.

3. A. Singh, C. Coughlan, D. J. Milliron and K. M. Ryan, *Chem. Mater.*, 2015, 27, 1517-1523.

4. A. Kudo and Y. Miseki, *Chem. Soc. Rev.*, 2009, 38, 253-278.

5. F. E. Osterloh, *Chem. Soc. Rev.*, 2013, 42, 2294-2320.

6. K. Maeda and K. Domen, *J. Phys. Chem. Lett.*, 2010, 1, 2655-2661.

7. N. Serpone and A. V. Emeline, *J. Phys. Chem. Lett.*, 2012, 3, 673-677.

8. W. Fan, Q. Zhang and Y. Wang, *Phys. Chem. Chem. Phys.*, 2013, 15, 2632-2649.

9. N. S. Lewis and D. G. Nocera, *Proc. Natl. Acad. Sci. USA*, 2006, 103, 15729-15735.

10. X. Hu, G. Li and J. C. Yu, *Langmuir*, 2010, 26, 3031-3039.

11. C. Harris and P. V. Kamat, *ACS Nano*, 2009, 3, 682-690.

12. M. D. Peterson, L. C. Cass, R. D. Harris, K. Edme, K. Sung and E. A. Weiss, *Annu. Rev. Phys. Chem.*, 2014, 65, 317-339.

13. G. D. Scholes, M. Jones and S. Kumar, *J. Phys. Chem. C*, 2007, 111, 13777-13785.

14. Y. Xie, M. B. Teunis, B. Pandit, R. Sardar and J. Liu, *J. Phys. Chem. C*, 2015, 119, 2813-2821.

15. P. V. Kamat, *J. Phys. Chem. Lett.*, 2012, 3, 663-672.

16. I. Robel, M. Kuno and P. V. Kamat, *J. Am. Chem. Soc.*, 2007, 129, 4136-4137.

17. N. Wu, J. Wang, D. N. Tafen, H. Wang, J.-G. Zheng, J. P. Lewis, X. Liu, S. S. Leonard and A. Manivannan, *J. Am. Chem. Soc.*, 2010, 132, 6679-6685.

18. K. Tvrdy, P. A. Frantsuzov and P. V. Kamat, *Proc. Natl. Acad. Sci. USA*, 2011, 108, 29-34.

19. F. E. Osterloh, *Chem. Mater.*, 2007, 20, 35-54.

20. K. Ramasamy, B. Tien, P. S. Archana and A. Gupta, *Mater. Lett.*, 2014, 124, 227-230.

21. Y. C. Choi, E. J. Yeom, T. K. Ahn and S. I. Seok, *Angew. Chem., Int. Ed.*, 2015, 54, 4005-4009.

22. F. Shen, W. Que, Y. Liao and X. Yin, *Ind. Eng. Chem. Res.*, 2011, 50, 9131-9137.

23. L. Zheng, Y. Xu, Y. Song, C. Wu, M. Zhang and Y. Xie, *Inorg. Chem.*, 2009, 48, 4003-4009.

24. Y.-S. Park, A. Dmytruk, I. Dmitruk, A. Kasuya, Y. Okamoto, N. Kaji, M. Tokeshi and Y. Baba, *J. Phys. Chem. C*, 2010, 114, 18834-18840.

25. A. W. Snow and E. E. Foos, *Synthesis*, 2003, 4, 509-512.

26. M. Kar, R. Agrawal and H. W. Hillhouse, *J. Am. Chem. Soc.*, 2011, 133, 17239-17247.

27. M. L. Steigerwald and L. E. Brus, *Acc. Chem. Res.h*, 1990, 23, 183–188.

28. L. E. Brus, *J. Chem. Phys*, 1984, 80, 4403-4409.

29. J. Jasieniak and P. Mulvaney, *J. Am. Chem. Soc.*, 2007, 129, 2841-2848.

30. N. C. Anderson, M. P. Hendricks, J. J. Choi and J. S. Owen, *J. Am. Chem. Soc.*, 2013, 135, 18536-18548.

31. K. E. Knowles, D. B. Tice, E. A. McArthur, G. C. Solomon and E. A. Weiss, *J. Am. Chem. Soc.*, 2009, 132, 1041-1050.

32. I. Moreels, B. Fritzinger, J. C. Martins and Z. Hens, *J. Am. Chem. Soc.*, 2008, 130, 15081-15086.

33. D. C. Reifsnyder, X. Ye, T. R. Gordon, C. Song and C. B. Murray, *ACS Nano*, 2013, 7, 4307-4315.

34. O. Yarema, D. Bozyigit, I. Rousseau, L. Nowack, M. Yarema, W. Heiss and V. Wood, *Chem. Mater.*, 2013, 25, 3753-3757.

35. M. G. Panthani, C. J. Stolle, D. K. Reid, D. J. Rhee, T. B. Harvey, V. A. Akhavan, Y. Yu and B. A. Korgel, *J. Phys. Chem. Lett.*, 2013, 4, 2030-2034.

36. E. Cassette, T. Pons, C. Bouet, M. Helle, L. Bezdetnaya, F. Marchal and B. Dubertret, *Chem. Mater.*, 2010, 22, 6117-6124.

37. J. Tang, S. Hinds, S. O. Kelley and E. H. Sargent, *Chem. Mater.*, 2008, 20, 6906-6910.

38. J.-J. Wang, Y.-Q. Wang, F.-F. Cao, Y.-G. Guo and L.-J. Wan, *J. Am. Chem. Soc.*, 2010, 132, 12218-12221.

39. Q. Guo, S. J. Kim, M. Kar, W. N. Shafarman, R. W. Birkmire, E. A. Stach, R. Agrawal and H. W. Hillhouse, *Nano Lett.*, 2008, 8, 2982-2987.

40. M. E. Norako and R. L. Brutchey, *Chem. Mater.*, 2010, 22, 1613-1615.

41. J. Xu, C.-S. Lee, Y.-B. Tang, X. Chen, Z.-H. Chen, W.-J. Zhang, S.-T. Lee, W. Zhang and Z. Yang, *ACS Nano*, 2010, 4, 1845-1850.

42. B. Koo, R. N. Patel and B. A. Korgel, *J. Am. Chem. Soc.*, 2009, 131, 3134-3135.

43. Y. Liu, D. Yao, L. Shen, H. Zhang, X. Zhang and B. Yang, *J. Am. Chem. Soc.*, 2012, 134, 7207-7210.

44. S. Dolai, P. R. Nimmala, M. Mandal, B. B. Muhoberac, K. Dria, A. Dass and R. Sardar, *Chem. Mater.*, 2014, 26, 1278-1285.

45. X. Wang, X. Liu, D. Yin, Y. Ke and M. T. Swihart, *Chem. Mater.*, 2015, 27, 3378-3388.

46. K. Nose, T. Omata and S. Otsuka-Yao-Matsuo, *J. Phys. Chem. C*, 2009, 113, 3455-3460.

47. H. Zhong, Z. Wang, E. Bovero, Z. Lu, F. C. J. M. van Veggel and G. D. Scholes, *J. Phys. Chem. C*, 2011, 115, 12396-12402.

48. P. M. Allen and M. G. Bawendi, *J. Am. Chem. Soc.*, 2008, 130, 9240-9241.

49. R. Schlaf, B. A. Parkinson, P. A. Lee, K. W. Nebesny and N. R. Armstrong, *J. Phys. Chem. B*, 1999, 103, 2984-2992.

50. L. S. Liao, M. K. Fung, C. S. Lee, S. T. Lee, M. Inbasekaran, E. P. Woo and W. W. Wu, *Appl. Phys. Lett.*, 2000, 76, 3582-3584.

51. J. P. Perdew, *Int. J. Quantum Chem.*, 1985, 28, 497-523.

52. F. Bechstedt and R. Del Sole, *Phys. Rev. B*, 1988, 38, 7710-7716.

53. M. Grüning, A. Marini and A. Rubio, *J. Chem. Phys*, 2006, 124, 154108.

54. T. Fabien, B. Peter and S. Karlheinz, *J. Phys. Condens. Matter*, 2007, 19, 196208.

55. V. Lesnyak, C. George, A. Genovese, M. Prato, A. Casu, S. Ayyappan, A. Scarpellini and L. Manna, *ACS Nano*, 2014, 8, 8407-8418.

56. H. Zhong, S. S. Lo, T. Mirkovic, Y. Li, Y. Ding, Y. Li and G. D. Scholes, *ACS Nano*, 2010, 4, 5253-5262.

57. M. Ahmadi, S. S. Pramana, S. K. Batabyal, C. Boothroyd, S. G. Mhaisalkar and Y. M. Lam, *Inorg. Chem.*, 2013, 52, 1722-1728.

58. A. J. F. Bard, L. R. , *Electrochemical Methods: Fundamentals and Applications*, 2nd edn., 2001.

59. M. Amelia, C. Lincheneau, S. Silvi and A. Credi, *Chem. Soc. Rev.*, 2012, 41, 5728-5743.

60. S. K. Haram, B. M. Quinn and A. J. Bard, *J. Am. Chem. Soc.*, 2001, 123, 8860-8861.

61. S. N. Inamdar, P. P. Ingole and S. K. Haram, *ChemPhysChem*, 2008, 9, 2574-2579.

62. E. Kuçur, W. Bücking, S. Arenz, R. Giernoth and T. Nann, *ChemPhysChem*, 2006, 7, 77-81.

63. E. Kucur, J. Riegler, G. A. Urban and T. Nann, *J. Chem. Phys*, 2003, 119, 2333-2337.

64. C. Querner, P. Reiss, S. Sadki, M. Zagorska and A. Pron, *Phys. Chem. Chem. Phys.*, 2005, 7, 3204-3209.

65. P. P. Ingole, G. B. Markad, D. Saraf, L. Tatikondewar, O. Nene, A. Kshirsagar and S. K. Haram, *J. Phys. Chem. C*, 2013, 117, 7376-7383.

66. S. K. Poznyak, N. P. Osipovich, A. Shavel, D. V. Talapin, M. Gao, A. Eychmüller and N. Gaponik, *J. Phys. Chem. B*, 2005, 109, 1094-1100.

67. J. Liu, W. Yang, Y. Li, L. Fan and Y. Li, *Phys. Chem. Chem. Phys.*, 2014, 16, 4778-4788.

68. E. Kucur, W. Bücking, R. Giernoth and T. Nann, *J. Phys. Chem. B*, 2005, 109, 20355-20360.

69. Z. Ding, B. M. Quinn, S. K. Haram, L. E. Pell, B. A. Korgel and A. J. Bard, *Science*, 2002, 296, 1293-1297.

70. N. Pradhan, D. Reifsnyder, R. Xie, J. Aldana and X. Peng, *J. Am. Chem. Soc.*, 2007, 129, 9500-9509.

71. S. Mourdikoudis and L. M. Liz-Marzán, *Chem. Mater.*, 2013, 25, 1465-1476.

72. M. E. Williams and R. W. Murray, *Chem. Mater.*, 1998, 10, 3603-3610.

73. M. E. Williams, H. Masui, J. W. Long, J. Malik and R. W. Murray, *J. Am. Chem. Soc.*, 1997, 119, 1997-2005.

74. R. Sardar, K. Lawrence, M. Johnson, S. Dolai and A. Kumbhar, *Nanoscale*, 2015.

75. K. N. Lawrence, S. Dolai, Y.-H. Lin, A. Dass and R. Sardar, *RSC Adv.*, 2014, 4, 30742-30753.

76. H. Qian, Y. Zhu and R. Jin, *ACS Nano*, 2009, 3, 3795-3803.

77. D. Lee, R. L. Donkers, G. Wang, A. S. Harper and R. W. Murray, *J. Am. Chem. Soc.* , 2004, 126, 6193-6199.

78. H. Ye, H. S. Park, V. A. Akhavan, B. W. Goodfellow, M. G. Panthani, B. A. Korgel and A. J. Bard, *J. Phys. Chem. C*, 2011, 115, 234-240.

79. J. W. Thackeray, M. J. Natan, P. Ng and M. S. Wrighton, *J. Am. Chem. Soc.*, 1986, 108, 3570-3577.

80. C. Wang, M. Shim and P. Guyot-Sionnest, *Science*, 2001, 291, 2390-2392.

81. S. Dolai, A. Dass and R. Sardar, *Langmuir*, 2013, 29, 6187-6193.

82. M. Soreni-Harari, N. Yaacobi-Gross, D. Steiner, A. Aharoni, U. Banin, O. Millo and N. Tessler, *Nano Lett.*, 2008, 8, 678-684.

83. J. Jasieniak, M. Califano and S. E. Watkins, *ACS Nano*, 2011, 5, 5888-5902.

84. R. W. Meulenberg, J. R. I. Lee, A. Wolcott, J. Z. Zhang, L. J. Terminello and T. van Buuren, *ACS Nano*, 2009, 3, 325-330.

85. J. M. Buriak, P. V. Kamat and K. S. Schanze, *ACS Appl. Mater. Interfaces*, 2014, 6, 11815-11816.

86. M. A. Holmes, T. K. Townsend and F. E. Osterloh, *Chem. Commun*, 2012, 48, 371-373.

87. H. Gerischer, *Electrochimica Acta*, 1990, 35, 1677-1699.

88. D. P. Chen, W. Bowers and S. E. Skrabalak, *Chem. Mater.*, 2015, 27, 174-180.

89. A. Mukherjee, V. V. Smirnov, M. P. Lanci, D. E. Brown, E. M. Shepard, D. M. Dooley and J. P. Roth, *J. Am. Chem. Soc.*, 2008, 130, 9459-9473.

90. R. A. MARCUS, *J. Chem. Phys*, 1956, 24, 966-978.

91. R. A. Marcus, *J. Chem. Phys*, 1965, 43, 679-701.

92. R. Memming, in *Electron Transfer I*, ed. J. Mattay, Springer Berlin Heidelberg, 1994, vol. 169, pp. 105-181.

93. N. Soltani, E. Saion, M. Z. Hussein, M. Erfani, A. Abedini, G. Bahmanrokh, M. Navasery and P. Vaziri, *Int. J. Mol. Sci.* 2012, 13, 12242.

94. J. Zhao, M. A. Holmes and F. E. Osterloh, *ACS Nano*, 2013, 7, 4316-4325.

95. Y. Ma, X. Wang, Y. Jia, X. Chen, H. Han and C. Li, *Chem. Rev.* , 2014, 114, 9987-10043.

4.7 Appendix

Appendix A: PL spectra of two different sizes of $CuInSe_2$ SNCs in toluene at 600 nm excitation.

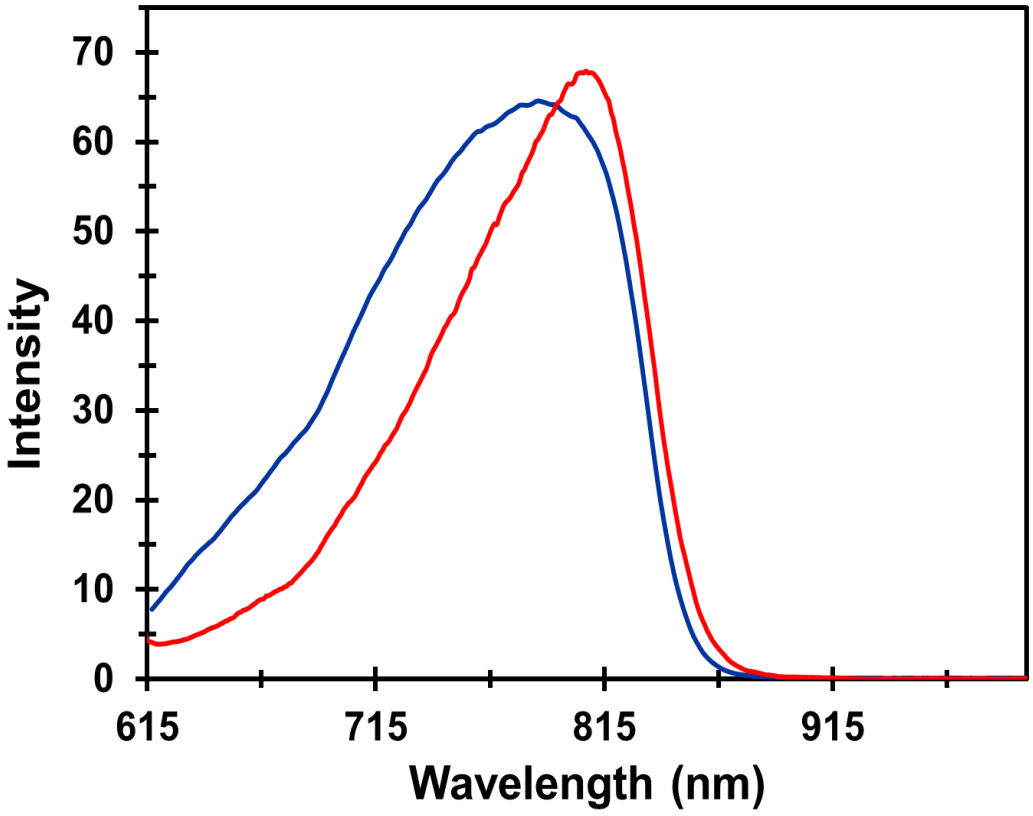

PL spectra of 1.8 (blue) and 2.4 (red) nm diameter, OLA-passivated $CuInSe_2$ SNCs in toluene at 600 nm excitation.

Appendix B: HRTEM images of OLA-coated $CuInSe_2$ SNCs.

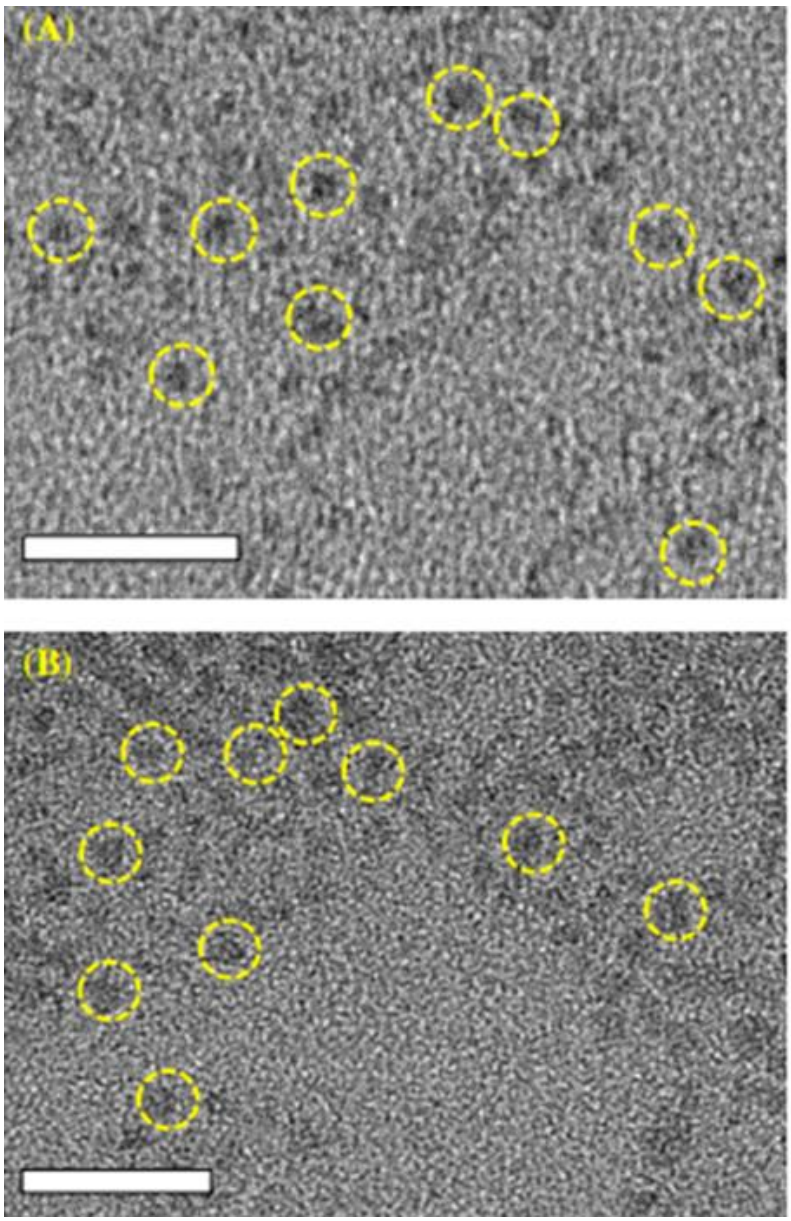

HRTEM images of OLA-coated, (A) 1.8 nm and (B) 2.4 nm diameter $CuInSe_2$ SNCs. The spherical nature of the SNCs is marked by circular outlines. Scale bars are 20 nm.

Appendix C: Size distribution of 1.8-5.3 nm diameter, $CuInSe_2$ SNCs.

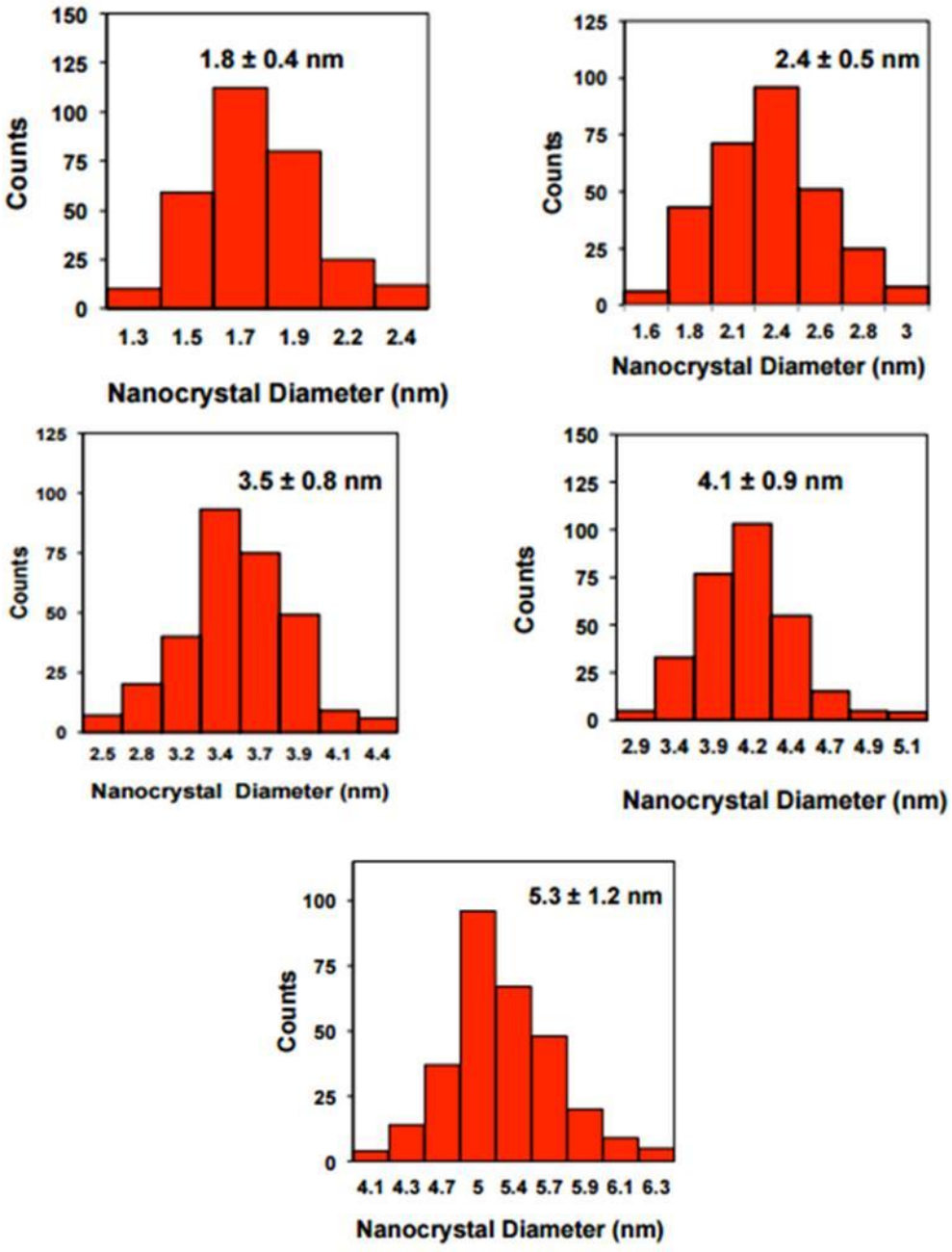

Size distribution of 1.8-5.3 nm diameter, $CuInSe_2$ SNCs. In each case, 300 SNCs were counted.

Appendix D: Expanded region XRD of 1.8 nm diameter $CuInSe_2$ SNCs.

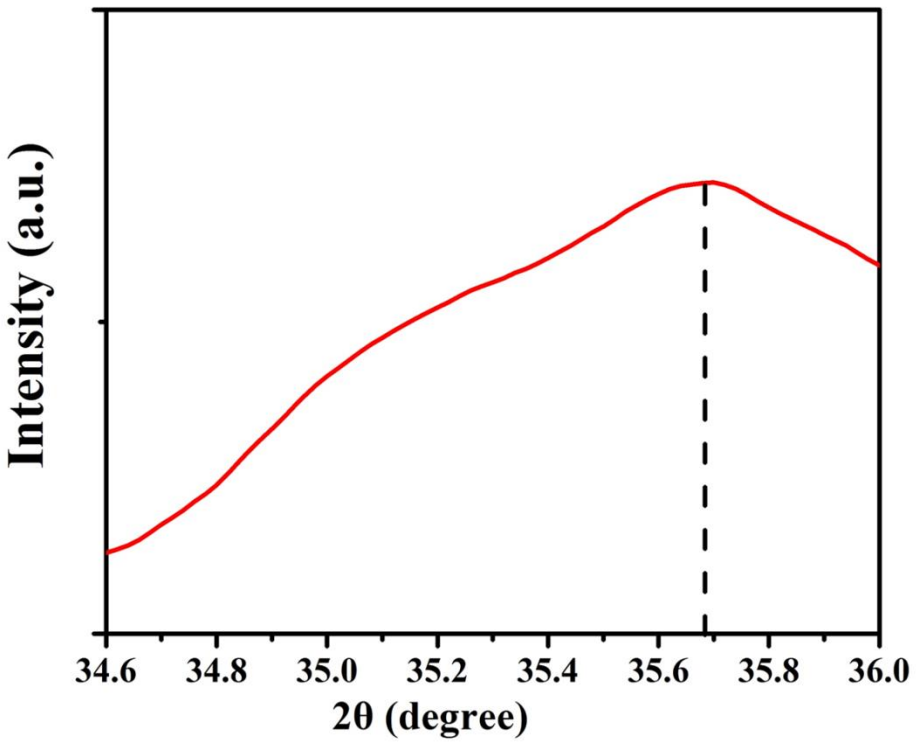

Expanded region XRD of 1.8 nm diameter $CuInSe_2$ SNCs. Dashed line marks the characteristic chalcopyrite peak of (211) at 35.68 °.

Appendix E: ^{1}H NMR spectra of OLA- and PEG6-tholate coated $CuInSe_2$ SNCs and TEM image of PEG_6-thiolate passivated $CuInSe_2$ SNCs.

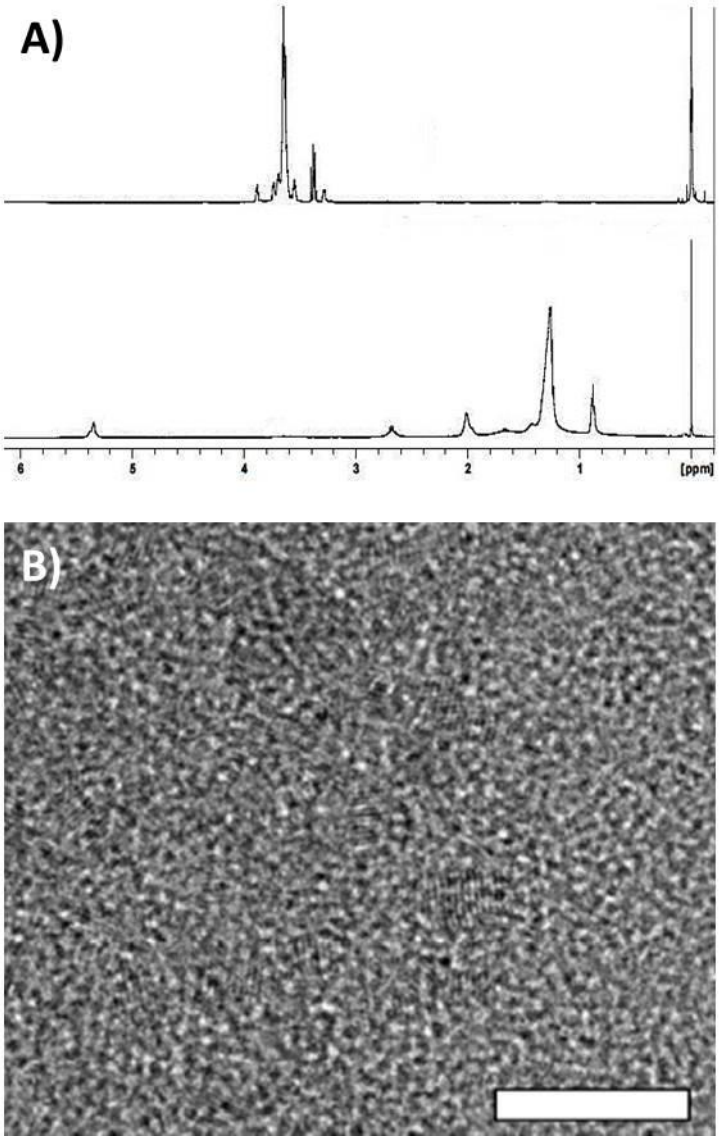

(A) ^{1}H NMR spectra of OLA- (bottom) and PEG6-tholate (top) coated, 1.8 nm diameter $CuInSe_2$ SNCs. Disappearance of the peak at 5.53 indicates complete removal of OLA from the surface of the SNC. (B) TEM image of PEG_6-thiolate passivated, 1.8 nm diameter $CuInSe_2$ SNCs. Scale bar is 10 nm.

Appendix G: First order rate constant of phenol decomposition using different sized $CuInSe_2$ SNCs as a function of time and diameter.

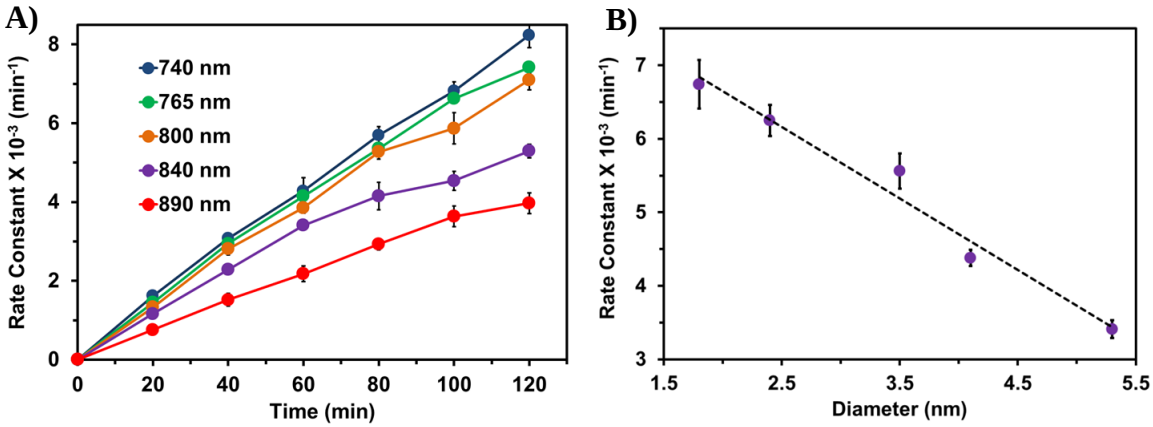

C)

Size	Rate constant ($minute^{-1}$)	Standard deviation	Degradation efficiency (%) (after 120 minute)	Standard deviation
1.8	$6.74x10^{-3}$	$3.3x10^{-4}$	57.0	0.8
2.4	$6.25x10^{-3}$	$2.1x10^{-4}$	53.0	0.7
3.5	$5.56x10^{-3}$	$2.4x10^{-4}$	51.0	1.3
4.1	$4.38x10^{-3}$	$1.1x10^{-4}$	42.0	0.5
5.3	$3.41x10^{-3}$	$1.2x10^{-4}$	33.0	1.3

First order rate constant of phenol decomposition using different sized $CuInSe_2$ SNCs as a function of (A) time and (B) diameter. (C) Tabulated phenol decomposition.

CONCLUSION

The purpose of this dissertation was to utilize surface ligand chemistry to investigate the optoelectronic properties of strongly quantum-confined SNCs without changing the parent structure. Through this work, we were able to explore the following specific aims: (1) investigate the delocalization of exciton wave functions of SNCs into the ligand monolayer, (2) explore ligand-controlled electronic coupling of SNCs both in colloidal and solid states, and (3) characterize solution-state electrochemical properties and photocatalytic activity of ternary SNCs as a function of their size and surface ligand chemistry.

Chapter 1 introduces the background and literature review of colloidal SNCs as well as the current problems faced by this material. Throughout this thesis, we utilize the large surface to volume ratio of ultrasmall SNCs to tailor the surface ligand chemistry which resulted in dramatic changes to the SNC properties. In Chapter 2, we studied the exciton delocalization in which the wave function expanded into the ligand monolayer. By using $Cd(O_2CPh)_2$ to bind to OLA-coated $(CdSe)_{34}$ SNCs we achieved mixed ligation that had a two-fold effect: (1) facilitating delocalization of the excitonic wave function into the ligand monolayer (~240 meV red-shift) and (2) passivation of trap states resulting in increased PL-QY (~73%). These observations were reversible upon displacement of $Cd(O_2CPh)_2$ with TMEDA. Furthermore, characterization by XRD and

additional control experiments has shown that the red-shifts in peak positions were a consequence of the delocalization of strongly confined exciton holes into the interfacial electronic states that were formed from interactions between the HOMO of the SNCs and the LUMO of the $Cd(O_2CPh)_2$ as oppose to originating from a change in the size or relaxation of the inorganic core. Additionally, attachment of $Cd(O_2CPh)_2$ to the OLA-coated $(CdSe)_{34}$ SNC surface increased the PL-QY to an unprecedentedly high 73% and causes a three-fold increase in radiative lifetime, which was attributed to both passivation of nonradiative surface trap states and exciton delocalization. This chapter demonstrated the importance of appropriate surface ligand chemistry in controlling the excitonic absorption and emission properties of ultrasmall $(CdSe)_{34}$ SNCs which has significant implications in solid state device fabrication.

This importance of surface ligand chemistry was further studied in Chapter 3 where we demonstrated the role of PEGn-thiolate in solubility, stability, and electronic coupling. We first developed a direct synthesis and purification procedure for PEGn-thiolate-coated $(CdSe)_{34}$ SNCs, in which the SNCs were synthesized in aqueous medium and purified using a simple solvent extraction method. The organic phase-extracted CdSe SNCs were readily soluble in a wide range of polar and nonpolar organic solvents including acetonitrile, ethanol, chlorobenzene, dichloromethane, and chloroform, as well as in water. This diverse solubility allowed us to perform a post-synthetic surface ligand treatment with TPP which increased the PL-QY 8 fold. This improvement of photophysical property is vital for many applications including biological imaging and optoelectronic devices. Additionally, PEGn-thiolate provided not only stability and solubility, but facilitated the expansion of the exciton wave function past the ligand

monolayer allowing for strong inter-SNC electronic coupling (170 meV). Furthermore, this interaction could be further modulated by changing the PEGn chain length and SNC diameter where the smallest size and shortest chain exhibited the largest coupling energy. Lastly, the electronic coupling was monitored as a function of annealing temperature where we provided some of the first crack-free films and therefore superior charge transport properties. We believe this work provides vital information for a variety of applications including bionanotechnology and large-scale production of highly efficient electronic materials for optoelectronic devices.

Lastly, in Chapter 4, we utilize the PEGn-thiolate ligand's unique solubility and ability to facilitate exciton delocalization in order to perform solution phase electrochemical characterization and photocatalytic activity of $CuInSe_2$ SNCs. This was the first report of the effects of structural parameters (size and surface chemistry) of $CuInSe_2$ SNCs on visible light driven photocatalysis. Due to the unique solubility provided by PEG-thiolate, inner-sphere electron transfer reactions (O_2 to $O_2^{\bullet-}$) at the SNC surface occurred allowing for sustainable photocatalytic decomposition of pollutants. Additionally, solution phase electrochemical characterization of our PEG-thiolate-coated $CuInSe_2$ SNCs showed that the thermodynamic driving force ($-\Delta G$) for oxygen reduction, which increased with decreased SNC size, was the dominate contributor to the photocatalytic process when compared to the light absorption and coulombic interaction energies of electron hole pair ($J_{e/h}$) contributions. Lastly, photocatalytic decomposition of pollutants as a function of ligand chain length was studied in which the shortest chain had the most photocatalytic activity. PEG-thiolate coated CuInSe2 was found to significantly increased pollutant degradation of a variety of pollutants both colored and clear.

Therefore, our PEGn-thiolate coated $CuInSe_2$ SNCs could be utilized for a variety of AOPs including H_2 evolution and decomposition of pollutants.

Overall, this dissertation provides valuable information for the use of ultrasmall SNCs over a variety of applications including: bionanotechnology, optoelectronics, and photocatalysis. Due to the large surface to volume ratio that these SNCs provide, we are able to minutely change the surface ligand chemistry to provide dramatic results.

VITA

VITA

Katie N. Lawrence, Ph.D.

EDUCATION

Indiana University-Purdue University Indianapolis **08/2016**
Doctorate (Ph.D.) in Analytical Chemistry
Dissertation: Tuning Optoelectronic Properties of Small Semiconductor Nanocrystals through Surface Ligand

Ball State University, Muncie, IN **05/2011**
Bachelors of Science in Chemistry *(ACS certification.)*
Food management minor

South Decatur Jr.-Sr. High School, Greensburg, IN **05/2007**
Academic Honors, Valedictorian

RELATED EXPERIENCE

American National University, Indianapolis, IN
2016-present
Adjunct Professor (Chemistry and Business Math)

- Prepare lectures and lesson plans
- Instruct students in chemistry and math
- Hold office hours and be available for questions

IUPUI Department of Chemistry and Chemical Biology, Indianapolis, IN
2011-2016
Teaching Assistant, Lab Advisor, and Recitation Instructor

- Accurately ran general chemistry laboratories with approximately 25-30 students each
- Knew all laboratory exercises and their procedures
- Followed and explained all safe practices and procedures as set by Environmental Health Services

Ball State Department of Chemistry, Muncie, IN
2009-2011
Teacher's Assistant and Lab Advisor

- Accurately ran general chemistry & organic chemistry laboratory with approximately 25 students each
- Kept office hours to tutor and be available to help teach chemistry
- Familiar with all laboratory exercises and their procedure

Student Affiliates of the American Chemical Society, Muncie, IN
2007-2011
Secretary

- Kept accurate documentation
- Helped plan and assist in community service outreach programs
- Taught children about chemistry and its importance in our everyday lives

Mansfield-King, Indianapolis, IN
Summer 2010
Cosmetic Chemist Paid Internship

- Researched and developed cosmetic products
- Interacted with clients and chemical providers
- Quality control including: pH, viscosity, color, fragrance, etc.
- Developed an electronic database of all syntheses and procedures
- Developed a material database and categorize all chemicals

Chemistry Research Immersion Summer Program, Muncie, IN
Summer 2009
Paid Student Researcher

- Planned research, explain reactions, and keep detailed documentation
- Worked with chemical machinery: ^{1}H NMR, IR, rotary evaporator, etc.
- Presented a poster and oral presentation at Ball State University
- Collaborated with other student chemists

Louis Stokes Alliances for Minority Participation, Muncie, IN
Summer 2009
Nationally Funded Student Researcher

- Worked hands on with chemicals and instrumentation
- Attended meetings to discuss research
- Created and presented poster and oral presentations

Center for Authentic Science Participation in Education, Muncie IN
Spring semester 2009
Student Researcher

- Planned new research on biofuel, explain reactions, and kept detailed documents
- Worked hands on with chemicals and instrumentation
- Collaborated with team members to produce and present research

PRESENTATIONS

Reversible Electron Delocalization of Molecule-Like CdSe Nanoclusters Using Z-type Ligand Functionalization

- Pittcon Conference and Expo., National Conference, Atlanta, GA (*Oral Presenter*, 2016)

Unique Design of $CuInSe_2$ Nanocrystal-decorated Gold Nanoprism Hybrid Conjugates for Advanced Photocatalytic Application

- IUPUI Research Day, Indianapolis, IN *(Poster Presenter,* 2015)

Controlling Electron Delocalization of Molecule-Like CdSe Nanoclusters using Z-type Ligand Functionalization

- Women in STEM Poster Session, Indianapolis, IN (*Poster Presenter,* 2015)

Investigating the Effects of Surface Ligand Chemistry of Electronic Coupling of Ultrasmall Semiconductor Nanocrystals

- Pittcon Conference and Expo., National Conference, Chicago, IL (*Poster Presenter,* 2014)
- Women in STEM Poster Session, Indianapolis, IN (*Poster Presenter,* 2014)
- IUPUI Nanotechnology Research Forum and Poster Symposium, Indianapolis, IN (*Poster Presenter*, 2014)

Investigation of Photophysical and Electrochemical Properties of Magic-Sized CdS Nanocrystals

- American Chemical Society National Meeting, Indianapolis, IN (*Poster Presenter,* 2013)
- IUPUI Departmental Poster Session, Indianapolis, IN (*Poster Presenter,* 2013)
- IUPUI Research Day, Indianapolis, IN (*Poster Presenter,* 2013)

Influence of Organic Solvents and Surface Passivating Ligands on the Stability of CdSe Nanoclusters

- American Chemical Society National Meeting, Indianapolis, IN (*Poster Presenter,* 2013)

Synthesis of Poly(ethylene glycol)-Thiolate Monolayer Coated CdSe Nanoclusters with Unique Solubility Properties

- IUPUI Departmental Poster Session, Indianapolis, IN (*Poster Presenter,* 2012)
- IUPUI Research Day, Indianapolis, IN (*Poster Presenter,* 2012)

Synthesis and Study of an Imine Functionalized Crown Ether

- Louis Stokes Alliances for Minority Participation Indiana Fall Research Conference, West Lafayette, IN (*Oral Presenter,* 2009)
- Tenth Annual Indiana Local Section American Chemical Society Poster Session, Indianapolis, IN (*Poster Presenter*, 2009)

PUBLICATIONS

Lawrence, K. N.; Liyanage, T.; Teunis, M. B.; Sardar, R. Localized Surface Plasmon Resonance-Enhanced Photocatalytic Performance of Ternary Semiconductor Nanocrystals. Manuscript in Progress.

Teunis, M. B.; **Lawrence, K. N.;** Dutta, P.; and Sardar, R. Ultra-small Organolead Halide Nanoparticles with Tunable White-Light Emission. Manuscript in Progress 2016.

Lawrence, K. N.; Dutta, P.; Nagaraju, M.; Muhoberac, B. B.; Tenuis, M.; and Sardar, R. Dual Role of Metal-Carboxylate Ligands: Reversible Exciton Delocalization and Passivation of Nonradiative Trap-States in Molecule-Like CdSe Semiconductor Nanocrystals. Submitted to Chemistry of Materials 2016.

Lawrence, K. N.; Jana, A.; Teunis, M. B.; Mandal, M.; Kumbhar, A.; and Sardar, R. Investigating the Control by Quantum Confinement and Surface Ligand Coating of Photocatalytic Efficiency in Chalcopyrite Copper Indium Diselenide Nanocrystals. Chemistry of Materials 2016, 28 (4), 1107–1120.

Joshi, G. K.; Deitz-McElyea, S.; Liyanage, T.; **Lawrence, K N..**; Mali, S.; Sardar, R.; Korc, M. Label-Free Nanoplasmonic-Based Short Noncoding RNA Sensing at Attomolar Concentrations Allows for Quantitative and Highly Specific Assay of MicroRNA-10b in Biological Fluids and Circulating Exosomes. ACS Nano 2015, 9 (11), 11075-11089.

Lawrence, K.N.; Sardar, R.; Johnson, M.; Dolai, S.; Kumbhar, A. Solvent-like ligand-coated ultrasmall cadmium selenide nanocrystals: Strong electronic coupling in a self-organized assembly. Nanoscale 2015, 7, 11667-11677.

Lawrence, K. N.; Dolai, S.; Lin, Y.-H.; Dass, A.; Sardar, R. Enhancing the physicochemical and photophysical properties of small (<2.0 nm) CdSe nanoclusters for intracellular imaging applications. RSC Advances 2014, 4, 30742-30753.

HONORS

Chemical and Chemical Biology Graduate Dissertation Award 2016
Dean's List 2007-2011
Midwest Society of Cosmetic Chemists Scholarship Recipient 2010-2011
Verizon Scholarship recipient 2007-2011
Delta Faucet Scholarship recipient 2007-2011
Verizon WAVE Scholarship recipient 2008-2009
Cardinal Chemist recipient 2007-2008
Community Foundation Scholarship recipient 2007-2008
Valedictorian 2007

INSTRUMENTATION PROFICIENCY

UV-Visible spectroscopy (UV-Vis)
Fluorescence spectroscopy (PL)
Fourier Transform Infrared spectroscopy (FTIR)
Proton and Phosphorus Nuclear Magnetic Resonance (^{1}H and ^{31}P NMR)
Energy-dispersive X-ray spectroscopy (EDS)
Scanning Electron Microscopy (SEM)
Dynamic Light Scattering (DLS)
Electrospray Ionization mass spectrometry (ESI)

SOFTWARE PROFICIENCY

Microsoft Excel & Word, Mathematic, Sigma Plot, ImageJ

ASSOCIATIONS

American Chemical Society, 2012-present
Society of Cosmetic Chemists, 2010-2012
National Society of Collegiate Scholars, 2007-2011

VOLUNTEER WORK

Rosedale Hills United Methodist Church, Indianapolis, IN
Children Ministries, 2015-current

Science Day, Muncie, IN
2nd and 3rd Grade Contest Coordinator and Volunteer, 2008-2011

ACS Science Day at the Children's Museum, Indianapolis, IN
Volunteer, 2008 and 2010